Improving Image Reconstruction for Digital Breast Tomosynthesis

by

Jiabei Zheng

A dissertation submitted in partial fulfillment
of the requirements for the degree of
Doctor of Philosophy
(Electrical Engineering: Systems)
in The University of Michigan
2018

Doctoral Committee:

Professor Heang-Ping Chan, Co-Chair
Professor Jeffrey A. Fessler, Co-Chair
Professor Mitchell M. Goodsitt
Associate Professor Clayton D. Scott

Jiabei Zheng
jiabei@umich.edu
ORCID iD: 0000-0002-4755-4655

ACKNOWLEDGEMENTS

First of all, I would like to express my deepest gratitude to Prof. Heang-Ping Chan and Prof. Jeffrey A. Fessler for being amazing research advisors and life mentors. I admire Prof. Heang-Ping Chan's immense and extensive knowledge and strict but caring personality. Her scientific attitude and self-disciplined working style deeply inspired me to be a better researcher and more importantly, to be a more mature and reliable person, that I will benefit from for the rest of my life. Prof. Jeffrey A. Fessler never ceases to amaze me with his scientific insights and passion about life. The brainstorming in his office has always been exciting and productive. His skills on piano, ping-pong and gateball also surprised me, making the parties in his house unforgettable experience. It is an honor for me to work with you. Thank you so much for always being on my side.

I would also like to thank my other dissertation committee members: Prof. Clayton D. Scott and Prof. Mitchell M. Goodsitt, for their time and helpful suggestions. Your participation in this dissertation is mostly appreciated.

Next, I would like to thank Paul F. Fitzgerald and Mingye Wu from GE Global Research and Pablo Milioni de Carvalho from GE Healthcare, for providing the access and support for CatSim, an excellent tomography simulation environment. Thank you so much for your generous help. I would also like to acknowledge the National Institutes of Health (NIH) for the grant R01 CA151443 as the financial support of my PhD study.

Inside the Computer-Aided Diagnosis Research Laboratory, I would like to thank Prof. Lubomir Hadjiyski, Dr. Ravi K. Samala and Dr. Kenny Heekon Cha for their consistent support on software and hardware and suggestions when I faced technical difficulties. I also appreciate Prof. Yuni Dewaraja and Dr. Se Young Chun, for being my research advisor and colleague when I was a master's student at the University of Michigan.

I would like to thank my friends in Ann Arbor: Huichao Ma, Luyao Ma, Yao Li, Hui Li, Lianli Liu and Tianrui Luo, for the happy time we spent together. Also Many thanks to Dr. Wenqing Sun for the insights and help in the field of deep learning.

Last but not least, I would like to thank my parents in China, Hongying He and Yongchao Zheng, for always being there to support and to encourage me. Your endless love is the most valuable thing in my life.

TABLE OF CONTENTS

LIST OF FIGURES

Figure

LIST OF TABLES

Table

LIST OF ABBREVIATIONS

ACR	American college of radiology
ART	algebraic reconstruction technique
ASF	artifact spread function
BB	beads
CC	cranial-caudal
CNR	contrast-to-noise ratio
CT	computed tomography
DBCN	detector blur and correlated noise
DBT	digital breast tomosynthesis
DFT	discrete Fourier transform
DQE	detective quantum efficiency
FBP	filtered back-projection
FFT	fast Fourier transform
FOM	figure of merit
FOV	field-of-view
FP-CBCT	flat-panel cone-beam CT
FWHM	full-width at half maximum
IR	iterative reconstruction
LCC	left cranial-caudal
LMLO	left mediolateral-oblique
LP	line pairs
MBIR	model-based image reconstruction
MC	microcalcification
MLO	mediolateral-oblique
MTF	modulation transfer function
NPS	noise power spectrum
OS	ordered subset
PDF	probability distribution function
PLWS	penalized weighted least-squares
PSF	point spread function
PV	projection view
RCC	right cranial-caudal

RMLO	right mediolateral-oblique
RMSE	root mean square error
RT	ray-tracing
SART	simultaneous algebraic reconstruction technique
SF	separable footprint
SG	segmented separable footprint
SIRT	simultaneous iterative reconstruction technique
SQS	separable quadratic surrogate
SWNC	spatially weighted non-convex
TPA	truncated projection artifact
TV	total variance
VOI	volume of interest

ABSTRACT

Digital breast tomosynthesis (DBT) has been developed to reduce the issue of overlapping tissue in conventional 2-D mammography for breast cancer screening and diagnosis. In the DBT procedure, the patient's breast is compressed with a paddle and a sequence of x-ray projections is taken within a small angular range. Tomographic reconstruction algorithms are then applied to these projections, generating tomosynthesized image slices of the breast, such that radiologists can read the breast slice by slice. Studies have shown that DBT can reduce both false-negative diagnoses of breast cancer and false-positive recalls compared to mammography alone.

This dissertation focuses on improving image quality for DBT reconstruction. Chapter I briefly introduces the concept of DBT and the inspiration of my study. Chapter II covers the background of my research including the concept of image reconstruction, the geometry of our experimental DBT system and figures of merit for image quality. Chapter III introduces our study of the segmented separable footprint (SG) projector. By taking into account the finite size of detector element, the SG projector improves the accuracy of forward projections in iterative image reconstruction. Due to the more efficient access to memory, the SG projector is also faster than the traditional ray-tracing (RT) projector. We applied the SG projector to regular and subpixel reconstructions and demonstrated its effectiveness. Chapter IV introduces a new DBT reconstruction method with detector blur and correlated noise modeling, called the SQS-DBCN algorithm. The SQS-DBCN algorithm is able to significantly enhance microcalcifications (MC) in DBT while preserving the appearance of the soft tissue and mass margin. Comparisons between the SQS-DBCN algorithm and several modified versions of the SQS-DBCN algorithm indicate the importance of modeling different components of the system physics at the same time.

Chapter V investigates truncated projection artifact (TPA) removal algorithms. Among the three algorithms we proposed, the pre-reconstruction-based projection view (PV) extrapolation method provides the best performance. Possible improvements of the other two TPA removal algorithms have been discussed. Chapter VI of this dissertation examines the effect of source

blur on DBT reconstruction. Our analytical calculation demonstrates that the point spread function (PSF) of source blur is highly shift-variant. We used CatSim to simulate digital phantoms. Analysis on the reconstructed images demonstrates that a typical finite-sized focal spot (~ 0.3 mm) will not affect the image quality if the x-ray tube is stationary during the data acquisition. For DBT systems with continuous-motion data acquisition, the motion of the x-ray tube is the main cause of the effective source blur and will cause loss in the contrast of objects. Therefore modeling the source blur for these DBT systems could potentially improve the reconstructed image quality. The final chapter of this dissertation discusses a few future studies that are inspired by my PhD research.

CHAPTER I.

Introduction

I.1 Breast cancer and mammography

Breast cancer is the most common non-skin cancer and second deadliest cancer in women. 1,677,000 new cases of breast cancer were diagnosed in 2012 [3]. The incidence rate of breast cancer is especially high in the United States that about one in eight women will be diagnosed with breast cancer at some point during their lifetime [4].

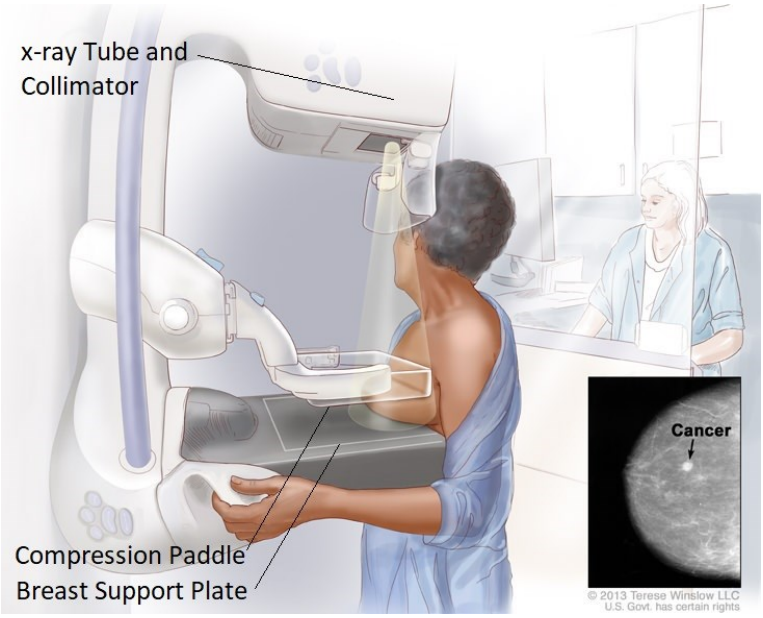

Figure 1.1. A typical full-field digital mammography system. An anti-scatter grid and a flat panel detector are enclosed inside the breast support structure.

The stage of breast cancer is the dominant prognostic factor [5]. A reliable breast cancer screening technique that can detect breast cancer at early stages can potentially save thousands of lives all around the world. Currently, the commonly used breast cancer screening technique is

mammography [6-9]. Mammography is a low-cost, high-resolution, fast and non-invasive breast imaging technique with low radiation dose. The mammography system is shown in Figure 1.1. During the mammography procedure, the breast of the patient is compressed along two directions, providing two dimensional (2-D) x-ray projection images of the breast from two views, the cranial-caudal (CC) view and the mediolateral-oblique (MLO) view. In this procedure, the compression of the breast reduces the breast tissue thickness that x-ray penetrates, which helps to reduce the noise and the scattered radiation. Radiologists use the scanned x-ray projection images to check whether there exist any abnormal growths in the breast.

Despite the high incidence rate of breast cancer and importance of early detection in treatment, the benefits of breast cancer screening are controversial due the relatively low sensitivity and specialty of mammography [9-11]. Standard mammography is known to suffer from the problem of overlapping tissue because of the 2-D nature of the method. The overlapping of lesion and dense glandular tissue can lead to false negative diagnosis, while overlapping normal features can appear to be lesion and result in false positive diagnosis. For women with heterogeneously or dense breast, the sensitivity of mammography could be lower than 70% [12]. It is also known that the sensitivity of mammography is low for young women [12]. As a result, in the United States screening of breast cancer is only recommended every two years in women between the ages of 50 to 74 who are at normal risk for breast cancer [13].

I.2 Digital breast tomosynthesis

To overcome the limitations of traditional mammography, researchers have proposed using tomosynthesis to enhance the quality of breast imaging for both screening and diagnosis by reducing the issue of overlapping tissue in mammography. When the concept of tomosynthesis first appeared, it was not proposed for medical use. The concept of tomosynthesis was derived by Ziedses des Plantes [14] in 1930s, which was referred to as ‘geometric tomography’. In conventional geometric tomography, the x-ray tube and the film were moved in opposite directions. By choosing the shift of the x-ray tube and the film, a certain plane inside the imaged object is in focus such that only features within this plane will get enhanced. Therefore, this technique can be used to reduce the issue of overlapping structures of the 2-D mammography.

Instead of enhancing the image at one specific depth, digital tomosynthesis enhances all slices of the imaged volume at the same time to generate a three dimensional (3-D) reconstructed

image. Digital tomosynthesis acquires a series of projections of the imaged object within a narrow angular range. A tomographic reconstruction algorithm is applied to the projections to generate a 3-D image of the object. This is equivalent to arbitrarily adjusting the shift of the x-ray tube and the film in conventional geometric tomography to choose an arbitrary focal plane. Because of the limited scan angle, the spatial resolution of tomosynthesis is anisotropic with high in-plane resolution and low in-depth resolution. The data acquisition is incomplete, such that tomosynthesis is sometimes called pseudotomographic imaging, in comparison with computed tomography (CT) where the source and detector make at least a complete 180 degree rotation to obtain a complete set of projections.

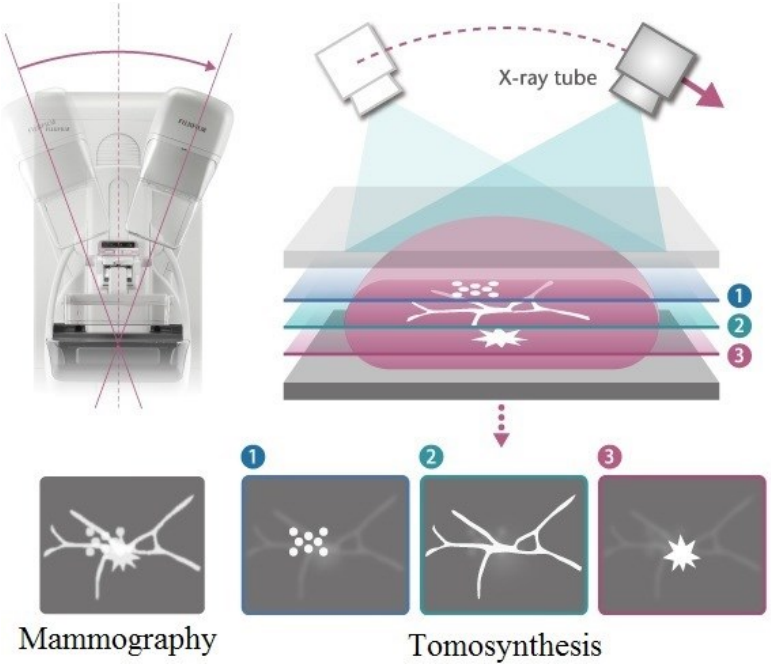

Figure 1.2. Principle of the DBT system (image source: Fujifilm website).

The application of tomosynthesis on breast imaging was first demonstrated by Niklason et al. in 1997 [15] after the invention of flat-panel detectors capable of measuring high-resolution x-ray projection images. The newer procedure is called digital breast tomosynthesis (DBT). The acquisition geometry of DBT is similar to mammography, as shown in Figure 1.2. In the DBT procedure, the breast of the patient is compressed in the same way as mammography. The x-ray tube swings to collect a set of digital projection images with lower x-ray dose. After image reconstruction, image slices will be obtained at each depth of the compressed breast, as shown in

the lower right corner of Figure 1.2. The overlapping tissue on the mammography image (lower left corner of Figure 1.2) now clearly displays a cluster of dots, a network of lines and a star-shaped area of dense tissue on three different slices with tomosynthesis. The clear structures of breast tissue on the DBT slices will help radiologists to make more accurate diagnosis. The DBT slices, on the other hand, can also be summed to produce an image similar to mammography. In fact, because of the similarity and connection between mammography and DBT, DBT is sometimes called '3D mammography' in the commercial systems and these systems are usually able to perform traditional mammography procedure at the same time. Clinically, the DBT procedure is usually done to assist traditional mammography. Studies have shown that a combination of DBT and mammography can reduce both false-negative diagnoses of breast cancer and false-positive recalls compared to mammography alone [16-24].

I.3 Limitations of DBT and the inspiration of this dissertation

Despite the advantages of DBT, it also has limitations in practice. The total dose of DBT is comparable with mammography; therefore each projection image of DBT is acquired with low x-ray dose, making them much noisier. The motion of the x-ray source in DBT can cause blurring for projections, especially for DBT systems using the continuous-motion data acquisition [25-27]. The acquisition time of DBT is also longer than mammography, increasing the discomfort of the patient due to breast compression and making the motion of the breast more likely to happen to cause blurring of the image. In fact, the DBT procedure has not been accepted as a reliable breast imaging technique and is usually used to assist the traditional mammography.

Considering DBT's potential in the diagnosis of breast cancer and its limitations, my PhD study aims to overcome the limitations of DBT to make it a more reliable breast imaging technique. In x-ray CT, studies have demonstrated the possibility of lowering the dose while maintaining the image quality with statistical image reconstruction methods [28, 29]. For DBT, studies have also shown the promise of iterative reconstruction (IR) methods in improving image quality [30-36]. Among the IR methods, model-based image reconstruction (MBIR) methods incorporate the physics model of the system and the statistical model of signal detection. Studies on different 3D modalities [37-45] have demonstrated the benefits of modeling the system physics to improve the image quality. Although some studies on MBIR methods for DBT have

been conducted [41, 42], they considered only limited aspects of the system model. The idea of MBIR needs further investigation to show its potential in DBT applications.

My PhD research focuses on improving the reconstructed image quality for DBT by developing improved post-acquisition reconstruction methods. The idea of MBIR inspires many studies introduced in this dissertation, as introduced in following chapters.

I.4 Outline of the dissertation

In this dissertation, Chapter II introduces the background of my study, including the concepts of tomographic reconstruction, statistical image reconstruction and MBIR, the geometry of our experimental DBT system, the projection compensation multiplier, the truncated projection artifact (TPA) and the figures of merit (FOM) for image quality in DBT. The concepts, notations and equations in this chapter will be used in the following chapters.

Chapter III introduces the segmented separable footprint projector (SG projector) and subpixel image reconstruction. The SG projector improves the accuracy and speed of forward and backward projections in DBT, which improves the accuracy of the system model and enhanced reconstructed image quality as demonstrated with the simulated phantoms. The advantage of the SG projector over the traditional ray-tracing (RT) projector is especially significant when used in subpixel reconstruction. This study also demonstrates that a better match between the digital implementation and the actual system physics can improve image quality in DBT reconstruction.

Chapter IV introduces the SQS-DBCN algorithm, a new image reconstruction algorithm for DBT that accounts for detector blur and correlated noise (DBCN). This method is inspired by MBIR. By incorporating the system physics, the SQS-DBCN method significantly enhanced the contrast-to-noise ratio (CNR) of the reconstructed microcalcifications (MC) in our experimental phantom. The SQS-DBCN method also controls the noise and preserves the image quality of soft tissue. Further tests with modified versions of the SQS-DBCN algorithm demonstrated the importance of incorporating different model components at the same time.

Chapter V introduces our comparative study on TPA removal. We proposed and tested three TPA removal methods based on the extrapolation of the measured projection images or the regularized image reconstruction. Among the three methods, the pre-reconstruction-based

projection view (PV) extrapolation method provides the best performance. Potential improvements of the other two methods have been discussed in this chapter.

Chapter VI investigates the effect of source blur on DBT reconstruction. We first studied the spatial shift-variance of the point spread function (PSF) of the source blur. Then we used simulated phantoms to demonstrate that for DBT systems with a typical focal-spot size (~0.3mm) and stationary data acquisition, the influence of the finite-sized focal spot can be neglected. For DBT systems with continuous-motion data acquisition, the motion of the x-ray tube is the main source of the effective source blur and might cause obvious degradation in image quality. Modeling the source blur could potentially improve image quality for these systems.

Chapter VII briefly summarizes the studies in the dissertation and discusses potential future studies based on the conclusions and limitations of this dissertation.

CHAPTER II.
Background

This chapter introduces the background of my PhD study. The concepts, notations, figures, equations and system parameters introduced in this chapter will be used in the following chapters of this dissertation.

II.1 Introduction to DBT image reconstruction

DBT is a type of X-ray tomographic imaging technique. By taking use the penetrating power of X-ray, it allows the user to see inside the scanned object. In the DBT procedure, cone-shaped x-ray beams are generated by the x-ray source to penetrate the scanned object from different angles. The attenuated x-ray beams are measured by a detector to create 2-D projection images or projection views (PV) of the scanned object at different angles. By processing the PVs, the distribution of the x-ray attenuation coefficient can be estimated in the 3-D volume. This 3-D distribution is the reconstructed image that reveals the structure inside the scanned object.

The procedure of estimating the 3-D distribution of the x-ray attenuation coefficient from the PVs is called tomographic reconstruction. Mathematically, tomographic reconstruction is a type of inverse problem. Let $f(x, y, z)$ denote the 3-D distribution of the x-ray attenuation coefficient. If we neglect the fluctuation of x-ray radiation and the scattered radiation, the attenuation of the x-ray beam inside the breast follows the Lambert-Beer law:

$$Y(t, s; i) = Y_0(t, s; i) \exp\left(- \int_{L(t,s;i)} f(x, y, z) \mathrm{d}l \right), \tag{2.1}$$

where (t, s) denotes a location on the detector, (x, y, z) denotes a location in the 3-D volume, i denotes the index of the projection angle, $L(t, s; i)$ denotes the line from the x-ray source to the location (t, s) for the ith projection angle, $Y(t, s; i)$ denotes the projection value at (t, s) and

$Y_0(t,s;i)$ denotes the projection value if there is no object is in the 3-D volume. $Y_0(t,s;i)$ can be measured with an air scan and is usually considered known. In this dissertation we focus on the case where this (mono-energetic) Lambert-Beer law (Equation 2.1) holds for the measured or simulated data from a poly-energetic x-ray source with beam hardening [46].

By taking log transform to both sides of Equation 2.1, we have:

$$y(t,s;i) = \int_{L(t,s;i)} f(x,y,z)dl, \tag{2.2}$$

where

$$y(t,s;i) = \log\left(\frac{Y_0(t,s;i)}{Y(t,s;i)}\right). \tag{2.3}$$

The right-hand side of Equation 2.2 is known as the Radon transform of $f(x,y,z)$, which is a linear transform [47]. Since both $Y(t,s;i)$ and $Y_0(t,s;i)$ are known, $y(t,s;i)$ can be easily calculated with Equation 2.3. Therefore the problem of tomographic reconstruction is to estimate the unknown distribution of $f(x,y,z)$ from the known values of $y(t,s;i)$ at different locations measured from different projection angles.

Equation 2.1-2.3 explains the concept of image reconstruction for a continuous 3-D image and continuous projections. In the practical implementation of image reconstruction, both the PVs and the reconstructed image are digitalized. We denote the discrete array of x-ray attenuation coefficients as **f**. Although **f** is a 3D distribution, we write it as a column vector such that a linear operation on **f** can be written as multiplying it by a matrix. Denoting the number of voxels in the imaged volume to be *N*, **f** is a length-*N* column vector. Assuming the number of pixels of one PV to be *M*, which is the same for all projection angles, we can use a length-*M* column vector $\mathbf{Y}_i$ to denote the *i*th measured projection image. Let N_p denote the total number of projection angles; we write all the projection images as one column vector, denoted as **Y**:

$$\mathbf{Y} = \begin{pmatrix} \mathbf{Y}_1 \\ \vdots \\ \mathbf{Y}_{N_\mathrm{p}} \end{pmatrix}. \tag{2.4}$$

The log-transformed PVs are written as:

$$\mathbf{y} = \log\left(\frac{I_0}{\mathbf{Y}}\right) = \begin{pmatrix} \mathbf{y}_1 \\ \vdots \\ \mathbf{y}_{N_\mathrm{p}} \end{pmatrix}, \tag{2.5}$$

where the length-*M* column vector $\mathbf{y}_i$ denotes the log-transformed PV at the *i*th projection angle. For simplicity we assume that $Y_0(t,s;i) = I_0$, that I_0 is a constant. In fact due to the heel effect

of the anode and the non-uniform incident angle of x-rays, $Y_0(t,s;i)$ is usually non-uniform. To consider the non-uniformity of $Y_0(t,s;i)$, one can simply replace the scalar I_0 with the measured air scans or an estimated distribution of the air scans.

With the digitalized $\mathbf{y}_i$ and $\mathbf{f}$, the linear Radon transform in Equation 2.2 can be written in the form of matrix multiplication:

$$\mathbf{y}_i = \mathbf{A}_i\mathbf{f}. \tag{2.6}$$

$\mathbf{A}_i$ is called the system matrix at the *i*th projection angle. The size of $\mathbf{A}_i$ is *M*×*N*. Since $\mathbf{y}_i$ is the 2-D projection generated by the 3-D image $\mathbf{f}$, the operation $\mathbf{A}_i\mathbf{f}$ is called the forward projection. $\mathbf{A}_i$ is also known as the forward projector in tomographic reconstruction. We call $\mathbf{A}_i\mathbf{f}$ 'forward projection' instead of just 'projection' to differentiate it from the backward projection. The backward projection applied to a PV $\mathbf{y}_i$ can be written as:

$$\mathbf{f}_i = \mathbf{A}_i'\mathbf{y}_i, \tag{2.7}$$

where $\mathbf{A}_i'$ is the transpose of the matrix $\mathbf{A}_i$. $\mathbf{f}_i$ is the result of the backward projection, which is a length-*N* vector (same size as $\mathbf{f}$). $\mathbf{A}_i'$ is called the backward projector. Obviously Equation 2.7 is not the inverse operation of Equation 2.6. In fact, $\mathbf{A}_i$ is usually not a square matrix and its inverse does not exist. The backward projection is commonly used in tomographic reconstruction to update the values of $\mathbf{f}$ from the measured data. The details will be discussed in the next section.

The value of the matrix element $\mathbf{A}_i(m,n)$ represents the contribution of the *n*th voxel of the image $\mathbf{f}$ to the *m*th pixel of the PV $\mathbf{y}_i$. In many studies on DBT reconstruction, $\mathbf{A}_i(m,n)$ is assumed to be the intersection length of the x-ray from the source to the center of the *m*th detector element with the *n*th voxel of the 3-D image. In Chapter III, we will show the derivation of $\mathbf{A}_i(m,n)$. The derivation indicates that assuming $\mathbf{A}_i(m,n)$ to be the intersection length is equivalent to using the simplified detection model that each detector element has infinite sensitivity at the center and zero sensitivity at all other locations. We will also introduce our new calculation of $\mathbf{A}_i(m,n)$ that improves the accuracy and speed of both the forward and backward projections in iterative DBT reconstruction.

According to Equation 2.6, the image reconstruction problem in DBT is to find a solution to the following set of linear equations:

$$\mathbf{y} = \mathbf{A}\mathbf{f}, \tag{2.8}$$

where $\mathbf{A}$ is the system matrix corresponding to all projection angles:

$$\mathbf{A} = \begin{pmatrix} \mathbf{A}_1 \\ \vdots \\ \mathbf{A}_{N_\mathrm{p}} \end{pmatrix}. \tag{2.9}$$

Due to the huge total number of voxels in DBT reconstruction ($N \sim 10^8$), Equation 2.8 is a large-scale inverse problem. Multiple methods to solve Equation 2.8 have been proposed and studied, as introduced in the next section.

II.2 Image reconstruction algorithms

The image reconstruction in Equation 2.8 is a simplified form of the problem. In practical DBT, the projection images are highly noisy due to the limited x-ray dose of each projection. In this section, we will discuss three categories of image reconstruction algorithms that have been studied or are practically used in commercial DBT systems. These three categories of algorithms are: (1) filtered back-projection (FBP); (2) the algebraic reconstruction algorithms; (3) the statistical reconstruction algorithms.

The FBP algorithm is a type of Fourier-domain reconstruction algorithm [45, 48-52]. Simply speaking, the FBP method is a frequency-domain-based transform applied to $\mathbf{y}$ that can be briefly written as:

$$\hat{\mathbf{f}} = \mathrm{FBP}(\mathbf{y}), \tag{2.10}$$

where the operation $\mathrm{FBP}(\cdot)$ consists of high-pass filters and backward projections.

The FBP reconstruction has been used in commercial DBT systems by Hologic and Siemens [44]. The high-pass filters needs to be carefully designed to preserve image quality without severely amplifying the noise. The details of the filters used in commercial DBT systems cannot be found in literatures. In the following chapters of this dissertation, we mainly focus on iterative reconstruction methods for DBT. As result, we will not discuss the FBP algorithm in detail.

Different from the FBP method that directly applies a transform to the projection images, the algebraic reconstruction algorithms [53-55] try to solve Equation 2.8 with iterative methods. The original algebraic reconstruction algorithm is known as the algebraic reconstruction technique (ART). It updates the distribution of the x-ray attenuation coefficients ($\mathbf{f}$) ray by ray to satisfy one row of the Equation 2.8 at a time. Due to the existence of noise, Equation 2.8 does not have a precise solution and the ART algorithm is known to generate highly noisy reconstructed images [31]. Several modified versions of the ART algorithm have been proposed such as the

simultaneous iterative reconstruction technique (SIRT) [53, 55] and the simultaneous algebraic reconstruction technique (SART) [56, 57]. The comparative study previously conducted by our lab demonstrated the effectiveness of SART in DBT reconstruction [31]. SART is an iterative reconstruction method that the update of the image $\mathbf{f}$ can be written as:

$$\mathbf{f}^{(i_{\mathrm{SART}},i+1)} = \mathbf{f}^{(i_{\mathrm{SART}},i)} + \lambda_{i_{\mathrm{SART}}} \left(\mathbf{A}_i{}' \left((\mathbf{y}_i - \mathbf{A}_i \mathbf{f}) \oslash (\mathbf{A}_i \mathbf{1}_N) \right) \right) \oslash (\mathbf{A}_i{}' \mathbf{1}_M), \tag{2.11}$$

where i is the index of the projection angle and i_{SART} is the index of the SART iteration. $\mathbf{1}_N$ and $\mathbf{1}_M$ denote length-N and length-M all-one vectors. The symbol $\oslash$ denotes the element-wise division. i_{SART} is increased by one after all PVs ($i = 1,2,\dots,N_{\mathrm{p}}$) have been used once. The forward projector $\mathbf{A}_i$ and its transpose, the backward projector $\mathbf{A}_i{}'$, were introduced in the previous section. $\lambda_{i_{\mathrm{SART}}}$ is the relaxation factor that is equal to or smaller than 1 to control the amplification of the noise.

We use SART to reconstruct the simulated digital phantoms in Chapter III and VI. SART is also used as a reference algorithm in Chapter IV to compare with our new reconstruction method. Although not state-of-the-art, SART has been shown to provide good image quality for reconstructing DBT acquired with our prototype DBT system [31] and has been evaluated by other investigators [44, 58]. SART will also be used to test our artifact removal methods in Chapter V.

One disadvantage of algebraic methods is the lack of statistical model of the noise. When using algebraic methods, it is also difficult to apply regularization to control the amplification of noise when using the iterations. For this reason, in the image reconstruction for our experimental DBT system, we usually do only 1 or 2 SART iterations [31]. The statistical reconstruction algorithms, on the other hand, allow the probability model of the noise to be considered and flexible choice of regularizations. For statistical image reconstruction algorithms, we include a noise vector $\boldsymbol{\epsilon}_i$ in Equation 2.6 for the ith projection angle. Therefore we have the following expression for the measurement model:

$$\mathbf{y}_i = \mathbf{A}_i \mathbf{f} + \boldsymbol{\epsilon}_i. \tag{2.12}$$

Here, the noise $\boldsymbol{\epsilon}_i$ has the same size as $\mathbf{y}_i$. It is a realization of a random vector with a known probability distribution function (PDF) that represents the statistical model of the noise. Therefore $\mathbf{y}_i$ is also a realization of a random vector. The PDF of this random vector can be derived from the noise model if $\mathbf{f}$ is given. We also include a probability model $P_{\mathbf{f}}(\mathbf{f})$ for $\mathbf{f}$ that

represents our prior knowledge or expectation for the image to be reconstructed. The statistical image reconstruction tries to find $\hat{\mathbf{f}}$ such that:

$$\hat{\mathbf{f}} = \underset{\mathbf{f}}{\operatorname{argmax}}\, P(\mathbf{f}|\mathbf{y}) = \underset{\mathbf{f}}{\operatorname{argmax}}\, P_{\mathbf{y}|\mathbf{f}}(\mathbf{y}|\mathbf{f}) P_{\mathbf{f}}(\mathbf{f}), \tag{2.13}$$

where $P_{\mathbf{y}|\mathbf{f}}(\mathbf{y}|\mathbf{f})$ is the PDF of $\mathbf{y}$ given $\mathbf{f}$. The function $P_{\mathbf{f}}(\mathbf{f})$ serves as a regularization term when we formulate the optimization problem.

A common choice of the probability model for $\boldsymbol{\epsilon}_i$ is the multivariate Gaussian distribution with zero mean. Let $\mathbf{K}_i$ denote the covariance matrix of this distribution. Assume that $P_{\mathbf{f}}(\mathbf{f})$ can be written as the exponent of a function: $P_{\mathbf{f}}(\mathbf{f}) = \exp\big(-R(\mathbf{f})\big)$, then Equation 2.13 simplifies to be a regularized quadratic optimization problem:

$$\hat{\mathbf{f}} = \underset{\mathbf{f}}{\operatorname{argmin}} \sum_{i=1}^{N_{\mathbf{p}}} \frac{1}{2} \|\mathbf{y}_i - \mathbf{A}_i \mathbf{f}\|^2_{\mathbf{K}_i^{-1}} + R(\mathbf{f}), \tag{2.14}$$

This is the commonly used form of the optimization problem in statistical image reconstruction. Similar to the algebraic image reconstruction, Equation 2.14 must be solved with iterative methods.

Compared with Equation 2.7, the expression of Equation 2.14 allows us to include a covariance matrix for the noise, which can be estimated from the measured data given the assumptions on the correlation of the noise. Equation 2.14 also allows us to choose $R(\mathbf{f})$ based on our expectation of the image $\mathbf{f}$. The linear operation $\mathbf{A}_i$ can include the modeling of the physics of the imaging system, such as the blurring of the detector. In summary, Equation 2.14 allows us to incorporate different model components into the image reconstruction. When these model components are incorporated based on the realistic system physics, the resulting reconstruction algorithm is called a model-based image reconstruction (MBIR) algorithm. Modeling system physics in image reconstruction has been investigated in CT and other 3D modalities and improvement in image quality has been observed [37-46, 59-62]. The idea of MBIR is a major inspiration of many studies introduced in this dissertation. The connection between the studies and the idea of MBIR will be discussed in details in each of the following four chapters.

The regularization term $R(\mathbf{f})$ in Equation 2.14 is especially important for DBT reconstruction. The system matrix $\mathbf{A}$ usually has more columns than rows in DBT, making Equation 2.14 an underdetermined problem without regularization. Due to the narrow scan angle of DBT, the unregularized image reconstruction is an ill-posed inverse problem that small measurement

fluctuation such as noise could cause large perturbations of the reconstructed. Several studies have been conducted on regularization of limited-angle reconstruction. For example, the total variation (TV) method was applied to DBT reconstruction [32, 63]. We have also proposed a spatially weighted non-convex (SWNC) regularization for enhancing microcalcifications (MC) in DBT reconstruction; this work was published as an SPIE proceedings paper [64]. Considering the limited practical value of this method, it is not included in this dissertation. In Chapter III and VI, we use noiseless simulated projections so unregularized SART provides satisfactory reconstruction results. In Chapter IV where we use the experimental data, the edge-preserving regularization has been demonstrated to play an important role in our new reconstruction method.

Before ending this section, we introduce a more general form for statistical image reconstruction. In Equation 2.12, the noise is considered to be additive to the log-transformed projection $\mathbf{y}_i$. In fact, a more general form of Equation 2.12 considers the noise to be additive to the originally measured projection images $\mathbf{Y}$ before the log transform. This will give us the following expression for statistical image reconstruction:

$$\hat{\mathbf{f}} = \underset{\mathbf{f}}{\operatorname{argmax}}\, P(\mathbf{f}|\mathbf{Y}) = \underset{\mathbf{f}}{\operatorname{argmax}}\, P_{\mathbf{Y}|\mathbf{f}}(\mathbf{Y}|\mathbf{f})P_{\mathbf{f}}(\mathbf{f}), \tag{2.15}$$

where $P_{\mathbf{Y}|\mathbf{f}}(\mathbf{Y}|\mathbf{f})$ is the PDF of $\mathbf{Y}$ given $\mathbf{f}$. $P_{\mathbf{y}|\mathbf{f}}(\mathbf{y}|\mathbf{f})$ in Equation 2.14 sometimes can be derived from $P_{\mathbf{Y}|\mathbf{f}}(\mathbf{Y}|\mathbf{f})$ with approximations, as shown in Chapter IV. Chapter IV starts from Equation 2.15 to derive our cost function. With approximations, the optimization problem formulated is similar to Equation 2.14.

II.3 The experimental DBT system

The DBT system studied in our lab is the GE second generation (GEN2) prototype DBT system. Most of our experimental DBT scans, including the phantom scans and the human-subject cases, were collected with this DBT system. The experimental data will be used in Chapter IV to test our SQS-DBCN reconstruction method for DBT. The CatSim simulation of projections of the digital phantoms in Chapter III matches the geometry of this DBT system. In Chapter VI we simulated projections with the same geometry as the prototype DBT but with enlarged size for the detector to match the commercial DBT systems by GE Healthcare.

Figure 2.1 shows the imaging geometry of the GE GEN2 prototype DBT system. We use *x*-*y*-*z* coordinate for the imaged volume and *t*-*s* coordinate for the detector. In our DBT system, the

source rotates in a plane. We use the term 'rotation center' to denote the point where the rotation axis intersects with the rotation plane of the source. The origin $x,y,z = 0$ (marked as O in Figure 2.1) is the rotation center and $t,s = 0$ is its perpendicular projection on the detector. The x-ray tube rotates in 3° increments to acquire 21 projection images within ±30°. In Chapter IV, we used the 9 central projections for reconstruction to simulate the DBT acquired with narrow-angle DBT system, corresponding to DBT of 24^o scan angle with 3^o increments, which was close to the 25^o scan angle and 3^o increments for the GE commercial system. The x-ray exposure for each DBT was therefore reduced to less than half of the original values.

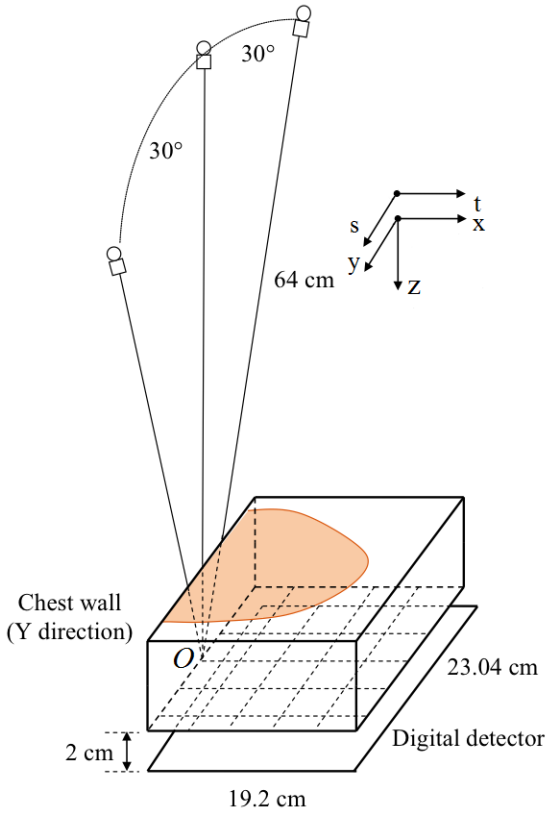

Figure 2.1. Geometry of the GE GEN2 prototype DBT system.

The digital detector is stationary during the acquisition. The system uses a CsI phosphor/a:Si active matrix flat panel detector with a resolution of 1920 × 2304, and the pixel size is 0.1 × 0.1mm^2. The distance from the source to rotation center is 64cm. There is a 2cm gap between the imaged volume and the digital detector. Different DBT systems may have different geometry (e.g., scan angle, angular increments) but the approaches introduced in this dissertation should be applicable to other geometries.

The patient stands in front of the system with the chest wall against the edge of the detector. In most cases, the *x*-direction width of the detector is larger than the width of the compressed breast. The patient's breast usually will not reach the anterior (nipple) side of the detector. As a result, we can trim projection measurements on the anterior side to save computation time. For example, if we trim 520 pixels, we would actually use PVs of resolution 1400 × 2304 in reconstruction.

Since DBT scans only cover a limited angular range around the normal to the detector plane (z-direction), there is not sufficient information from the projection images to determine the breast thickness without adding fiducial markers in the volume being imaged. On the other hand, the distance between the compression paddle and the breast support plate is recorded by the mammography/DBT system and can be used as the thickness of the imaged volume for reconstruction. In clinical DBT systems, the thickness of the imaged volume is usually set to be slightly larger than the recorded distance to allow for uncertainty in the thickness measurement. In DBT reconstruction, the *x*- and *y*-direction resolution of the voxel size is usually set to be the same as the detector pixel size although some systems use pixel binning to reduce reconstruction time and space at the expense of image resolution. The *z*-dimension of the voxel is usually chosen to be 1mm because the z-direction resolution is inherently low. An imaged volume with a voxel size of $0.1 \times 0.1 \times 1\text{mm}^3$ is therefore used in most part of this dissertation. As an example, if the breast thickness is 6 cm and we trim 520 pixels of projection measurements, we will reconstruct an image of the size 1400 × 2304 ×60. An exception is the subpixel reconstruction in Chapter III where we used smaller voxel size and demonstrated that super-resolution can be achieved in DBT. Details of the subpixel reconstruction will be introduced in Section III.4.

II.4 Simulation of digital phantoms by CatSim

In additional to the experimental data, we also used digital phantoms in the studies in Chapters III, IV and VI. The simulation of the digital phantoms was completed by CatSim [65, 66], a computer assisted tomography simulation environment developed by GE Global Research. In this section, I briefly introduce the functions of CatSim and the advantages of using CatSim simulated phantoms. The configurations of the digital phantoms and the simulation will be introduced in details respectively in each chapter.

In our studies on DBT reconstruction, using the simulated phantoms by CatSim has two main advantages. First, CatSim allows us to configure digital phantoms based on the purpose of our study. Since the configuration of the digital phantoms is known, we can define reliable figures of merit (FOM) to quantitatively evaluate the reconstructed image quality. While this is a common advantage of digital phantoms, CatSim can simulate the complicated physics in x-ray imaging. The physics modeling includes x-ray polychromaticity, realistic quantum and electronic noise models, finite focal spot size and shape, finite detector cell size, detector cross-talk, scatter etc. [65]. Therefore the projections generated by CatSim are closer to a real DBT experiment than the projections generated by a simple Radon transform, as used in many researches on tomographic reconstruction. Second, CatSim allows us to flexibly control different components (e.g., detector blur, source blur, noise correlation etc.) of the physics modeling. By purposely turning off the other components, we can focus on the model components that we are interested in. This approach has been used in Chapter III and Chapter VI of this dissertation.

Each CatSim simulation requires a configuration file to specify the geometry and other parameters of the tomographic system. In our CatSim simulation, we specified these parameters (e.g., system geometry, target/filter material, target angle, peak kilovoltage, detector material etc.) to match our experiment conditions with the GE GEN2 prototype DBT system. Although CatSim provides the option to simulate multiple projections with one configuration file, the option was designed for CT systems that the source and the detector move at the same time. For our DBT system with a stationary detector, the rotation of the source is configured by setting an offset distance for the x-ray source. As a result, each projection needs a configuration file in our simulation.

In each CatSim configuration file, the phantom is specified with the FORBILD syntax [65]. Geometrical shapes including boxes, ellipsoids, elliptical cylinders, cones, and cut planes can be specified analytically. The simulation is based on the analytical locations of the geometrical shapes rather than a pixelated phantom. As a result, we can configure high spatial-frequency objects regardless of the detector pixel size or the voxel size of the imaged volume and use the precise locations of the objects to calculate FOMs.

II.5 The projection compensation multiplier

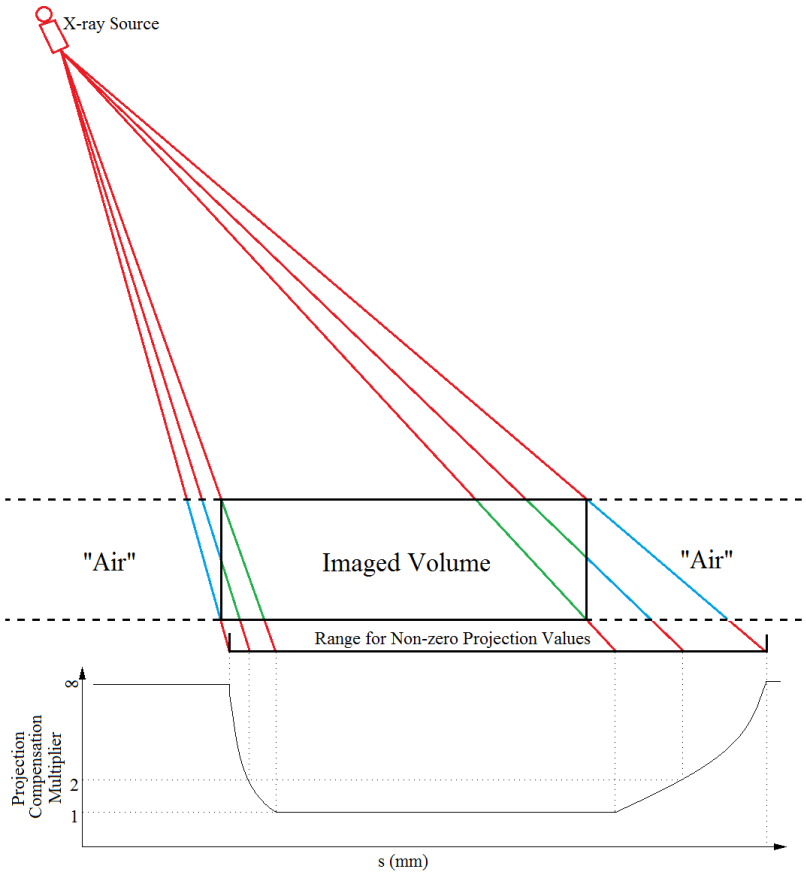

Figure 2.2. The projection compensation multiplier. The DBT system is viewed along the axis of the rotation of the source (*x*-direction in Figure 2.1). A conventional forward projection method treats the region marked as "Air" as having an attenuation coefficient of 0, while in fact it might have breast tissue, especially for the MLO view of the DBT scan.

This section introduces the projection compensation multiplier that is commonly used in our reconstruction methods. Figure 2.2 illustrates the reason that the projection compensation multiplier is needed for DBT reconstruction. Given an imaged volume, only the x-ray attenuation coefficients inside the imaged volume are stored during the DBT reconstruction. When we calculate the forward projection, we only consider the contribution of the imaged volume. In other words, a basic forward projector would treat the region outside the imaged volume as having an attenuation coefficient of 0, which is equivalent to air. In the DBT geometry that the breast is compressed between the compression paddle and the breast support plate, the regions beyond the top layer of the imaged volume and under the bottom layer do not contribute to the measured projection values. However, the regions on the left and right sides of the imaged

volume (marked as "Air" in Figure 2.2) can have breast tissue, especially for the MLO view of the DBT scan. A forward projection method that considers only the breast tissue inside the imaged volume will likely underestimate the projection values in these regions. For reconstruction, this means that we will get abnormally high reconstructed values in the lower-left corner and upper-right corner of the imaged volume when using the PV in Figure 2.2 to update the image. This is known as the glaring artifact for DBT reconstruction [67, 68].

To reduce the glaring artifact and to obtain a more accurate forward projection, we include a projection compensation multiplier as part of the forward projection. Six rays are shown in Figure 2.2. For these six rays, the segments intersecting inside the imaged volume are colored in green. The parts colored blue might contain breast tissue, but are not included in the standard forward projection. Assuming the mean x-ray attenuation coefficient is the same for the blue part and the green part for each ray, for the location (t, s) on the detector plane, we should compensate the projection value by multiplying it with a factor of:

$$M(t,s) = \frac{l_{\text{green}}(t,s) + l_{\text{blue}}(t,s)}{l_{\text{green}}(t,s)}, \tag{2.16}$$

where $l_{\text{green}}(t,s)$ and $l_{\text{blue}}(t,s)$ denote the sections of x-ray path-length plotted in green and blue, respectively, in Figure 2.2.

Given the geometry of the DBT system, the thickness of the imaged volume and the projection angle, this factor can be calculated at any location on the detector plane, even for locations outside the digital detector. Usually we need the projection compensation multiplier only within the detector. But for our truncated projection artifact (TPA) removal methods introduced in Chapter V, where we extrapolate the PVs, we calculate the projection compensation multiplier over the area of the extrapolated PVs, which is larger than the digital detector. For the rays that do not intersect with the imaged volume, the projection compensation multiplier is infinity by Equation 2.16. The projection compensation multiplier is not important for these rays since they will not be used in DBT reconstruction.

For implementation, the projection compensation multiplier is calculated and stored as a real-value vector of the same size of one PV (mathematically a length-*M* column vector). We use $\mathbf{m}_i$ to denote this vector for the *i*th projection angle. Given the thickness of the imaged volume and the projection angle, one can calculate the intersection length with the 'slab' between the top and bottom planes of the imaged volume for each ray from the source to the detector elements

using the imaging system geometry. The result, denoted as $\mathbf{l}_{\text{slab},i}$, is also a vector with the same size of one PV (length-*M* column vector). Then the vector $\mathbf{m}_i$ is calculated with the following equation for the *i*th projection angle:

$$\mathbf{m}_i = \min(\mathbf{l}_{\text{slab},i} \oslash \mathbf{A}_i \mathbf{1}_N, m_{\max}), \tag{2.17}$$

where $\mathbf{1}_N$ denotes an all-one vector of the same size of the imaged volume (length-*N*) and $\oslash$ denotes the element-wise division. $m_{\max}$ is the maximum threshold for the projection compensation multiplier since $\mathbf{A}_i \mathbf{1}_N$ can be very small or zero at some locations as shown in Figure 2.2. The value of $m_{\max}$ does not affect the reconstructed image as long as it is not too small since it is mostly present in the region of the detector plane not used for image reconstruction (the region outside the 'Range for Non-zero Projection values' in Figure 2.2). We empirically use $m_{\max} = 100$. Figure 2.3 shows the calculated projection compensation multiplier map with Equation 2.17 for a 6cm-thick imaged volume at the projection angle of -30°.

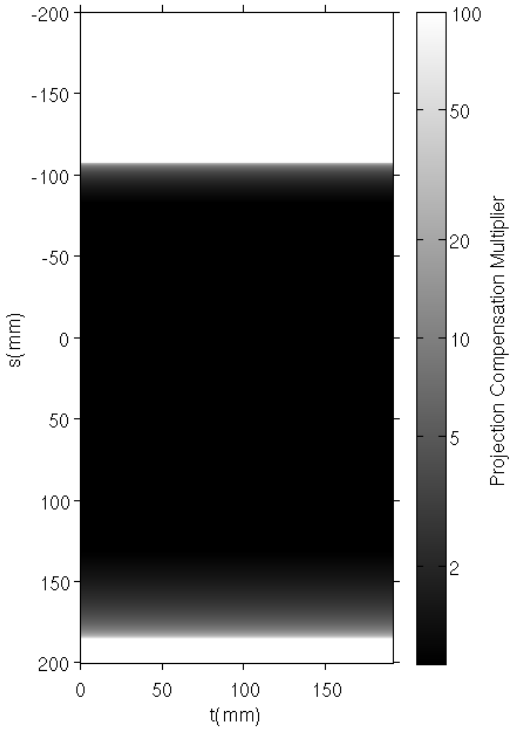

Figure 2.3. Distribution of projection compensation multiplier for a 6cm-thick imaged volume with the same size of the digital detector (23.04cm x 19.20 cm) at projection angle of -30o. The image is displayed with log-scale grayscale bar.

For an image **f**, the compensated forward projection operation that includes the projection compensation multiplier can be expressed in the form of matrix multiplication as:

$$\mathbf{y}_i = \mathbf{M}_i \mathbf{A}_i \mathbf{f}, \tag{2.18}$$

where

$$\mathbf{M}_i = \text{diag}\{\mathbf{m}_i\}. \tag{2.19}$$

To implement Equation 2.18, we simply need to calculate the element-wise product of the projection compensation multiplier vector $\mathbf{m}_i$ and the result of applying the forward projector $\mathbf{A}_i$ to the imaged volume $\mathbf{f}$.

The operation of backward projection that includes the projection compensation multiplier can be expressed as:

$$\mathbf{f}_i = \mathbf{A}_i{}' \mathbf{M}_i \mathbf{y}_i, \tag{2.20}$$

where we calculate the element-wise product of the projection compensation multiplier vector $\mathbf{m}_i$ and the projection $\mathbf{y}_i$ before applying the backward projector $\mathbf{A}_i{}'$.

In the following chapters, if not specified, the projection compensation multiplier is always included in the forward projection and the backward projection. For simplicity, the matrix $\mathbf{M}_i$ will not be expressed in the following chapters. One can think of it as part of the matrix $\mathbf{A}_i$.

II.6 Truncated projection artifact in DBT reconstruction

Besides the glaring artifact, another type of common artifact in DBT reconstruction is the TPA [67, 69, 70]. Figure 2.4 shows the DBT system viewed along the rotation axis of the x-ray source and illustrates the cause of TPA in DBT reconstruction. Given a fixed location (e.g., the $(i+1)^{th}$ projection in Figure 2.4) for the x-ray source, a cone can be formed by connecting the source to the field-of-view (FOV) of the detector. Since the projection values are measured only within the range of the detector, this PV provides no information about the x-ray attenuation coefficients outside the cone. As a result, the back-projection step of typical unregularized algorithms will introduce discontinuities at the boundary of the cone. The discontinuity will appear as step artifacts on the reconstructed DBT slices at the locations marked by the blue stars in Figure 2.4.

Figure 2.5 shows the TPA in a human-subject DBT case, where two (unregularized) SART iterations were used to reconstruct the image. The reconstruction used the PVs in the order shown in Figure 2.4 that the source moved from the left side (the side with negative y-coordinate values) to the right side (the side with positive y-coordinate values). TPA is stronger on the right side of Figure 2.5(a) and the bottom side of Figure 2.5(b). Due to the access order of the PVs in

image reconstruction, TPA is first created in these areas and gets further enhanced by the subsequent updates, making it more obvious for human eyes.

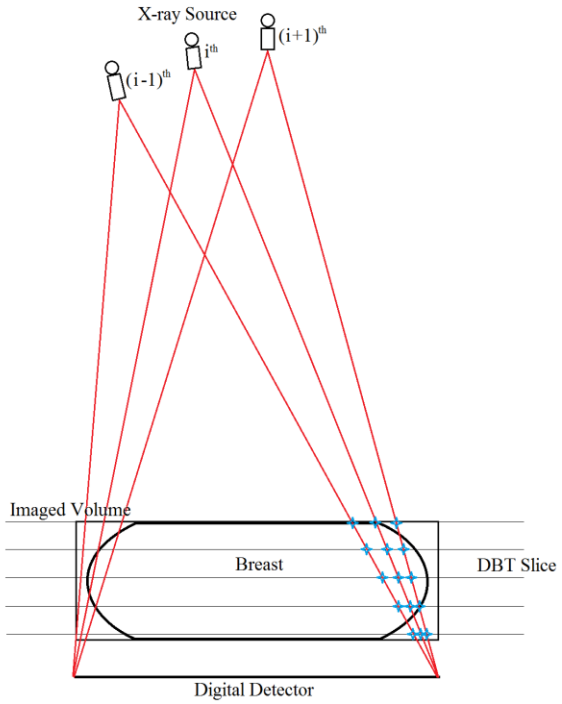

Figure 2.4. Cause of TPA in DBT reconstruction. The blue stars mark the locations where TPA will appear on the right side of the volume. TPA also appears on the left side of the volume similarly but it is not marked for simplicity.

As seen on the DBT slice in Figure 2.5(b), TPA will overlap with the reconstructed structures. For example, a suspicious region of dense tissue can be seen at around x = 10mm, y = 65mm near the chest wall as marked by the red box. For this region of dense tissue, the overlapping TPA can potentially affect the diagnosis. In fact, after removing TPA, the dense tissue proves not to be a tumor. For DBT scans, especially the ones with large breast thickness and wide scan angle, TPA can propagate very deep inside the imaged volume, as shown in Figure 2.5(a). Therefore, a reliable TPA removal algorithm is crucial for preserving the image quality in DBT.

Lu et al. previously developed a TPA removal algorithm that used diffusion to compensate for the discontinuity in the gray levels in the region across the step caused by the $(i-1)^{th}$ PV updating. By removing the sharp boundary before updating by the i^{th} PV, the step artifact would not be enhanced by the subsequent updates in the same iteration [67]. This TPA removal algorithm provides satisfactory results in our iterative DBT reconstructions. In Chapter III, IV and VI, we will use Lu's TPA removal algorithm. In our study on the SQS-DBCN algorithm in

Chapter IV, we realized that one of the limitations of this algorithm is that it lacks a convergence theory which is crucial for statistical image reconstruction. Chapter V introduces our comparative study on TPA removal and our new TPA removal algorithms to overcome this limitation.

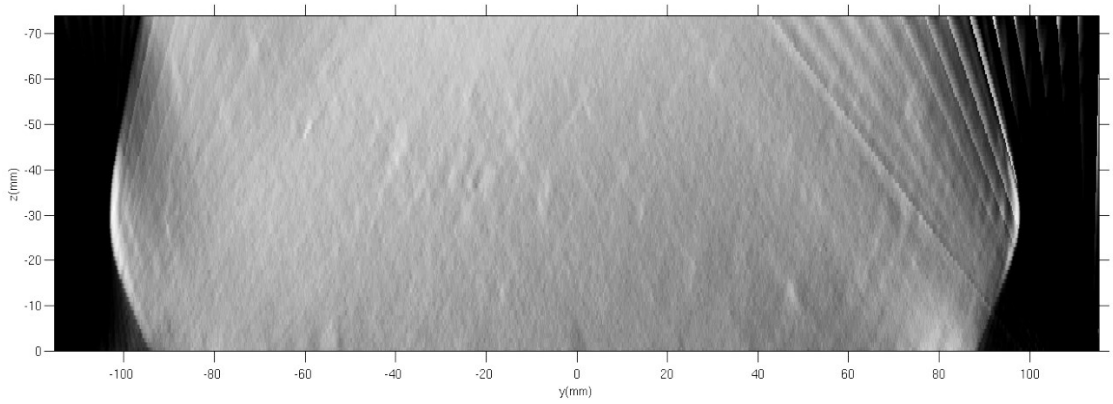

(a)

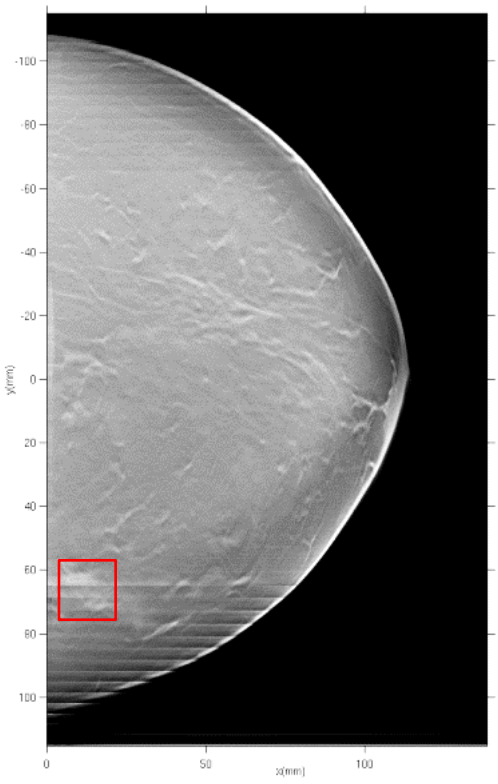

(b)

Figure 2.5. TPA in a human-subject DBT (RCC view) with SART reconstruction. (a) A *yz*-plane of the reconstructed volume at x = 29.95mm. (b) A slice of the reconstructed volume at z = -45.5mm. The thickness of the breast is 74mm so the slice is at the depth of 28.5 mm from the top. Refer to Figure 2.1 for the coordinate system of the reconstruction. The red box on (b) marks a suspicious area of dense tissue affected by TPA.

II.7 Image quality of DBT image reconstruction

The quality of a medical image refers to its capacity to convey clinically relevant information. When evaluating image quality for DBT, we are most interested in typical features of breast cancer that help radiologists to make the diagnosis. The typical features we focus on are the microcalcifications (MC) and the spiculated masses.

MCs are small calcium deposits in the breast of sizes from about 0.1 mm to 0.5 mm. While single MC is commonly observed in breast imaging and is most likely benign, clustered MCs are important signs of breast cancer [71-74]. Figure 2.6 shows one example of such a lesion that has been diagnosed as breast cancer with biopsy.

Besides MCs, the reconstructed soft tissue is also important in the diagnosis of breast cancer. Masses with spiculations are highly suspicious for breast cancer. Figure 2.7 shows one example of such a lesion that has been confirmed as breast cancer with biopsy.

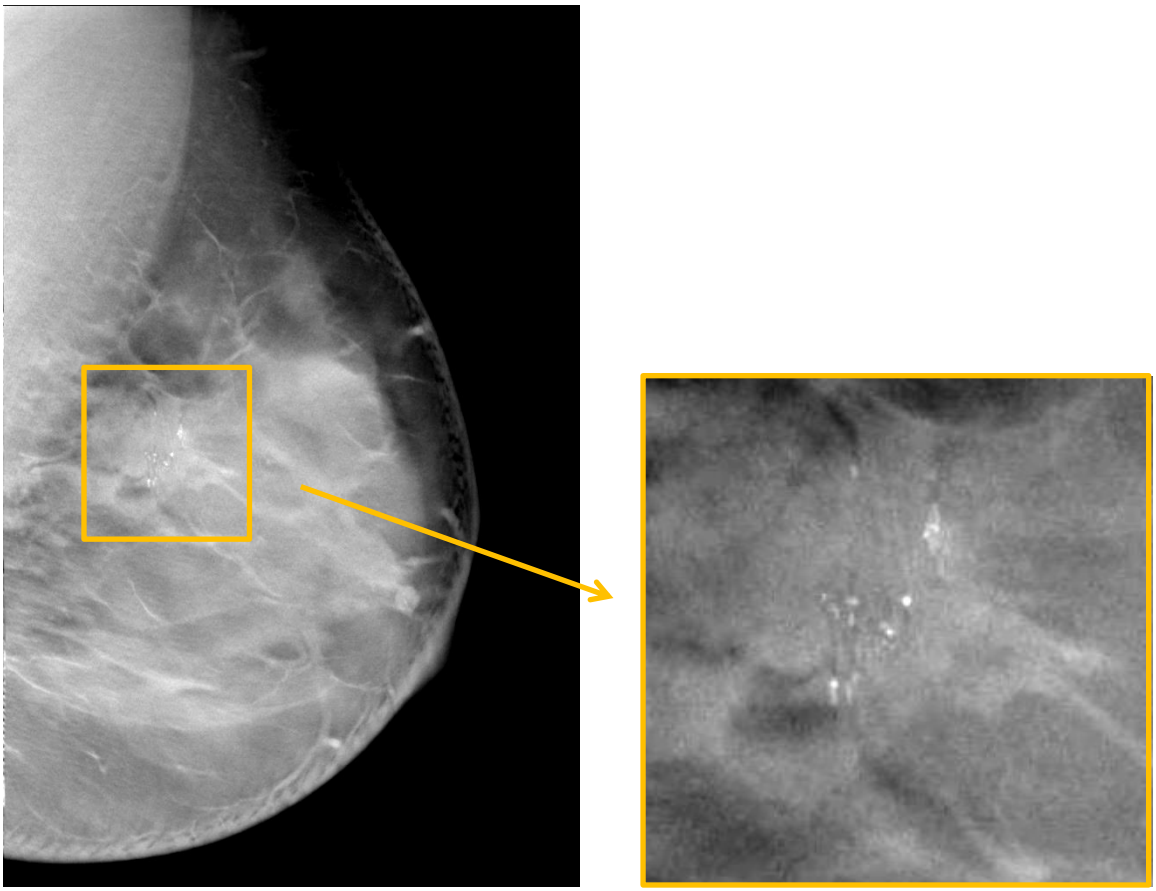

Figure 2.6. An MC cluster indicating a cancerous lesion on a DBT slice (marked with the yellow box) and the enlarged region of interest. Image source: [1].

As introduced in Section II.3, for a typical DBT reconstruction of our GE GEN2 prototype DBT system, the voxel size is $0.1\times0.1\times1.0$ mm^3. An MC will only occupy 1 to 5 pixels along one direction on the reconstructed slices. Such a small object is very different to be differentiated from the reconstruction noise. Therefore, one of the main challenges in the DBT reconstruction is to reduce noise while enhancing MCs and preserving the features of mass margins and the texture of the parenchyma.

Since MC is a typical feature that we are interested in, most studies (i.e. Chapter III, IV and VI) in this dissertation used FOMs based on MCs. In Chapter III and Chapter VI where we used digital phantoms, we configured pairs of small spheres to simulate MCs. The contrast of a pair of spheres is calculated with the profile along the center of the two spheres. In Chapter IV, we tested our reconstruction algorithms with an experimental phantom with clusters of calcium carbonate specks sandwiched between heterogeneous slabs to simulate the MCs. The FOMs based on the fitted image of each MC are used to quantitatively evaluate the enhancement of MCs for each method.

Figure 2.7. A region of a breast showing a large spiculated mass. The star-shaped spiculations are highly suspicious for breast cancer.

As previously mentioned, spiculated masses are also important features of the diagnosis of breast cancer. Reliable reconstruction algorithms for DBT need to preserve high-quality soft tissues while enhancing MCs. Reconstruction algorithms which create artificially looking soft tissues are considered to be of poor image quality, even if they can enhance the MCs significantly. To our knowledge, there are no reliable methods to quantitatively measure the image quality of soft tissue. As a result, the quality of the reconstructed soft tissue is evaluated empirically by observing how clearly the spiculations can be seen and whether there exists any artificially looking structure (for example, the plastic appearance as observed in CT MBIR studies [75, 76]). This empirical evaluation is mainly used in Chapter IV. We also used the noise power spectrum (NPS) to analyze the quality of reconstructed soft tissue. Although NPS does not reflect the visual clearance of the spiculations, it provides information about the frequency response of our reconstructed images.

Besides FOMs for MCs and visual evaluation of spiculated masses, we also used other FOMs to evaluate image quality. In Chapter III and Chapter IV, we configured digital phantoms with line pairs of different spatial frequencies to estimate the spatial resolution of the image reconstruction. The relative contrast of each set of line pairs is calculated and plotted as a function of the spatial frequency. The contrast curves are then used to compare different reconstruction methods or conditions. These contrast-to-frequency curves are similar to the commonly used modulation transfer function (MTF) in x-ray imaging, but they are calculated with rectangular waves instead of sinusoidal waves. Despite the difference, these curves still represent the spatial resolution of the reconstruction with the influence of different factors. The methods to calculate the contrast of line pairs are different in Chapter III and Chapter VI, based on different requirement of the study.

CHAPTER III.
Segmented Separable Projector and its Application for Subpixel DBT Reconstruction[1]

III.1 Introduction to the SG projector

In this chapter, I introduce our work on improving the accuracy and speed of forward and backward projectors in iterative image reconstruction for DBT. A better match between the digital implementation and the actual system physics can improve the quality of reconstructed images in iterative reconstruction methods, as has been found in other 3D modalities [37-45]. As shown in the updating step of SART (Equation 2.11), the inaccuracy of the forward and backward projectors $\mathbf{A}_i$ and $\mathbf{A}_i{}'$ will introduce error in each update of the reconstructed image $\mathbf{f}^{(i_{\mathrm{SART}},i)}$. Such error will also occur in other iterative image reconstruction algorithms, including the SQS-DBCN algorithm in the Chapter IV.

For DBT reconstruction, the ray-tracing (RT) projector is commonly used. This projector calculates the line integral along the ray from the source to the center of each detector element, ignoring the detector element size. With a discrete image volume, the integral becomes a summation that one can calculate efficiently with Siddon's method or its accelerated implementations [78-80].

Considering the finite size of the detector element, a more accurate projection model is the average of x-ray paths over the entire detector element [81]. In cone-beam CT, the separable footprint projector (SF projector) provides an efficient approximate implementation of this projection model [39]. However, the separable approximation in the SF projector is inaccurate for the DBT geometry. Because of the small scan angle, DBT has limited depth resolution. The

[1] This chapter is a reorganization of our paper on Medical Physics [77]. Part of the content in our published paper has been moved to Chapter II that it is also used by other studies discussed in this dissertation.

voxel dimension along the depth direction is usually set to be much longer than those parallel to the detector plane in DBT reconstruction. The approximation used in the SF projector is inadequate for DBT, especially at large projection angles. In this chapter, we present the segmented separable footprint projector (SG projector), which is a modified version of the SF projector specially designed for the DBT geometry. To evaluate the performance of the SG projector, we compared the projection errors of the SG projector and the other projectors. In addition, we digitally simulated DBT projections of a phantom embedded with test objects without noise and blur, and compared the resolution and contrast in the images reconstructed with the different projectors. The projectors were also applied to subpixel reconstruction, in which the DBT volume is reconstructed with voxel sizes smaller than the detector element size. The quality of the test objects in the reconstructed DBT and the computational efficiency of the projectors were evaluated and compared at different subpixel ratios.

III.2 Principle of the SG projector and subpixel reconstruction

III.2.1 Derivation of the SF projector

To explain the principle the SG projector, we first review the SF projector [39]. This derivation is similar to that described by Long et al.[39] except that the notations are changed to match the coordinates defined for our DBT system (Figure 2.1 or Figure 3.1). Same as the notations in Section II.1, we let $\mathbf{f}$ denote the 3D image to be reconstructed, i.e., a discrete array of x-ray attenuation coefficient values. More specifically, we use $\mathbf{f}[\vec{n}]$ to denote one element of $\mathbf{f}$, where $\vec{n} = (n_x, n_y, n_z)$ corresponds to one voxel of the imaged volume. Let $\vec{m}$ denote the index of the array of detector elements, the forward projection in Equation 2.6 can be rewritten as $\mathbf{y}_i[\vec{m}] = \sum_{\vec{n}} \mathbf{A}_i[\vec{m}, \vec{n}]\mathbf{f}[\vec{n}]$. Letting $\vec{\Delta} = (\Delta_x, \Delta_y, \Delta_z)$ denote the grid spacing of the imaged volume, the continuous object $\mathbf{f}(\vec{r})$ corresponding to the discrete image array $\mathbf{f}[\vec{n}]$ is

$$\mathbf{f}(\vec{r}) = \sum_{\vec{n}} \mathbf{f}[\vec{n}]\beta_0(\vec{r} - \vec{c}[\vec{n}]) , \tag{3.1}$$

$$\beta_0(\vec{r}) = \mathbf{1}_{|r_x|<\frac{\Delta_x}{2}}\mathbf{1}_{|r_y|<\frac{\Delta_y}{2}}\mathbf{1}_{|r_z|<\frac{\Delta_z}{2}}, \tag{3.2}$$

where $\beta_0(\vec{r})$ is the basis function of a cuboid voxel and $c[\vec{n}]$ is the center of the *n*th voxel, and $\mathbf{1}$ denotes the indicator function.

Let $(t_{\vec{m}}, s_{\vec{m}})$ denote the center of the $\vec{m}$th detector element. The ideal projection model assumes the projection value at a detector element to be the average of ray-tracing result throughout the detector element:

$$\mathbf{y}_i[\vec{m}] = \iint h(t_{\vec{m}} - t, s_{\vec{m}} - s)p(t, s; i)\mathrm{d}t\mathrm{d}s, \tag{3.3}$$

where $h(t, s)$ is the sensitivity response of one detector element. The RT projector treats $h(t, s)$ as a Dirac impulse such that only one ray per detector element is traced with the Siddon's algorithm or its accelerated versions. The sparse sampling of the rays through the imaged volume causes numerical errors and artifacts in the reconstructed images. The SF projector reduces the sampling errors by approximating the average of the ray paths over each voxel. $p(t, s; i)$ is the continuous projection of $\mathbf{f}(\vec{r})$ at the *i*th angle:

$$p(t, s; i) = \int_{L(t,s;i)} \mathbf{f}(\vec{r})\mathrm{d}l, \tag{3.4}$$

where $L(t, s; i)$ is the line from the source to the coordinate (t, s) of the detector.

By combining (3.1)-(3.4), we obtain the expression of an element $\mathbf{A}_i[\vec{m}, \vec{n}]$ of the system matrix:

$$\mathbf{A}_i[\vec{m}, \vec{n}] = Q(t_{\vec{m}}, s_{\vec{m}}; i; \vec{n}), \tag{3.5}$$

where $Q(t, s; i; \vec{n})$ is a continuous function from a 2-D convolution:

$$Q(t, s; i; \vec{n}) = h(t, s) ** q(t, s; i; \vec{n}) , \tag{3.6}$$

$$q(t, s; i; \vec{n}) = \int_{L(t,s;i)} \beta_0(\vec{r} - \vec{c}[\vec{n}])dl . \tag{3.7}$$

$q(t, s; i; \vec{n})$ is the continuous projection function of the $\vec{n}$th voxel. We call this the 'footprint' of the $\vec{n}$th voxel. $Q(t, s; i; \vec{n})$ is the 'blurred footprint', blurred by the sensitivity response of the detector element. In summary, the value of $\mathbf{A}_i[\vec{m}, \vec{n}]$ is equal to the blurred footprint of the $\vec{n}$th voxel evaluated at the center of the $\vec{m}$th detector element.

As a 2-D convolution, $Q(t, s; i; \vec{n})$ would be expensive to compute exactly. For typical cone-beam CT geometries, the footprint function $q(t, s; i; \vec{n})$ is approximately separable [39]:

$$q(t, s; i; \vec{n}) \approx l(t, s; i; \vec{n})q_t(t; i; \vec{n})q_s(s; i; \vec{n}) , \tag{3.8}$$

where $q_t(t; i; \vec{n})$ is a rect function and $q_s(s; i; \vec{n})$ is a trapezoid function, both with unit amplitude. The amplitude function $l(t, s; i; \vec{n})$ equals the maximum value of $q(t, s; i; \vec{n})$.

Assuming the detector pixel sensitivity response is uniform over each detector element, then we have:

$$h(t, s) = h_t(t)h_s(s) = \frac{1}{\Delta_t \Delta_s}\mathbf{1}_{|t|<\frac{\Delta_t}{2}}\mathbf{1}_{|s|<\frac{\Delta_s}{2}}, \tag{3.9}$$

and $\mathbf{A}_i[\vec{m},\vec{n}]$ becomes the product of two 1-D convolutions:

$$\mathbf{A}_i[\vec{m},\vec{n}] = l(t_{\vec{m}}, s_{\vec{m}}; i; \vec{n}) Q_t(t_{\vec{m}}; i; \vec{n}) Q_s(s_{\vec{m}}; i; \vec{n}) \,, \tag{3.10}$$

where

$$Q_t(t_{\vec{m}}; i; \vec{n}) = \left(h_t(t) * q_t(t; i; \vec{n})\right)_{t=t_{\vec{m}}} \,, \tag{3.11}$$

$$Q_s(s_{\vec{m}}; i; \vec{n}) = \left(h_s(s) * q_s(s; i; \vec{n})\right)_{s=s_{\vec{m}}} \,. \tag{3.12}$$

To compute the 1-D convolutions for $Q_t(t_{\vec{m}}; i; \vec{n})$ and $Q_s(s_{\vec{m}}; i; \vec{n})$ is much faster than a 2-D convolution and can be used repeatedly in the implementation of the SF projector.

III.2.2 The SG approximation and the SG projector

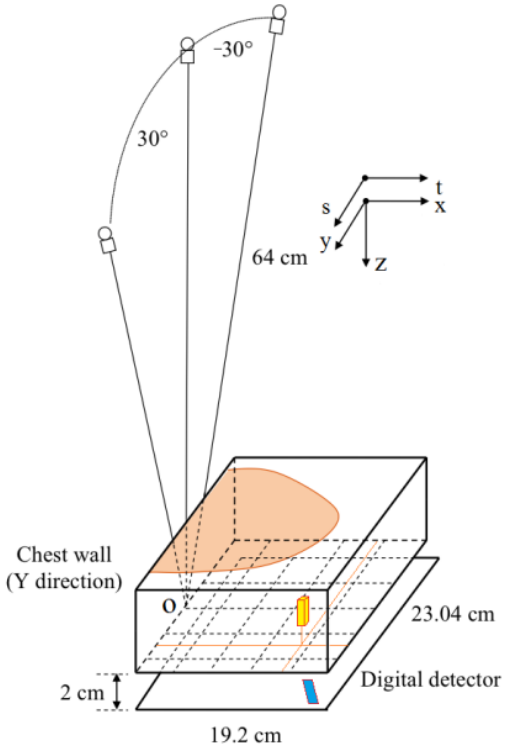

Figure 3.1. The box (yellow) illustrates the location of the voxel in the example shown in Figure 3.2. The parallelogram (blue) illustrates the location of the 'footprint' of the yellow voxel. Note that both the box and the parallelogram are much larger than their actual size. The breast is drawn schematically as a 2D plane to illustrate the positioning of the breast relative to the x-ray source scanning and the detector. In reality the breast is a 3D object filling the imaged volume between the compression paddle and the breast support plate (the top and bottom of the rectangular block) with a curved anterior as shown.

In DBT, because of the small tomographic angle (11-60 degrees), the depth resolution along the z-direction perpendicular to the detector plane is much lower than those on the detector (x-y)

plane [82]. For example, a DBT system generally uses a digital mammography detector that has pixel pitch ranging from 0.07 × 0.07 mm^2 to 0.1 × 0.1 mm^2 for the commercial systems. The slice spacing (z-dimension of a voxel) in the reconstructed imaged volume may be set to be 0.5 mm to 1 mm while the x- and y-dimensions of the voxel are set to be the same as the detector pixel pitch. The ratio of the z-dimension and the x- and y-dimension, i.e., the height-to-width ratio, of a voxel can be as large as 10:1. We use one voxel as an example to demonstrate why the SF approximation is inaccurate for a typical DBT geometry. This voxel is located at (*x, y, z*) = (160.05, 70.05, -10.5) mm, drawn approximately in Figure 3.1. The distance from the center of this voxel to the bottom of the imaged volume is 10.5 mm. The analytical projection (footprint) of the voxel at the projection angle $\theta = -30°$ is shown in Figure 3.2(a). The long parallelogram-shape footprint $q(t, s; i; \vec{n})$ is apparently non-separable. Figure 3.2(e) shows the blurred separable footprint that obviously poorly approximates $Q(t, s; i; \vec{n})$ as shown in Figure 3.2(d). Thus, the original SF projector does not help improve the accuracy of the projector in DBT application.

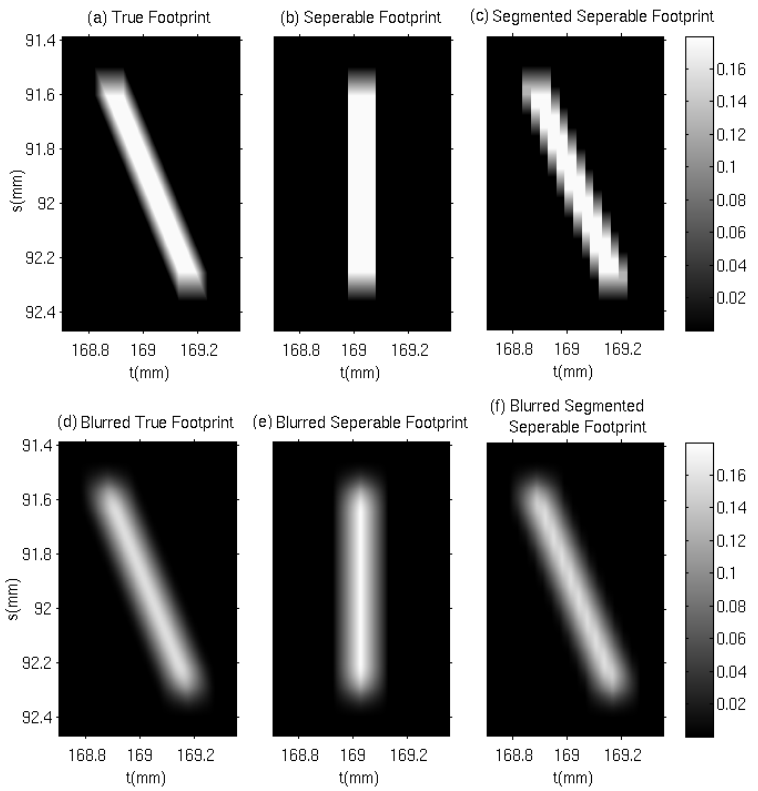

Figure 3.2. Separable footprint (SF) and segmented separable footprint (SG) approximation applied to a DBT image voxel located at (*x*, *y*, *z*) = (160.05, 70.05, -10.5) mm at projection angle $\theta = -30°$. All images share the same grayscale bar, *t*- and *s*-coordinate.

The parallelogram-shape of the footprint results from the shape of the voxel in DBT system. This problem increases with increasing projection angles. To deal with the shape of voxels in DBT, we propose a 'segmented separable footprint' (SG) approximation: we equally divide each voxel along the z-direction into several segments, apply SF approximation to each segment, and sum the footprints of each segment. Figure 3.2(c) shows the summed footprint with 10 segments. Although Figure 3.2(c) still differs from Figure 3.2(a), the difference becomes much less noticeable after blurring (Figure 3.2(d) and Figure 3.2(f)). Since the value of $\mathbf{A}_i[\vec{m},\vec{n}]$ depends only on the blurred footprint $Q(t,s;i;\vec{n})$, the error in the non-blurred footprint $q(t,s;i;\vec{n})$ only slightly affects the accuracy of the projector. The proposed projector based on the SG approximation is referred to as the SG projector in the following.

The accuracy of the SG method depends on the number of segments used. More segments will improve projection accuracy at the expense of longer computation time. The memory cost of the SG projector does not depend on the number of segments and is negligible compared to the memory that is needed for the reconstructed volume. The proper number of segments depends on the height-to-width ratio of the voxels used in the reconstruction, and on the tomographic scan angle of the DBT system.

The accuracy of the projector also depends on the choice of the form of $q_t(t;i;\vec{n})$. We used a rect function as $q_t(t;i;\vec{n})$ in our implementation. Using a trapezoid function would further improve the similarity between Figure 3.2(d) and Figure 3.2(f) and reduce the projection error. This approach is called the trapezoid-trapezoid (TT) method [39]. However, the decrease in the projection error is very small and the trapezoid $q_t(t;i;\vec{n})$ increases the computation time by a factor of about 2.6 times. We consider this extra computation time not worth the slight improvement in projection accuracy and use the rect function for the SG projector.

III.2.3 Subpixel DBT reconstruction

The SG projector not only provides a more accurate projection result than RT, but also makes subpixel DBT reconstruction more efficient. The in-plane direction voxel dimensions of the imaged volume in DBT reconstruction are commonly set to be the same as the detector pixel dimensions along the *t*- and *s*-direction. Studies have shown that, by interpolating the PVs and using a finer voxel grid, one can reconstruct higher resolution images with better image quality [83, 84]. That approach is called subpixel reconstruction or super-resolution reconstruction. For

example, assuming the original detector pixel size to be 0.1 × 0.1 mm^2, we can interpolate each pixel into four 0.05 × 0.05 mm^2 subpixels. Using a 1 mm slice interval, the interpolated projections can be used to reconstruct an imaged volume with a 0.05 × 0.05 × 1 mm^3 voxel size. With subpixel reconstruction, super-resolution can be observed in the reconstructed image slices with frequency exceeding the Nyquist limit of the detector pixels.

In the method described above, interpolation of the projections is inevitable when one uses the RT projector. The RT back projector contributes only to voxels that intersect the line from the source to the center of each detector pixel. If one attempted subpixel reconstruction with non-interpolated projections, many voxels would not obtain any back-projected value due to the small voxel size compared with the pixels of the detector along the in-plane direction. This would create a lot of gap artifacts on the reconstructed slices.

The SG projector overcomes this problem in subpixel DBT reconstruction. We need not interpolate the projections since back projection of each detector pixel will affect all voxels that intersect with the cone subtended at the source by the detector pixel. Thus, the SG projector effectively covers all voxels in the imaged volume, improves the estimate of the x-ray paths through the voxels while saves computation time by avoiding interpolation and working with only the original detector pixel values in the projections. In this study, we applied both the RT and the SG projector to subpixel DBT reconstruction and compared the results qualitatively and quantitatively.

III.3 Simulation of the projections for the digital phantom

We generated a digital phantom using the CatSim simulation program [65, 66] to study different projectors and subpixel image reconstruction. We configured the x-ray system in the CatSim simulation to match the geometry of the experimental system shown in Figure 2.1. The x-ray source was an Rh target/Rh filter x-ray tube and the peak voltage was set to 29 kV. The oversampling rate of the detector along *t*- and *s*-directions was 20 to simulate the projection of an analog object being imaged. A complete set of simulated projections contains 21 projections every 3^o from -30^o to $+30^o$, with a detector pixel pitch of 0.1 × 0.1 mm^2 and an image size of 1920 × 2304 pixels, corresponding to the experimental DBT system. CatSim was designed for CT simulation, where the detector rotates with the source. Since our DBT system has a stationary detector, we did not use the rotation option in CatSim and only simulated one projection with

one configuration file at a time. The x-ray focal spot was assumed to be a point source; we also turned off the quantum noise, detector noise, and scattered radiation in the simulation so that we can focus on the investigation of the effects of the projector on the spatial resolution of DBT reconstruction.

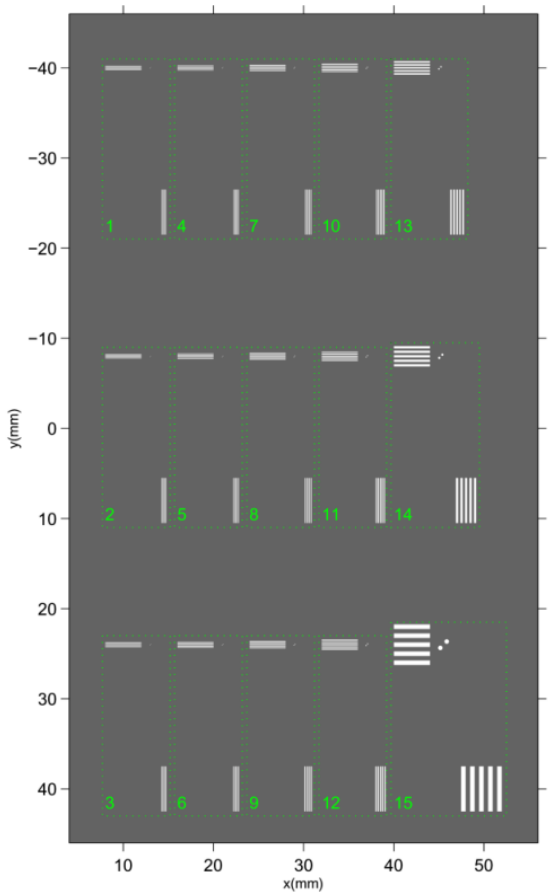

Figure 3.3. Setup of a digitally generated resolution phantom. Each set (marked by box) contains three types of objects: horizontal line pairs, vertical line pairs, and two lead spheres (BBs). The sizes of all objects are shown in Table 3.1.

The geometric features of the digital phantom are analytically specified in a configuration file using the FORBILD syntax [66]. The background material is set to 5-cm-thick breast tissue, based on data from ICRU report 46 [85]. The phantom contains 15 sets of objects. The distance from each object to the bottom of the imaged volume is the same, which is 25.6 mm. As a result, all objects are located on the same slice, as shown in Figure 3.3. Each set contains two small lead spheres (BBs) and two sets of line pairs along x- and y-direction with the same spatial frequency. Each group of line pairs is composed of five lead bars and four spacings, i.e., 4.5 line pairs, with

the width of the lead bar same as the width of the spacing. The group of horizontal line pairs and the group of vertical lines are offset in the x-direction so that the in-plane reconstruction artifacts from one group will not affect the other group. The diameter of the BBs is the same as the width of one bar in the line pairs and the center-to-center spacing of the two spheres is equal to one line pair. The two spheres are arranged along a 45^{o} line relative to the pixel grid. The pairs of BBs are included to demonstrate the spatial resolution for small objects under various reconstruction conditions, at a representative angle (e.g., diagonal) to the voxel grid, which combines the effect of the spatial resolutions in the x- and y-directions. Table 3.1 shows the line pair frequency and the sizes of the individual bars and spheres. The y-direction distance between the centers of two sets of line pairs or BBs is 32 mm, which is chosen to minimize the y-direction in-plane reconstruction artifacts from two sets of line pairs or BBs to affect each other while keeping the entire phantom area to be small enough to be covered by the reconstruction matrix at high resolution (see below). The material of all line pairs and BBs is pure lead (Pb). The thickness of all line pairs is set to be 0.03 mm, similar to the thickness of commercial lead line pair phantoms for testing spatial resolution of mammography systems (e.g., Fluke Medical). The z-direction location of all objects is 0.6 mm from the lower boundary of the slice if the reconstruction uses a 1-mm slice interval. We chose this instead of 0.5 mm because we used half of the original slice interval in one set of the subpixel reconstruction; objects located right at the center of the original slice will be split into two slices, which would be difficult to analyze.

Table 3.1. Objects sizes (mm) in the digital phantom. The object set number corresponds to the number next to each box in Figure 3.3. The center-to-center distance between the two BBs in a pair is equal to the BB diameter.

Object Set Number	1	4	7	10	13
line pairs/mm	9.5	8.0	6.5	5.0	3.0
Line or space width	0.053	0.063	0.077	0.100	0.167
BB Diameter	0.053	0.063	0.077	0.100	0.167
Object Set Number	2	5	8	11	14
line pairs/mm	9.0	7.5	6.0	4.5	2.0
Line or space width	0.056	0.067	0.083	0.111	0.250
BB Diameter	0.056	0.067	0.083	0.111	0.250
Object Set Number	3	6	9	12	15
line pairs/mm	8.5	7.0	5.5	4.0	1.0
Line or space width	0.059	0.071	0.091	0.125	0.500
BB Diameter	0.059	0.071	0.091	0.125	0.500

The alignment of the objects to the pixel grid will affect the resolution and contrast of the reconstructed objects, especially for objects of sizes close to the pixel size. The alignment affects the different objects in the phantom to different degrees because of their different locations relative to the pixel grid. To compare different reconstruction methods, it is more useful to study the "average" effect when objects are imaged by a DBT system without knowledge of their alignment to the pixel grid, as in actual situation. We simulated this average effect by generating projections with the test patterns placed at 25 locations with respect to the pixel grid and the results were averaged over the different alignments. We shifted the locations of the entire array of phantom objects by 1/5 pixel (0.02 mm), 2/5 pixel (0.04 mm), 3/5 pixel (0.06 mm) and 4/5 pixel (0.08 mm) along both x and y direction. At each phantom location, a set of DBT projections (21 projections in 3^o increments, 60^o total scan angle) was simulated so that a total of 25 sets of projections were generated for reconstruction. We denote the 25 alignment locations by a 'shift tag' L$d_x d_y$, where d_x and d_y are both integers. For example, the shift tag 'L23' ($d_x = 2, d_y = 3$) means the shift along x-direction was 2/5 pixel and the shift along y-direction was 3/5 pixel. The shift tag 'L00' represents the non-shifted projections. The simulation of all projections angles for all 25 shifted locations took about one week to complete.

III.4 Reconstruction method and the subpixel tag

We used the SART method [56] for both the original and subpixel reconstructions in this study. The updating step of the SART method can be found in Equation 2.11. The TPA is removed with the algorithm previously developed in our laboratory [67, 68]. The glaring artifact is removed by including the projection compensation multiplier in the forward and backward projection, as introduced in Section II.5. The simulated DBT used 21 projections so that each SART iteration consisted of 21 updates. The SART reconstruction was initialized with a uniform imaged volume with zero values.

We used the subpixel tag 'xyαzβ' to denote the subpixel ratio of a reconstruction, with α being the subpixel ratio along the x- and y-directions and β being the subpixel ratio along the z-direction. For a reconstruction at the subpixel ratio xyαzβ, each $0.1 \times 0.1 \times 1.0$ mm^3 voxel was divided into $\alpha^2\beta$ of $(\frac{0.1}{\alpha}) \times (\frac{0.1}{\alpha}) \times \left(\frac{1.0}{\beta}\right)$ mm^3 voxels. The matrix size of the voxel grid of the reconstructed imaged volume increases by a factor of $\alpha^2\beta$ for subpixel reconstruction.

We used the following 6 subpixel ratios: xy1z1, xy2z1, xy3z1, xy1z2, xy2z2 and xy3z2 in this study. xy1z1 denotes the regular reconstruction. When reconstructing with an *xy*-ratio larger than one with the RT projector, the input projections were interpolated to the same *xy*-ratio using 2-D bilinear interpolation. For the SG projector, the non-interpolated projections were used as input. To demonstrate the effect of the new SG projector, we also reconstructed all subpixel ratios with the original SF projector. In summary, with 25 shift locations of the phantom, 6 subpixel ratios and 3 different projectors, there were a total of 450 image reconstructions.

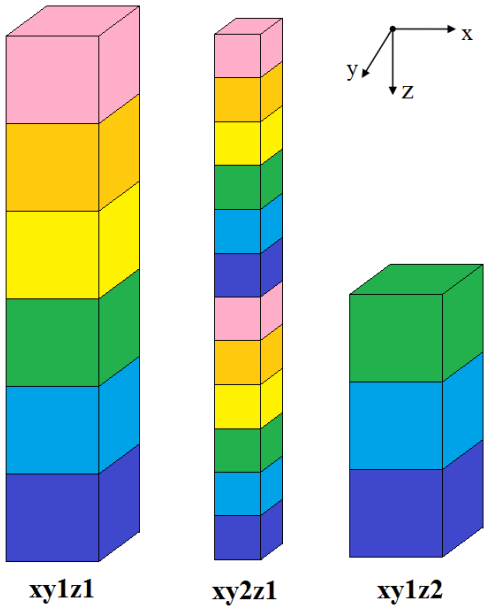

Figure 3.4. Relative voxel sizes and segments for xy1z1, xy2z1 and xy1z2 subpixel ratios. The entire stack of color blocks indicates a voxel, and each color block indicates a segment. In the examples shown, the voxel of xy1z1, xy2z1 and xy1z2 was cut into 6, 12 and 3 segments, respectively, to maintain the same height-to-width ratio.

For the SG projector, the proper number of segments depends on the shapes of the voxel and its projection to the detector plane. For narrower voxels, more segments are necessary to make a good approximation of the blurred footprint of each voxel. According to our initial experimentation with different number of segments, for our DBT system where the detector pixel pitch is $0.1 \times 0.1\ \text{mm}^2$ and the maximum projection angle is $\pm 30°$, at a reconstructed slice interval of 1 mm, we found that 5 or 6 segments, i.e., a voxel height-to-width ratio of about 2:1 to 1.7:1, are sufficient. We chose to use 6 segments for two reasons: (1) an even number of segments for the xy1z1 case yields an integer value in the number of segments for cases with z2,

and (2) to maintain the same height-to-width ratio of the segments and therefore similar accuracy of the SG projector for all subpixel ratios studied. For example, 3 segments were used for xy1z2 and 6 segments for xy1z1. For the subpixel ratio of xy2z1, 12 segments were used because each voxel is half the size of that of xy1z1 in the x- and y-dimension. Figure 3.4 shows the relative sizes of one voxel for xy1z1, xy2z1 and xy1z2.

III.5 Results and discussions

III.5.1 Comparison of projections of single voxels

To illustrate the difference in the projectors, we compared the projection generated by the 3 different projectors (RT, SF and SG) when there was only one non-zero voxel in the imaged volume. We set the non-zero voxel value to 1. This was equivalent to comparing one column of the system matrix $\mathbf{A}_i$. The projections generated by the digital projectors were compared with the ideal projection. To simulate the ideal projection, we divided each detector element into a 20 × 20 mini pixels in a Cartesian grid, calculated the projection value at the center of each mini-pixel and then calculated the average of the 400 mini-pixels as an approximation of the surface integral over the detector element. The projected location of a given voxel was calculated analytically and the ideal projection was only calculated within a small region. The calculation of the ideal projection for a full-sized detector would take more than one hour, which is too slow to be used in iterative image reconstruction in practice.

Figure 3.5 and Figure 3.6 show the projections of the single voxel in the imaged volume with the ideal projector, RT, SF and SG at projection angle $\theta = -30°$. The root-mean-square errors (RMSE) of RT, SF and SG relative to the ideal projection were given at the top of the figures. Visually, the pattern generated by the SG projector is much more similar to the ideal projection compared with the RT projector. Compared with the ideal projection, the RT projection is narrower and values at several pixels are missing because the analytical footprint does not cover the centers of those detector elements, i.e., the ray path between the focal spot and the center of each of these detector elements does not intersect the voxel. When reconstructing small objects such as subtle MCs, the narrower projections by the RT projector might cause the reconstructed objects to be more blurred. Quantitatively, the SG projector reduces the RMSE by 96.4% and 62.6% at the two locations, respectively, compared with the RT projector. The projections

generated by the original SF projector are also shown in Figure 3.5 and Figure 3.6. These projections appear symmetric in the *s*-direction due to the SF approximation, which is inaccurate in DBT as seen from the ideal projection.

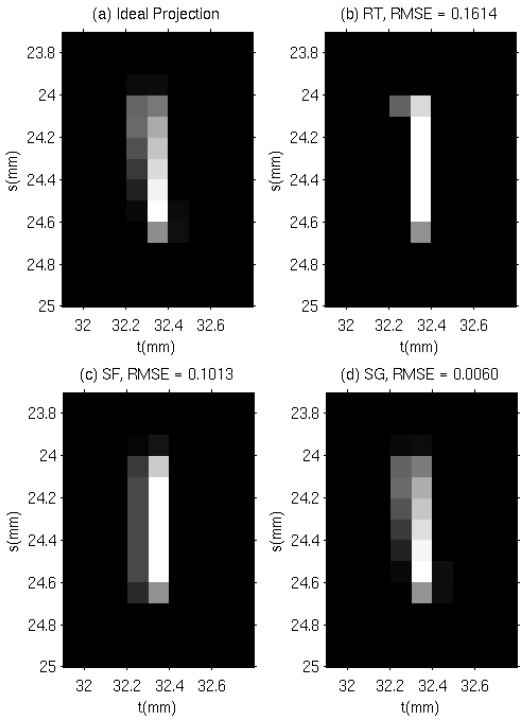

Figure 3.5. Projection of a single voxel located at (30.05, 0.05, -19.5) mm at projection angle $\theta = -30°$.

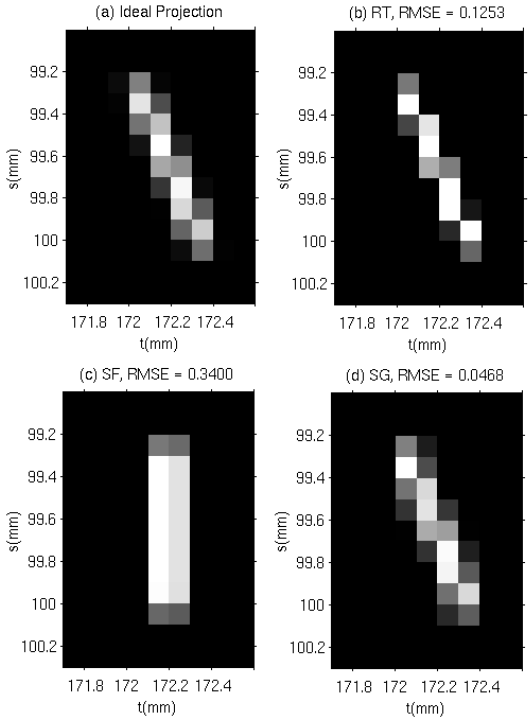

Figure 3.6. Projection of a single voxel located at (160.05, 70.05, -19.5) mm. at projection angle $\theta = -30°$.

The difference between the projectors depends strongly on the voxel location in the imaged volume and the source angle. Generally, the difference is greater when the angle between the z-direction and the ray from the source to the center of the voxel is larger. In the two examples in Figure 3.5 and Figure 3.6, the source angle of the projection was -30^{o}. Figure 3.6 shows a voxel located near the edge of the field of view of the detector so that it represents an extreme case where the voxel is projected at almost the largest angle in the entire imaged volume. Figure 3.5 shows a voxel essentially at the central ray of the projection.

III.5.2 Error map for voxels at different locations

In addition to the single voxel examples shown in the previous section, we investigated the distribution of the RMSE for voxels over one slice of the imaged volume at different projection

angles to further evaluate the accuracy of the SG projector. We chose the slice at z = -29.5 mm as an example. The distributions of RMSE, relative to the ideal projector, over the 1920 × 2304 voxels on this slice at projection angles $\theta = 0°$ and $\theta = -30°$ are shown in Figure 3.7. The projection error of a given voxel depends strongly on the alignment of the projection with the detector pixels, which leads to periodic patterns in the error maps. Figure 3.7 has been filtered with a 7 × 7 sliding maximum window to reduce the periodic pattern, representing the maximum error within a 0.7×0.7 mm^2 patch centered at each pixel.

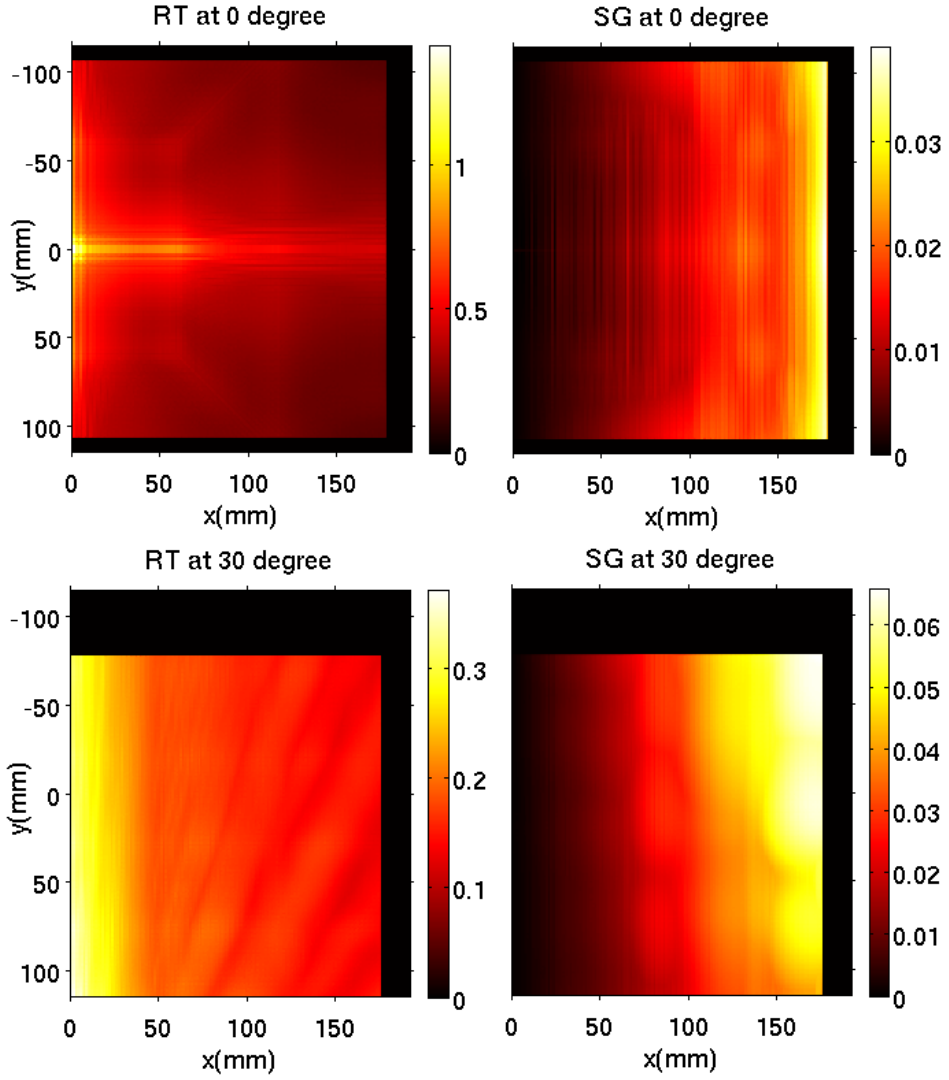

Figure 3.7. RMSE map of the RT (left column) and the SG (right column) projectors, relative to the ideal projection, of voxels on a slice of the imaged volume at z = -29.5 mm. The upper row shows the maps at projection angle $\theta = 0°$, and the lower row shows the maps at $\theta = -30°$. Note the difference in the scale of the heat maps.

The error map is black near the top, bottom and right boundaries, representing an RMSE of 0. Due to the diverging x-ray beam, the projection of voxels in this region was already outside the field of view of the detector; the projected voxels were ignored so that both the ideal projection and the projection by SG or RT were set to zero. For the area where the RMSE is non-zero, the SG projector reduces the projection error by 1 to 2 orders of magnitude at most locations, especially for the projection angle $\theta = 0°$. Generally, the error of the RT projector is larger when the area of the analytical projection of a voxel is smaller, making it more likely to miss larger fraction of pixel values. For $\theta = 0°$ (upper row of Figure 3.7), the minimum non-zero value of the RT RMSE map (the upper right corner) is 0.1543, and the maximum value of the SG RMSE map (middle point of the right edge) is 0.0386. For $\theta = -30°$ (lower row of Figure 3.7), the minimum non-zero value of RT (the upper right corner) is 0.1254, and the maximum value of the SG error map (the upper right corner) is 0.0643. Therefore, even in the worst case, the SG projector still provides a much more accurate projection.

As shown in the DBT imaging geometry (Figure 2.1 or Figure 3.1), the center of the cone beam is centered at the chest wall of the compressed breast, which corresponds to the left boundary of the error maps shown in Figure 3.7. The right side of the DBT slice (anterior of breast) where the x-ray incident angle is large is usually outside the breast volume unless the compressed breast is very large. The relatively large RMSE of the SG projector near the right boundary is therefore less problematic. On the contrary, the error maps of the RT projector show larger RMSE on the left side (chest wall) where the main breast volume is located, introducing errors into the reconstructed DBT for all breast sizes.

III.5.3 Qualitative comparison of reconstructed images

To study the effects of the projectors on the DBT image quality, we first made a qualitative comparison of the reconstructed images using different projectors at several subpixel ratios. As an example, the images reconstructed from the projections with the phantom location at L00 are shown. Figure 3.8 shows the in-focus slice (centered at z = - 25.5 mm) reconstructed with the SG projector at the original voxel size. Detailed analysis is discussed below.

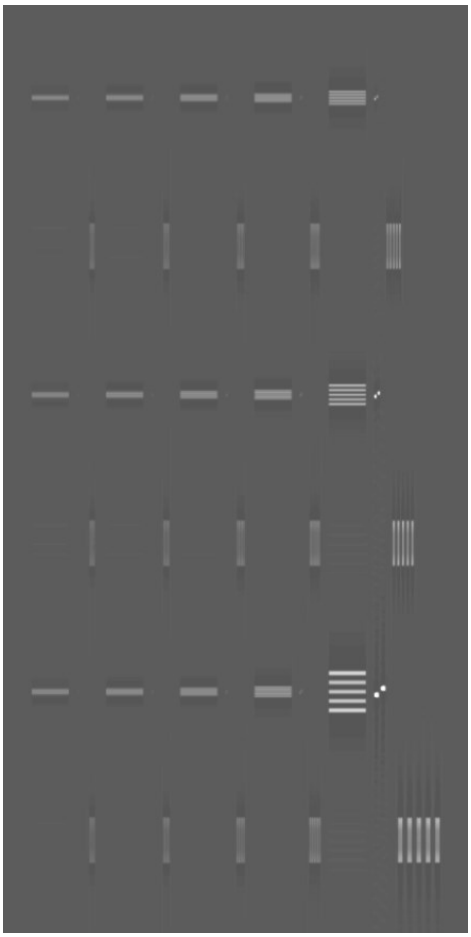

Figure 3.8. The in-focus slice (centered at z = -25.5 mm) of the line-pair phantom (L00, xy1z1, 5 SART iterations with the SG projector). In-plane artifacts are seen as shadows above and below the objects.

An example to illustrate the difference in the image quality for different projectors is shown in the zoomed image patches in Figure 3.9. From left to right, we replaced the RT projector with the SG projector and replaced the regular reconstruction with the subpixel reconstruction. The spatial resolution dramatically improves after each replacement. The test pattern shown has 6 line pairs/mm, which is higher than the Nyquist limit of the detector (5 cycles/mm). In the xy1z1 reconstructions, aliasing can be seen clearly; although the line pairs appear resolved in the image, it contains only 3 and a half line pairs while the object actually contains 4 and a half line pairs (5 bright lines and 4 dark lines). The xy3z2 reconstructions clearly resolve all the line pairs. The difference between the SG and RT projectors are also well demonstrated; the SG projector provides higher-contrast line pair images in both directions compared to the RT projector. In addition, although the simulated projections are noiseless, the RT images appear 'noisy',

especially for the horizontal line pairs. The 'noise' shows regular periodic pattern, indicating it is actually periodic numerical error rather than random noise. One possible reason may be that the discrete and sparse rays being traced through the voxel grid in the RT projector causes periodic sampling errors in the projected values. The images of the BBs further demonstrate the increased resolution of the subpixel reconstruction. The BBs are well resolved in the xy3z2 reconstruction but they become neighboring voxels in the xy1z1 reconstruction. The BBs are also more blurred by the RT projector than the SG projector. This observation is similar to that of a previous study by our laboratory [83]. Generally, the subpixel reconstruction provides better image quality among the conditions studied. However, the improved resolution is gained at the expense of longer computation time and more memory as well as storage space. The SG projector is more efficient than the RT projector so that the increase in the computation time is less dramatic.

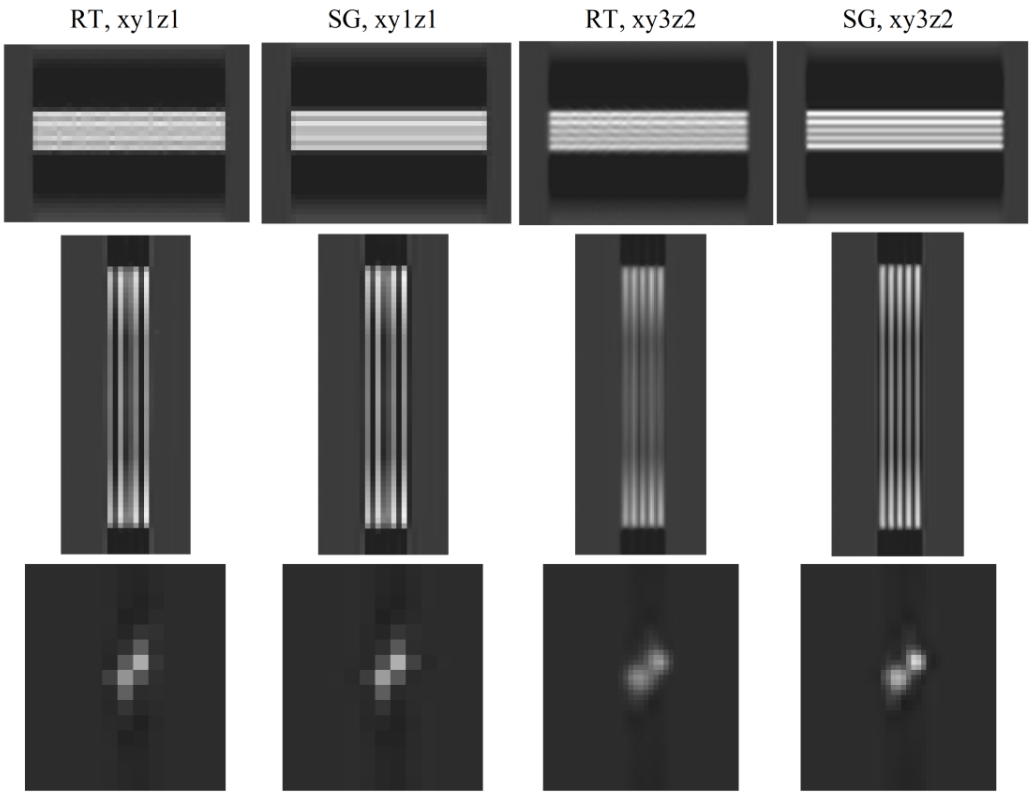

Figure 3.9. Object set #8 (see Figure 3.3, Figure 3.8, Table 3.1) reconstructed with RT or SG projector with subpixel ratios of 'xy1z1' and 'xy3z2'. All line pair images are shown with the same window setting. All BB images also share the same window setting (different from that of the line pairs). Line pair frequency = 6 line pairs/mm. BB diameter = 0.083 mm. detector pixel pitch = 0.1 mm and Nyquist frequency = 5 cycles/mm, SART iterations = 5. Note that the line pairs are not correctly resolved in the xy1z1 reconstructions while both the line pairs and the BBs are well resolved in the xy3z2 reconstructions.

III.5.4 Figures of merit for quantitative analysis of subpixel image reconstruction

To evaluate quantitatively the performance of the SG projector and the subpixel reconstruction, we defined FOMs based on the reconstructed line pairs and BBs. We first obtained the profiles of different objects. For each set of line pairs, we extracted 9 profiles at the central part of the line pairs and took the average. For BB, we only extracted one profile through the line that passed through the centers of the two spheres. The profiles were calculated from the analytical locations of the objects as defined in the configuration of the phantom. These "true" locations do not change when we perform subpixel reconstructions. A profile was obtained by bilinear interpolation from the reconstructed values at the voxel grid points on the in-focus slice. For each set of line pairs, one profile contained 81 sampling points, while for each BB, one profile contained 51 sampling points. The sampling distance was reduced as the line pair frequency increased to allow for adequate sampling of the peaks and valleys of the profiles. The actual length of the profiles was therefore inversely proportional to the spatial frequency but always covered the entire set of line pairs or the two BBs.

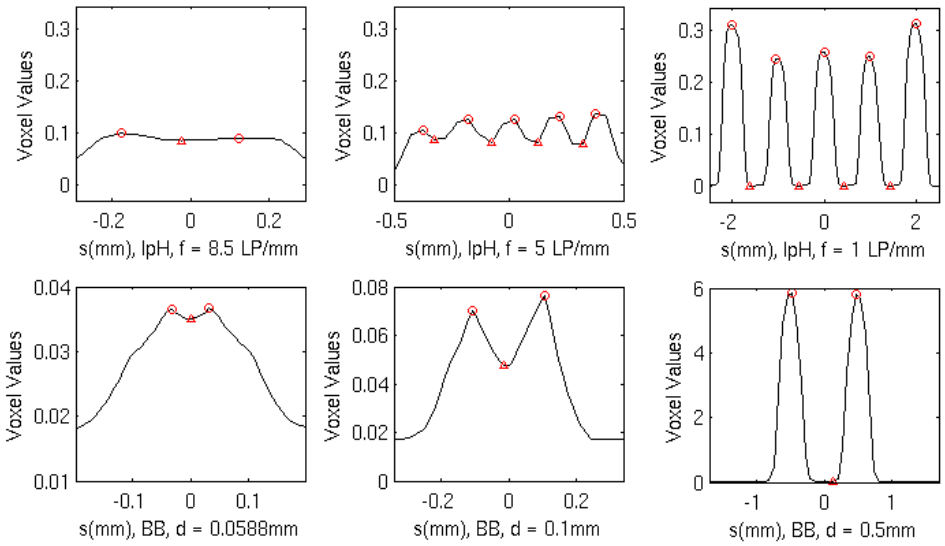

Figure 3.10. Examples of peak detections (L00, RT projector, subpixel ratio xy2z2). The circles mark the detected peaks and the triangles mark the detected valleys. Fewer than 5 peaks are detected at the frequency f = 8.5 line pairs/mm, indicating that the line pairs are non-resolvable. lpH = horizontal line pairs, f = frequency, LP = line pairs, d = diameter. The profiles of the vertical line pairs are analyzed similarly but not shown.

After extracting the profile, we used automatic peak detection to identify peaks and valleys of the profile as shown in Figure 3.10. For each set of line pairs, the numbers of detected peaks

and valleys were counted. If 5 peaks and 4 valleys were detected, the contrast was calculated as the difference between the mean peak value and the mean valley value, normalized to the contrast value of the line pairs in the voxelized image of the analytical phantom, which had the same constant value for all line pair frequencies. If less than 5 peaks were detected, the line pairs was considered to be non-resolvable and the contrast of the line pairs was assigned 0. The two plots in the first row of Figure 3.10 show examples of these two situations.

For the BB profiles, similarly, if less than 2 peaks were detected the contrast was considered to be 0. If 2 peaks and 1 valley were detected, we used the following equation to define the relative contrast of the BB:

$$\text{Relative Contrast} = \frac{(p_1+p_2)/2-v}{\max(p_1,p_2)-b} \tag{3.13}$$

where p_1 and p_2 are the values at two peaks, v is the value at the valley and b is the background voxel value. The relative contrast instead of the absolute contrast is used because BBs with different diameters have different thicknesses along the z-direction. For BBs located entirely within a single reconstructed slice (diameter < slice interval), the highest voxel values of the BBs are approximately proportional to their diameters. Even if the reconstruction is ideal (exactly matches the voxelized ground truth), there are large differences between the absolute contrasts of BBs of different diameters, making the contrast-versus-diameter curve less meaningful. On the contrary, the relative contrast of ideally reconstructed BBs will always be 1, so it better describes whether the two BBs can be resolved. When the two peaks are not equal, we use the larger one of the two peaks in the denominator to be conservative in estimating the relative contrast. For simplicity, the relative contrast is simply referred to as "contrast" in the following discussion.

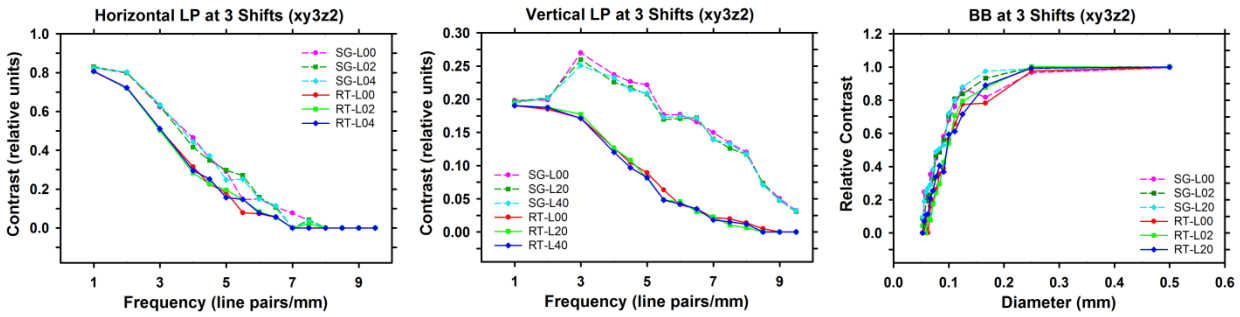

Figure 3.11. The dependence of the contrast on the frequency of line pairs and the diameter of BBs for 3 shifted locations. The RT projector is compared with the SG projector at a given subpixel ratio (xy3z2).

The contrasts of line pairs and BBs were computed for all 25 shifted locations of the imaged objects. When the object was shifted, we shifted the starting point and ending point of profiles by the same value to make sure that all profiles represented features of the objects at the same location. Figure 3.11 shows an example comparing the SG and RT projectors when the subpixel ratio was fixed at xy3z2. The variation of the contrasts of the line pairs and BBs is very large at the different alignment of the spheres with the voxel grid, especially for the mid-frequency line pairs and small spheres. However, for a given shift location, the SG projector always gives better contrast than the RT projector. As a result, the mean contrast over all shifted locations can be used to represent the trend when the objects are imaged at random locations by the DBT system.

For the horizontal (or vertical) line pair objects, only 5 of the 25 shifted locations produces different measurements of contrast values because the objects are parallel to the vertical (or horizontal) direction. The mean contrasts were obtained by averaging the five values from the shifted locations perpendicular to the line pairs. For the BBs, the contrasts at all 25 shifted locations were used for the estimate of the mean. The mean contrast will be used in the following discussions unless it is specified otherwise.

III.5.5 Quantitative analysis: dependence of contrast on the number of iterations

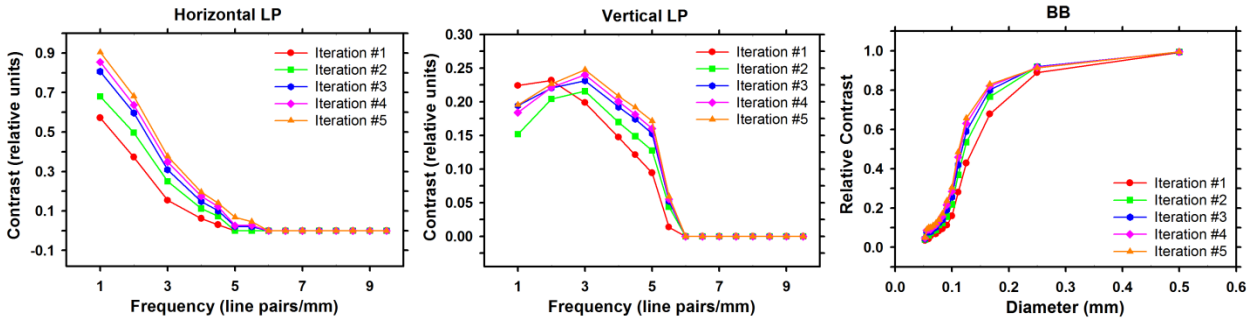

Figure 3.12. Dependence of mean contrast on number of iterations. All reconstructions used SART with the SG projector and xy1z1. Left: horizontal line pairs. Middle: vertical line pairs. Right: BBs.

We first analyzed the dependence of the mean contrast on the number of iterations. Figure 3.12 shows the contrast-versus-line pair frequency curves of xy1z1 reconstructed with the SG projector. The trends shown in Figure 3.12 are similar for reconstruction with other projectors.

The contrasts of the objects generally increase with increasing number of iterations. The only exception is the vertical line pairs, where the contrast after 1 iteration is higher than that after 2 iterations for the lowest two frequencies. It can be seen that the increase in contrasts leveled off when we performed more iterations, representing convergence of the SART reconstruction [86].

In the reconstruction of clinical DBT images, the number of iterations needed may depend on the reconstruction method and the imaging techniques used, as well as the acquisition geometry (total scan angle, number of projections and angular increments) of the DBT system. In this study, we chose to use 5 iterations for SART in the following discussions. We expect that the relative trends observed would not change after the reconstruction reaches relatively stable levels.

III.5.6 Quantitative analysis: dependence of contrast on the subpixel ratio

Figure 3.13 shows the mean contrasts of the line pairs and spherical objects at different subpixel ratios for the fixed projector (SG). The contrasts of the line pairs were averaged over 5 shifted locations of the phantom while the contrasts of the BBs were average over 25 shifted locations of the phantom, as explained above. Similar trends can be observed with the RT projector. When the *z* ratio is fixed and a higher xy-ratio is used (first row of Figure 3.13), a higher contrast is achieved for the three types of objects. The Nyquist frequency of the detector is 5 line pairs/mm. Without the subpixel reconstruction, it is difficult to differentiate line pairs with higher frequencies due to aliasing. After increasing the xy-ratio from 1 to 2, the contrasts increase dramatically for the vertical line pairs, especially for frequencies higher than 5 line pairs/mm. The vertical line pairs with a frequency higher than or equal to 6 line pairs/mm become resolvable with the subpixel reconstruction. For the horizontal line pairs, however, they are still not resolvable at frequencies higher than or equal to 6 line pairs/mm even with a higher xy-ratio. This is because that the DBT reconstruction artifacts spread along the vertical direction (*y*-direction) and subpixel reconstruction cannot alleviate this problem. The two BBs can be resolved down to the smallest diameter and spacing (0.053 mm) included in this study, which is smaller than the pixel size of the detector and Nyquist limit. When the xy-ratio is increased from 2 to 3, the improvement in the contrasts of the objects is relatively small.

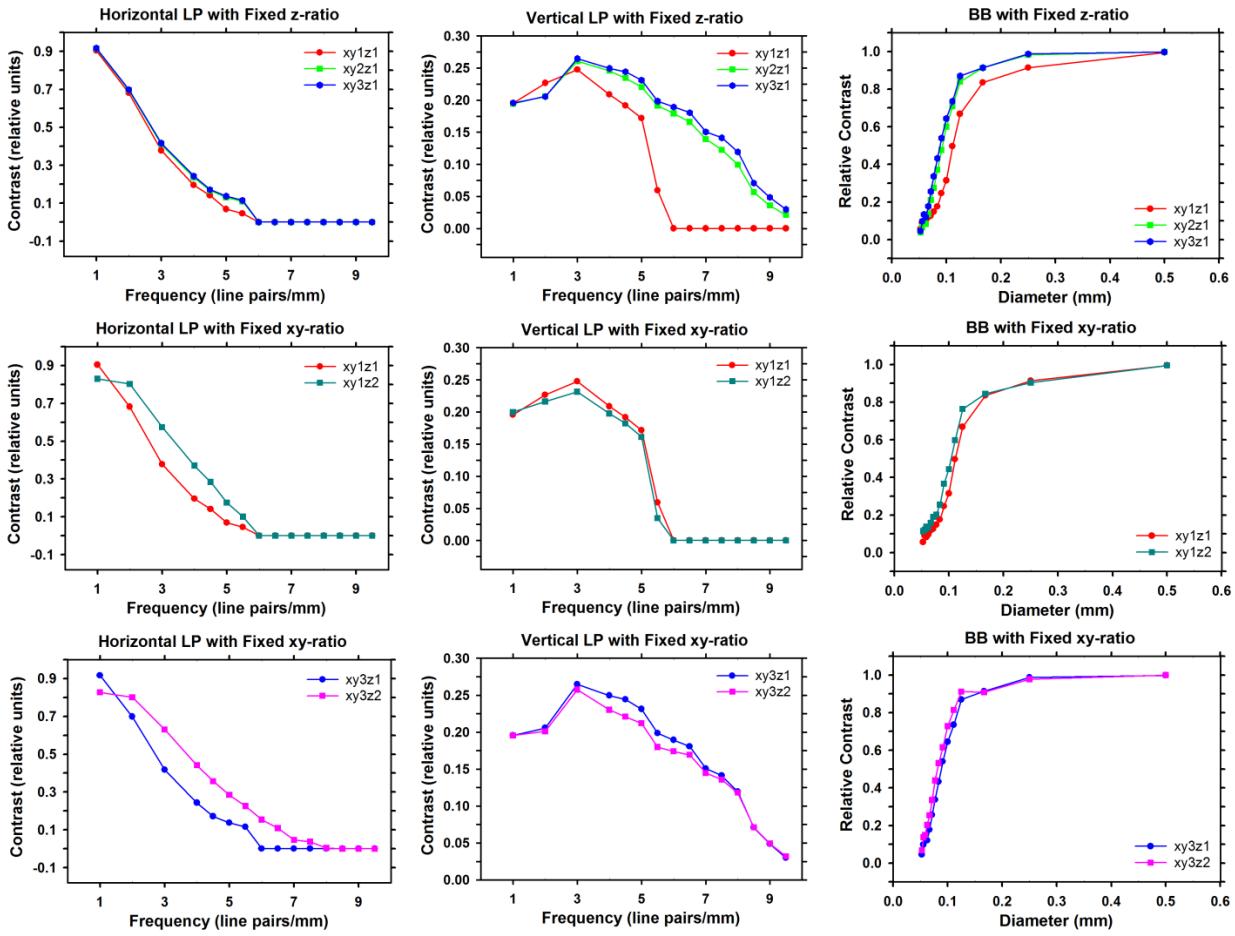

Figure 3.13. Dependence of mean contrast on subpixel ratios. All reconstructions used SART with the SG projector and 5 iterations. Left column: horizontal line pairs. Middle column: vertical line pairs. Right column: BBs. Upper row: subpixel ratios of xy1z1, xy2z1, xy3z1. Middle row: subpixel ratios of xy1z1, xy1z2. Lower row: subpixel ratios of xy3z1, xy3z2.

The different observations for the horizontal and vertical line pairs indicate that the DBT system has different frequency response along the x and y-direction. However, the difference should be less in DBT of human breasts because the in-plane reconstruction artifacts for lower contrast tissues will not be as strong as that of the lead line pair patterns, and the artifacts due to dense calcifications or metal biopsy clips can be corrected to reduce their influence on the visibility of other features in the image [87, 88].

When the xy-ratio is fixed at 1 and the z-ratio is increased from 1 to 2 (second row of Figure 3.13), the contrasts of horizontal line pairs and BBs increase. The increase in the contrasts of BBs is similar to what we observed in our previous study [83]. The exception is the vertical line pairs, where a z-ratio of 2 appears to reduce the contrasts. The reason is the different locations of

the line pairs relative to the voxel along the z-direction. As mentioned in the Section III.3, we placed the line pair objects at a depth of 25.6 mm from the bottom of the imaged volume. At the reconstruction with a z-ratio of 1 (i.e., slice interval of 1 mm), the line pair objects were contained well within the slice between 25.0 and 26.0 mm. When the z-ratio was set to be 2, the slice interval was reduced to 0.5 mm, the location of the line pairs was only 0.1 mm from the boundary of the sub-voxels along the z-direction, which was 20% of the slice interval. Part of the contrast of the line pairs leaked into the neighboring slices. It is impossible to set up a phantom where the objects are located at the center of a voxel along the z-direction for all z-ratios studied. If we set up two phantoms where the objects are located at the center of the focal slice (along the z-direction) for both z-ratios of 1 and 2, the difference in the contrasts for the z-ratio = 1 and z-ratio = 2 conditions would likely be smaller and not reversed. However, such an approach would change the premise of the study that the available DBT projections are the same and only the projectors and subpixel ratios are changed. The third row of Figure 3.13 shows the change in contrasts when the xy-ratio is fixed at 3 and the z-ratio increases from 1 to 2. For the horizontal line pairs, several of the line pairs with spatial frequency higher than 5 line pairs/mm become resolvable when a larger z-ratio is used, as observed in Figure 3.9.

III.5.7 Quantitative analysis: dependence of contrast on the projector type

Figure 3.14 shows the dependence of the contrasts of line pairs and BBs on the projector. The SG projector outperforms the RT and the SF projector under most conditions. However, the advantage of using the SG projector also depends on the type of the objects, the subpixel ratio and the number of iterations. With the subpixel ratio of xy1z1 (first column of Figure 3.14), the increase in contrast for the SG projector is not obvious, except for the vertical line pairs. A possible reason is that the in-plane “shadow” artifact of DBT due to the limited scan angle is a dominant factor on the contrast of the horizontal line pairs, which masks the differences of the projectors. For the vertical line pairs, the SG projector shows the advantage of a more accurate system model using the SG projector.

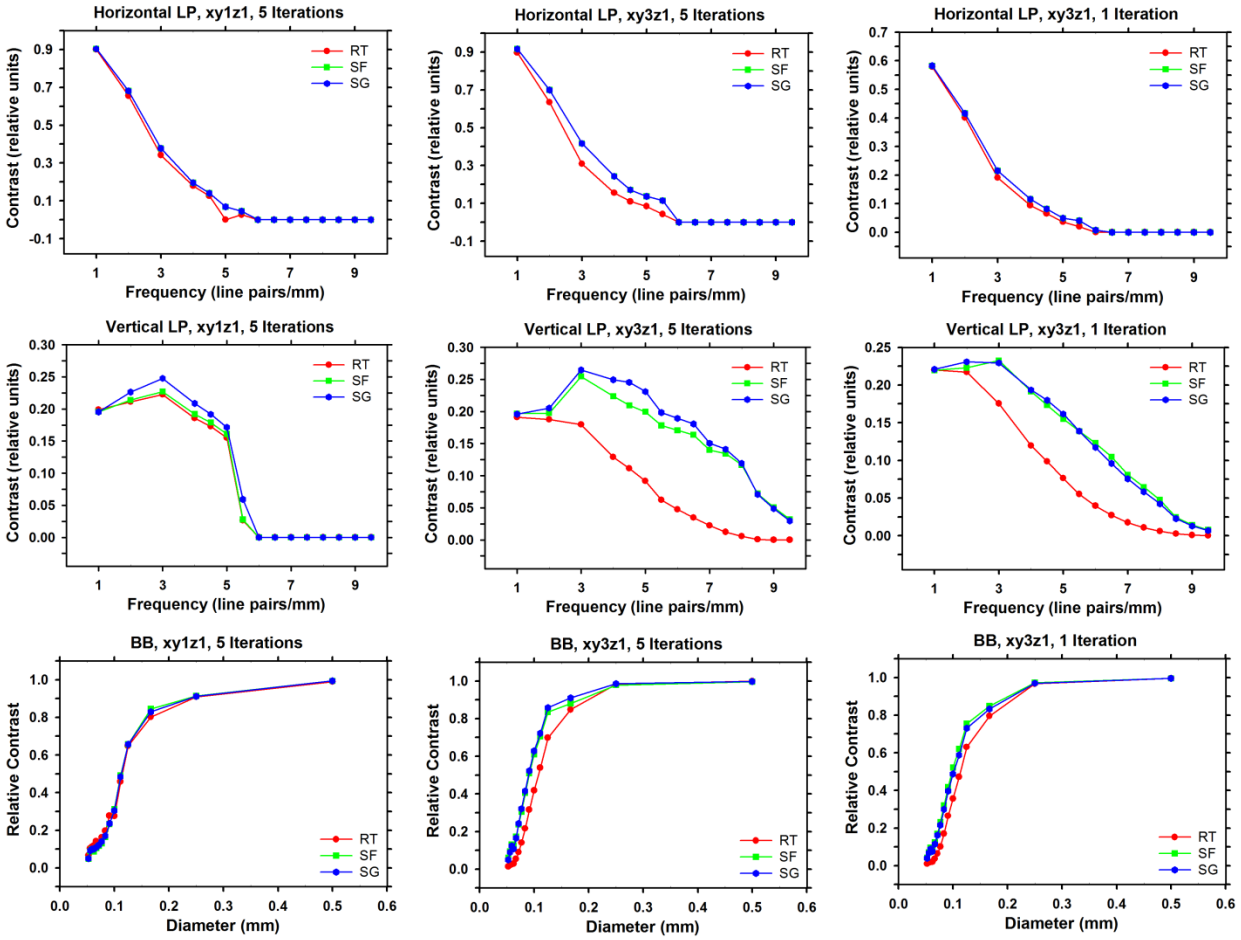

Figure 3.14. Dependence of mean contrast on the RT, SF and SG projectors. Upper row: horizontal line pairs. Middle row: vertical line pairs. Lower row: BBs. Left column: xy1z1, 5 iterations. Middle column: xy3z1, 5 iterations. Right column: xy3z1, 1 iteration.

For the subpixel reconstruction, the SG projector substantially improves the contrasts of the objects as shown in the second column of Figure 3.14. When using the RT projector for subpixel reconstruction, the input projections have to be interpolated to reduce the sparsity of the rays and missing elements in the system matrix, which would lead to empty voxels in the reconstructed volume. The interpolation increases the number of rays to trace and may cause additional blur across sharp edges on the projections. With the SG projector, the original projections are used as input and no interpolation is needed. Therefore, there will be no blurring due to interpolation and the reconstructed line pairs may be sharper with higher contrasts.

For xy1z1 reconstruction or the horizontal line pairs, the improvement in resolution by the SG projector is not obvious compared to the RT projector. The main advantage of the SG projector is reducing noisy artifacts (see example in Figure 3.9) due to numerical imprecision.

The contrast of a specific set of line pairs is calculated from the average profile from 9 individual profiles for a reconstructed in-focus slice, which has a denoising effect, masking partly the problem with the RT projector in terms of contrast.

Another interesting observation is that the SF and SG projectors perform very similarly for the horizontal line pairs. This may be intuitively explained. If we have several consecutive voxels with the value of 1, the summed projection of all of them will be the sum of their footprints. As shown in Figure 3.5, the SF and the SG footprints are very different when projected to the t-axis (parallel to x) and very similar when projected to the *s*-axis (parallel to y). As a result, the sum of several consecutive SF and SG footprints will be similar for consecutive voxels along the x-direction and will be different for the voxels along the y-direction. So it is reasonable that the horizontal line pairs (along the x-direction) have similar reconstruction results with the SF or the SG projector.

The advantage of the SG projector also depends on the number of iterations, as seen by comparing the second and the third column of Figure 3.14. With only 1 iteration, the SF projector actually produces slightly higher contrasts than the SG projector. As the number of iterations increases, the contrasts of objects increase faster with the SG projector, making it the best performing projector at 5 iterations. In fact, although a more accurate projector should improve the finally converged reconstructed image, there is no guarantee that it will also improve the intermediate reconstruction results. A sufficient number of iterations might be necessary to gain advantage from using the SG projector. It is difficult to estimate this number analytically. Experiments with different projectors might be necessary for a specific DBT system. This also indicates the importance of regularization in DBT image reconstruction [67, 89], which allows us to do more iterations without amplifying the noise at the same time.

III.5.8 Image blur in the depth direction

We evaluated the effect of the projectors on image blur in the z direction. The image blur is quantified by the artifact spread function (ASF) of the BBs, which is defined as the ratio between the contrast at each depth and the contrast at the focal plane [90] of the object:

$$\mathrm{ASF}(z) = \frac{\mathrm{Contrast}(z)}{\mathrm{Contrast}(z_0)}, \tag{3.14}$$

where z_0 is the depth of the focal plane. The contrast of a BB at a given depth is defined as the value at the pixel nearest to the analytical location of the center of the BB above the background value, which is a constant for the phantom images. The ASF is calculated for a single BB rather than a pair of BBs. For a given BB diameter, with a pair of BBs at each of the 25 shifted locations, we calculated the average of the ASFs over the 50 BB locations to reduce the dependence of the alignment of the BB with the pixel grid. The average ASFs were compared for the three projectors under different reconstruction conditions.

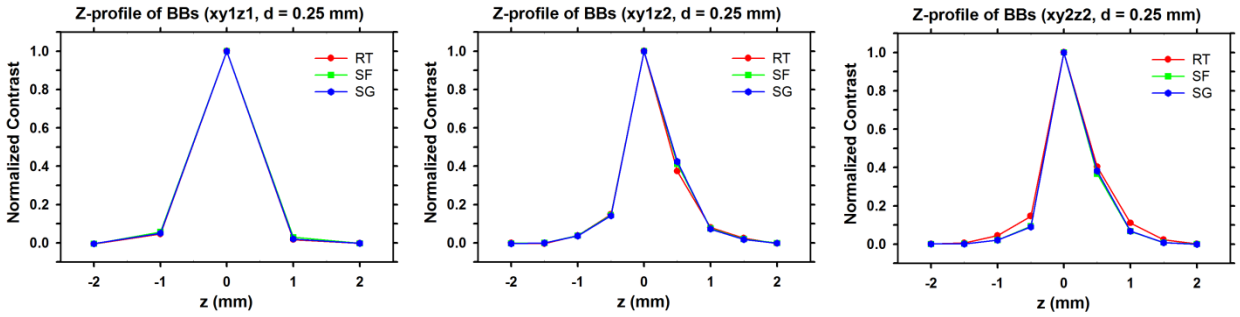

Figure 3.15. Comparison of ASF along the depth direction (z) from the RT, SF and SG projectors for the 0.25-mm-diameter BBs. The images reconstructed with subpixel ratios xy1z1, xy2z1, xy2z2 and 5 iterations were analyzed. The depth z_0 of the focal plane of the BB is plotted at 0 in the graphs.

Table 3.2. FWHMs (in mm) of the ASFs in Figure 3.15

Projector	xy1z1	xy1z2	xy2z2
RT	1.03	0.69	0.71
SF	1.05	0.71	0.67
SG	1.04	0.72	0.68

Figure 3.15 shows the ASFs of different projectors for the BBs with a diameter of 0.25 mm. Table 3.2 shows the FWHMs of the ASFs in Figure 3.15. The FWHMs were calculated based on the linear interpolation of the data points. We found the two *z* values where the ASF was equal to 0.5, and calculated the difference between them as the FWHM. For the xy1z1 subpixel ratio, the three different projectors give very similar results. For the xy2z2 subpixel ratio, the SG and SF projectors show slightly narrower ASFs than that of the RT projector in the midrange but all ASFs decrease to near background value at about the same depth. The ASFs for the subpixel ratios xy2z1 and xy3z1 (not shown) are similar to the ASF of xy1z1, and the ASF of xy3z2 (not

shown) is similar to that of xy2z2. Similar trends were also observed for the 0.5-mm-diameter BBs. The difference in the depth resolution among the projectors therefore is negligible for the objects studied.

III.5.9 Computation speed

To save computation time and the space to store the reconstructed images, we reconstructed a volume of interest (VOI) of size $5 \times 10 \times 5$ cm^3 instead of the full volume ($19.2 \times 23.04 \times 5.0$ cm^3, as shown in Figure 2.1) using the full-size projections as input. We positioned this VOI such that it contained all line pairs and spheres in the phantom and was beyond the extent of the TPAs [67, 69]. For different subpixel ratios, the reconstructed VOI had the same physical size, resulting in more voxels for higher subpixel ratios. The computation times of one iteration for reconstructing the same VOI using the different projectors and subpixel ratios are compared in Table 3.3. The computation times shown here include the time for outputting the reconstructed volume. The RT projector was implemented with the accelerated version of Siddon's algorithm [79], which was about 3 times faster than the original algorithm according to our tests. All reconstructions were performed with the same Linux workstation (Intel Xeon(R) CPU E5-2690, 8 cores, 2.9 GHz, 32 RAM). We used 16 threads for all reconstructions with each projector.

Table 3.3. Computation time (in seconds) of one iteration. The value in the parenthesis is the ratio of computation time relative to that using the RT projection at xy1z1.

Projector	xy1z1	xy2z1	xy3z1	xy1z2	xy2z2	xy3z2
RT	16.32 (1.0)	76.1 (4.7)	263.9 (16.2)	19.97 (1.2)	91.66 (5.6)	278.7 (17.1)
SF	7.16 (0.4)	17.59 (1.1)	34.31 (2.1)	10.62 (0.7)	30.66 (1.9)	62.0 (3.8)
SG	14.12 (0.9)	55.58 (3.4)	143.38 (8.8)	15.91 (1.0)	63.34 (3.9)	161.4 (9.9)

Obviously, a higher subpixel ratio will take more computation time. The xy-ratio affects the computation time more than the z-ratio due to the fact that it is squared for the total number of voxels in the volume. Despite more computation, both the SF and SG projectors are more efficient than the RT projector because they access the memory array of the imaged volume sequentially. The SF projector is faster than the SG projector, since it is basically the SG

projector with only one segment. For the xy3z1, the SG projector uses 18 segments to maintain the same height-to-width ratio as that used for the other subpixel ratios, which cost a substantial amount of extra computation time compared with the SF projector. The time saving by the SG projector compared with the RT projector increases with increasing xy-ratio, because the SG projector does not use interpolated projections, which becomes a more serious problem at high xy-ratios.

III.6 Limitations of the study

III.6.1 Absence of noise and other factors

In this study, many factors in the imaging system, such as detector blur, correlated noise, focal spot blur and other effects were ignored in generating the simulated DBT projections. This allows us to focus on the analysis of the role of the projector in the resolution of the reconstructed images. We observed improved resolution under this idealized situation, reinforcing the idea that a more accurate system model has the potential to improve DBT reconstruction. The overall effects of the projectors in the presence of these factors will warrant further studies. The study introduced in Chapter IV takes into account the detector blur and the correlated noise [91], as a further step towards a model-based DBT reconstruction framework. The study introduced in Chapter VI shows the effect of source blur on DBT reconstruction, especially for DBT systems with the continuous-motion data acquisition mode [44].

III.6.2 Comparison with the distance-driven projector

We used a rect function, $q_t(t;i;\vec{n})$, and a trapezoid function, $q_s(t;i;\vec{n})$, in our implementation of the SG projector (Equation 3.8). This implementation is called the TR method [39]. In principle, the distance-driven projector [81] is equivalent to using rect functions in both *t*- and *s*-directions (the RR method). Compared with the TR method, we expect the RR method to reduce the computation time while reducing the projector accuracy. Whether the distance-driven approximation (or the RR method) to each segment is adequate for the DBT geometry will be a topic of research interest in future studies.

III.6.3 Efficient usage of the subpixel reconstruction

Although the subpixel reconstruction provides better quality images, it costs dramatically longer computation time as shown in Table 3.3. It also costs much more memory, since we need to store the reconstructed volume at a finer voxel grid. Considering the trade-off between the improvement in contrasts and the computation time and storage space, the small gain from *xy*2 to *xy*3 (Figure 3.13) may not be cost-effective. The projectors we developed, either the RT or the SG projector, only cost a small amount of memory compared to that used for the voxel grid. For the phantom DBT in this study, if we use a voxel size of $0.1 \times 0.1 \times 1.0\ \mathrm{mm}^3$ for reconstruction, the number of voxels in the imaged volume is $1920 \times 2304 \times 50$, which will cost 0.82 GB of memory with single precision in floating point format. For the xy3z2 subpixel ratio, the memory cost is 14.8 GB. This size is only about that of an average breast and the DBT of many breasts can be much larger. As a result, it will be difficult to apply the subpixel method to the full imaged volume in clinical practice. An efficient way of using the subpixel reconstruction is to perform subpixel reconstruction only within selected VOIs. In fact, all the reconstructions in our study were performed based on the VOI-specific reconstruction. We have confirmed that if the VOI is properly selected and far from the regions affected by the TPA [67, 69], the reconstructed image slices should be identical to the same region from the full volume image reconstruction.

III.6.4 Shift-variance of spatial resolution in DBT

DBT essentially uses a limited-angle cone-beam CT geometry, the spatial resolution of which is known to be shift-variant. In this study, we only used one phantom embedded with a set of line pairs and spherical objects at fixed locations arranged centrally and near the chest wall in the DBT field of view. Because we used the same phantom projections for the reconstruction under all conditions, the relative performance should be a reasonable representation of the ranking of the conditions studied. As demonstrated in Figure 3.5 to Figure 3.7, the RMSE values of both the SF and SG projectors increase but that of the RT projector decreases as the x-ray incident angle increases. The RMSE value of the SG projector remains much lower than those of the other two projectors. For objects located at large x-ray incident angles and away from the chest wall, it is likely that the quality of the reconstructed images by the SG projector would still be superior to those by the other two projectors although the relative ranking of the RT and SF projectors is uncertain. In addition, the simulated array of line-pairs was placed parallel to the

detector plane and the reconstructed slices. The effects of different projectors on the spatial resolution of line pairs or objects that are rotated out of plane relative to the detector and/or the reconstructed slices are still unknown. The degree of shift variance of resolution in DBT and the spatial and angular dependences of the relative ranking of the different projectors for DBT reconstruction will be a topic of research interest in future studies.

III.7 Conclusion

This chapter proposed an improved digital projector, the SG projector, for DBT reconstruction. Theoretically and experimentally, we demonstrated that the SG projector is able to generate very good approximations of the ideal projector. The SG projector outperforms the RT projector in terms of reconstruction quality without increasing the computation time. We applied the new projector to regular and the subpixel DBT reconstructions and illustrated its effectiveness. We compared the subpixel DBT reconstruction with the traditional RT projector and the SG projector. Results showed that the subpixel reconstruction can significantly improve image resolution, especially when it is used with the SG projector. The trade-off of using the subpixel reconstruction is the extra computation time and memory, which may be reduced by performing subpixel reconstruction only within selected VOIs.

CHAPTER IV.
Detector Blur and Correlated Noise Modeling for Digital Breast Tomosynthesis Image Reconstruction[2]

IV.1 Introduction

IV.1.1 Introduction to the SQS-DBCN algorithm

In this chapter, I will introduce the SQS-DBCN algorithm for DBT reconstruction. Inspired by the idea of MBIR, the SQS-DBCN algorithm incorporates the detector blur into the forward model to improve the reconstructed image quality. The detector blur in DBT causes correlation in the measurement noise. By making a few approximations that are reasonable for breast imaging, we formulated a regularized quadratic optimization problem with a data-fit term that incorporates models for detector blur and correlated noise (DBCN). We derived a computationally efficient separable quadratic surrogate (SQS) algorithm to solve the optimization problem that has a non-diagonal noise covariance matrix. We evaluated the SQS-DBCN method by reconstructing DBT scans of breast phantoms and human subjects. The results indicate that the contrast-to-nose ratio (CNR) and sharpness of MCs were enhanced by the SQS-DBCN algorithm compared to SART, while the reconstruction quality for soft tissue is preserved. A series of modified versions of the SQS-DBCN algorithms were then compared to explain the effectiveness of the original algorithm.

[2] This chapter is a reorganization of our paper on IEEE Transactions on Medical Imaging and its supplementary material [92]. Part of the content in our published paper has been moved to Chapter II that it is also used by other studies discussed in this dissertation.

IV.1.2 Inspiration of the study

Studies have demonstrated the promise of iterative reconstruction methods in DBT [30-36]. Among the IR methods, MBIR methods incorporate the physics model of the system and the statistical model of signal detection. For DBT, although some studies on MBIR methods have been conducted [41, 42], they considered only limited aspects of the system model, such as modeling the scattered radiation or the statistical model of the measurement noise. To our knowledge, no studies have incorporated the models of image degradation factors of the DBT imaging system, including the crosstalk of the flat-panel detector and the resulting noise correlation. Our goal is to develop MBIR methods with more comprehensive modeling of the system physics and computationally efficient algorithms for DBT reconstruction.

In a DBT system using an indirect detector, light diffusion in the phosphor or the scintillator introduces crosstalk between neighboring pixels. The finite pixel size and light diffusion contribute to blurring of the measured image and correlation in noise. Neglecting detector blur leads to blurring of the reconstructed objects, strongly affecting small features such as MC. In CT applications, several projectors have been proposed that account for the finite pixel size, such as the distance-driven projector [81] and the separable footprint projector [39]. In this dissertation, I have introduced the SG projector for DBT geometries [77]. Current DBT reconstruction algorithms generally treat the measurement at each detector element to be independent random variables, which differs from the physical process in the DBT detector. Tilley et al. and Stayman et al. studied the effect of modeling the detector blur and correlated noise in least-squares reconstruction for CBCT with simulated phantoms and found superior noise-resolution trade-offs with their proposed approach [93-95]. Our feasibility study [91] showed similar promise for DBT scans. In this chapter, we further refine our implementation of DBT reconstruction accounting for detector blur and the resulting noise correlation, incorporate adaptive regularization strength, analyze the image quality by the contrast and sharpness of the signals and the tissue texture using phantom and human subject DBT scans, and compare the reconstructed image quality with and without modeling detector blur and noise correlation.

We have already discussed the importance of regularization in DBT reconstruction in Section II.2. In this chapter, we use a regularization strategy based on a hyperbola potential function, which is convex and edge-preserving. We model detector blur and noise correlation and formulate the reconstruction as a regularized quadratic optimization problem. The problem needs

to be solved with an iterative algorithm. Based on the form of the data-fit term and the regularization, we chose to apply a slightly modified separable quadratic surrogate (SQS) [96] method. Although the SQS method requires more iterations to converge than coordinate descent methods, it enforces non-negativity constraints on the reconstructed image [97, 98].

IV.2 The reconstruction problem and algorithms

IV.2.1 Formulation of the reconstruction problem

We first mathematically formulate the reconstruction problem using a few assumptions based on the imaging characteristics of DBT. Similar to Chapter II, we use $\mathbf{A}_i$ to denote the $M \times N$ projector matrix for the ith projection angle, for $i = 1, \ldots, N_\mathrm{p}$. Let M denote the number of pixels in a DBT projection image and N the number of object voxels to be reconstructed. Let $\mathbf{f}$ denote the length-N vector corresponding to the unknown array of attenuation coefficients in the imaged volume and $\mathbf{Y}_i$ the length-N vector corresponding to the measured PV image at the ith projection angle. Considering the detector blur and the Lambert-Beer law for attenuation, a reasonable model for the expectation $\overline{\mathbf{Y}}_i$ is [94]:

$$\overline{\mathbf{Y}}_i = I_0 \mathbf{B}_i \exp\left(-\mathbf{A}_i \mathbf{f}\right), \tag{4.1}$$

where $\mathbf{B}_i$ denotes the blurring operation in $M \times M$ matrix form. In this work, we assume that $\mathbf{B}_i$ is projection-angle-dependent but linear shift-invariant within a given projection. Focal spot blur is ignored in the current study. If the incident intensity I_0 is nonuniform over the PV then one could replace the scale I_0 with a diagonal matrix.

One challenge in performing image reconstruction with the model in Equation 4.1 is that the matrix $\mathbf{B}_i$ before the exponential is not diagonal [93-95]. To address this challenge for DBT, we assume that the image $\mathbf{f}$ consists of two parts ($\mathbf{f} = \mathbf{f}_b + \mathbf{f}_s$), where $\mathbf{f}_\mathrm{b}$ is a low-frequency background whose projections are approximately uniform within the support of the blurring kernel ($\mathbf{B}_i \mathbf{A}_i \mathbf{f}_\mathrm{b} \approx \mathbf{A}_i \mathbf{f}_\mathrm{b}$), and $\mathbf{f}_\mathrm{s}$ is a small structure such as MC in DBT whose attenuation contributes only a small amount to the projection values ($\mathbf{A}_i \mathbf{f}_\mathrm{s} \ll 1$). These assumptions are more reasonable in breast imaging than in CT of body parts that include bone or other high-attenuation objects. Under these assumptions, we use the following approximation:

$$
\begin{aligned}
&\mathbf{B}_i \exp(-\mathbf{A}_i\mathbf{f}) = \mathbf{B}_i \exp(-\mathbf{A}_i\mathbf{f}_s)\exp(-\mathbf{A}_i\mathbf{f}_b)\\
&\approx \mathbf{B}_i(\mathbf{1}-\mathbf{A}_i\mathbf{f}_s)\exp(-\mathbf{B}_i\mathbf{A}_i\mathbf{f}_b)\\
&= (\mathbf{1}-\mathbf{B}_i\mathbf{A}_i\mathbf{f}_s)\exp(-\mathbf{B}_i\mathbf{A}_i\mathbf{f}_b)\\
&\approx \exp(-\mathbf{B}_i\mathbf{A}_i\mathbf{f}_s)\exp(-\mathbf{B}_i\mathbf{A}_i\mathbf{f}_b)\\
&= \exp(-\mathbf{B}_i\mathbf{A}_i\mathbf{f}).
\end{aligned}
\tag{4.2}
$$

Then we have the following simplification of Equation 4.1 for DBT:

$$\bar{\mathbf{Y}}_i \approx I_0 \exp(-\mathbf{B}_i\mathbf{A}_i\mathbf{f}). \tag{4.3}$$

The expectation $\bar{\mathbf{y}}_i$ of the log-transformed projection $\mathbf{y}_i$ is approximately:

$$\bar{\mathbf{y}}_i = \log(I_0/\mathbf{Y}_i) = \mathbf{B}_i\mathbf{A}_i\mathbf{f}. \tag{4.4}$$

Compared with the reconstruction problem without detector blur, we simply need to include a blurring operation in the forward projection step. The transpose of $\mathbf{B}_i$ is also relatively easy to implement in the back-projection step needed for iterative image reconstruction.

The cost function of the reconstruction problem should also account for the covariance matrix of the noise in the measurements $\mathbf{y}_i$. DBT systems usually use a flat-panel direct or indirect detector. In our model, we assume an indirect CsI phosphor/a:Si active matrix flat panel detector. The image noise contains two major components: quantum noise from the x-ray photons and electronic noise of the detector. The quantum noise in the imaging process is affected by the detector blur but the detector electronic noise is not.

Accounting for both quantum and electronic noise, we use the following model for the noise covariance $\mathbf{K}_i$ of the *i*th PV:

$$\mathbf{K}_i = \mathbf{B}_i\mathbf{K}_i^{\mathrm{q}}\mathbf{B}_i' + \mathbf{K}_i^r, \tag{4.5}$$

where $'$ denotes the transpose of a matrix. $\mathbf{K}_i^q$ and $\mathbf{K}_i^r$ denote diagonal matrices with elements corresponding to the variances of quantum noise and readout noise at each detector element, respectively.

The derivation of the noise covariance $\mathbf{K}_i$ is similar to the Appendix of the paper by Tilley et al. [22]. The difference is that our application is for DBT geometry in which the imaged volume is very close to the detector. As a result, we neglect the focal spot blur so the blurring operation $\mathbf{B}_i$ in our study only includes the detector blur. This approximation will be revisited in Chapter VI. For the directly measured projection $\mathbf{Y}_i$ before the log transform, we treat it as having a Gaussian distribution:

$$\mathbf{Y}_i \sim N(\overline{\mathbf{Y}}_i, \mathbf{K}_i^Y), \tag{4.6}$$

where

$$\overline{\mathbf{Y}}_i = I_0 \mathbf{B}_i \exp(-\mathbf{A}_i \mathbf{f}), \tag{4.7}$$

$$\mathbf{K}_i^Y = \mathbf{B}_i \mathbf{K}_i^{\mathrm{Q}} \mathbf{B}_i' + \mathbf{K}_i^{\mathrm{R}}, \tag{4.8}$$

where the capital letters Q and R in the superscripts denote that these values are for the projections before the log transform. Respectively, the lower-case letters q and r in Equation 4.5 denote that $\mathbf{K}_i^q$ and $\mathbf{K}_i^r$ are for the projections after the log transform. $\mathbf{K}_i^q$ and $\mathbf{K}_i^r$ are directly used in the reconstruction algorithm since the log-transformed projection images are directly used in the implementation of the SQS-DBCN algorithm.

According to Equation 4.3, the expectation of the log-transformed projection $\mathbf{y}_i$ is approximately:

$$\bar{\mathbf{y}}_i = \log\left(\frac{I_0}{\overline{\mathbf{Y}}_i}\right) \approx \mathbf{B}_i \mathbf{A}_i \mathbf{f}. \tag{4.9}$$

Similar to Tilley et al. [22], we consider the fluctuation of the random noise to be small compared with the mean value:

$$\frac{\mathbf{Y}_i - \overline{\mathbf{Y}}_i}{\overline{\mathbf{Y}}_i} \ll 1. \tag{4.10}$$

Then we have:

$$\begin{aligned} \mathbf{y}_i &= \log\left(\frac{I_0}{\mathbf{Y}_i}\right) \\ &= \log\left(\frac{I_0}{\overline{\mathbf{Y}}_i}\right) - \log\left(1 + \frac{\mathbf{Y}_i - \overline{\mathbf{Y}}_i}{\overline{\mathbf{Y}}_i}\right) \\ &\approx \bar{\mathbf{y}}_i - \frac{\mathbf{Y}_i - \overline{\mathbf{Y}}_i}{\overline{\mathbf{Y}}_i}. \end{aligned} \tag{4.11}$$

As a result, $\mathbf{y}_i$ also follows approximately a Gaussian distribution:

$$\mathbf{y}_i \sim N(\bar{\mathbf{y}}_i, \mathbf{K}_i), \tag{4.12}$$

where

$$\mathbf{K}_i = \mathrm{diag}\left(\frac{1}{\overline{\mathbf{Y}}_i}\right) \mathbf{B}_i \mathbf{K}_i^{\mathrm{Q}} \mathbf{B}_i' \mathrm{diag}\left(\frac{1}{\overline{\mathbf{Y}}_i}\right) + \mathrm{diag}\left(\frac{1}{\overline{\mathbf{Y}}_i}\right) \mathbf{K}_i^{\mathrm{R}} \mathrm{diag}\left(\frac{1}{\overline{\mathbf{Y}}_i}\right). \tag{4.13}$$

In our application, the blurring kernel $\mathbf{h}_i$ is symmetric along the horizontal and vertical directions. So $\mathbf{B}_i$ is a symmetric matrix. As we discussed previously in this section, we assume the low-frequency background to be approximately uniform over the support of the blurring

kernel while a small structure such as MC contributes only a small amount of projection values. As a result, $\overline{\mathbf{Y}}_i$ is approximately uniform over the support of the blurring kernel. Thus we make the following approximation:

$$\mathrm{diag}\left(\frac{1}{\overline{\mathbf{Y}}_i}\right)\mathbf{B}_i \approx \mathbf{B}_i\mathrm{diag}\left(\frac{1}{\overline{\mathbf{Y}}_i}\right). \tag{4.14}$$

The covariance matrix $\mathbf{K}_i$ then simplifies as:

$$\begin{aligned}\mathbf{K}_i &\approx \mathbf{B}_i\mathrm{diag}\left(\frac{1}{\overline{\mathbf{Y}}_i}\right)\mathbf{K}_i^{\mathrm{Q}}\mathrm{diag}\left(\frac{1}{\overline{\mathbf{Y}}_i}\right)\mathbf{B}_i' + \mathrm{diag}\left(\frac{1}{\overline{\mathbf{Y}}_i}\right)\mathbf{K}_i^{\mathrm{R}}\mathrm{diag}\left(\frac{1}{\overline{\mathbf{Y}}_i}\right)\\ &= \mathbf{B}_i\mathbf{K}_i^{\mathrm{q}}\mathbf{B}_i' + \mathbf{K}_i^{\mathrm{r}},\end{aligned} \tag{4.15}$$

where

$$\mathbf{K}_i^{\mathrm{q}} = \mathrm{diag}\left(\frac{1}{\overline{\mathbf{Y}}_i}\right)\mathbf{K}_i^{\mathrm{Q}}\mathrm{diag}\left(\frac{1}{\overline{\mathbf{Y}}_i}\right), \tag{4.16}$$

$$\mathbf{K}_i^{r} = \mathrm{diag}\left(\frac{1}{\overline{\mathbf{Y}}_i}\right)\mathbf{K}_i^{\mathrm{R}}\mathrm{diag}\left(\frac{1}{\overline{\mathbf{Y}}_i}\right). \tag{4.17}$$

According to Equation 4.12, $\mathbf{y}_i$ follows approximately a Gaussian distribution. We formulate for DBT the following regularized image reconstruction problem with non-diagonal weighting:

$$\begin{aligned}\hat{\mathbf{f}} &= \underset{\mathbf{f}}{\mathrm{argmin}}\frac{1}{2}\sum_{i=1}^{N_{\mathrm{p}}}\|\mathbf{y}_i - \mathbf{B}_i\mathbf{A}_i\mathbf{f}\|^2_{(\mathbf{B}_i\mathbf{K}_i^{\mathrm{q}}\mathbf{B}_i' + \mathbf{K}_i^{r})^{-1}} + R(\mathbf{f})\\ &= \underset{\mathbf{f}}{\mathrm{argmin}}\frac{1}{2}\sum_{i=1}^{N_{\mathrm{p}}}\|\mathbf{S}_i\mathbf{y}_i - \mathbf{S}_i\mathbf{B}_i\mathbf{A}_i\mathbf{f}\|_2^2 + R(\mathbf{f}),\end{aligned} \tag{4.18}$$

where $R(\mathbf{f})$ denotes the regularization term and the inverse matrix square root of the noise covariance is

$$\mathbf{S}_i = (\mathbf{B}_i\mathbf{K}_i^{\mathrm{q}}\mathbf{B}_i' + \mathbf{K}_i^{r})^{-1/2}. \tag{4.19}$$

IV.2.2 Implementing $\mathbf{S}_i$

Since $(\mathbf{B}_i\mathbf{K}_i^{q}\mathbf{B}_i' + \mathbf{K}_i^{r})$ is non-diagonal, implementing multiplication by $\mathbf{S}_i$ is usually very challenging, and this is the key difficulty in using the optimization formulation of Equation 4.18. The inverse of $(\mathbf{B}_i\mathbf{K}_i^{q}\mathbf{B}_i' + \mathbf{K}_i^{r})$ is non-diagonal with approximately 10^{13} elements in DBT, therefore it cannot be stored. To obtain the result of the linear operation $\left(\mathbf{B}_i\mathbf{K}_i^{q}\mathbf{B}_i' + \mathbf{K}_i^{r}\right)^{-1}\mathbf{v}$, one has to solve for $\mathbf{u}$ in the large-scale inverse problem $\left(\mathbf{B}_i\mathbf{K}_i^{q}\mathbf{B}_i' + \mathbf{K}_i^{r}\right)\mathbf{u} = \mathbf{v}$. In CT applications, one possible method is to solve it with a set of conjugate gradient iterations [94]. In DBT, we can dramatically simplify the implementation by making some reasonable assumptions.

Unlike body CT where there exist large bones and even perhaps metal objects of significant size that are strongly attenuating, the compressed breast has a fairly consistent thickness mainly composed of soft tissue. As a first-order approximation, we treat quantum noise variance as constant across all detector elements in a given projection angle:

$$\mathbf{K}_i^{\mathrm{q}} = {\sigma_i^{\mathrm{q}}}^2 \mathbf{I}, \tag{4.20}$$

where $\mathbf{I}$ denotes the $M \times M$ identity matrix. Equation 4.20 is the key approximation for the SQS-DBCN algorithm. We will study the influence of this approximation in Section IV.4.3 and Section IV.4.7.

In addition, we treat all detector elements in a given PV as having similar readout noise variance:

$$\mathbf{K}_i^{\mathrm{r}} = {\sigma_i^{\mathrm{r}}}^2 \mathbf{I}. \tag{4.21}$$

Equation 4.16 and 4.17 indicate that when we assume $\mathbf{K}_i^{\mathrm{q}} = {\sigma_i^{\mathrm{q}}}^2 \mathbf{I}$ and $\mathbf{K}_i^{\mathrm{r}} = {\sigma_i^{\mathrm{r}}}^2 \mathbf{I}$, it is equivalent to assuming $\mathrm{diag}\left(\frac{1}{\bar{\mathbf{Y}}_i}\right) \mathbf{K}_i^{\mathrm{Q}} \mathrm{diag}\left(\frac{1}{\bar{\mathbf{Y}}_i}\right)$ and $\mathrm{diag}\left(\frac{1}{\bar{\mathbf{Y}}_i}\right) \mathbf{K}_i^{\mathrm{R}} \mathrm{diag}\left(\frac{1}{\bar{\mathbf{Y}}_i}\right)$ to be constant along the diagonal for the *i*th projection angle.

Let $\mathbf{h}_i$ denote the point spread function (PSF) of the detector. We obtained $\mathbf{h}_i$ by the inverse Fourier transform of the MTF of the detector for a GE Essential mammography system [99], which also agreed with our own measurement on the prototype DBT system using the edge method [100]. We diagonalize the blurring operation by $\mathbf{B}_i = \mathbf{Q}^{-1}\mathbf{H}_i\mathbf{Q}$, where $\mathbf{Q}$ denotes the discrete Fourier transform (DFT) matrix, and $\mathbf{H}_i = \mathrm{Diag}(\mathrm{DFT}\{\mathbf{h}_i\})$ denotes the corresponding frequency response. We then implement the operation of multiplying $\mathbf{S}_i$ by a vector using FFT operations without needing any iterative method for matrix inversion:

$$\mathbf{S}_i = \mathbf{Q}^{-1}({\sigma_i^{\mathrm{q}}}^2 \mathbf{H}_i \mathbf{H}_i' + {\sigma_i^{\mathrm{r}}}^2 \mathbf{I})^{-1/2} \mathbf{Q}, \tag{4.22}$$

where σ_i^{q} and σ_i^{r} with lower case superscripts q and r denote noise standard deviations for the PVs after log transform, or equivalently the noise level relative to the recorded x-ray intensity. The corresponding noise standard deviations before log transform are denoted by σ_i^{Q} and σ_i^{R} with upper case superscripts Q and R. We estimate σ_i^{R} from dark current images without x-ray exposure by subtracting two dark current images to remove possible structured noise from the detector, then calculating a mean standard deviation σ_i^{R} from noise patches on the subtracted image and dividing it by $\sqrt{2}$. The breast boundary is automatically detected on each PV [101].

We then estimate the mean x-ray intensity $\bar{Y}_i$ incident on the detector as the mean pixel value within the breast boundary and calculate σ_i^{r} as the ratio of σ_i^{R} over $\bar{Y}_i$.

Estimating σ_i^{q} is more complicated since it is difficult to remove the heterogeneous tissue background from the projection images. Therefore, we use a DBT scan of a uniform Lucite slab of approximately the thickness of the phantom or a breast to estimate σ_i^{q}. For each PV of the Lucite slab, we select an array of noise patches and remove the background trend with a 2-D second order polynomial fitting. Then we calculate the standard deviation σ_i as the mean of the standard deviations estimated from each noise patch. This calculated σ_i contains the contribution of both σ_i^{R} and σ_i^{Q} as given by:

$$\sigma_i^2 = \sigma_i^{\mathrm{Q}^2} \|\mathbf{h}_i\|_2^2 + \sigma_i^{\mathrm{R}^2}. \tag{4.23}$$

We then derive σ_i^{Q} of the Lucite slab from the above relationship using the estimated σ_i and σ_i^{R}:

$$\sigma_i^{\mathrm{Q}} = \sqrt{\frac{\sigma_i^2 - \sigma_i^{\mathrm{R}^2}}{\|\mathbf{h}_i\|_2^2}}. \tag{4.24}$$

Treating σ_i^{Q} as approximately Poisson noise, $\sigma_i^{\mathrm{Q}^2}$ is proportional to $\bar{Y}_i$ and therefore $\sigma_i^{\mathrm{q}^2}$ is inversely proportional to $\bar{Y}_i$. Using the ratio of $\bar{Y}_i$ between a DBT scan and the Lucite slab, we estimate σ_i^{q} for the DBT scan to be reconstructed. In practical implementation, this may be accomplished by predetermining sets of σ_i^{Q} (i = 1, ... , N_{p}) for all N_{p} projections from Lucite slabs over a range of thicknesses and x-ray spectra (anode, filter, kilovoltage) combinations and storing them as a library of look up values. For a given DBT scan acquired with a certain exposure technique, one can select an appropriate set that approximates the breast thickness and exposure technique for reconstruction.

IV.2.3 The regularization

In the implementation of Equation 4.22, $\mathbf{S}_i$ acts as a filter that boosts high spatial frequencies. With the approximations of constant σ_i^{q} and σ_i^{r} for a given projection angle, we implemented $\mathbf{S}_i$ in the frequency domain with fast Fourier transform (FFT). Figure 4.1 shows the normalized frequency response of $\mathbf{S}_i$ that corresponds to the central PV of our experimental phantom. The

specific frequency response of $\mathbf{S}_i$ will change based on the estimated σ_i^{q} and σ_i^{r}, which depend on the projection angle. As a typical case, Figure 4.1 shows that the high-frequency response of $\mathbf{S}_i$ is not extremely high such that noise of the PVs will not be amplified excessively.

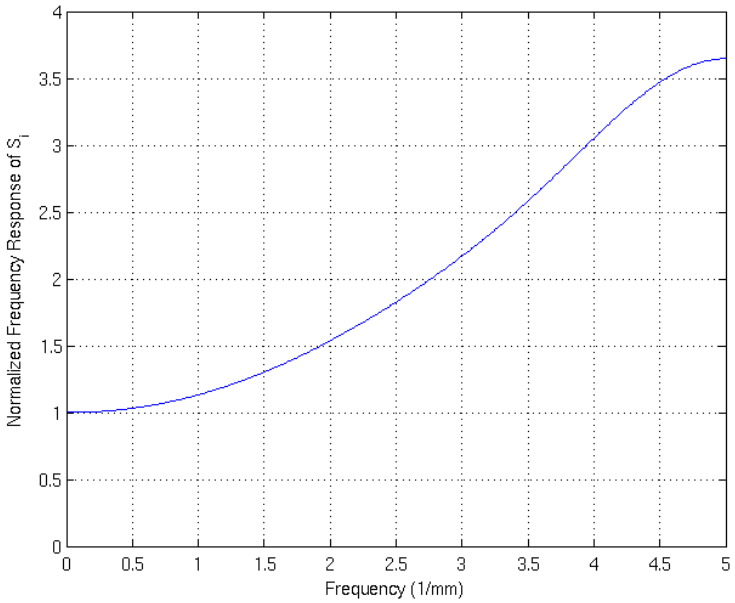

Figure 4.1. Normalized frequency response of S_i for the central projection angle of the experimental phantom.

Despite the shape of the curve in Figure 4.1, $\mathbf{S}_i$ would still amplify noise in reconstruction if used without regularization. Regularization is important for stable reconstruction. We use a regularization term of the following form:

$$R(\mathbf{f}) = \frac{\alpha\beta}{1+\gamma}\left(\sum_j \eta\left([\mathbf{C}_x\mathbf{f}]_j\right) + \eta\left(\left[\mathbf{C}_y\mathbf{f}\right]_j\right) + \gamma\eta\left(\left[\mathbf{C}_{x-y}\mathbf{f}\right]_j\right) + \gamma\eta\left(\left[\mathbf{C}_{x+y}\mathbf{f}\right]_j\right)\right), \tag{4.25}$$

where $\mathbf{C}_x$ and $\mathbf{C}_y$ denote matrices that calculate differences between neighboring pixels along the x and y-direction of the imaged volume, respectively, as defined in Figure 2.1. $\mathbf{C}_{x-y}$ and $\mathbf{C}_{x+y}$ compute finite differences along the two diagonal directions. j is the index for all neighboring pixel pairs along one direction. The distance between two neighboring pixels along the diagonal direction is larger, resulting in relatively weaker correlation between their pixel values. We therefore use the parameter γ ($\gamma \leq 1$) to control the weight of regularization in the diagonal directions. We chose γ to be 0.5 for this study following [102]. The parameter β controls the

strength of the regularization term. From reconstructing DBT at different noise levels, we observed that the regularization parameter needs to be adapted to keep an appropriate balance between the data-fit term and the regularizer, because the covariance-based weighting of the data-fit term in Equation 4.18 depends on the noise level. Therefore we include a scaling factor α to adaptively adjust the regularization strength based on the noise level of the projections. We define α as:

$$\alpha = \frac{N_{\mathrm{p}}}{\sum_{i=1}^{N_{\mathrm{p}}} {\sigma_i^{\mathrm{q}}}^2 \|\mathbf{h}_i\|_2^2 + {\sigma_i^{\mathrm{r}}}^2}. \tag{4.26}$$

For the regularizer in Equation 4.25, we use a hyperbola potential function $\eta(t)$:

$$\eta(t) = \delta^2 \left(\sqrt{1 + (t/\delta)^2} - 1\right). \tag{4.27}$$

This form of $\eta(t)$ is edge-preserving. $\eta(t)$ is also differentiable, making it easy to implement the optimization algorithm of the cost function. The parameters δ and β need to be chosen properly as discussed in Section IV.4.1. When δ is large relative to *t,* Equation 4.27 is approximately $\eta(t) = t^2$, which is equivalent to a quadratic regularization. In the result section of this chapter, we studied the effect of using a quadratic regularization by setting $\delta = 1/mm$. The details can be found in Section IV.4.8.

IV.2.4 The SQS-DBCN algorithm

Both the quadratic function of the data-fit term and $\eta(t)$ are convex and the second-order derivative of $\eta(t)$ in Equation 4.27 is

$$\ddot{\eta}(t) = \left(1 + \left(\frac{t}{\delta}\right)^2\right)^{-3/2}, \tag{4.28}$$

which is less than or equal to 1, enabling the use of the SQS algorithm to solve the optimization problem [97]. To apply the SQS algorithm, we need to find an upper bound on the Hessian of the cost function

$$\Psi(\mathbf{f}) = \frac{1}{2}\left\|\tilde{\mathbf{y}} - \widetilde{\mathbf{A}}\mathbf{f}\right\|_2^2 + R(\mathbf{f}), \tag{4.29}$$

where the whole system matrix and whole (prewhitened) data vector are given by:

$$\widetilde{\mathbf{A}} = \begin{pmatrix} \widetilde{\mathbf{A}}_1 \\ \cdots \\ \widetilde{\mathbf{A}}_{N_{\mathrm{p}}} \end{pmatrix} = \begin{pmatrix} \mathbf{S}_1\mathbf{B}_1\mathbf{A}_1 \\ \cdots \\ \mathbf{S}_{N_p}\mathbf{B}_{N_p}\mathbf{A}_{N_p} \end{pmatrix}, \tag{4.30}$$

$$\tilde{\mathbf{y}} = \begin{pmatrix} \tilde{\mathbf{y}}_1 \\ \cdots \\ \tilde{\mathbf{y}}_{N_\mathrm{p}} \end{pmatrix} = \begin{pmatrix} \mathbf{S}_1 \mathbf{y}_1 \\ \cdots \\ \mathbf{S}_{N_\mathrm{p}} \mathbf{y}_{N_p} \end{pmatrix}. \tag{4.31}$$

We first find an upper bound on the Hessian of the regularization term $R(\boldsymbol{f})$. Since the second-order derivative of the potential function $\eta(t)$ is less than or equal to 1, we have

$$\nabla^2 \sum\nolimits_j \eta\big([\mathbf{Cf}]_j\big) \le \mathrm{diag}\{|\mathbf{C}'||\mathbf{C}|\mathbf{1}\} = 4\mathbf{I}, \tag{4.32}$$

where $\mathbf{1}$ denotes a length-N all-one vector, $|\cdot|$ denotes element-wise absolute value, $\mathbf{I}$ denotes the identity matrix and $\mathbf{C}$ denotes any one of $\mathbf{C}_x$, $\mathbf{C}_y$, $\mathbf{C}_{x+y}$ and $\mathbf{C}_{x-y}$. As a result, we have:

$$\nabla^2 R(\mathbf{f}) \le \frac{\alpha\beta}{1+\gamma}(4+4+4\gamma+4\gamma)\mathbf{I} = 8\alpha\beta\mathbf{I}. \tag{4.33}$$

By finding (derived in Equation 4.35-4.37 below) a diagonal majorizing matrix $\mathbf{D}$ such that $\mathbf{D} \ge |\widetilde{\mathbf{A}}'||\widetilde{\mathbf{A}}|$, the modified SQS algorithm for minimizing the DBT cost function is (with nonnegativity constraint):

$$\mathbf{f}^{(n+1)} = \max\big(\mathbf{f}^{(n)} - (\mathbf{D} + 8\alpha\beta\mathbf{I})^{-1}\nabla\Psi\big(\mathbf{f}^{(n)}\big), 0\big). \tag{4.34}$$

The usual choice of $\mathbf{D}$ would be $\mathbf{D} = \mathrm{diag}\big\{|\widetilde{\mathbf{A}}'||\widetilde{\mathbf{A}}|\mathbf{1}\big\}$. However, implementing $|\widetilde{\mathbf{A}}'||\widetilde{\mathbf{A}}|\mathbf{1}$ is difficult since $\widetilde{\mathbf{A}}$ has negative values because of the high-frequency boosting feature of $\mathbf{S}_i$. Instead, note that the blur frequency response matrix $\mathbf{H}_i$ satisfies $\mathbf{H}_i\mathbf{H}_i' \le \mathbf{I}$, then we have from Equation 4.22:

$$\begin{aligned} \mathbf{B}_i'\mathbf{S}_i'\mathbf{S}_i\mathbf{B}_i &= \mathbf{Q}^{-1}\mathbf{H}_i'\left(\sigma_i^{\mathrm{q}2}\mathbf{H}_i\mathbf{H}_i' + \sigma_i^{\mathrm{r}2}\mathbf{I}\right)^{-1}\mathbf{H}_i\mathbf{Q} \\ &\le \mathbf{Q}^{-1}\left(\left(\sigma_i^{\mathrm{q}2} + \sigma_i^{\mathrm{r}2}\right)^{-1}\mathbf{I}\right)\mathbf{Q} = \left(\sigma_i^{\mathrm{q}2} + \sigma_i^{\mathrm{r}2}\right)^{-1}\mathbf{I}. \end{aligned} \tag{4.35}$$

This inequality leads to the following diagonal majorizer:

$$\begin{aligned} \widetilde{\mathbf{A}}'\widetilde{\mathbf{A}} &= \sum\nolimits_{i=1}^{N_p} \mathbf{A}_i'\mathbf{B}_i'\mathbf{S}_i'\mathbf{S}_i\mathbf{B}_i\mathbf{A}_i \\ &\le \sum\nolimits_{i=1}^{N_p} \left(\sigma_i^{\mathrm{q}2} + \sigma_i^{\mathrm{r}2}\right)^{-1}\mathbf{A}_i'\mathbf{A}_i \le \mathbf{D}, \end{aligned} \tag{4.36}$$

where

$$\mathbf{D} = \sum\nolimits_{i=1}^{N_p} \left(\sigma_i^{\mathrm{q}2} + \sigma_i^{\mathrm{r}2}\right)^{-1} \mathrm{diag}\{\mathbf{A}_i'\mathbf{A}_i\mathbf{1}\}. \tag{4.37}$$

This diagonal majorizer is as easy to implement as the usual SQS majorizer [96].

In iterative DBT reconstruction, usually only one PV is used at a time to update the image. We use the ordered subset (OS) approximation [96] to further accelerate the SQS reconstruction:

$$\nabla \sum_{i=1}^{N_{\mathrm{p}}} \left\| \tilde{\mathbf{y}}_i - \widetilde{\mathbf{A}}_i \mathbf{f} \right\|_2^2 \approx N_{\mathrm{p}} \nabla \left(\left\| \tilde{\mathbf{y}}_i - \widetilde{\mathbf{A}}_i \mathbf{f} \right\|_2^2 \right). \tag{4.38}$$

The OS reconstruction update is given by:

$$\mathbf{f}^{(n,i+1)} = \mathbf{f}^{(n,i)} - (\mathbf{D} + 8\alpha\beta\mathbf{I})^{-1} \nabla \Psi_i \left(\mathbf{f}^{(n,i)} \right), \tag{4.39}$$

$$\nabla \Psi_i \left(\mathbf{f}^{(n,i)} \right) = \nabla R \left(\mathbf{f}^{(n,i)} \right) + N_p \widetilde{\mathbf{A}}_i' \left(\widetilde{\mathbf{A}}_i \mathbf{f}^{(n,i)} - \tilde{\mathbf{y}}_i \right), \tag{4.40}$$

$$\begin{aligned} \nabla R(\mathbf{f}^{(n,i)}) = \frac{\alpha\beta}{1+\gamma} \big(& \mathbf{C}_x' \dot{\eta}(\mathbf{C}_x \mathbf{f}^{(n,i)}) + \mathbf{C}_y' \dot{\eta}(\mathbf{C}_y \mathbf{f}^{(n,i)}) \\ & + \gamma \mathbf{C}_{x-y}' \dot{\eta}(\mathbf{C}_{x-y} \mathbf{f}^{(n,i)}) + \gamma \mathbf{C}_{x+y}' \dot{\eta}(\mathbf{C}_{x+y} \mathbf{f}^{(n,i)}) \big). \end{aligned} \tag{4.41}$$

The iteration counter *n* is incremented by 1 after all projections have been used once.

The OS approximation used in the reconstruction makes the method somewhat similar to SART, where also one projection is used in each update, and facilitates their comparison. The OS algorithm was proposed for PET and CT reconstruction [103] where the subsets are better "balanced" than in DBT. For both CT and DBT, the standard OS-SQS algorithm is not guaranteed to converge. The OS algorithm could be made convergent by some relaxation [104], which has not been implemented in this study.

We use SART as a reference algorithm in this chapter; although not state-of-the-art, SART has been shown to provide good image quality for reconstructing DBT acquired with our prototype DBT system [31] and has been evaluated by other investigators [44, 58]. We implemented the SQS-DBCN reconstruction with the SG projector [77] and implemented SART with the ray-tracing (RT) projector [31, 78]. We previously compared the effects of RT and SF projectors to SG using SART in Chapter III and our paper [77], so here we focus on examining the new DBCN effects. Artifact reduction methods [67, 69] were implemented for all reconstruction methods in this study.

Although used in our implementation, the TPA removal algorithm [67, 68] will cause some problem to the convergence of the cost function. This issue inspires our comparative study on TPA removal and will be introduced in Chapter V.

IV.2.5 Reconstruction without detector blur or correlated noise

We investigated the role of each model component in the SQS-DBCN method. The SQS-DBCN method includes the detector blur, the corresponding noise correlation and the regularization. To examine the effects of the detector blur and the noise correlation, we studied the following two reconstruction algorithms:

$$\hat{\mathbf{f}}_{\text{noDB}} = \underset{\mathbf{f}}{\operatorname{argmin}} \frac{1}{2} \sum_{i=1}^{N_\text{p}} \|\mathbf{y}_i - \mathbf{A}_i \mathbf{f}\|^2_{(\mathbf{K}_i^q + \mathbf{K}_i^r)^{-1}} + R(\mathbf{f}), \tag{4.42}$$

$$\hat{\mathbf{f}}_{\text{noNC}} = \underset{\mathbf{f}}{\operatorname{argmin}} \frac{1}{2} \sum_{i=1}^{N_\text{p}} \|\mathbf{y}_i - \mathbf{B}_i \mathbf{A}_i \mathbf{f}\|^2_{(\mathbf{K}_i^q + \mathbf{K}_i^r)^{-1}} + R(\mathbf{f}). \tag{4.43}$$

The no-detector-blur (noDB) reconstruction method neglects the detector blur by setting the point spread function to a Kronecker impulse such that $\mathbf{B}_i$ becomes an identity matrix. This is equivalent to a common approach to SQS regularized reconstruction that ignores detector blur and noise correlation. For the no-noise-correlation (noNC) reconstruction, we kept the detector blur in the system model while neglecting the noise correlation caused by the detector blur to evaluate the effect of the correlated noise model in SQS-DBCN. Another case we investigated was keeping both the detector blur and noise correlation while neglecting the regularization. In this case, however, the reconstructed image became extremely noisy after only 2 or 3 SQS iterations, making it difficult even to recognize the reconstructed MCs. As a result, we omit the no-regularization results.

IV.2.6 Reconstruction with the penalized weighted least-squares cost function

In addition to the SQS-DBCN, SQS-noDB and SQS-noNC methods, we studied a fourth DBT reconstruction method using the penalized weighted least-squares (PWLS) cost function [18, 36], which is equivalent to the SQS-noDB method with location-dependent noise variance. Such a cost function is widely used in statistical iterative reconstruction for clinical CT systems where the detector pixel crosstalk can be ignored. For this implementation, we used the usual diagonal weighting matrix based on the estimated statistical variance at each detector pixel. Specifically, the PWLS cost function is:

$$\Psi_{\text{PWLS}}(\mathbf{f}) = \frac{1}{2} \sum_{i=1}^{N_\text{p}} \|\mathbf{y}_i - \mathbf{A}_i \mathbf{f}\|^2_{\mathbf{D}_i} + R(\mathbf{f}), \tag{4.44}$$

where $\mathbf{D}_i$ is a diagonal matrix. Let j denote the index of pixels for the ith projection angle, the jth element of the diagonal matrix $\mathbf{D}_i$ is:

$$\mathbf{D}_i[j] = \frac{1}{{\sigma_{\mathbf{y}_i[j]}}^2}, \tag{4.45}$$

where

$$\sigma_{\mathbf{y}_i[j]} = \frac{\sigma_{\mathbf{Y}_i[j]}}{\mathbf{Y}_i[j]} = \sqrt{\frac{1}{\mathbf{Y}_i[j]}}. \tag{4.46}$$

Since we are no longer using constant σ_i^{q} and σ_i^{r} in this implementation, the formula for the adaptive-regularization scaling factor α is different from Equation 4.26:

$$\alpha_{\mathrm{PWLS}} = \frac{1}{\sum_{i=1}^{N_{\mathrm{p}}} \sum_j \omega_{\mathbf{y}_i}[j] {\sigma_{\mathbf{y}_i[j]}}^2 / \sum_{i=1}^{N_{\mathrm{p}}} \sum_j \omega_{\mathbf{y}_i}[j]}, \tag{4.47}$$

where $\omega_{\mathbf{y}_i}[j] = 1$ if j is within the detected breast boundary [39] for the ith PV and $\omega_{\mathbf{y}_i}[j] = 0$ otherwise.

We still use the SQS algorithm to minimize the cost function $\Psi_{\mathrm{PWLS}}(\mathbf{f})$. We refer to this reconstruction algorithm as the SQS-PWLS method. The SQS-PWLS method is basically the SQS-noDB method (Equation 4.42) with detector pixel location-dependent noise variance.

IV.3 Materials and figures of merit

IV.3.1 DBT system

We used a GE GEN2 prototype DBT system for image acquisition in this study. Despite the difference in geometry, the proposed method should be applicable to other DBT systems. The DBT system and its geometry have been introduced in Section II.3.

IV.3.2 Breast phantom and human subject DBT

The concept of MC has been introduced in Section II.7. Due to their small size, one of the main challenges in DBT reconstruction is to reduce noise while enhancing MCs and preserving the features of mass margins and the texture of the parenchyma. In this study, we used a breast phantom with embedded simulated MCs for evaluating reconstruction methods and parameter selection on the image quality of MCs. It is difficult to build mass phantoms with realistic spiculated or ill-defined margins that are strong indicators of breast cancer; we therefore used real breast DBT for visual evaluation of the image quality of masses. The human subject DBTs

were previously acquired with approval of our Institutional Review Board and informed consent for a lesion detection project.

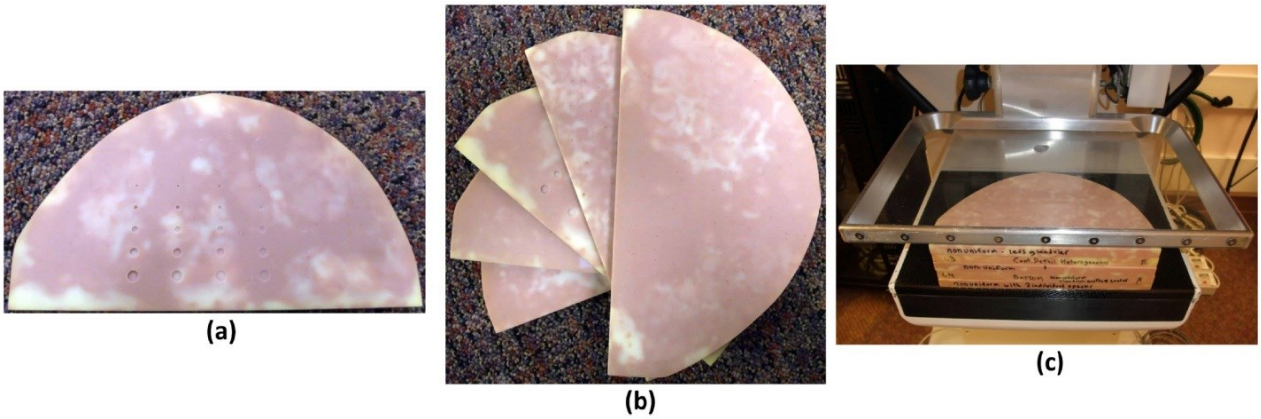

Figure 4.2. The experimental phantom to simulate MCs in DBT (figure from [2]).

The breast phantom is shown in Figure 4.2. It consists of a stack of five 1-cm-thick slabs of breast tissue mimicking material [2]. Eight clusters of calcium carbonate specks of nominal size range of 0.15-0.18 mm, eight clusters of 0.18-0.25 mm, and five clusters of 0.25-0.30 mm were sandwiched at random locations and depths between the slabs to simulate MCs of different conspicuity levels. For the human subject DBT, we selected cases with spiculated masses that were biopsy-proven to be invasive ductal carcinomas. Both the phantom and human subject DBT were acquired with 60^{o} scan angle, 3^{o} increments and 21 projections. The DBT system used an Rh-target/Rh-filter x-ray source. In the scan of the breast phantom, the kilovoltage was 29 kVp and the total current-time product of all 21 PVs was 50.0 mAs. To simulate the DBT acquired with narrow-angle DBT system, we used the 9 central projections for reconstruction, corresponding 24^{o} scan angle with 3^{o} increments, which was close to the 25^{o} scan angle and 3^{o} increments for a GE commercial system. The x-ray exposure for each DBT was therefore reduced to less than half of the original values. For the breast phantom, the total current-time product of the central 9 projections was 21.4 mAs.

IV.3.3 Figures of merit

Figure 4.3(a) shows a reconstructed slice of the experimental phantom. The MC clusters on this slice are marked with green boxes and numbers. Each MC cluster is enlarged and shown in Figure 4.3(b). The reconstruction algorithm used here is SART with 2 iterations with 21PVs. We

know the location of all MC clusters in the phantom and use all of them to calculate the average detectability of MCs of different sizes. To reduce bias in picking MCs, (e.g. to avoid picking relatively bright MCs), all recognizable MCs (including MCs on all slices, not just this slice) were used in the calculation of average FOM.

We use two FOMs for quantitative comparisons of reconstruction quality of MCs: CNR and full-width at half maximum (FWHM). We would like reconstructed MCs to be strong and sharp, so larger CNR and smaller FWHM are preferable.

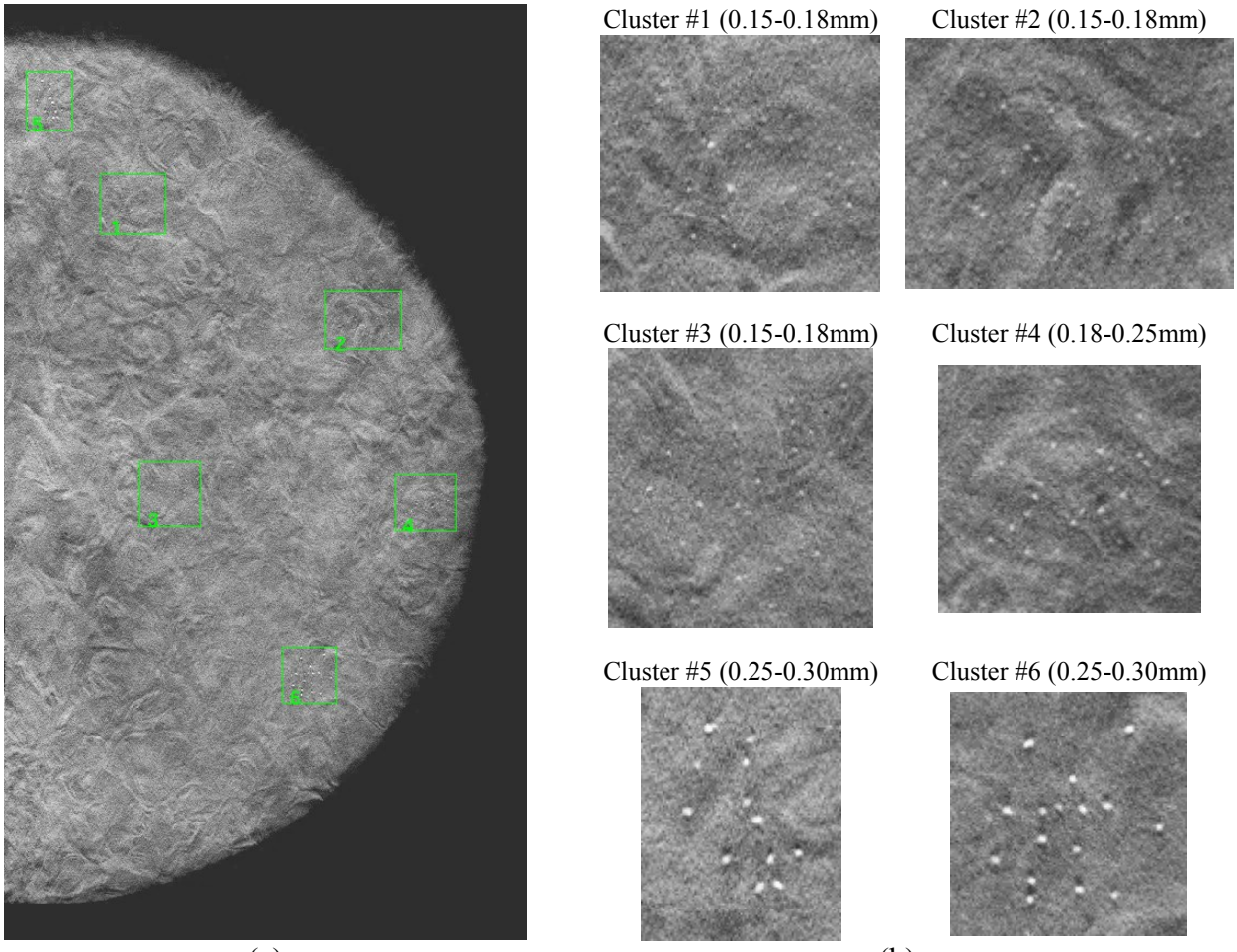

Figure 4.3. A slice of the reconstructed experimental phantom with MC clusters. (a) The whole slice with the MC clusters marked with green boxes and numbers; (b) Each marked MC cluster and their nominal size range. The image slice and all MC patches are displayed with the same window width setting.

The reconstructed MCs are noisy, especially for the subtlest ones of size 0.15-0.18mm. As a result, we apply a 2-D least-square Gaussian fitting to each MC and define CNR and FWHM

with the fitted parameters. The fitting is applied to an 13 × 13 patch centered at each MC, where the 2-D Gaussian function has 6 parameters:

$$g(x,y) = ax + by + A\exp(-\frac{(x-\mu_x)^2 + \left(y-\mu_y\right)^2}{2\sigma_{\mathrm{MC}}^2}). \tag{4.48}$$

After the fitting is done for a MC, we remove the linear background $ax + by$ from the MC patch and define the contrast of the MC to be the largest value of the MC patch after removing background. This value is denoted as $A_{\max}$. Note that under most conditions: $A_{\max} \neq A$. We do not use A as the contrast of MC since the value A is usually achieved between pixels of the MC patch. Using A instead of $A_{\max}$ will overestimate the contrast of MCs under most conditions.

We select a 40 × 40 noise patch near each cluster, which contains no recognizable MCs. An 2-D 2nd-order polynomial fitting is applied to the noise patch. The fitted function is subtracted from the noise patch to reduce the influence of non-uniform background. Let σ_{NP} denote the standard deviation of the corrected noise patch. The CNR of each MC is defined as:

$$\mathrm{CNR} = \frac{A_{\max}}{\sigma_{\mathrm{NP}}}. \tag{4.49}$$

The definition of FWHM is more straightforward. It is decided by the fitted parameter σ_{MC}:

$$\mathrm{FWHM} = 2.355\sigma_{\mathrm{MC}}. \tag{4.50}$$

The Gaussian fitting might fail to characterize MCs when the MC patch is too noisy. We use the coefficient of determination, denoted as r^2 to measure the quality of fitting. Let the noisy MC patch be g_{patch} and the fitted MC patch be g_{fit}, r^2 is defined as:

$$r^2 = 1 - \frac{\sum_{x,y}\left(g_{\mathrm{fit}}(x,y) - g_{\mathrm{patch}}(x,y)\right)^2}{\sum_{x,y}\left(g_{\mathrm{patch}}(x,y) - \overline{g_{\mathrm{patch}}}\right)^2}, \tag{4.51}$$

where $\overline{g_{\mathrm{patch}}}$ is the mean value of $g_{\mathrm{patch}}(x,y)$. If $r^2 < 0.8$, we consider the fitting to fail and the MC will be eliminated in the analysis of mean CNR and FWHM.

When comparing multiple reconstruction conditions, the MC fitting needs to be done separately for each condition. It could happen that one MC fails to fit in only one or more of the many conditions. Such a MC will be eliminated in the calculation of mean CNR and FWHM to make sure that all the MC fittings are reliable. After eliminating these MCs, we have 30 MCs of 0.15-0.18 mm size, 48 MCs of 0.18-0.25 mm size and 44 MCs of 0.25-0.30 mm size for the FOM calculation for all reconstruction techniques and parameters compared in this study.

Although the SQS-DBCN reconstructed DBT is not a linear, shift-invariant system, we calculate an average noise power spectrum (NPS) of the heterogeneous phantom background to provide a comparison of the relative change in the global texture for the various reconstruction techniques and parameters. For each different reconstruction, we calculated the average NPS using sixty 200 × 200-pixel noise patches from 4 reconstructed slices at 4 different depths. We then took the radial average NPS for each reconstruction condition. The locations of the noise patches were chosen such that they did not contain any MC clusters and the same patch locations were used for all conditions. There is no FOM to reliably evaluate the fine details of the margin or spiculations of a cancerous lesion at present so that these features are compared visually on the reconstructed breast images.

IV.4 Results and analyses

IV.4.1 Effects of regularization parameters

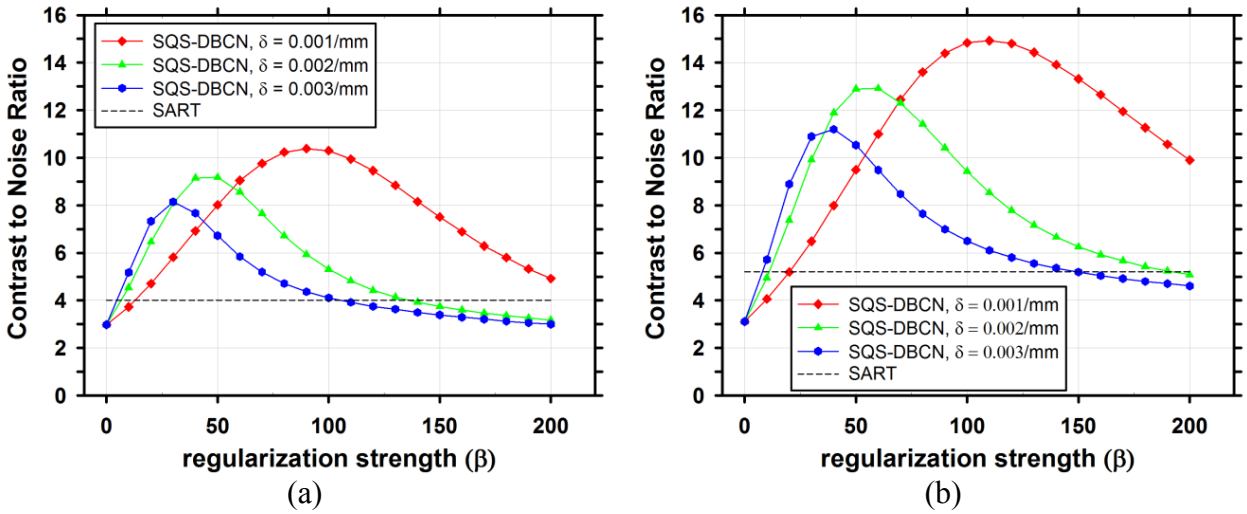

Figure 4.4. Dependence of CNR on reconstruction parameters. The CNR is plotted as a function of β for a range of δ. The black dashed lines indicate the CNR level of the SART. (a) MCs of nominal size 0.15-0.18mm, (b) MCs of nominal size 0.18-0.25mm.

The performance of the SQS-DBCN method depends on the parameters of the regularization term. We reconstructed the phantom DBT with different parameter combinations and plotted the corresponding CNR curves for the small-sized (0.15-0.18mm) and medium-sized (0.18-0.25mm) MCs, as shown in Figure 4.4. These CNR curves provide some guidance for parameter selection. The curves for the large-sized (0.25-0.30mm) MCs have similar trends but they are not shown

because their CNRs are very high and the parameter settings are not expected to have a strong influence on their visibility. We did not show the FWHM curves either because they monotonically increase as β increases due to the increasing blurring effect of regularization, which is not useful for guiding parameter selection.

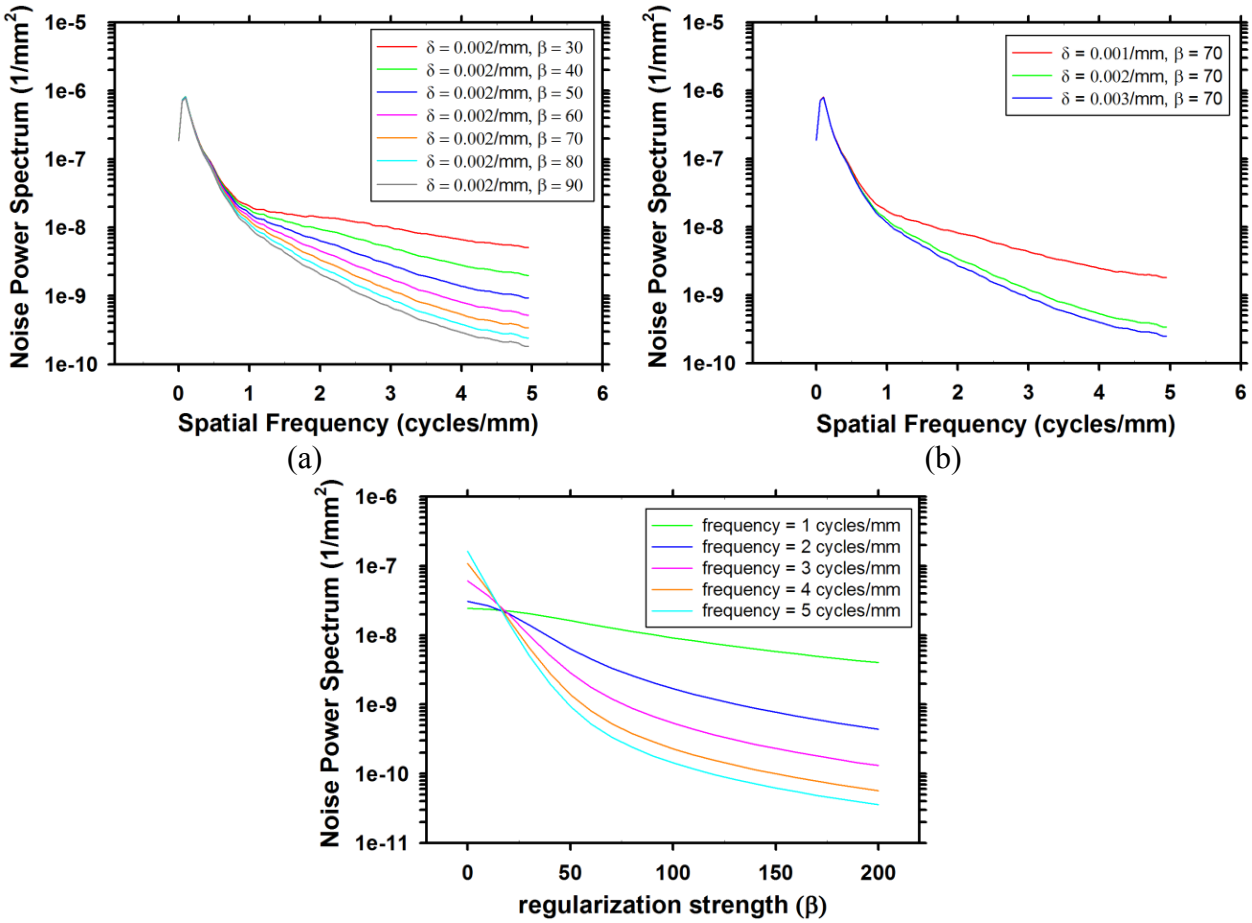

Figure 4.5. Dependence of NPS on regularization parameters. (a) NPS with different β values at $\delta = 0.002/\text{mm}$. (b) NPS with different δ values at $\beta = 70$. (c) Dependence of noise power on β at five different frequencies at $\delta = 0.002/\text{mm}$.

For the breast phantom, Figure 4.5 shows the rotational average of the 2-D in-plane NPS for several sets of parameters. The pixel size of the slices is 0.1mm × 0.1mm, yielding a Nyquist frequency of 5 cycles/mm. As the parameters change, the middle and high frequency noise are mainly affected, while the low frequency noise almost stays the same. Figure 4.5(c) shows the dependence of the NPS values on β at several frequencies. When weaker regularization is used ($\beta < 18$), the high-frequency NPS is higher than low-frequency NPS. On reconstructed images,

the high level of high-frequency noise is superimposed with some salt-and-pepper noise, which is a very unfavorable visual feature. As the regularization strength is increased (larger β values), these noisy spikes become less and less noticeable.

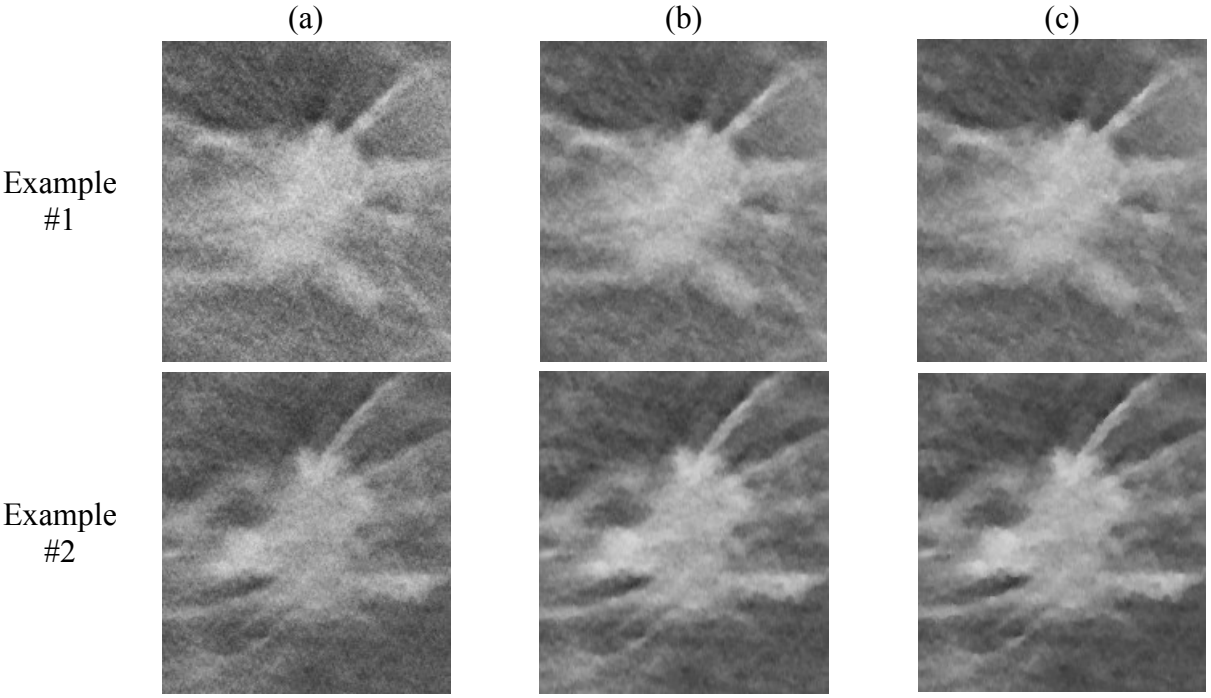

Figure 4.6. Comparison of reconstruction methods and parameters using human subject DBTs with invasive ductal carcinomas. Column (a) SART, (b) SQS-DBCN, $\beta = 70$, $\delta = 0.002/\text{mm}$, (c) SQS-DBCN, $\beta = 100$, $\delta = 0.001/\text{mm}$. All image patches shown are 180 × 200 pixels in size. The CNR of the MCs increases from (a) to (c). However, the spiculations and the tissue textures become more patchy and artificial in (c). All images are displayed with the same window width setting.

For each MC size, there is a different 'optimal' parameter combination that yields maximum CNR. However, the parameter combination that yields the best CNR for MCs may generate artificially appearing texture for soft tissues or spurious noise in the background. Combining curves for both small-sized and medium sized MCs, the optimal parameter selection is about $\beta = 100$ and $\delta = 0.001/\text{mm}$. Figure 4.6 shows image patches from two DBTs containing spiculated invasive ductal carcinoma from a human subject reconstructed using the SART algorithm and SQS-DBCN with two sets of parameters as examples, one of which is $\beta = 100$, $\delta = 0.001/\text{mm}$. Although this set of parameters provides superior denoising effects compared with SART, it gives the texture a patchy appearance (Figure 4.6(c)). After visually comparing

the images for a range of δ and β values and considering both the MC enhancement and the appearance of the soft tissue structure, we empirically chose $\beta = 70$ and $\delta = 0.002/\text{mm}$ for the SQS-DBCN algorithm. This parameter pair has a slightly larger β than the "optimal" value for MC enhancement at $\delta = 0.002/\text{mm}$, but the soft tissue texture is less patchy as shown in Figure 4.6(b).

IV.4.2 Effects of detector blur and noise correlation modeling

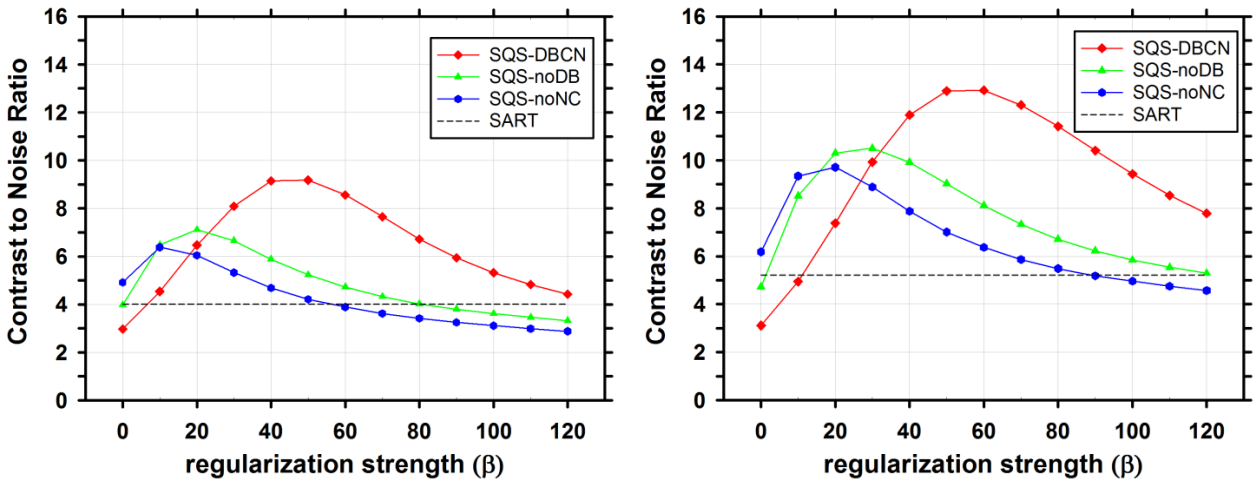

Figure 4.7. Comparison of reconstruction with different model components. CNR is plotted as a function of β at δ = 0.002/mm. (a) MCs of nominal size 0.15-0.18mm, (b) MCs of nominal size 0.18-0.25mm. The SQS-DBCN method yields MCs with higher CNR compared with the SQS-noDB or the SQS-noNC reconstruction over a wide range of β values.

We compared the performance of SQS-DBCN with SQS-noDB and SQS-noNC for MC enhancement. Figure 4.7 shows the dependence of CNR on β values at $\delta = 0.002/\text{mm}$ for these three different methods, together with the CNR level of SART as a reference. When δ is fixed at other values, $\delta = 0.001/\text{mm}$ or $0.003/\text{mm}$, the CNR-vs-β curves of the three methods (not shown) have a similar trend as Figure 4.7. Figure 4.7 indicates that, compared with SQS-noDB and SQS-noNC, SQS-DBCN can achieve a much higher CNR over a wide range of β, providing more flexible choice of β to preserve the texture quality while enhancing the MCs. Compared with SART, the SQS-noDB and SQS-noNC can still provide enhancement for MCs within a small range of β values. Similar to the SQS-DBCN method, by visual evaluation of soft tissue texture we observed that using a slightly larger β than the optimal value yielded better texture

quality with a tradeoff in MC enhancement. Therefore we chose to use $\beta = 40$ for SQS-noDB and $\beta = 30$ for SQS-noNC in the following discussions.

IV.4.3 Reconstruction with the SQS-PWLS algorithm

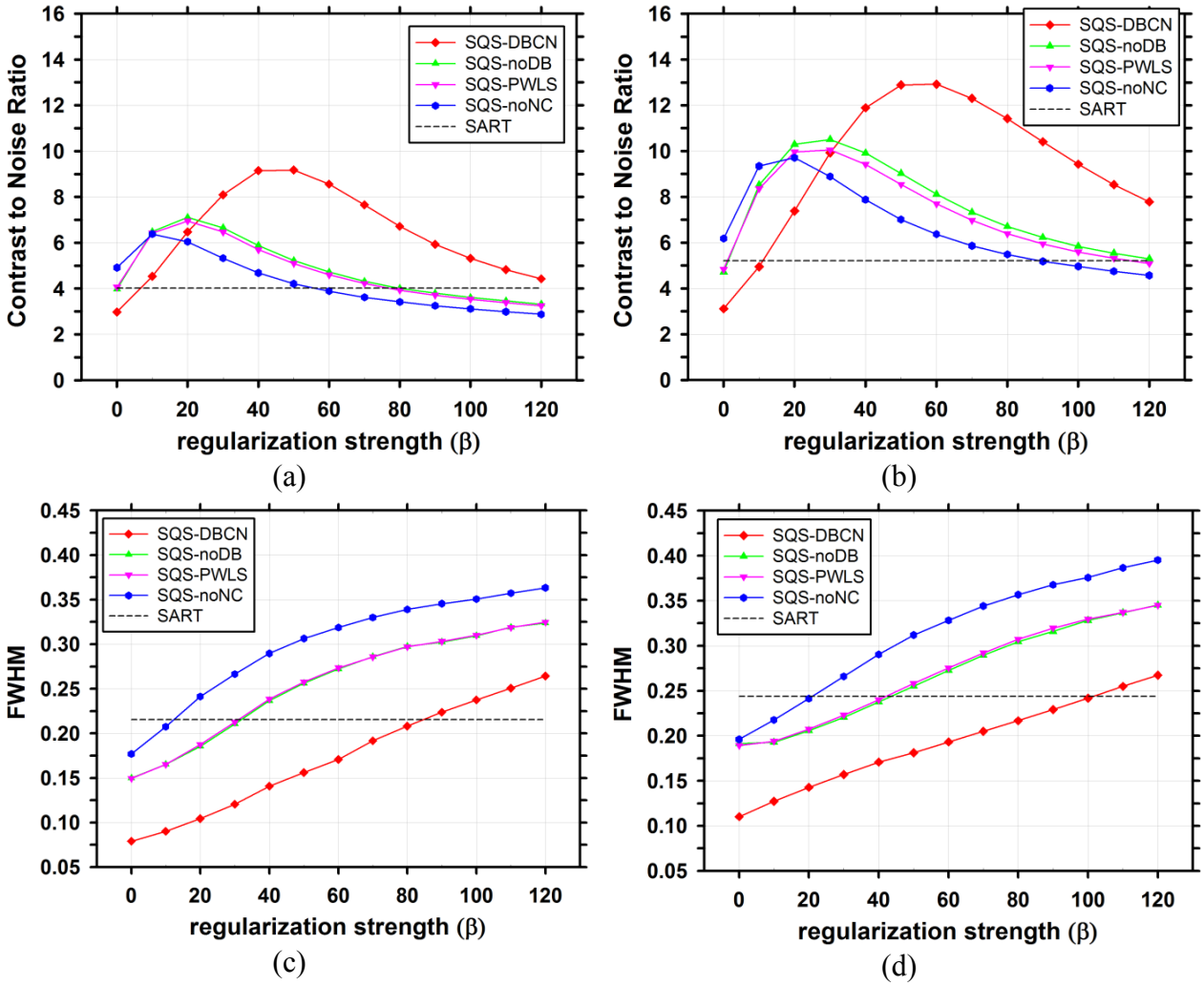

Figure 4.8. Dependence of CNR and FWHM on β for SQS-DBCN, SQS-noDB and SQS-PWLS at $\delta = 0.002/mm$. (a) and (c) MCs of nominal size 0.15-0.18 mm, (b) and (d) MCs of nominal size 0.18-0.25 mm. The SQS-DBCN, SQS-noDB, SQS-noNC CNR curves are the same as those in Figure 4.7.

As introduced in Section IV.2.6, the PWLS cost function [18, 36], which is equivalent to the SQS-noDB method with location-dependent noise variance, is widely used in statistical iterative reconstruction for clinical CT systems where the detector pixel crosstalk can be ignored. Figure 4.8 shows the dependence of CNR and FWHM on β at $\delta = 0.002/mm$ for the SQS-PWLS

algorithm. The results of the SQS-PWLS method are very similar to those of the SQS-noDB method. The CNRs of the SQS-PWLS method are slightly lower than those of the SQS-noDB method, with a maximum difference of 5.3% for the 0.18-0.25 mm MCs at $\beta = 50$. The FWHM curves of SQS-PWLS and SQS-noDB overlap almost completely. We also examined the reconstructed image patches of the SQS-PWLS method. There is no visual difference between the images reconstructed by SQS-PWLS and SQS-noDB since a CNR difference of 5.3% is basically indistinguishable for human eyes. Due to the similarity between the SQS-PWLS and the SQS-noDB method, in the following sections we will not include the SQS-PWLS method in the comparisons.

The results of the SQS-PWLS method demonstrate that the MBIR method in CT that does not consider detector blur is not sufficient for DBT, where detector blur is one of the major image quality degrading factors. The little different between the SQS-noDB method and the SQS-PWLS method partially justifies the approximation of using constant noise variance in the SQS-DBCN method (Equation 4.20).

IV.4.4 Reconstructed MC clusters breast phantom

Figure 4.9 shows the reconstructed images for two MC clusters with SART, SQS-DBCN, SQS-noDB and SQS-noNC. Because the SART method does not have explicit regularization, we stopped with 3 iterations to avoid noise amplification. The mean FWHMs and the CNRs calculated for these clusters reconstructed with the different methods are also shown. Compared with SART, the MC clusters by the SQS-DBCN method are sharper on a much less noisy background. Benefiting from the denoising effect of the regularization, the SQS-noDB and the SQS-noNC methods are also able to enhance the MCs. All three methods provide higher CNRs than SART. However, the SQS-noDB method generates coarser texture in the background, while the SQS-noNC images are more blurred with "bumpy" background texture. The MCs reconstructed by the SQS-DBCN method have smaller FWHMs than those by the SART method, indicating that the MCs are sharper. On the other hand, the MCs reconstructed by the SQS-noDB and the SQS-noNC methods are more blurred, as indicated by the larger FWHMs. Among the four different methods, the SQS-DBCN method provides the best CNR enhancement and the sharpest MCs along with smoother background texture.

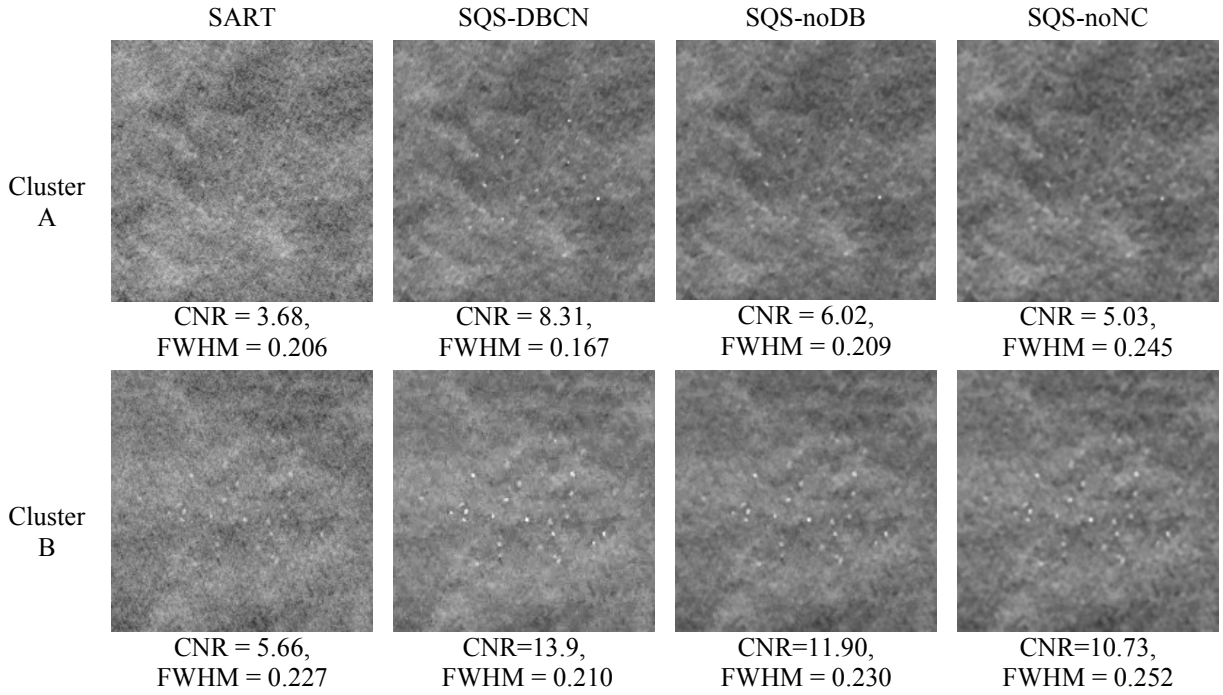

Figure 4.9. Comparison of MC clusters reconstructed by four methods. The size of these image patches is 180 × 180 pixels. Cluster A: nominal size 0.15-0.18 mm, Cluster B: nominal size 0.18-0.25 mm. The SART method used 3 iterations. The CNR and FWHM (mm) are mean values of MCs from the clusters shown here. The parameters used for the SQS-DBCN method were $\beta = 70, \delta = 0.002/\text{mm}$. The last two columns show the reconstructed MC cluster when one of the model components was removed. The parameters used for SQS-noDB were $\beta = 40$, $\delta = 0.002/\text{mm}$, and for SQS-noNC were $\beta = 30, \delta = 0.002/\text{mm}$. All SQS reconstructions were run for 10 iterations. The images of the same cluster are displayed with the same window width setting.

To make a more quantitative comparison, we calculated the mean CNR and mean FWHM of the set of over 30 MCs in each size range. Figure 4.10 shows the mean values of both FOMs and their standard deviations for the four reconstructed methods. Compared with SART, SQS-DBCN generates more conspicuous and sharper MCs (see examples in Figure 4.9), as indicated by higher CNRs and smaller FWHMs. For the small MCs (0.15-0.18mm) the mean CNR increases by 90.3% from 4.02 to 7.65 when using the SQS-DBCN reconstruction. The mean CNRs increase by 136.0% and 205.5% for the medium and large MCs, respectively. The sharper and more conspicuous MCs in the SQS-DBCN images are expected to be detected more easily by radiologists or by machine vision. The mean CNRs of MCs reconstructed with the SQS-noNC and the SQS-noDB methods are also higher than those with SART, due to the enhancement of the signals with more iterations while the regularization controls the noise in the background.

The mean FWHMs of these two methods, on the other hand, become almost homogenized for three different sized MCs, indicating the blurring of the reconstructed images.

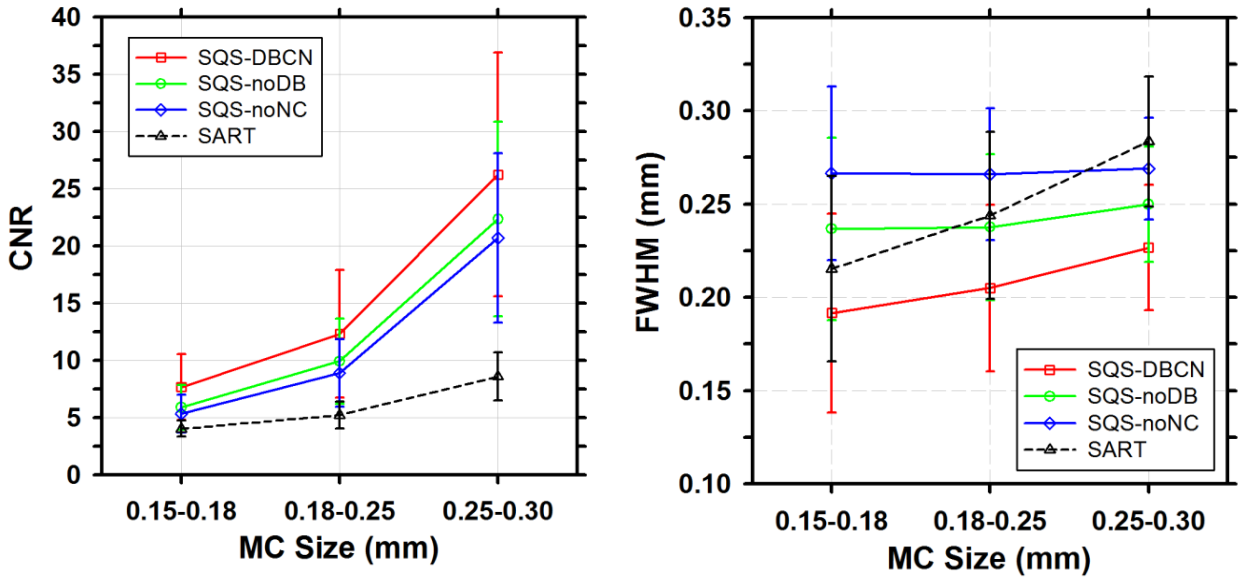

(a) (b)

Figure 4.10. Comparison of the (a) mean CNR and (b) mean FWHM averaged over MCs sampled from all clusters in the phantom. The error bars represent the standard deviations of CNR or FWHM for all MC samples of a given size.

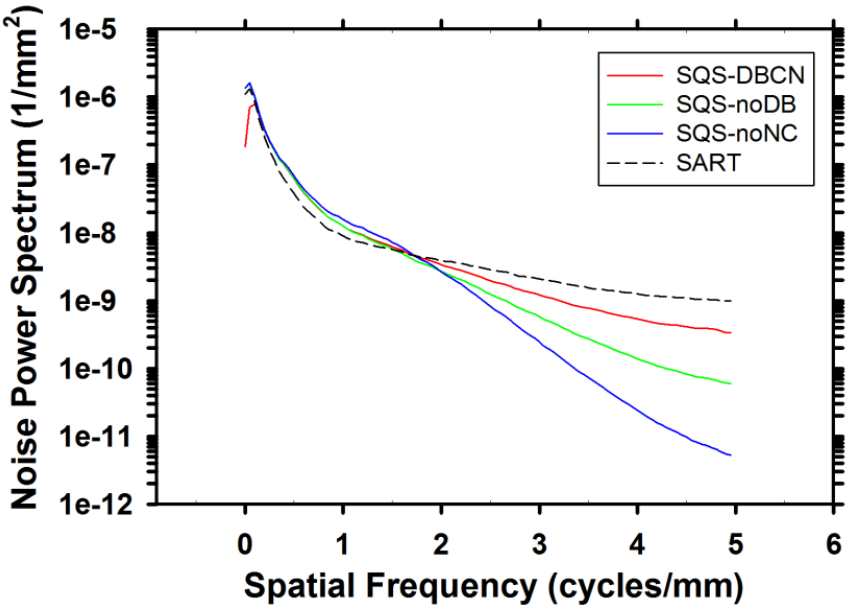

Figure 4.11. Dependence of NPS on reconstruction methods: SQS-DBCN ($\beta = 70$, $\delta = 0.002/\text{mm}$), SQS-noDB ($\beta = 40$, $\delta = 0.002/\text{mm}$), SQS-noNC ($\beta = 30$, $\delta = 0.002/\text{mm}$) and SART. The NPS curves of SQS-DBCN and SQS-noDB overlaps in the low-frequency range.

Figure 4.11 compares the rotationally averaged NPS of the background of the phantom DBT reconstructed with the four methods. Compared to SART, the SQS-DBCN, SQD-noDB, and SQS-noNC methods reduce the high-frequency noise but increase the lower frequency noise. The SQS-noNC method with $\beta = 30, \delta = 0.002/\text{mm}$ causes the largest changes in the NPS, which result in the blurry and bumpy background texture. The SQS-DBCN method with the selected parameters $\beta = 70, \delta = 0.002/\text{mm}$ changes the NPS moderately, corresponding to the less patchy texture on the images.

IV.4.5 Reconstructed ACR phantom and the uniform Lucite phantom

In addition to the heterogeneous phantom, we also used the American College of Radiology (ACR) phantom and a uniform Lucite phantom to study the difference between SART and SQS-DBCN. The observations for the ACR phantom are similar to that for the heterogeneous phantom. The results are shown in Figure 4.12 and Figure 4.13. Figure 4.13 shows the third speck group on the ACR phantom. The visibility of the MCs is enhanced with the SQS-DBCN method, as indicated by the increased mean CNR of the six MCs.

We also compared the noise pattern in DBT slices of a uniform background reconstructed by the SART and the SQS-DBCN method. DBT scan of a 2-inch-thick uniform Lucite slab (about 5 cm) was acquired and reconstructed with the two methods. Figure 4.14 shows noise patches from a slice at a depth of 2.7 cm in the Lucite phantom reconstructed by SART and the SQS-DBCN ($\delta = 0.002/\text{mm}$, $\beta = 70$). Figure 4.15 compares the noise power spectra obtained from averaging the noise power spectra of multiple noise patches at the same depth as the noise patches shown in Figure 4.14 for each method. The SQS-DBCN method smooths the high-frequency noise but the low frequency noise is stronger compared to the SART method. The SQS-DBCN method does not generate obvious artifacts on the background with the parameters selected in our study.

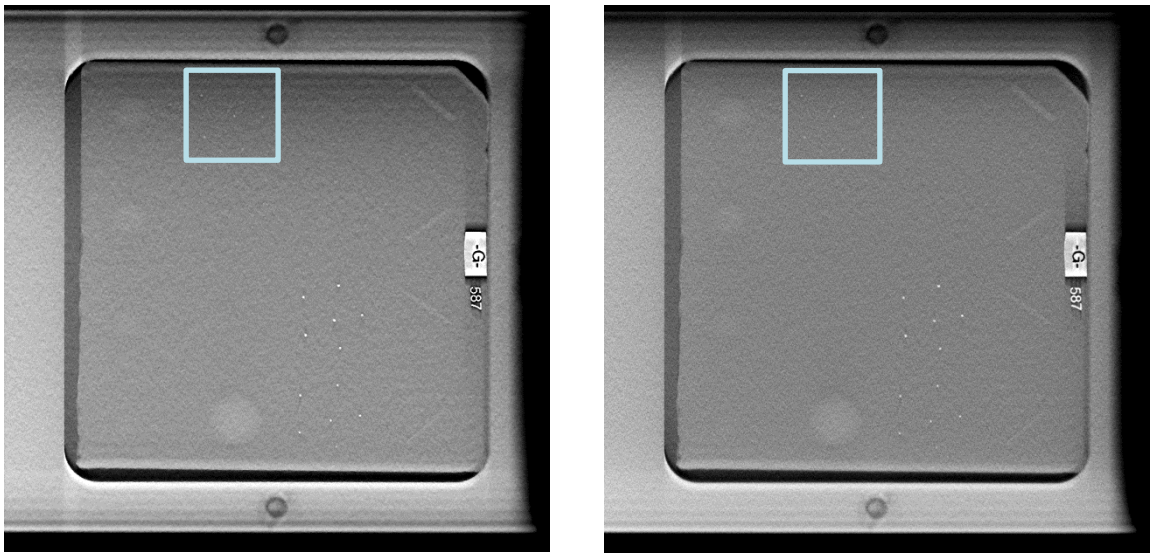

(a) SQS-DBCN (b) SART

Figure 4.12. Comparison of reconstructed ACR phantom images. The images are displayed with the same window width setting. Figure 4.13 shows a close-up view of the speck group marked by the box shown in Figure 4.12. The x-ray source moves along the vertical direction. The horizontal artifacts on top and at the bottom of the images are caused by the rectangular block shape of the ACR phantom that results in an abrupt transition to air at the edge of the phantom. This artifact does not happen in a real breast and is different from the truncation artifacts caused by the finite field-of-view coverage by the detector. The stronger enhancement of SQS-DBCN compared to SART also causes stronger enhancement of the artifact.

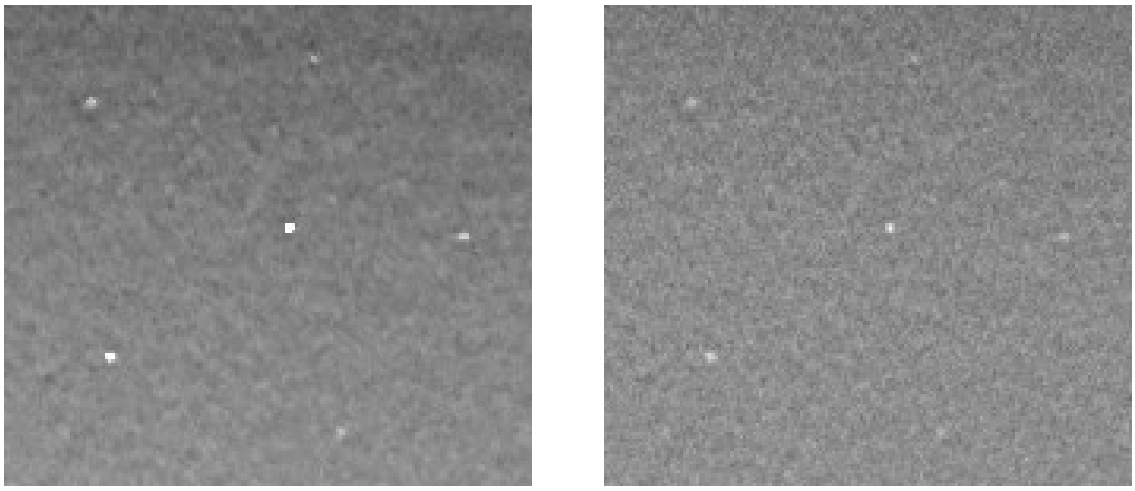

(a) SQS-DBCN
(CNR = 17.5, FWHM = 0.33 mm)

(b) SART
(CNR = 7.07, FWHM = 0.38 mm)

Figure 4.13. MC patches of reconstructed ACR phantom. The images are displayed with the same window width setting.

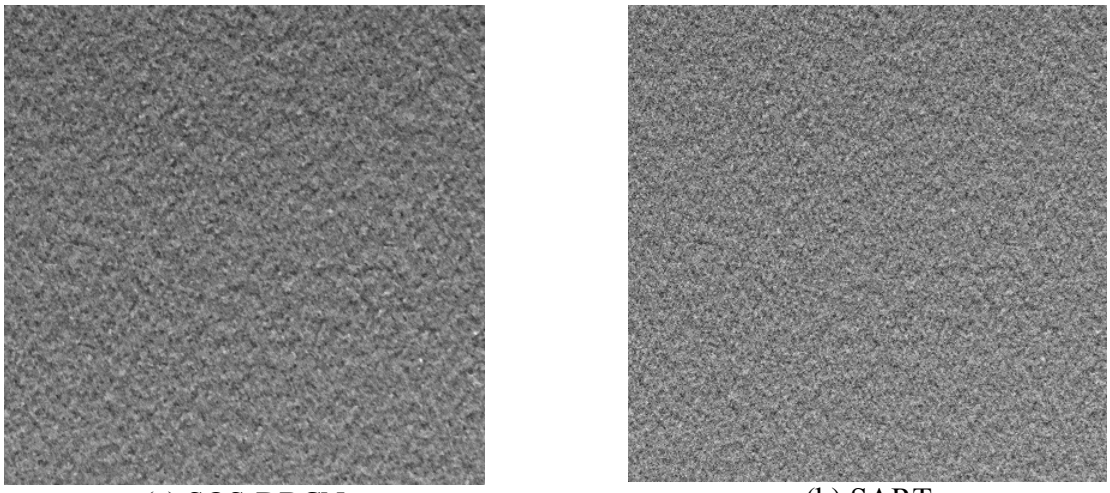

(a) SQS-DBCN (b) SART

Figure 4.14. Comparison of noise patches from a DBT slice of a uniform Lucite phantom reconstructed by SQS-DBCN ($\delta = 0.002$, $\beta = 70$) and SART. Both image patches are obtained from the same location in the two reconstructed DBT volume and the size of is 400×400 pixels (40×40 mm^2). The images are displayed with the same window width setting.

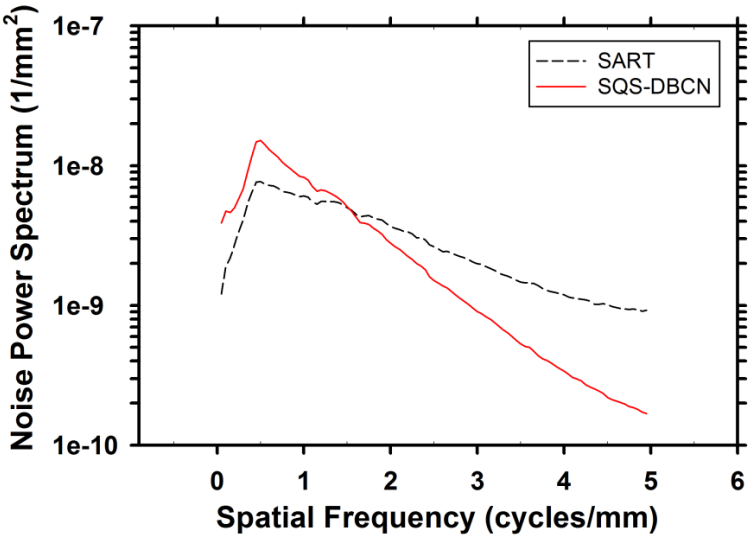

Figure 4.15. Comparison of noise power spectra of noise patterns for the DBT slice of a uniform Lucite phantom reconstructed by SQS-DBCN ($\delta = 0.002$, $\beta = 70$) and SART at the same depth of the noise patches shown in Figure 4.14.

IV.4.6 Human subject DBT

To evaluate the visual quality of the tissue texture, we applied SQS-DBCN to the human subject DBT images. Figure 4.16 shows examples of masses reconstructed from the four different methods. The parameters used here are the same as what have been used for the

phantom. Similar to the phantom images, the SQS-DBCN method is able to reduce noise compared with SART; the MCs appear to be the sharpest and have the highest contrast among the four methods. When one of the model components is ignored, although the contrasts of the MCs still appear higher than those of the SART, they are more blurry and the tissue texture becomes coarser, affecting the appearance of the mass margin.

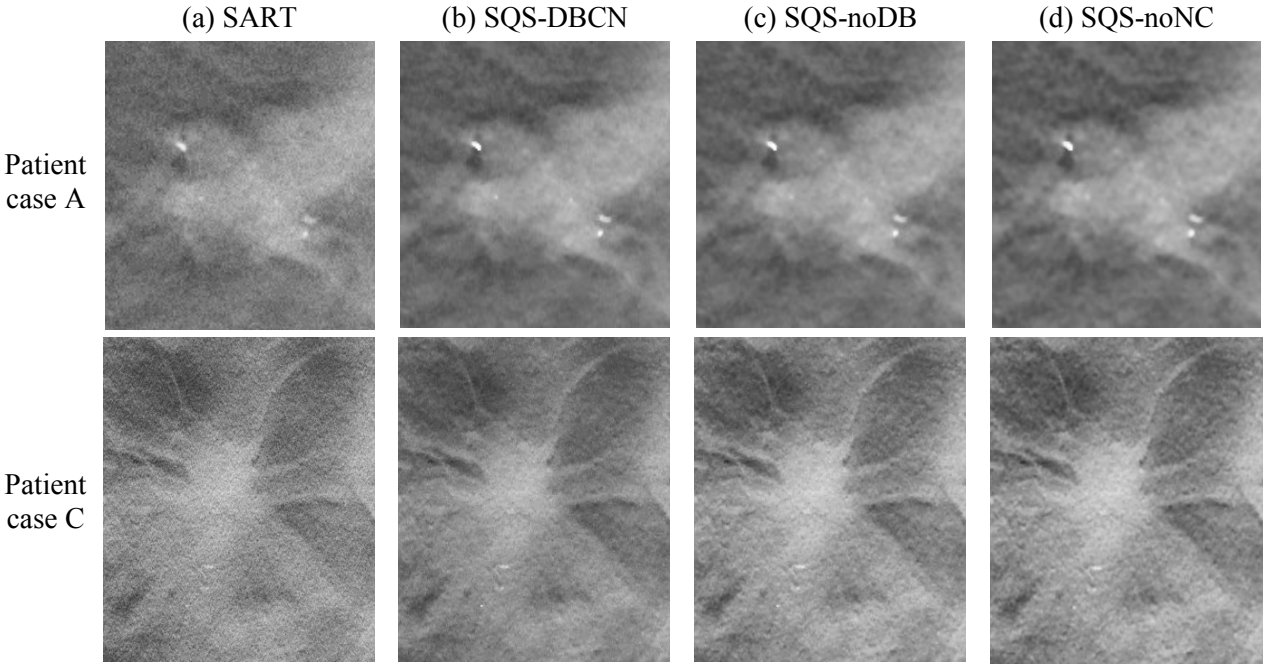

Figure 4.16. Comparison of four methods using human subject DBT images with invasive ductal carcinomas. The sizes of the image patches are 150 x 160 pixels (top row) and 300 x 360 pixels (bottom row). The SART method used 3 iterations. The parameters were $\beta = 70$, $\delta = 0.002/\text{mm}$ for the SQS-DBCN method, $\beta = 40$, $\delta = 0.002/\text{mm}$ for the SQS-noDB method, and $\beta = 30$, $\delta = 0.002/\text{mm}$ for the SQS-noNC method. All SQS methods were run for 10 iterations. All images are displayed with the same window width setting.

IV.4.7 Justification of the approximation of constant quantum noise variance

In the SQS-DBCN algorithm, we treated the quantum noise standard deviation σ_i^q as approximately a constant for a given projection angle. The approximation of constant quantum noise is the key approximation in the efficient implementation of the SQS-DBCN algorithm. It has been briefly discussed in Section IV.4.3. In this section, we present a more systematic justification of this approximation.

IV.4.7.1 Estimation of the standard deviation of the readout noise (σ_i^{R})

With the experimental data, we first justify the approximation of treating the standard deviation of the readout noise σ_i^{R} as a constant. As mentioned in Section IV.2.2, we estimated σ_i^{R} from dark current images without x-ray exposure by subtracting two dark current images to remove possible structured noise from the detector. Figure 4.17 (a) shows the subtraction result of two dark current images measured during the DBT scan of the uniform Lucite slab. Note that the dark current images were acquired by the system before exposing the Lucite slab. For each pixel of the subtraction result, we selected a 151 × 151 noise patch centered at the pixel to calculate the local standard deviation. The standard deviation was then divided by $\sqrt{2}$ to obtain σ_i^{R} since it had the contribution of two dark current images with independent random noise. The distribution of the locally estimated σ_i^{R} is shown in Figure 4.17 (b). The maximum and minimum estimated σ_i^{R} are 4.03 and 3.88. The average σ_i^{R} of the entire plane in Figure 4.17 (b) is 3.95. Therefore the maximum fluctuation of σ_i^{R} is only 2.0%. These results justify the approximation of considering all detector elements to have the same σ_i^{R}. We can treat σ_i^{R} as a constant when using Equation 4.24 to estimate σ_i^{q}.

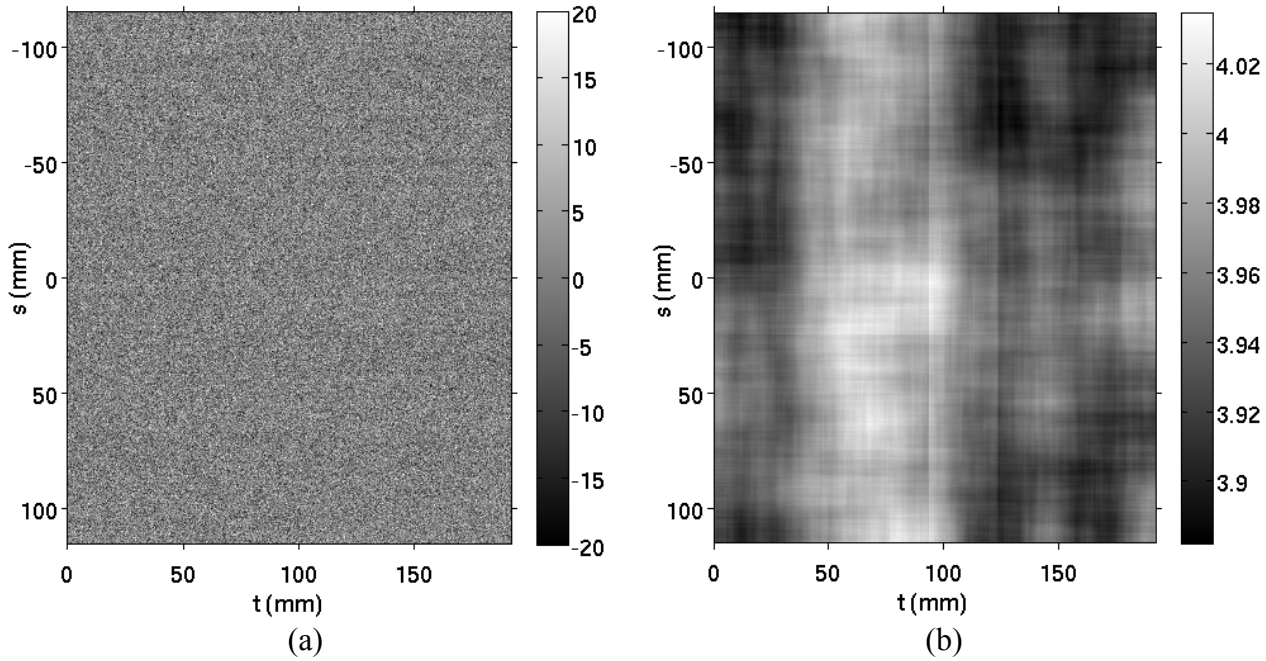

Figure 4.17 Estimation of the standard deviation of the readout noise σ_i^{R}. (a) The subtraction result of two dark current images. (b) The distribution of the locally estimated standard deviation of the readout noise (σ_i^{R}).

IV.4.7.2 Estimation of the change of σ_i^{q} due the x-ray incident angle and the anode heel effect

We studied the combined influence of the x-ray incident angle and the anode heel effect on σ_i^{q} with a DBT scan of a uniform Lucite slab. The kilovoltage was 29 kVp and the total current-time product of all 21 PVs was 48.3 mAs, similar to the experiment of the breast phantom as introduced in Section IV.3.2. Figure 4.18 and Figure 4.19 show the PVs of the Lucite slab at the central projection angle and the projection angle $\theta = 12°$. Twenty noise patches were selected on either of them. We applied a 2-D second order polynomial fitting to each noise patch to remove the non-uniform background. The standard deviation of each noise patch was then calculated. This standard deviation consists of the contribution of both the readout noise and the quantum noise. σ_i^{Q} was then estimated by subtracting the contribution of the readout noise (σ_i^{R}) from the total noise variance as shown in Equation 4.24. Then we obtained σ_i^{q} for each noise patch by dividing the estimated σ_i^{Q} by the mean value of the noise patch.

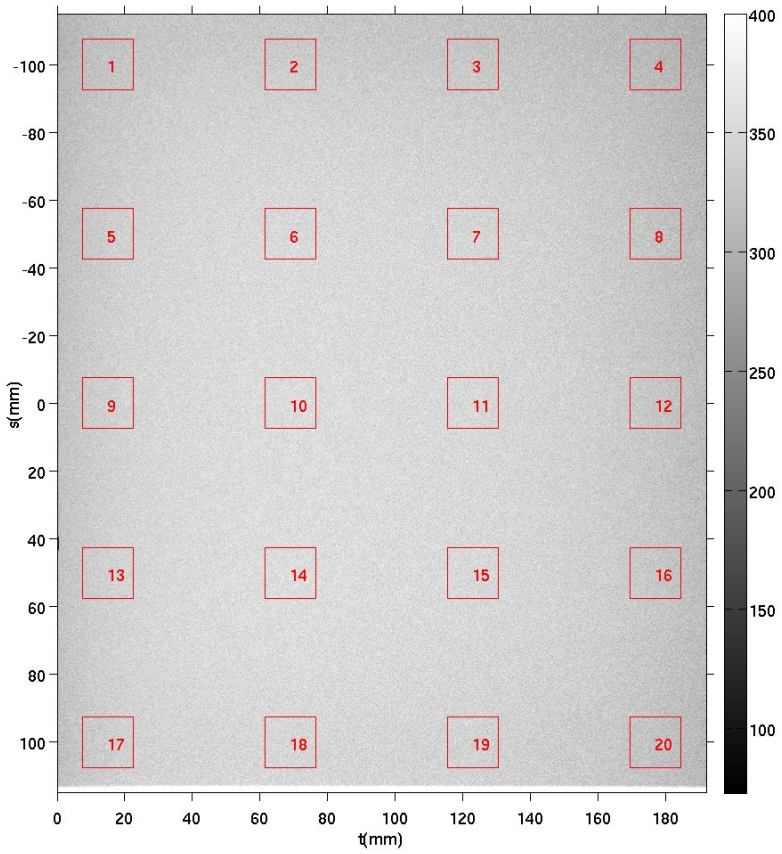

Figure 4.18 The measured PV of the Lucite slab before the log transform for the central projection angle. A brighter pixel indicates a higher measured x-ray intensity. σ_i^{q} was estimated for each noise patch (marked with a red box and number). The results are shown in Table 4.1.

Table 4.1 Estimated σ_i^q for each noise patch in Figure 4.18. The maximum and minimum σ_i^q are 0.1107 and 0.0826, marked with the red text. Slightly higher quantum noise is observed on the anode side (right side) of the image, as expected from the heel effect.

Patch Number	1	2	3	4
Estimated σ_i^q	0.0934	0.0936	0.0990	0.1107
Patch Number	5	6	7	8
Estimated σ_i^q	0.0874	0.0859	0.0894	0.1026
Patch Number	9	10	11	12
Estimated σ_i^q	0.0848	0.0826	0.0879	0.0994
Patch Number	13	14	15	16
Estimated σ_i^q	0.0855	0.0840	0.0872	0.0994
Patch Number	17	18	19	20
Estimated σ_i^q	0.0917	0.0895	0.0941	0.1039

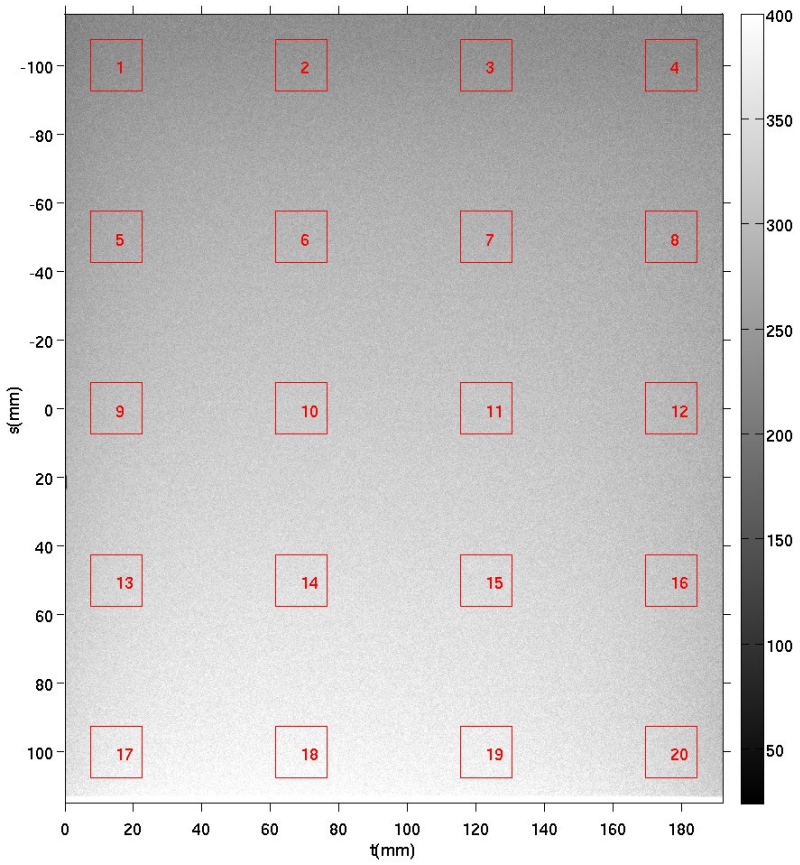

Figure 4.19 The measured PV of the Lucite slab before the log transform for the projection angle $\theta = 12°$. A brighter pixel indicates a higher measured x-ray intensity. σ_i^q was estimated for each noise patch (marked with a red box and number). The results are shown in Table 4.2.

Table 4.2 Estimated σ_i^q for each noise patch in Figure 4.19. The maximum and minimum σ_i^q are 0.1315 and 0.0843, marked with the red text. Slightly higher quantum noise is observed on the upper side of the image because x-ray attenuation by the Lucite slab is greater due to the longer path lengths at the projection angle $\theta = 12°$.

Patch Number	1	2	3	4
Estimated σ_i^q	0.1127	0.1119	0.1159	0.1315
Patch Number	5	6	7	8
Estimated σ_i^q	0.0973	0.0955	0.0988	0.1128
Patch Number	9	10	11	12
Estimated σ_i^q	0.0904	0.0873	0.0931	0.1071
Patch Number	13	14	15	16
Estimated σ_i^q	0.0856	0.0843	0.0895	0.1016
Patch Number	17	18	19	20
Estimated σ_i^q	0.0871	0.0855	0.0882	0.1023

Table 4.1 and Table 4.2 show the estimated σ_i^q for each noise patch in Figure 4.18 and Figure 4.19. For the central projection angle (Figure 4.18 and Tab1e 4.1), the maximum σ_i^q is 0.1107 in patch #4. The minimum σ_i^q is 0.0826 in patch #10. The ratio between the maximum and the minimum σ_i^q is 1.34. For the projection angle $\theta = 12°$ (Figure 4.19 and Tab1e 4.2), the maximum σ_i^q is 0.1315 in patch #4 and the minimum σ_i^q is 0.0843 in patch #14, giving a ratio of 1.56 between the maximum and the minimum σ_i^q. These ratios represent the non-uniformity of σ_i^q for one projection angle caused by the varying incident angle and the anode heel effect. Section IV.7.4 shows the influence of the non-uniformity of σ_i^q on the image reconstruction.

To efficiently implement $\mathbf{K}_i^{-1}$ in the SQS-DBCN algorithm, we treated σ_i^q as a constant for each projection angle. The value of the constant σ_i^q used in the SQS-DBCN algorithm was the mean σ_i^q for each PV. One approach to obtain the mean σ_i^q is to calculate the mean σ_i^q from many selected noise patches across the detector. We called this the noise patch approach. In practice, we used a more reliable and efficient approach that we subtracted two PVs of the Lucite slab at the same projection angle measured from two independent experiments with the same conditions (kVp, mAs etc.). The background trend (as shown in Figure 4.18 and Figure 4.19) was removed by the subtraction; therefore we did not need to apply the 2-D second order

polynomial fitting. For each pixel of the subtraction result, we used a 151 × 151 noise patch centered at the pixel to calculate the local standard deviation and divided the value by $\sqrt{2}$, similar to Section IV.4.7.1. Then we used Equation 4.24 to obtain the local σ_i^{Q}. The mean σ_i^{q} was calculated by dividing the mean σ_i^{Q} of the entire PV by the mean pixel value of the entire PV. We also took average of the estimated σ_i^{q} at symmetric projection angles (e.g., $\pm 3°, \pm 6°, \ldots$ or $\pm 30°$) as the final estimation result of σ_i^{q} for both angles. The estimated mean σ_i^{q} at each projection angle is shown in Figure 4.20. As expected, the standard deviation of the relative quantum noise σ_i^{q} is higher for larger projection angles. The estimated mean σ_i^{q} for the first and the last projection angles is different from the trend of the rest of the curve since the x-ray tube is still ramping up its full current during the acquisition of the first projection image. These mean σ_i^{q} values as a function of the projection angle were implemented in our SQS-DBCN algorithm for estimation of the σ_i^{q} values for a given breast thickness as described in Section IV.2.2. With enough number of noise patches selected, the noise patch approach gave similar results to Figure 4.20 with a maximum difference of 2% for all projection angles. But the computation time of the noise patch approach was much longer due to the 2-D polynomial fitting.

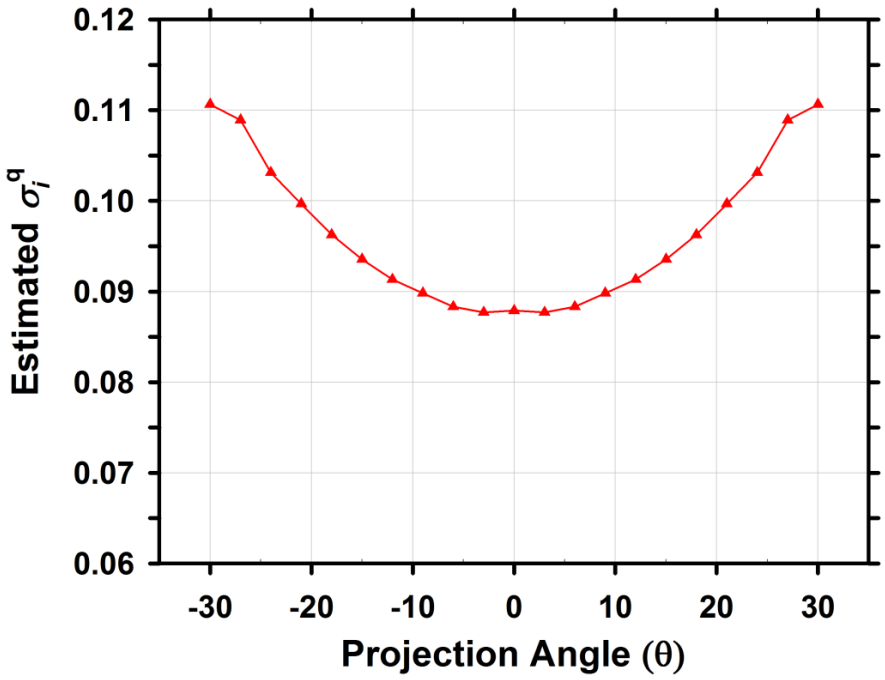

Figure 4.20. Estimated mean σ_i^{q} for each projection angle by subtracting two PVs of the Lucite slabs from two independent experiments.

IV.4.7.3 Estimation of the change of σ_i^{q} due to the non-uniformity of the breast tissue

We simulated a breast phantom with CatSim [65, 66] to estimate the change of σ_i^{q} due to the non-uniformity of breast tissue. We turned off the readout noise in the simulation so that the estimation below simulates the situation where the noise variance is only contributed by the quantum noise. The geometry of the simulated DBT system matches the geometry of the experimental system shown in Figure 2.1 in Section II.3. The phantom consists of a half cylinder of fatty tissue embedded with a small cylinder of glandular tissue (Figure 4.21). The radius of the half cylinder is 6 cm and the radius of the small cylinder is 2 cm. The thickness of both blocks of material is 5 cm. The phantom simulates a compressed breast of an average thickness with glandular and fatty tissue regions such that the dynamic range of the transmitted x-ray intensities incident on the detector approximates an extreme situation. In a real breast, the glandular tissue and fatty tissue are heterogeneously mixed so that the range will be within this extreme. Figure 4.22 shows simulated projections at scan angle $\theta = -12°, 0°, 12°$ of the phantom.

The range of σ_i^q is estimated from the patches marked with red boxes in Figure 4.22. Table 4.3 shows the results. According to Table 4.3, the ratio between the maximum and minimum σ_i^{q} for a given projection angle could be as large as 2.09. This ratio represents the non-uniformity of σ_i^{q} caused by the non-uniformity of the breast tissue.

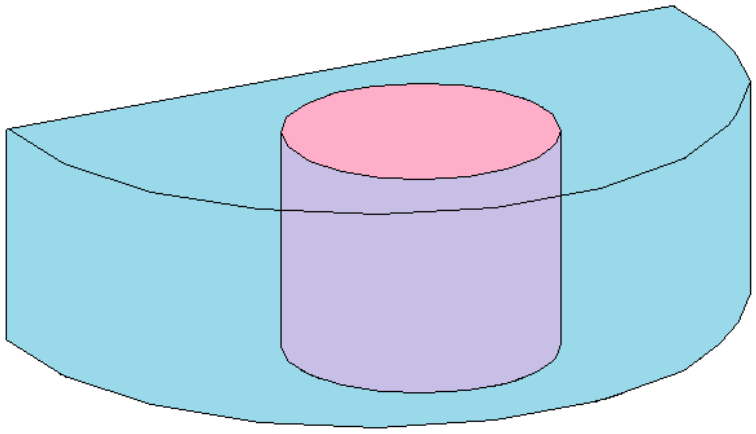

Figure 4.21. The simulated breast phantom with 100% glandular tissue (pink) surrounded by 100% fatty tissue (blue).

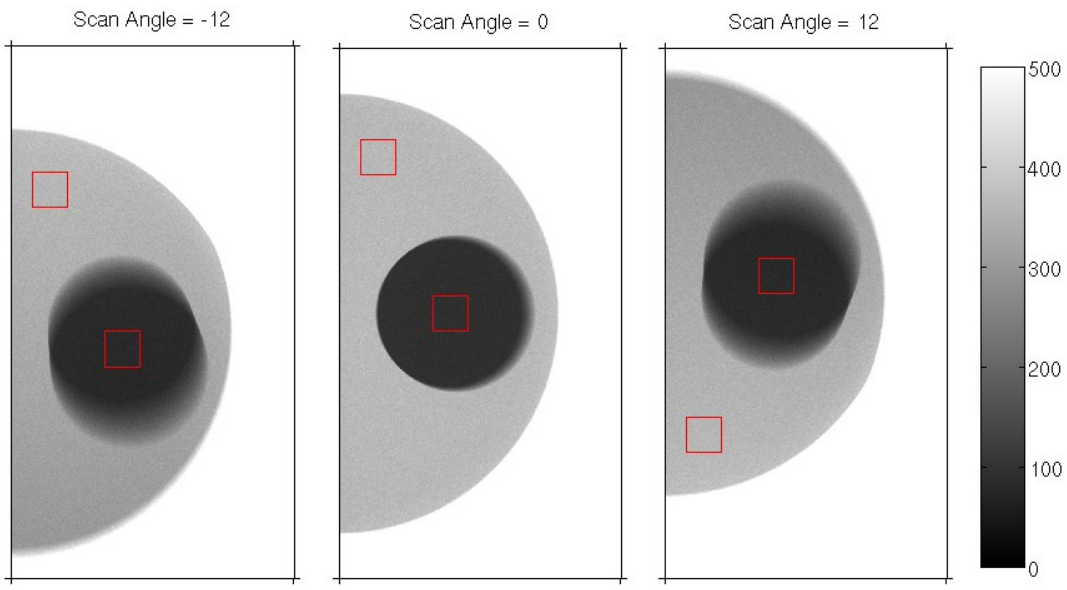

Figure 4.22. Simulated projections at scan angles $\theta = -12°, 0°, 12°$. The brightness represents relative x-ray intensity. The red boxes mark the locations for estimating the range of σ_i^{q}. All three images share the same grayscale bar.

Table 4.3. The range of σ_i^{q} due to the non-uniformity of the breast tissue.

Projection angle	σ_i^{q} behind the fatty tissue	σ_i^{q} behind the glandular tissue	σ_i^{q}(glandular)/σ_i^{q}(fatty)
-12	0.0666	0.1369	2.06
0	0.0651	0.1284	1.97
12	0.0659	0.1378	2.09

IV.4.7.4 Influence of the non-uniform σ_i^{q} on image reconstruction

Based on the estimation of the change of σ_i^{q} in the previous two sections, σ_i^{q} can change by a factor of 2.09 × 1.56 = 3.26 for a projection angle under the conditions studied. This is a conservative estimate in terms of breast density as it is unlikely that a breast has a 100% glandular region through its entire thickness. On the other hand, we obtained the ratio of 2.09 from a 5-cm breast phantom (section IV.4.7.3), which is only about the average thickness in the patient population. In reality the breast can be as thick as 10 cm, resulting in a larger change of σ_i^{q} across the detector. Considering these factors together, we chose a ratio of 3 above and below the current estimate of σ_i^{q} as a reasonable range to investigate the influence of the non-uniformity of σ_i^{q} on image reconstruction. Therefore when we use the σ_i^{q} value averaged over

the entire PV to represent the noise in our SQS-DBCN reconstruction for a human breast image, the error in treating the noise standard deviation as a constant may range from over-estimating σ_i^{q} by 200% to underestimating σ_i^{q} by 67% in local regions of the PV.

We therefore studied the effect of noise estimation error by an amount varying within this range. We multiplied all estimated σ_i^{q} by an 'estimation factor', denoted as τ, to simulate the cases where we overestimate or underestimate the values of σ_i^{q}. We performed a series of reconstructions for our breast phantom with clusters of MCs, by varying the range of τ from 0.33 to 3, while keeping the other parameters the same ($\delta = 0.002/mm, \beta = 70$). The CNR and FWHM of MCs are shown in Figure 4.23. Examples of reconstructed image patches are shown in Figure 4.24.

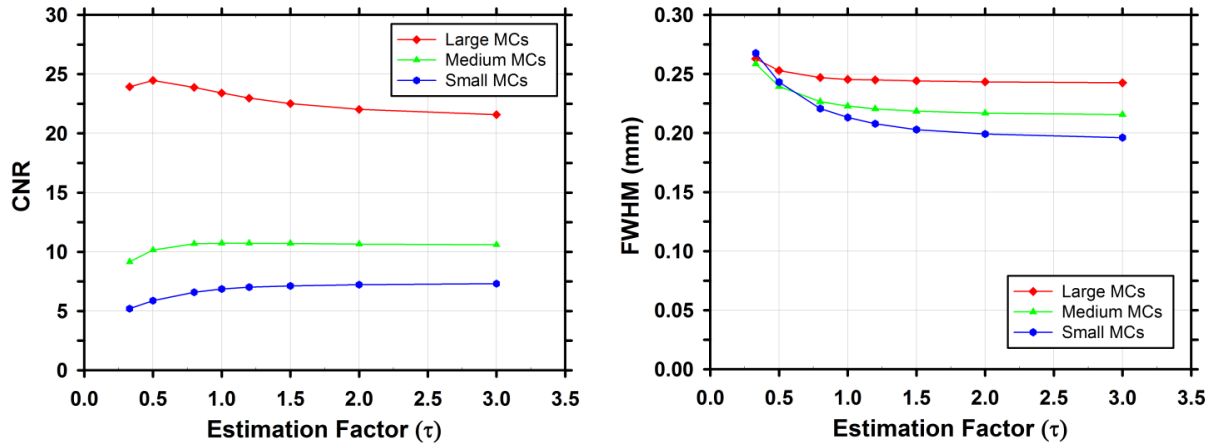

Figure 4.23. CNR and FWHM curves as the estimated noise varies by a factor of τ.

Figure 4.23 shows that the reconstructed CNRs of MCs are not strongly affected by small deviations from the estimation of σ_i^{q}. The CNR curves are relatively flat in a wide range of τ. The FWHM curves are also relatively flat except for the two cases that we underestimated σ_i^{q} by 50% or 66%. The maximum changes of CNR and FWHM for all values of τ are 41% and 36%, respectively, as observed for the small MCs when τ changes from 3 to 0.33. This may not happen in a real experiment since it is not possible to underestimate σ_i^{q} by 66% in some regions of the PV while overestimating σ_i^{q} by 200% in other regions at the same time. For MCs of other sizes, the change in CNR and FWHM is smaller. Figure 4.24 shows examples of reconstructed MC patches of three different sizes. It can be observed that the quality does not change drastically in the range of $\tau = 0.5$ to $\tau = 3$. When τ =0.33, the small MCs are substantially

degraded in contrast and sharpness. As a result, using a constant σ_i^q for each projection angle is a reasonable approximation except when it is underestimated by more than 50%.

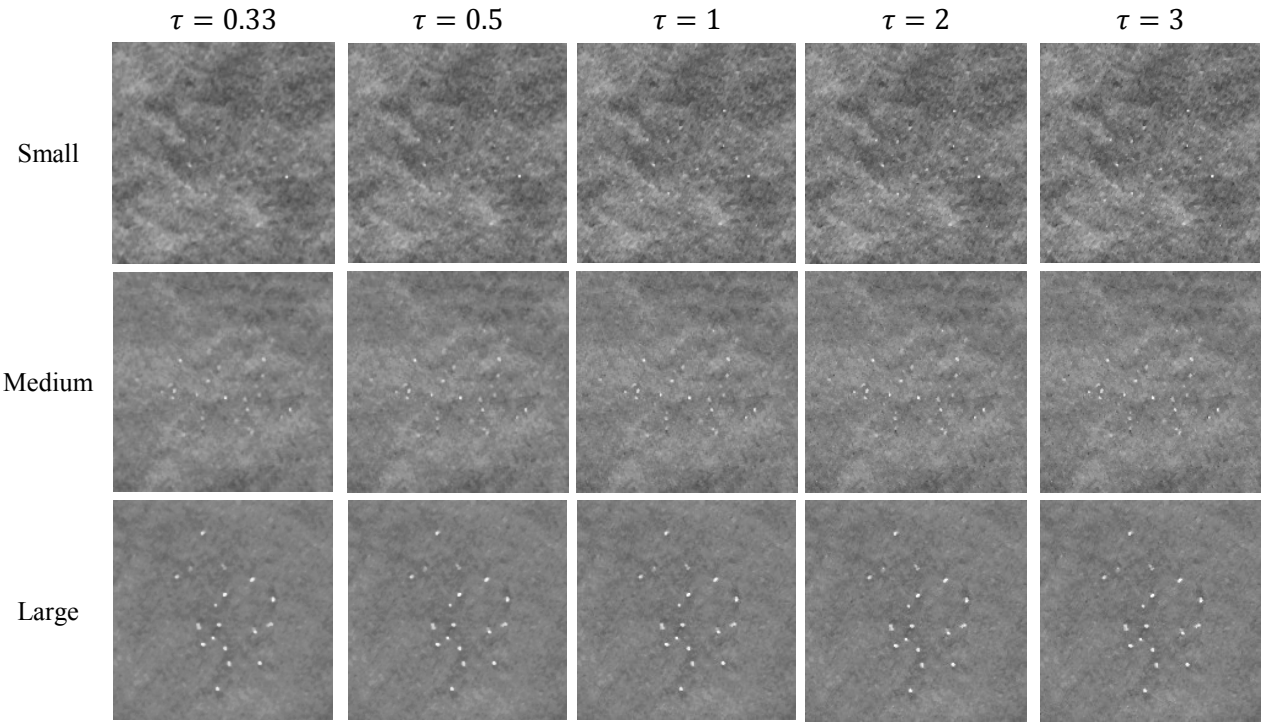

Figure 4.24. Reconstructed MC patches with a range of estimation factors. The images of the same cluster are displayed with the same window width setting.

Despite these results, treating quantum noise variance as a constant is a limitation of our current implementation of the MBIR. The fact that the image quality obtained from our SQS-DBCN method was improved even with the simplifying approximations shows the potential of MBIR methods for DBT, but further studies are needed to continue the development and relax the assumptions.

IV.4.8 SQS-DBCN with quadratic regularization

In the implementation of the SQS-DBCN algorithm, we chose an edge-preserving regularization method by using the hyperbola potential function $\eta(t)$ in Equation 4.27. In this section, we use the quadratic regularization instead and study the corresponding performance of the SQS-DBCN algorithm. We also compared the SQS-DBCN algorithm using quadratic regularization with and without detector blur modeling. The results indicate the importance of

the edge-preserving hyperbola regularization and the detector blur modeling for enhancing the MCs and preserving tissue texture in DBT reconstruction.

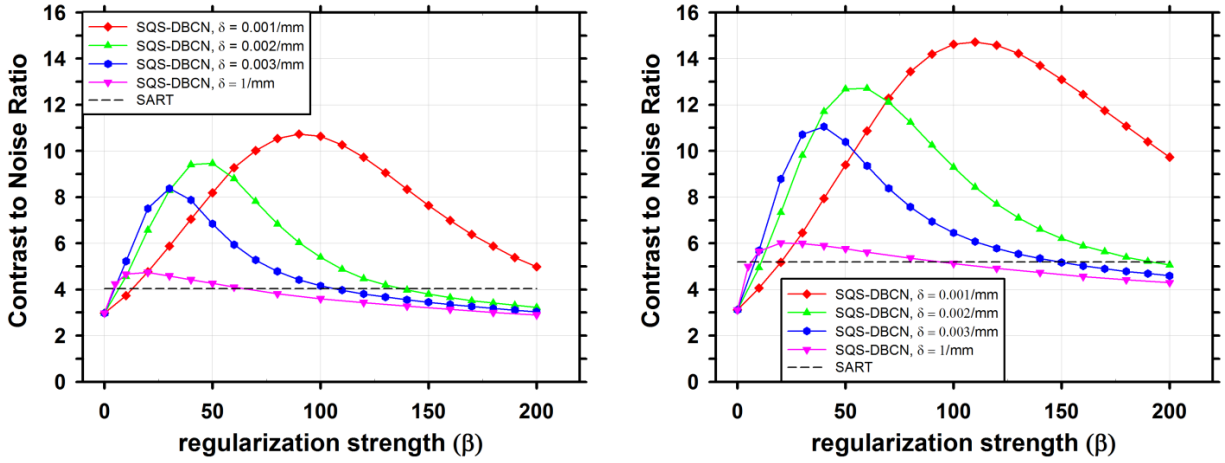

Figure 4.25. Dependence of CNR on reconstruction parameters. (a) MCs of nominal size 0.15-0.18mm, (b) MCs of nominal size 0.18-0.25mm. These plots are the same as Figure 4.4 with the addition of $\delta = 1/mm$ to approximate quadratic regularization.

As shown in Equation 4.27, when δ is very large, the hyperbola potential function is approximately a quadratic function $\eta(t) = t^2$. The quadratic regularization can be simply implemented by setting δ to a very large value in the original SQS-DBCN algorithm. Empirically, we found that the value $\delta = 1/mm$ is large enough for the regularization to be considered quadratic. A larger δ will not obviously change the results in this section.

Figure 4.25 shows the dependence of CNR of MCs on β. The peak of the curve moves to the lower-left corner when δ increases. When $\delta = 1/mm$, the peak CNR is only slightly higher than that of SART. The MC enhancement is much weaker when a quadratic regularization is used with the SQS-DBCN method. On a DBT slice, small MCs usually only occupy a few pixels. From the perspective of image processing, the entire MC may be processed as an 'edge' due to the high local gradient. So the MCs are strongly suppressed by a non-edge-preserving regularization. Figure 4.26 and Figure 4.27 show, respectively, examples of MCs in our phantom and soft tissue structures in human breast, such as a spiculated mass, reconstructed by SQS-DBCN with quadratic regularization for a range of β. The MCs are much more blurred than those by SQS-DBCN with hyperbola regularization as shown in Figure 4.26, especially when β is large, so that small β is preferred for MCs. For soft tissue structures in human breast, SQS-

DBCN with quadratic regularization produces texture that appears increasingly rough and "bumpy" when β decreases as shown in Figure 4.27 so that large β is needed for more smooth and natural tissue texture. These results demonstrate that for quadratic regularization a single β cannot provide good image quality for both MCs and tissue texture or mass margin, which is crucial for DBT reconstruction.

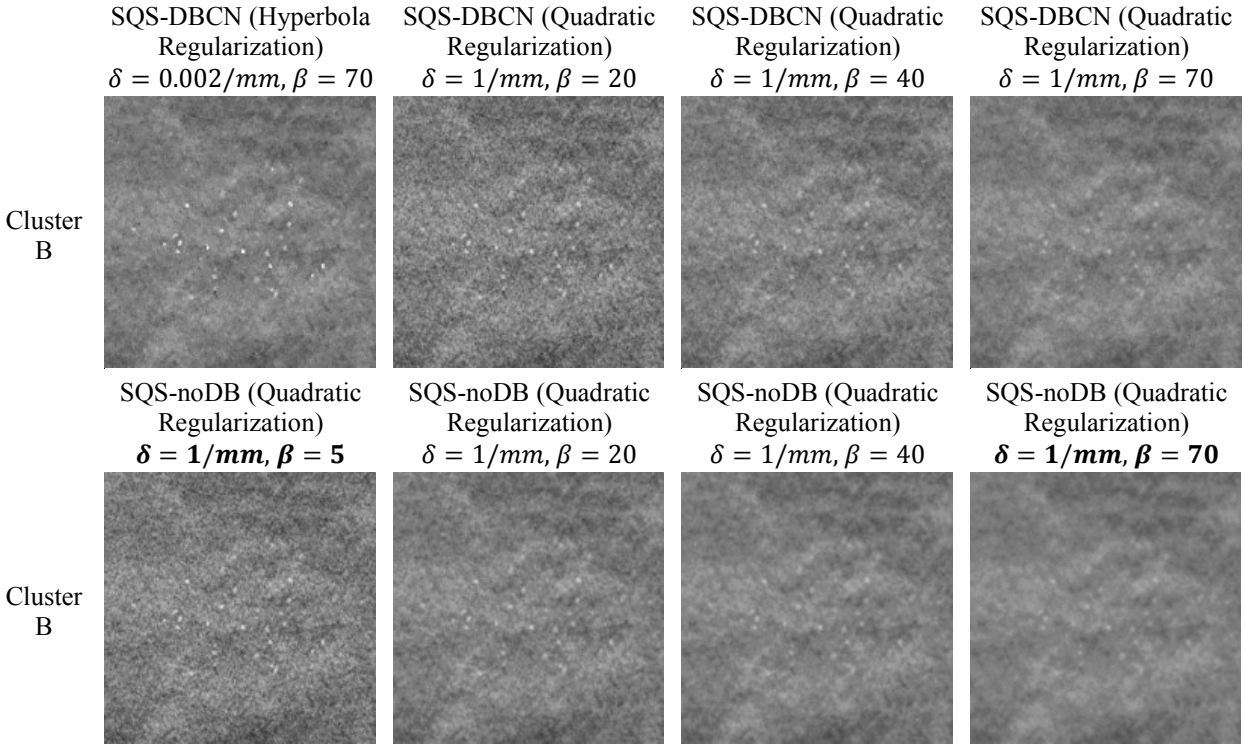

Figure 4.26. Comparison of MC clusters reconstructed with different reconstruction conditions. The SQS methods (SQS-DBCN or SQS-noDB) use 10 iterations. The images are displayed with the same window width setting.

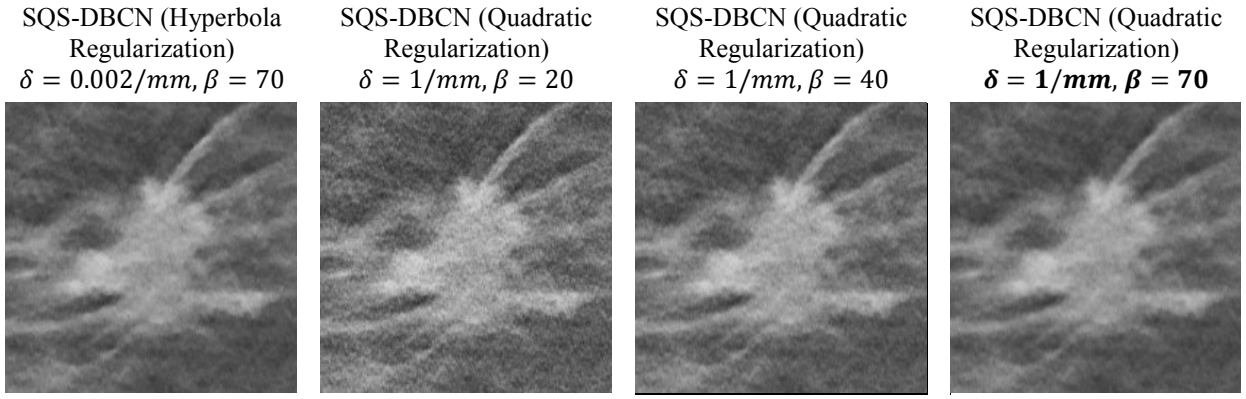

Figure 4.27. Comparison of spiculated mass in human subject DBT. The images are displayed with the same window width setting.

We have shown in Figure 4.7, 4.9 – 4.11 and 4.16 the comparison of the SQS-DBCN model to that without modeling detector blur, i.e., SQS-noDB (Equation 4.42), when the same hyperbola regularization was used. To further demonstrate the contribution of detector blur modeling, independent of the edge-preserving hyperbola regularizer, we compare the SQS-DBCN model and the SQS-noDB model, both with quadratic regularization, i.e., by setting $\delta = 1/mm$. Figure 4.28 shows the CNR of MCs as a function of β. With or without modeling detector blur, the CNR curve reaches its peak value at small β. The SQS-noDB curves reaches its peak at smaller β, making it even more difficult to find a good trade-off to enhance the MCs while preserving the texture of soft tissue. Figure 4.26 shows examples of MCs reconstructed with the SQS-DBCN model and the SQS-noDB model using quadratic regularization for a range of β values. For a given β, the MCs by the SQS-noDB model are much more blurred and have lower contrast than that by the SQS-DBCN model, indicating that the proposed detector blur modeling improves both the image sharpness and the CNR values. This experiment shows that the advantages of detector blur modeling persist until β becomes very small regardless of whether edge-preserving regularization is used.

In summary, the edge-preserving regularization is crucial for the performance of the SQS-DBCN algorithm. Modeling the detector blur is still important for DBT reconstruction even if a sub-optimal regularization is used in the cost function.

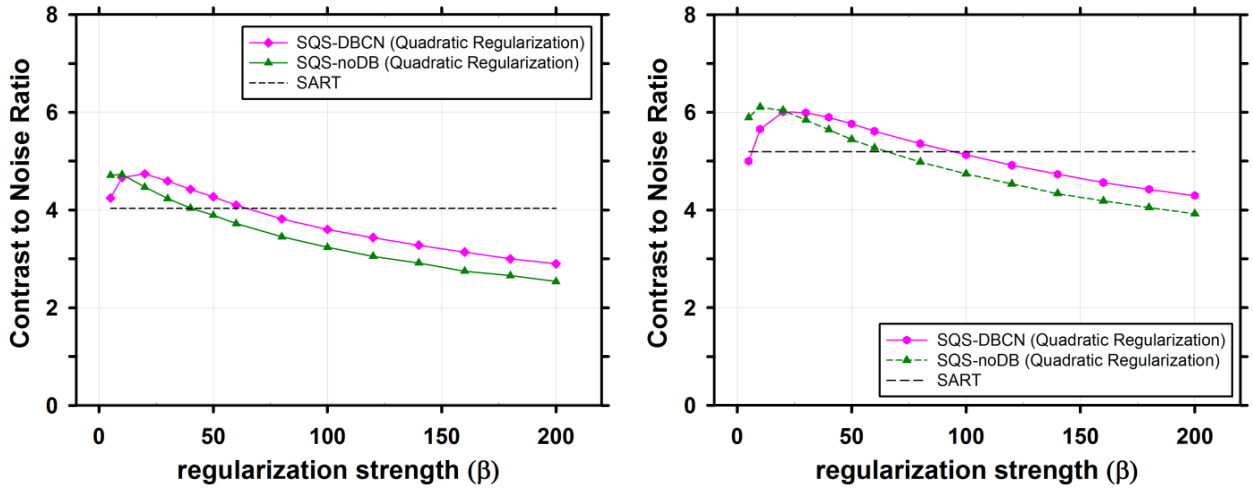

Figure 4.28. CNR of MCs of the SQS-DBCN method and the SQS-noDB method when the quadratic regularization is used ($\delta = 1/mm$). (a) MCs of nominal size 0.15-0.18mm, (b) MCs of nominal size 0.18-0.25mm.

IV.5 Discussion and limitations of the study

In this study, we proposed a new SQS-DBCN reconstruction method for DBT applications. By accounting for the detector blur and the correlated noise model, the SQS-DBCN method is able to improve the reconstruction quality of DBT images both visually and quantitatively. Based on the results, we discuss the significances and limitations of the SQS-DBCN method in this section.

IV.5.1 Parameter selection for the SQS-DBCN method

Parameter selection is a crucial step for achieving good image quality with the SQS-DBCN method. We investigated using the CNR of MCs as an FOM for guiding parameter optimization. We found that this FOM has limitations. First, CNR does not consider the spurious enhancement of noise points that may cause false MCs, which often occurs concurrently with strong enhancement of high frequency signals such as MCs. In this study, the CNR values are measured at known MC locations. If a reconstruction generates false MCs, it will not be penalized by the CNR values. Second, MCs are not the only sign of breast cancer; radiologists also need to recognize important signs such as architectural distortion or subtle spiculations from non-calcified lesions in the breast. Some reconstruction methods or parameter combinations can generate strong artifacts on the tissue texture, as observed in CT [75]. As a result, CNR curves provide only an approximate guide for selecting parameters. As shown in Figure 4.4, there is a wide range of β values where the SQS-DBCN method outperforms the SART method for enhancing the CNR of MCs. We used the parameters within this range to reconstruct human subject images and compared the visual quality of the soft tissue texture among these selections. We found that $\delta = 0.002/\text{mm}, \beta = 70$ is a reasonable choice for the SQS-DBCN method that does not cause strong artifacts and only trades off a fraction of the MC enhancement.

One challenge in the parameter selection is that different cases may require different parameter combinations for the best image quality due to the variations in the noise level of images. For the phantom DBT, we can use the CNR of MCs to guide the parameter selection. However, the selected parameters may not work well for some patient cases. It is difficult to define an FOM for a patient case to help parameter selection because the target lesion of a given patient case is usually unknown. For this reason, we implemented the adaptive parameter

adjustment as shown in Equation 4.26. Only β is adjusted in the procedure while the value of δ is fixed. The meanings of the two parameters (β and δ) are very different in the SQS-DBCN method. δ serves as a threshold to differentiate MCs from soft tissues. Strictly speaking, its value should be decided based on experimental measurement of the x-ray attenuation coefficients of MC with different x-ray spectra that depend on the kilovoltage, target material and filter material of the x-ray source. Considering that the value of δ should not change dramatically for different cases, two or three δ values could be used for reconstruction to provide different levels of enhancement for MCs. The value of β, on the other hand, controls the strength of the regularization and needs to be adaptively adjusted for different cases. The adjustment we currently implemented in Equation 4.26 is likely not the optimal choice. Further investigation is required to design a better strategy for choosing the optimal β for the best performance of the SQS-DBCN method.

Another way to simplify the parameter selection is to use the quadratic regularization. A quadratic regularization will avoid δ in the potential function and reduce the number of hyperparameters by one. However, our experiments (Section IV.4.8) indicate that the hyperbola regularization is superior to quadratic regularization for DBT reconstruction because of the dual roles played by the hyperbola potential function $\eta(t) = \delta^2\left(\sqrt{1 + (t/\delta)^2} - 1\right)$. For reconstructing soft tissue, the difference between neighboring pixels is small such that $\delta = 0.002/mm$ is large enough for the potential function to work in the 'quadratic' part of the curve. It therefore behaves like quadratic regularization that produces relatively smooth and natural soft tissue texture at large β. For MCs with high gradient between neighboring pixels, the potential function behaves like linear regularization such that MCs are preserved even when relatively strong regularization with large β is used to reduce noise. The property of the hyperbola function thus matches well with the requirements for DBT reconstruction.

IV.5.2 The importance of different model components for the SQS-DBCN method

The comparison of SQS-DBCN, SQS-noDB and SQS-noNC demonstrates that the effectiveness of the SQS-DBCN method relies on the completeness of all three model components: detector blur, noise correlation and regularization. Although intuitively, the MC enhancement might result from the deblurring effect of modeling detector blur, our results with

the SQS-noNC method demonstrate that modeling noise correlation is equally important. Our comparison of SQS-DBCN with the PWLS reconstruction algorithm used in CT further indicates that statistical iterative reconstruction methods developed for CT are not sufficient for DBT because they ignore detector blur and noise correlation. Similar to the SQS-DBCN method, parameters of SQS-noDB and SQS-noNC methods were chosen based on both the CNR performance and the soft tissue texture. We found that over the range of β values where the CNR is relatively high ($\beta = 10$ to 40 for SQS-noDB and $\beta = 10$ to 30 for SQS-noNC), it is more difficult to find a proper β with satisfactory tissue texture. As shown in Figure 4.10(a), with the chosen β values for these two methods, the mean CNRs for MCs of all three sizes are lower than those of the SQS-DBCN method. Figure 4.10(b) shows that with the SQS-noDB or the SQS-noNC methods, the mean FWHMs become similar for MCs of all three sizes, which is undesirable. The image patches in Figure 4.9 also demonstrate that the background texture obtained with the SQS-noDB or the SQS-noNC methods looks blurry and coarse and the MCs are less sharp compared to those with the SQS-DBCN method. The reconstructed images of human subject DBT in Figure 4.16 support the same conclusion. Further comparison of SQS-DBCN and SQS-noDB with quadratic regularization also leads to similar observations as discussed in Section IV.4.8. These results indicate that both the detector blur and the correlated noise modeling in the SQS-DBCN method are important components in the reconstruction and that its superior CNR performance is not simply a result of the regularization.

Another interesting observation is that the SQS-noDB method generally performs better than the SQS-noNC method. Figure 4.9 shows that the SQS-noNC images looks more blurry compared with the SQS-noDB images. Figure 4.10 shows that the SQS-noNC method gives lower CNR values and larger FWHM values for all three different-sized MCs. In fact, the SQS-noDB method is equivalent to the SQS-DBCN method if the true point spread function of the detector blur is a Kronecker impulse. For the SQS-noDB method, although the detector blur is ignored, the noise model still matches the forward model in the data-fitting term of Equation 4.18. On the other hand, the SQS-noNC method incorporates the detector blur in the forward model and ignores the corresponding noise correlation. The results reveal that such a mismatch in the modeling degrades image quality. The comparison between SQS-noDB and SQS-DBCN indicates the importance of the noise correlation model.

IV.5.3 Inverting the noise covariance matrix $\mathbf{K}_i$ with the matrix inversion lemma

The SQS-DBCN algorithm treats the quantum noise and readout noise as having constant variance for each projection angle such that the inversion of the covariance matrix $\mathbf{K}_i$ can be efficiently implemented. While using a constant variance for the readout noise is reasonable, treating the quantum noise as having a constant variance might be questionable. The results in Section IV.4.7 demonstrate that σ_i^{q} can vary by a factor 3 for a given projection view but this does not have strong influence on the reconstructed image. One might consider using the matrix inversion lemma to transform $\mathbf{K}_i$ in hopes that the approximation of the constant quantum noise could be relaxed. We discuss this approach in this section.

We still assume the readout noise to have constant variance: $\mathbf{K}_i^r = \sigma_i^{\mathrm{r}2}\mathbf{I}$. By applying the matrix inversion lemma to $\mathbf{K}_i^{-1}$, we have:

$$\begin{aligned}\mathbf{K}_i^{-1} &= \left(\mathbf{B}_i\mathbf{K}_i^{\mathrm{q}}\mathbf{B}_i' + \mathbf{K}_i^r\right)^{-1} \\ &= \left(\sigma_i^{\mathrm{r}2}\mathbf{I}\right)^{-1} - \left(\sigma_i^{\mathrm{r}2}\mathbf{I}\right)^{-1}\mathbf{B}_i\left(\mathbf{K}_i^{\mathrm{q}-1} + \mathbf{B}_i'\left(\sigma_i^{\mathrm{r}2}\mathbf{I}\right)^{-1}\mathbf{B}_i\right)^{-1}\mathbf{B}_i'\left(\sigma_i^{\mathrm{r}2}\mathbf{I}\right)^{-1} \\ &= \frac{1}{\sigma_i^{\mathrm{r}2}}\mathbf{I} - \frac{1}{\sigma_i^{\mathrm{r}2}}\mathbf{B}_i\left(\sigma_i^{\mathrm{r}2}\mathbf{K}_i^{\mathrm{q}-1} + \mathbf{B}_i'\mathbf{B}_i\right)^{-1}\mathbf{B}_i'.\end{aligned} \tag{4.52}$$

$\mathbf{B}_i'\mathbf{B}_i$ is a circulant matrix and $\sigma_i^{\mathrm{r}2}\mathbf{K}_i^{\mathrm{q}-1}$ is a diagonal matrix with changing diagonal elements. The summation of these two matrices cannot be inverted analytically [105]. As a result, our approximation of constant quantum noise is still necessary to efficiently implement the inversion of $\mathbf{K}_i$.

Despite the conclusion, if we consider the diagonal elements of $\mathbf{K}_i^{\mathrm{q}}$ to be slowly changing, $\left(\sigma_i^{\mathrm{r}2}\mathbf{K}_i^{\mathrm{q}-1} + \mathbf{B}_i'\mathbf{B}_i\right)^{-1}$ could be implemented as a piecewise shift-invariant filter. This is a potential way to relax the approximation of constant quantum noise. The results in Section IV.4.7 indicate that treating σ_i^{q} as a constant does not have strong influence on the reconstructed image. Therefore the influence of using the piecewise shift-invariant filter to implement $\mathbf{K}_i^{-1}$ on the reconstructed image quality is yet to be investigated.

IV.5.4 Other limitations of the study

There are a number of limitations for this preliminary study of an MBIR method for DBT. The SQS-DBCN method depends on several approximations. We approximate the detector blur

as linear shift-invariant for a given projection and as independent of the x-ray incident angle to the detector. The reconstructed object approximately consists of a relatively uniform background, where the fibrous tissue and MCs are treated as high-frequency structures embedded in the background. We also treat the quantum noise to be relatively constant over the field of view for a given projection angle. The model for the SQS-DBCN method only includes the detector blur and the corresponding noise correlation. Other factors such as x-ray focal spot blur, beam hardening and scatter are not considered in our current model. However, even with such a simplified model and approximations, the SQS-DBCN method enhances MCs and suppresses noise compared to SART reconstruction, while preserving tissue texture and mass spiculations for low-dose DBT scans. The SQS-DBCN implementation not only provides a practical DBT reconstruction method, but also indicates the potential value of MBIR for DBT.

IV.6 Conclusion

We proposed a DBT reconstruction method that incorporates detector blur and a correlated noise model. We have shown quantitatively and qualitatively that the new SQS-DBCN method can better enhance MCs compared with SART while preserving the image quality of mass spiculations and tissue texture. We have also demonstrated the effectiveness of the SQS-DBCN method as a result of incorporating the detector blur, the noise correlation and the regularization at the same time, indicating that a more complete model-based reconstruction may further improve the DBT image quality.

CHAPTER V.
Truncated Projection Artifact Removal for DBT

V.1 Introduction

This chapter introduces our work on TPA removal algorithms. Unlike other studies in this dissertation where we try to provide insight for the DBT image reconstruction, this study focuses on solving a crucial technical problem commonly observed in DBT reconstruction. TPA removal is important not only for the practical use of DBT in breast cancer screening and diagnosis, but also for other research on improving the DBT reconstruction quality that could be distracted by the reconstruction artifacts.

V.1.1 Existing TPA removal algorithms for CT and DBT systems

We first review existing TPA removal algorithms developed for CT and DBT systems. Generally speaking, these TPA removal algorithms can be classified into two categories: (1) methods that extrapolate the PVs and use the extrapolated PVs for reconstruction; (2) methods that compensate for the TPA in the imaged volume during the reconstruction.

The first category of TPA removal algorithms is more thoroughly studied and more commonly used in commercial CT systems. The idea is to use the measured PVs to estimate the projection values outside the detector, such that the extended PV is large enough that TPA is outside the volume of interest. The idea can be implemented in different ways [106-110], including the methods used in commercial CT systems by GE [111] and Siemens [112]. A principle commonly used in the PV extrapolation algorithms is that for parallel-beam CT, the total attenuation should remain constant if all PVs are fully captured by the detector without truncation. The total attenuation is calculated by integrating each PV. If the integral is found to be smaller for a few PVs, these are the truncated PVs that need to be extrapolated. The PV

extrapolation algorithm should complete these PVs such that their total attenuation reaches the same level as the non-truncated PVs. The parallel-beam geometry is not used in modern commercial CT systems. To use the principle of the constant total attenuation, the measured PVs are first converted to parallel-beam geometry before the PV extrapolation and then converted back to the original geometry if needed. Using this approach, many studies first set up an archetype function (e.g. a polynomial function with parameters) for the projection values outside the detector based on experience. Then they fit the parameters of the archetype function such that a smooth transition near the detector boundaries is achieved and the total attenuation reaches the same level as the non-truncated PVs. The method by Ohnesorge et al. [112] replicated the shape of the PV near and inside the detector boundaries to extrapolate the PV. For many algorithms, patch-up steps are necessary to generate natural-looking extrapolated PVs. Considering that some of these methods have been used in commercial CT scanners, apparently the empirical parts of these algorithms do not affect the diagnosis.

The first category of TPA removal methods allows flexible choice for reconstruction algorithms because the extrapolated PVs can simply be used in image reconstruction as if they were directly measured with a larger detector without truncation. The second category of TPA removal algorithms, on the other hand, is usually designed for a specific reconstruction algorithm or a type of reconstruction algorithms. For example, Kunze et al. proposed to optimize a cost function with the regularization to control TPA in CT reconstruction [113]. Such a method cannot be used in other iterative or analytical reconstruction methods. Li et al. studied TPA in DBT slices reconstructed with filtered back-projection. For a location in the imaged volume, the reciprocal of the total number of PVs that affected this location was used as the weight compensate for TPA [114]. In our laboratory, Lu et al. previously developed a TPA removal algorithm that used diffusion to compensate for the discontinuity in the gray levels in the region across the step caused by the $(i-1)^{th}$ PV updating. By removing the sharp boundary before updating by the i^{th} PV, the step artifact would not be enhanced by the subsequent updates in the same iteration [67]. Lu's method is efficient and reliable that it generates satisfactory TPA removal results without causing other artifacts. One can apply it to any iterative reconstruction method that accesses the PVs in successive order.

We used Lu's method in our work on the SWNC regularization [64] and the SQS-DBCN reconstruction [91, 92]. At the same time, there are limitations of Lu's method for MBIR. First,

Lu's method is implemented as an extra processing step after each update, which greatly complicates any analysis of the convergence of the cost function. As a result, although we can prove mathematically that our DBT reconstruction algorithms converge without the TPA removal method [64, 91, 92], including Lu's method precludes known algorithm convergence guarantees. Second, Lu's TPA removal method requires all PVs to be used in successive order. If ordered subset acceleration is not used in our SQS-DBCN reconstruction, Lu's TPA removal method cannot be applied since all PVs are used at the same time to update the image. If one wants to use the PVs in an arbitrary order, Lu's TPA removal method cannot be used either. These limitations inspired us to develop and investigate more universal TPA removal methods for DBT.

V.1.2 Organization of this chapter

In this chapter, we will introduce the algorithms and results of three different TPA removal methods we proposed and tested. Since these methods share some principles and algorithms, we will first discuss them in Section V.2. In Section V.3, we will describe each method step by step with two examples that represent CC view and MLO view DBT scans. The first and the second methods belong to the first category of TPA removal algorithms introduced in Section V.1.2. For these two methods, we will mainly focus on the PV extrapolation algorithms. The third method belongs to the second category of TPA removal algorithms, where we attempt to use regularization to control TPA. In Section V.4 of this chapter, we will present the results of the three methods and discuss their effectiveness and possible improvements. Section V.5 is a summary of this chapter.

V.2 Principles and Algorithms for PV Extrapolation in DBT

V.2.1 Regions to be extrapolated

We first calculate the regions that need to be extrapolated for the PV extrapolation-based TPA removal methods. The purpose of PV extrapolation is to move the TPA outside our VOI. Using the imaging system geometry, we can calculate the cone formed by connecting the boundaries of the extrapolated PV and the x-ray source. The cone needs to be large enough to cover the entire imaged volume for a given breast thickness. Figure 5.1 shows the source rotation

plane of the DBT system (Figure 2.1 viewed along the *x*-direction). The region to be extrapolated is decided by the location of the source and the corners of the imaged volume and it is different for different projection angles. The region to be extrapolated can be on one side of the digital detector as shown by the first and the last PV or on both sides as shown by the *i*th PV. The maximum extents of the extrapolated area are decided by the first and the last projection angle. We can either extrapolate every PV up to the maximums on both sides, or we can extrapolate every PV up to the required region of the corresponding projection angle. In fact, even if we extrapolate the PVs beyond the required region, the extra extrapolation will not affect the reconstruction since its backward projection does not affect the imaged volume.

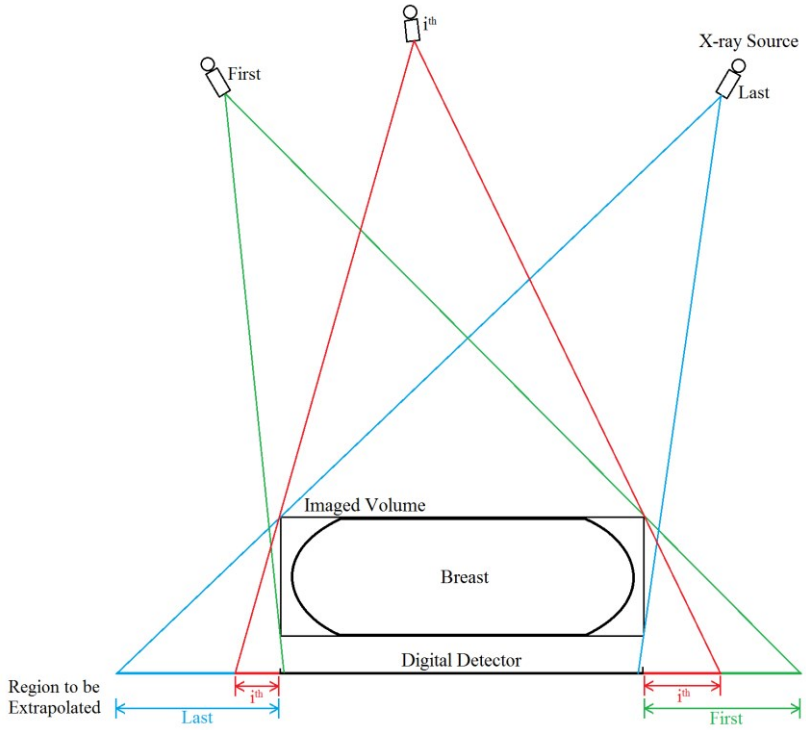

Figure 5.1. Regions to be extrapolated for different projection angles. The green region is needed by the first projection angle. The blue region is needed for the last projection angle. The red region represents the situation where an extrapolated region is needed on both sides of the digital detector.

V.2.2 The weighted k-means breast boundary detection algorithm

Since the breast boundary on each PV is used in both of our PV extrapolation methods, we introduce the breast boundary detection algorithm in this section. We consider the breast boundary detection as a binary image segmentation problem. Image segmentation has been

studied extensively in the past fifty years. Established methods include thresholding [115, 116], gradient-based edge detection methods [117, 118], model-based active contour [119-121], and texture-based algorithms [122, 123]. Among these methods, thresholding is simple but it works well for segmenting the breast boundary from the air region outside the breast. Considering that x-ray is attenuated while penetrating the breast, the projection of the breast generally has a lower x-ray intensity value compared with the projection of air. Practically, the x-ray projection of air is not uniform due to the heel effect of the x-ray anode and the varied path-length from the x-ray source to the detector plane, especially for cone-beam x-ray systems such as DBT. This non-uniformity varies slowly over for the entire projection, so it can be fitted and removed before the image segmentation. After removing the non-uniform background, the segmentation algorithm is simplified to finding a proper threshold to segment the projection.

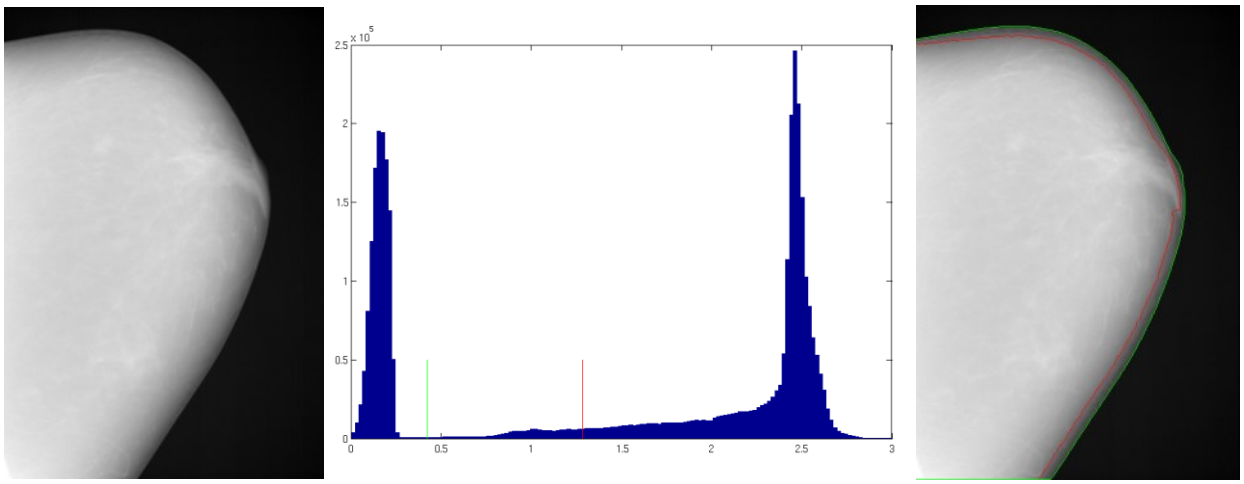

(a) (b) (c)

Figure 5.2. A typical PV in DBT (RMLO view), its histogram and two detected breast contours based on different thresholds. (a) The PV image. (b) The histogram. The red bar marks a threshold of 1.28, which is given by the classic k-means clustering with 2 clusters. The green bar marks a threshold of 0.42. (c) The breast contours when the two thresholds on the histogram are used. The color of the contour matches the color of the threshold in (b).

Our breast boundary detection is based on the PV after log-transform. Figure 5.2(a) shows a typical PV of DBT, which is basically a low-dose mammography image. This PV is the central projection of an RMLO view human-subject DBT. Figure 5.2(b) is the histogram of the PV, showing two groups of pixel values, one inside and the other outside the breast boundary. To distinguish the two clusters of values, we used the classical k-means method with k = 2. This method gives us a threshold of 1.28, marked as the red bar in Figure 5.2(b). The threshold is unit-

less since the displayed PV in Figure 5.2(a) is after the log transform. The red curve in Figure 5.2(c) shows the breast contour if this threshold is used. The contour is obtained from the processed breast mask after thresholding. The processing of the breast mask is described in Step (5) of Algorithm 5.1 that will be introduced later.

Obviously, the red curve is not our desired breast contour because the relative dark area near the breast boundary is not correctly included. Our desired contour, shown as the green curve in Figure 5.2(c), actually requires a threshold of 0.42, marked as the green bar in Figure 5.2(b). Such a threshold ensures that the cluster on the right side of Figure 5.2(b) includes the long tail between the two peaks.

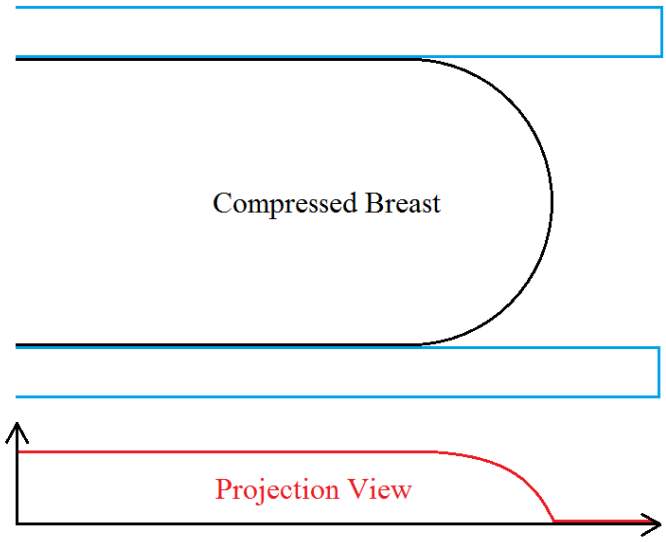

Figure 5.3. Schematic illustration of the shape of a compressed breast (upper) and its corresponding PV profile (lower, the x-ray intensity profile after log-transform).

Similar result was observed when we applied the k-means clustering method to many PV images. On the PV gray level histogram, we observe that the right cluster usually has a long tail with contributions from the gray area right inside the breast boundary (Figure 5.2(c)). The k-means clustering tends to split the tail into two clusters and does not provide good segmentation results. The reason that the gray area appears can be explained from the shape of the compressed breast as shown in Figure 5.3. The PV profile, which is the projected x-ray attenuation coefficient in the compressed breast, drops to zero gradually with a discontinuous first-order derivative at the boundary, creating the gray area near the breast boundary. Therefore, the traditional k-means clustering is suboptimal for breast boundary detection.

Based on these considerations, we propose a weighted-k-means breast boundary detection algorithm. Given a set of observations $(\boldsymbol{v}_1, \boldsymbol{v}_2, \dots, \boldsymbol{v}_n)$, the k-means clustering aims to partition the n values into k sets $\mathbf{S} = \{\mathrm{S}_1, \mathrm{S}_2, \dots, \mathrm{S}_k\}$ such that:

$$\hat{\mathbf{S}}_{\mathrm{k-means}} = \underset{\mathbf{S}}{\operatorname{argmin}} \sum_{i=1}^{k} \sum_{\boldsymbol{v} \in \mathrm{S}_i} \|\boldsymbol{v} - \boldsymbol{\mu}_i\|_2^2, \tag{5.1}$$

where $\boldsymbol{\mu}_i$ is the mean of the observations within the set S_i.

The weighted k-means approach is defined by generalizing the traditional k-means clustering:

$$\hat{\mathbf{S}}_{\mathrm{weighted\ k-means}} = \underset{\mathbf{S}}{\operatorname{argmin}} \sum_{i=1}^{k} w_i \sum_{\boldsymbol{v} \in \mathrm{S}_i} \|\boldsymbol{v} - \boldsymbol{\mu}_i\|_2^2, \tag{5.2}$$

where we include a user-specified weight w_i to each set.

The weighted k-means clustering is solved iteratively similarly to the traditional k-means clustering. The only difference is that when updating the cluster index l_i for the observation $\boldsymbol{v}_i$, we set the updated cluster index ${l_i}^{(m+1)}$ to the value that minimizes the weighted distance:

$${l_i}^{(m+1)} = \underset{l}{\operatorname{argmin}}\, w_l \left\| \boldsymbol{v}_i - \boldsymbol{\mu}_l^{(m)} \right\|_2^2, \tag{5.3}$$

where m is the iteration index and $\boldsymbol{\mu}_l^{(m)}$ is the mean of the lth cluster after the previous iteration.

Obviously, giving a cluster a larger weight will make observations less likely to be included in this cluster. We therefore adjust the weights to assign more values to the cluster with higher mean value (Figure 5.2(b)). More specifically, we use the minimum and maximum value of the entire PV as the initial mean values of the two clusters. Then we assign the cluster with the smaller mean value a weight that is larger than 1. We use w_1 to denote this value. The weight of the cluster with the larger mean value is fixed at 1. In fact, the green bar in Figure 5.2(b) with a threshold value of 0.42 is obtained using the weighted k-means clustering with $w_1 = 50$.

In summary, we propose the weighted k-means breast boundary detection algorithm, as shown in Algorithm 5.1:

Algorithm 5.1. Weighted k-means breast boundary detection

(1) Let $\mathbf{y}$ denote the log-transformed PV. For all pixel values of $\mathbf{y}$, we apply the weighted k-means clustering with $w_1 = w_{1st}$ to obtain the threshold t_{1st}. The area with smaller pixel values than t_{1st} is denoted as $\mathbf{B}$.

(2) Perform a 2D 2nd-order polynomial fitting for $\mathbf{y}$ in the area $\mathbf{B}$. The fitted 2D polynomial

background is extended to the entire PV. Let $\mathbf{b}_{\text{fit}}$ to denote this image (same size as $\mathbf{y}$)

(3) Calculate $\mathbf{y}_{\text{fit}} = \mathbf{y} - \mathbf{b}_{\text{fit}}$

(4) Apply the weighted k-means clustering with $w_1 = w_{2nd}$ to all pixel values of $\mathbf{y}_{\text{fit}}$ to obtain the threshold t_{2nd}. The area with larger pixel value than t_{2nd} is denoted as $\mathbf{M}$.

(5) Eliminate all connected areas of $\mathbf{M}$ with fewer than 80 pixels. For the remaining connected areas, fill in all the holes and apply a morphological opening with a disk-shaped structuring element of diameter = 9 pixels. The boundary of the processed area $\mathbf{M}_{\text{processed}}$ yields the final breast boundary.

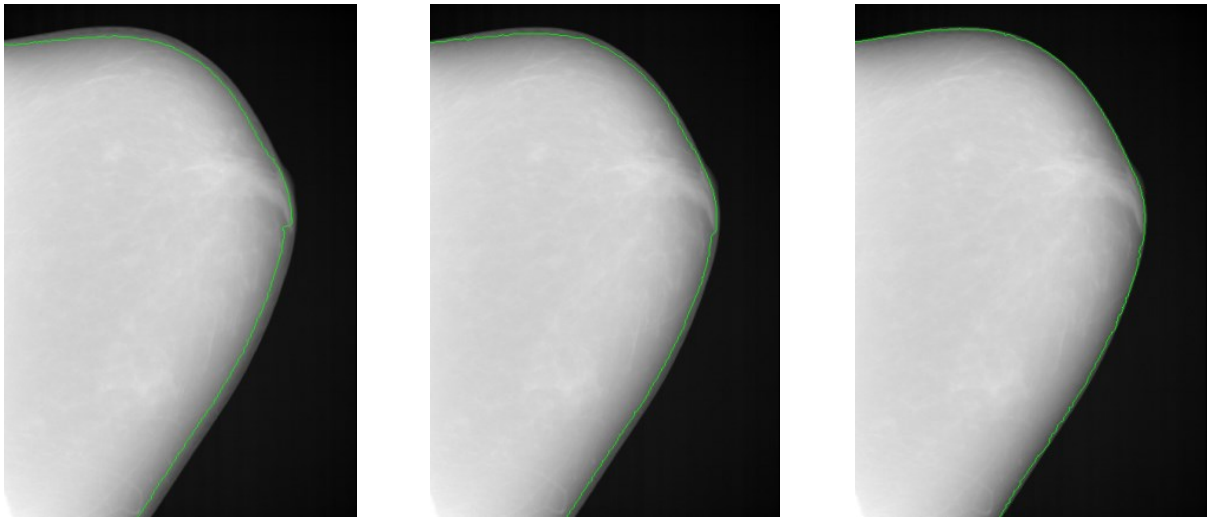

(a) $w_{2nd} = 1$ (b) $w_{2nd} = 2$ (c) $w_{2nd} = 4$

(d) $w_{2nd} = 8$ (e) $w_{2nd} = 500$ (f) $w_{2nd} = 1000$

Figure 5.4. Boundary detection results with different weight w_{2nd}. $w_{1st} = 50$ is used for all results.

The purpose of step (1)-(3) of Algorithm 5.1 is to eliminate the influence of the non-uniform background. In principle, we recommend using a larger value for w_{1st} to make sure that no pixels within the breast boundary are used in the polynomial fitting of step (2). In this work, we actually used the same value for w_{1st} and w_{2nd}, which actually generates good breast boundary detection result.

We empirically evaluated the sensitivity of the detected breast boundary to w_{1st} and w_{2nd} and found that the breast boundary detection result is very insensitive to the weights, as shown in Figure 5.4. Any w_{2nd} values between 8 and 500 generate similar breast boundary results.

We tested Algorithm 5.1 with 1407 PV images from 67 DBT scans (21 PVs for each scan), the parameter $w_{1st} = w_{2nd} = 50$ can correctly detect the breast boundary for 1401 PV images. For the other 6 PV images, the parameter $w_{1st} = w_{2nd} = 100$ generates satisfactory breast boundary results. As the focus of this work is not to develop a fully automatic breast boundary detection algorithm, we consider Algorithm 5.1 to be adequate for TPA removal. With an adaptive strategy for choosing w_{1st} and w_{2nd}, Algorithm 5.1 has the potential to be developed into a reliable breast boundary detection algorithm for more general applications.

V.3 The TPA removal algorithms

V.3.1 TPA removal with contour-extension-diffusion PV extrapolation

This section introduces our TPA removal algorithm based on contour-extension-diffusion PV extrapolation. We will first introduce our contour extension algorithm to complete the truncated breast boundaries. Then we will introduce the algorithm to fill pixel values in the extended regions. We will mainly use the contours of breast boundaries in this section. For simplicity, we call them breast contours. In the result section, we used SART to reconstruct the DBT image with the extrapolated PVs. Since SART has been discussed previously and in principle the extrapolated PVs can be used for any reconstruction algorithms, we will not repeat the details of image reconstruction.

The first step of the contour-extension-diffusion PV extrapolation is to extend the breast contours beyond the FOV of the detector. Figure 5.5 shows the detected breast contours of all 21 PVs for an RCC view and an RMLO view. For both views, all contours are not complete since they are truncated at the top, at the bottom, or on both sides. However, for the part of the contour

that has not been cut, all contours have similar shapes. This observation is not limited to these two examples. In fact, because of the geometry of the DBT system, all breast contours of the same view are similar but shifted sequentially as the x-ray projection angle changes in small increments. We have checked the all 67 human-subject DBT scans (CC view or MLO view) and confirmed this observation for all cases.

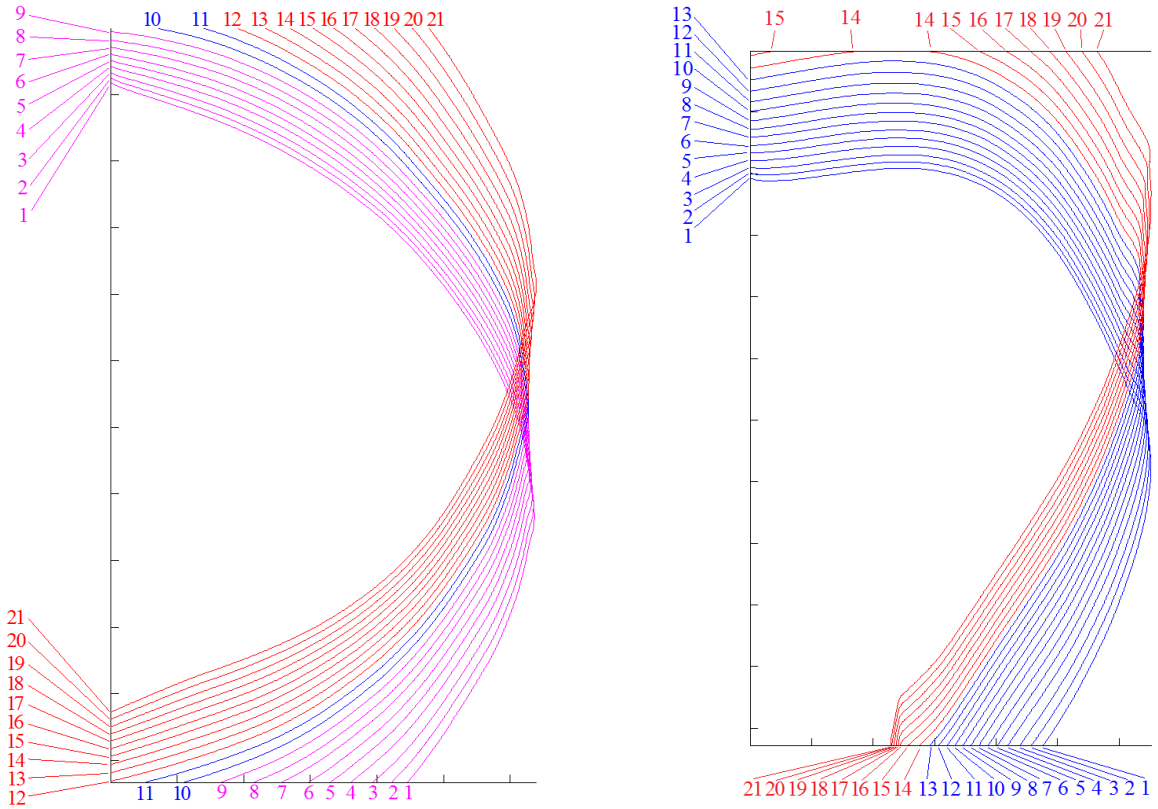

(a) (b)

Figure 5.5. Breast contours of all PV images for an RCC view and an RMLO view. (a) RCC view. The red contours are cut at the top, the magenta contours are cut at the bottom and the blue contours are cut on both sides. (b) RMLO view. The red contours are cut at top. All contours are cut at bottom.

Based on the observation, we propose to use the uncut breast contours or relatively more complete breast contours to estimate the breast contours beyond the FOV of the detector. The idea is based on the fact that neighboring breast contours are even more similar since their scan angles only have a 3 degree difference. The same idea also applies to the DBT systems by other manufacturers since the angle between neighboring projections is even smaller. For example, the angle between neighboring projections is 2°, 1° and 1° for the FDA-approved commercial DBT

systems by Siemens, Hologic [44] and Fujifilm [124]. If one breast contour is cut but its neighboring contour is uncut, we can estimate its missing part from the neighboring complete contour. We will use the examples in Figure 5.5 to explain the idea.

Figure 5.5(a) represents a typical CC-view DBT scan (LCC or RCC). Its 21 contours have been labeled with a number in the order that the PVs are acquired in the DBT scan. All 21 contours can be classified into three categories. The nine magenta contours (#1 – 9) are cut at the bottom and not cut at the top, the ten red contours (#12 – 21) are cut at the top but not cut at the bottom, while the blue ones (#10, 11) are cut on both sides. As a result, on the bottom side of the CC view, contour #12 can be used to extend contour #11 to complete it. After contour #11 is extended, we use the extended contour #11 to complete contour #10. The extended contour #10 therefore takes a part from contour #11 and a part from contour #12. We repeat the same operation for contours #9, 8, …, 2, 1 in successive order. The last contour #1 is extended with the information from contour #2 – contour #12. The same method is then applied to the top part to extend contour #10 – 21 in order. After all extensions are done, all contours are complete at both the top and the bottom side.

Figure 5.5(b) represents a typical MLO-view DBT scan (LMLO or RMLO). The MLO views are different from CC views since all breast contours are cut on the side of the pectoral muscle (at the bottom for RMLO view and at the top for LMLO view). As a result, we do not have a breast contour that is complete on the side of the pectoral muscle. In this case, we use the most complete contour to extend the others. We start by using contour #21 to extend contour #20. Then we use the extended contour #20 to extend the next contour and repeat this for all of the remaining contours. In the end, contour #1 is extended with the information from all the other 20 contours. Extending the top part of the contours is similar to the CC view, where we start by extending contour #14. After all extensions are done, all contours are complete at the top but incomplete at the bottom. It is possible that the extended contours are not enough to reach the required size shown in Figure 5.1. This exception will be discussed later.

With the idea introduced above, we propose the contour extension algorithm that uses one contour to estimate another. Before describing the algorithm, we need to introduce the expression of a contour and the definition of the distance from one contour to another one. A contour, denoted as *C*, is described with parametric equations:

$$C = \big(t_C(q), s_C(q)\big), \tag{5.4}$$

where q is the arc distance from a point to the starting point of the contour:

$$q \in [0, q_C]. \tag{5.5}$$

We will use the operation Shift(·) to shift a contour, defined as:

$$\text{Shift}(C; t_0, s_0) = (t_C(q) + t_0, s_C(q) + s_0), \tag{5.6}$$

where q is the same as that defined in (5.5).

The distance from a point (t, s) to a contour C is defined as the minimum Euclidean distance from the point to the contour:

$$d_C(t, s) = \inf_q ((t_C(q) - t)^2 + (s_C(q) - s)^2). \tag{5.7}$$

Naturally, the distance from one contour C_1 to another contour C_2 is defined as:

$$d_{C_1 \to C_2} = \int_0^{q_{C_1}} d_{C_2}\left(t_{C_1}(q), s_{C_1}(q)\right) \mathrm{d}q. \tag{5.8}$$

The distance between the two contours is asymmetric that $d_{C_2 \to C_1}$ is different from $d_{C_1 \to C_2}$ in most situations.

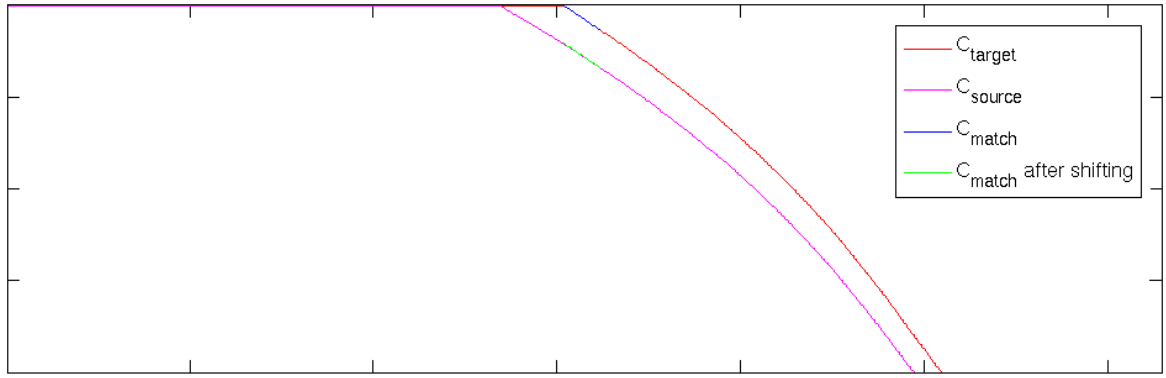

(a)

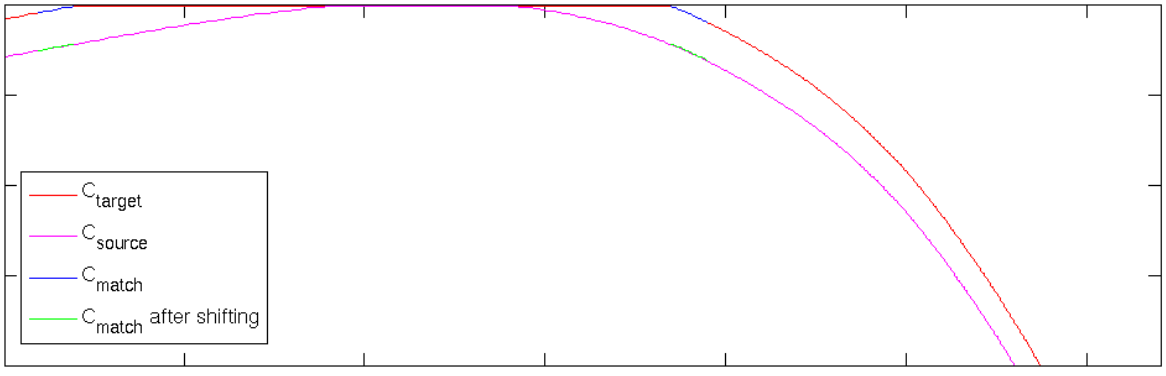

(b)

Figure 5.6. The matching sections before and after the shifting for (a) RCC view. (b) RMLO view

We extend an incomplete contour with another contour by shifting the more complete contour along the vertical direction such that the two contours can connect. The contour to be extended is called the target contour, denoted as C_{target}. The more complete contour is called the source contour, denoted as C_{source}. By definition, the source contour does not have to be uncut, as shown in Figure 5.6. The shifting distance is determined by minimizing the distance from a matching section of the target contour to the source contour. The matching sections, denoted as C_{match}, are shown as the blue curves in Figure 5.6. They start from the point where a contour is cut and propagate towards the direction that the contour is not cut. The number of matching sections for a contour can be more than one, as shown in Figure 5.6(b). Even for the CC view, the number of matching sections can be two or more, depending on the shape of the contour. The distance of the shift is estimated by minimizing the distance from the shifted matching sections to the source contour:

$$\hat{s}_{C_{\text{match}} \to C_{\text{source}}} = \underset{s \in [0, s_{\max}]}{\operatorname{argmin}} \, d_{\text{Shift}(C_{\text{match}};0,s) \to C_{\text{source}}}, \tag{5.9}$$

where $s_{\max}$ is the maximum shifting distance that is allowed. We empirically choose $s_{\max} = 2\text{cm}$ in our study. This value has been found to suffice even for the thickest breast in the studied data set. We solved the optimization problem in Equation 5.9 with an exhaustive search method that calculates the values of $d_{\text{Shift}(C_{\text{match}};0,s) \to C_{\text{source}}}$ for all values of s every 0.1mm within the range of $[0, s_{\max}]$ and finds the minimizer. With $s_{\max} = 2\text{cm}$, the exhaustive search takes less than 2 seconds to find the shifting distances for all PVs for all the cases we have tested. The time cost can be neglected compared with the time cost of the DBT reconstruction. The shifted C_{match} curves (colored green in Figure 5.6) almost overlap with the C_{source} curves (the red curves in Figure 5.6) for both the CC view and the MLO view, which indicates the similarity between C_{target} and C_{source}.

After finding the optimal distance $\hat{s}_{C_{\text{match}} \to C_{\text{source}}}$, we shift C_{source} in the opposite direction. The operation can be written as $\text{Shift}\left(C_{\text{source}}; 0, -\hat{s}_{C_{\text{match}} \to C_{\text{source}}}\right)$. The shifted source contours are shown as the blue curves in Figure 5.7. As we expected, the shifted source contours connect smoothly with the target contours. Then we find the part of the shifted source contours outside the detector region and use that part to complete cut part of the target contours.

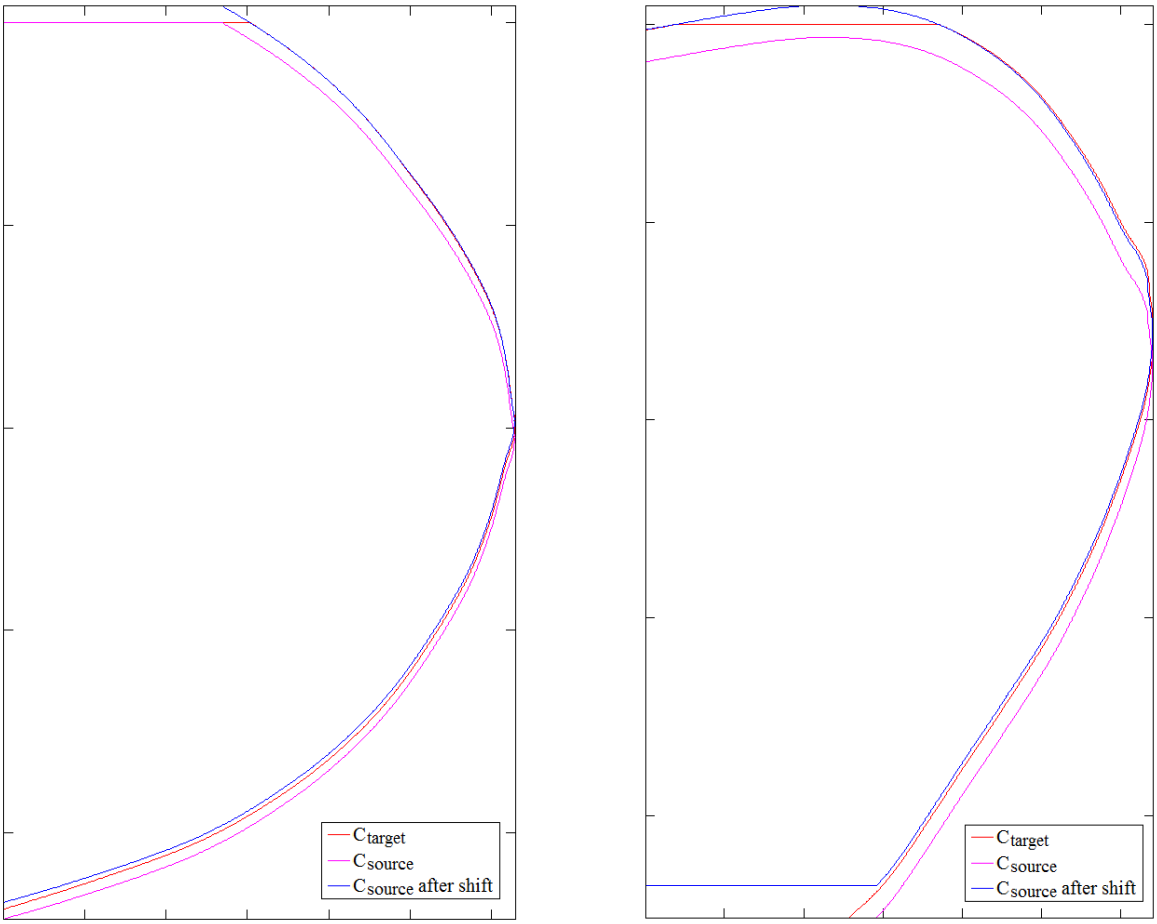

(a) (b)

Figure 5.7. The shifted source curves in comparison with the target curves for (a) RCC view. (b) RMLO view.

Based on the algorithm described above, for all contours in Figure 5.5(a), we extend contour #11 to contour #1 at the bottom consecutively and contour #10 to contour #21 at the top consecutively. The extended contours are shown in Figure 5.8(a), following the same color schemes as that of Figure 5.5. It can be seen that all contours are smooth after the extension.

For the RMLO view, the process is similar but one additional step needs to be done. Since none of the contours is complete at the bottom, it is possible that the extended contours have not reached the location to eliminate the TPA. There is no guarantee that the extended contours can cover the required extended detector size in Figure 5.1. For a final step, we further extend all contours in Figure 5.8(b) vertically to cover the maximum required extended region. The final extended contours for the RMLO view is shown in Figure 5.8(c).

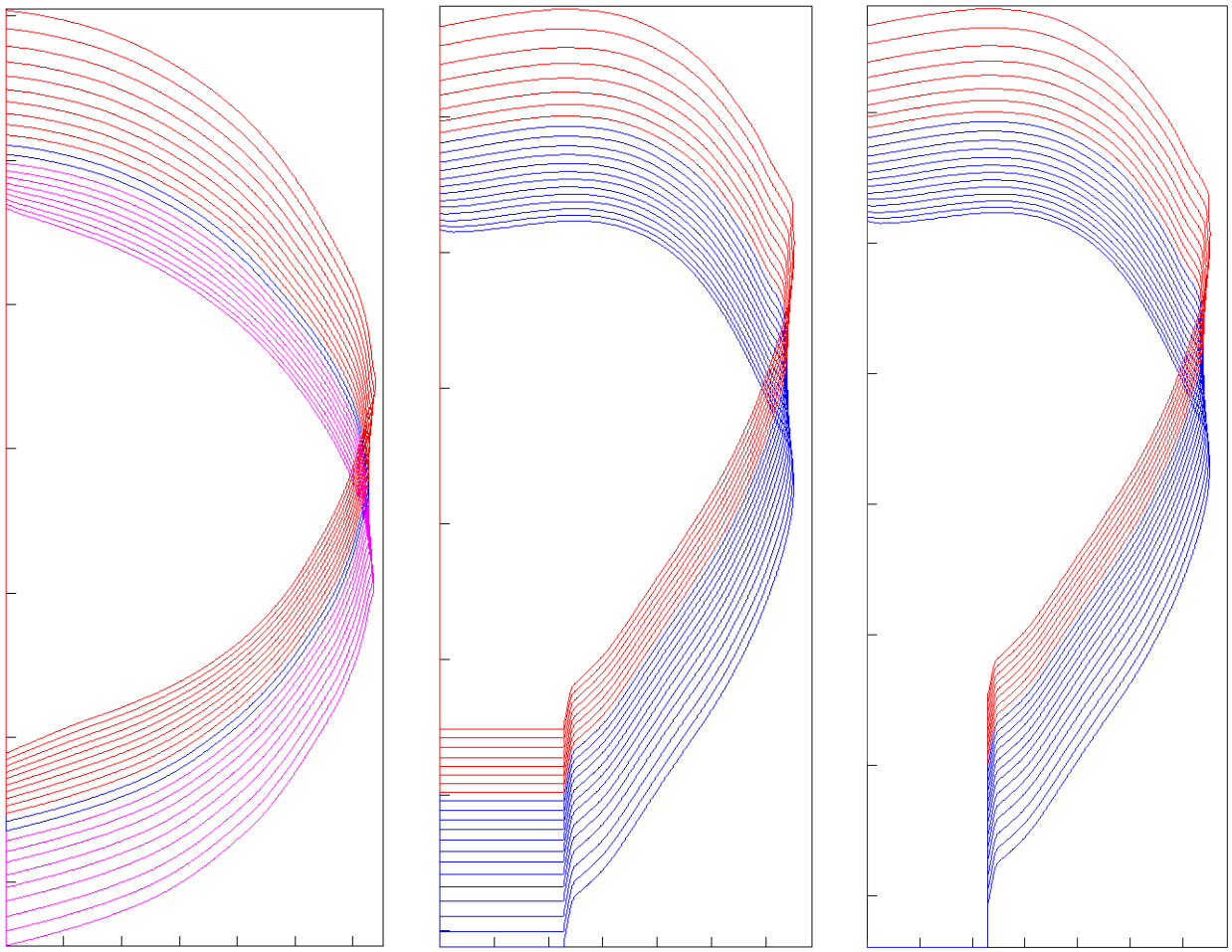

(a) (b) (c)

Figure 5.8. All extended breast contours for an (a) RCC view and an (b) RMLO view after the contour extension. (c) RMLO view after the complete extension.

To summarize the algorithm, given two contours C_{target} and C_{source}, we define two operations $\text{ExtUp}(C_{\text{target}}, C_{\text{source}})$ and $\text{ExtDown}(C_{\text{target}}, C_{\text{source}})$. $\text{ExtUp}(C_{\text{target}}, C_{\text{source}})$ is defined as:

Algorithm 5.2. $\text{ExtUp}(C_{\text{target}}, C_{\text{source}})$

(1) If C_{target} is uncut at top, $\text{ExtUp}(C_{\text{target}}, C_{\text{source}}) = C_{\text{target}}$

(2) Otherwise, find the matching sections C_{match} on C_{target}.

(3) Calculate $\hat{s}_{C_{\text{match}} \to C_{\text{source}}}$ based on Equation 5.9

(4) $\text{ExtUp}(C_{\text{target}}, C_{\text{source}}) = \begin{cases} C_{\text{target}}, \text{in the measured detector region} \\ \text{Shift}(C_{\text{source}}; 0, -\hat{s}_{C_{\text{match}} \to C_{\text{source}}}), \text{in the extended region} \end{cases}$.

For implementation, step (2) of Algorithm 5.2 uses the second derivative of the first row of the breast mask M_{target} (corresponding to C_{target}). The first row of M_{target} is a 1-D vector with values of 0 or 1. We use $M_{\text{target,1st row}}$ to denote this 1-D vector. As shown in Figure 5.6, at each location where the value of $M_{\text{target,1st row}}$ changes from 0 to 1 or from 1 to 0, a matching section needs to be created. These locations are indicated by a negative value of the second derivative of $M_{\text{target,1st row}}$. Step (4) of Algorithm 5.2 is implemented by shifting the breast mask M_{source} (corresponding to C_{source}) and combining it with M_{target}.

Similarly, $\text{ExtDown}(C_{\text{target}}, C_{\text{source}})$ is defined as:

Algorithm 5.3. $\text{ExtDown}(C_{\text{target}}, C_{\text{source}})$

(1) If C_{target} is uncut at bottom, $\text{ExtDown}(C_{\text{target}}, C_{\text{source}}) = C_{\text{target}}$

(2) Otherwise, find the matching sections C_{match} on C_{target}.

(3) Calculate $\hat{s}_{C_{\text{match}} \to C_{\text{source}}}$ based on Equation 5.9

(4) $\text{ExtDown}(C_{\text{target}}, C_{\text{source}}) = \begin{cases} C_{\text{target}}, \text{in the measured detector region} \\ \text{Shift}(C_{\text{source}}; 0, -\hat{s}_{C_{\text{match}} \to C_{\text{source}}}), \text{in the extended region} \end{cases}$.

Then the breast contour extension algorithm is described as:

Algorithm 5.4. The Breast Contour Extension Algorithm

(1) Load all N_{p} PV images. Sort them such that all the projection angles are in ascending order.

(2) Perform the two-step k-means breast boundary detection for all PV images to obtain all breast masks M_1, M_2, …, M_{N_p} and breast contours C_1, C_2, …, C_{N_p}.

(3) $C_{1,\text{ext,up}} = C_1$.

(4) for $i = 2,3, \ldots N_{\text{p}}$

$C_{i,\text{ext,up}} = \text{ExtUp}(C_i, C_{i-1,\text{ext,up}})$

end

(5) $C_{N_{\text{p}},\text{ext}} = C_{N_p,\text{ext,up}}$.

(6) for $i = N_{\text{p}} - 1, N_{\text{p}} - 2, \ldots 1$

$C_{i,\text{ext}} = \text{ExtDown}(C_{i,\text{ext,up}}, C_{i+1,\text{ext,up}})$

end

(7) If the scan is RMLO view, extend $C_{1,\text{ext}}, C_{2,\text{ext}}, \ldots . C_{N_{\text{p}},\text{ext}}$ vertically at the bottom till the

bottom of the extended detector. If the scan is LMLO view, extend $C_{1,\text{ext}}, C_{2,\text{ext}}, \ldots . C_{N_\text{p},\text{ext}}$ vertical at the top till the top of the extended detector.

(8) $C_{1,\text{ext}}, C_{2,\text{ext}}, \ldots . C_{N_\text{p},\text{ext}}$ is the final set of extended contours.

After obtaining the extended breast boundary contours, we need to fill in values in the extended region. We expect the filled values inside the extended breast mask to have a smooth transition at the boundaries of the detector FOV. To achieve this, we implemented a diffusion algorithm similar to Lu et al. [67]. Given an image $\mathbf{y}$ and an ROI S, the projection operator $\mathrm{P}_\mathbf{S}$ is defined as:

$$\mathrm{P}_\mathbf{S}\mathbf{y} = \begin{cases} \mathbf{y} & \text{inside the ROI S} \\ 0 & \text{outside the ROI S} \end{cases} \tag{5.10}$$

Let F denote a 2D low-pass filtering operator. The ROI S is selected to be the extended regions. The diffusion is done with the following iterations:

$$\mathbf{y}_t = (\mathrm{I} - \mathrm{P_S})\mathbf{y}_{t-1} + \mathrm{P_S}(\mathrm{F}\mathbf{y}_{t-1}) \tag{5.11}$$

where *t* is the iteration index and I is the identity operator. The entire diffusion operation can be written as:

$$\mathbf{y}_\text{diffuse} = \mathrm{C_S}(\mathbf{y}; \mathrm{T}, \mathrm{F}, \mathbf{y}_0) \tag{5.12}$$

where T denotes the total number of iterations, F denotes the filtering operator and $\mathbf{y}_0$ denotes the initial condition of the diffusion.

The choice of initial condition $\mathbf{y}_0$ is crucial for getting a smooth transition at the detector boundaries. Figure 5.9 shows the initialization of the diffusion for the RCC and RMLO views. For all three images, the extended regions are the part above the highest colored horizontal line and below the lowest colored horizontal line. The first few rows of the measured PV and the last few rows are referred to as the boundary bands, as shown in Figure 5.9. The part of the boundary band within the breast mask is marked with a pink outline. We take average of the values inside this area and use the average pixel values to fill in the extended breast mask nearby. The average pixel values of the boundary bands outside the breast mask are used to fill in the extended region outside the extended breast mask. In other words, the top boundary band is used to fill in the top extended region and the bottom boundary band is used to fill in the bottom extended region. Therefore if the PV is truncated on both sides such that there are two extended regions within the extended breast mask, the values to fill in the top and bottom regions of the extended breast mask

can be different, as shown in Figure 5.9(c). After filling in the values, we have the initial condition for the diffusion in Figure 5.9.

As mentioned above, the purpose of the diffusion is to create a smooth transition at the detector boundaries. A long rectangular kernel along the vertical direction can serve the purpose. We empirically choose a uniform rectangular kernel of size 7×61 pixels ($0.7\text{mm} \times 6.1\text{mm}$), 400 iterations for the diffusion, and a width of 20 for the boundary bands. With these parameters, the results after diffusion are shown in Figure 5.10.

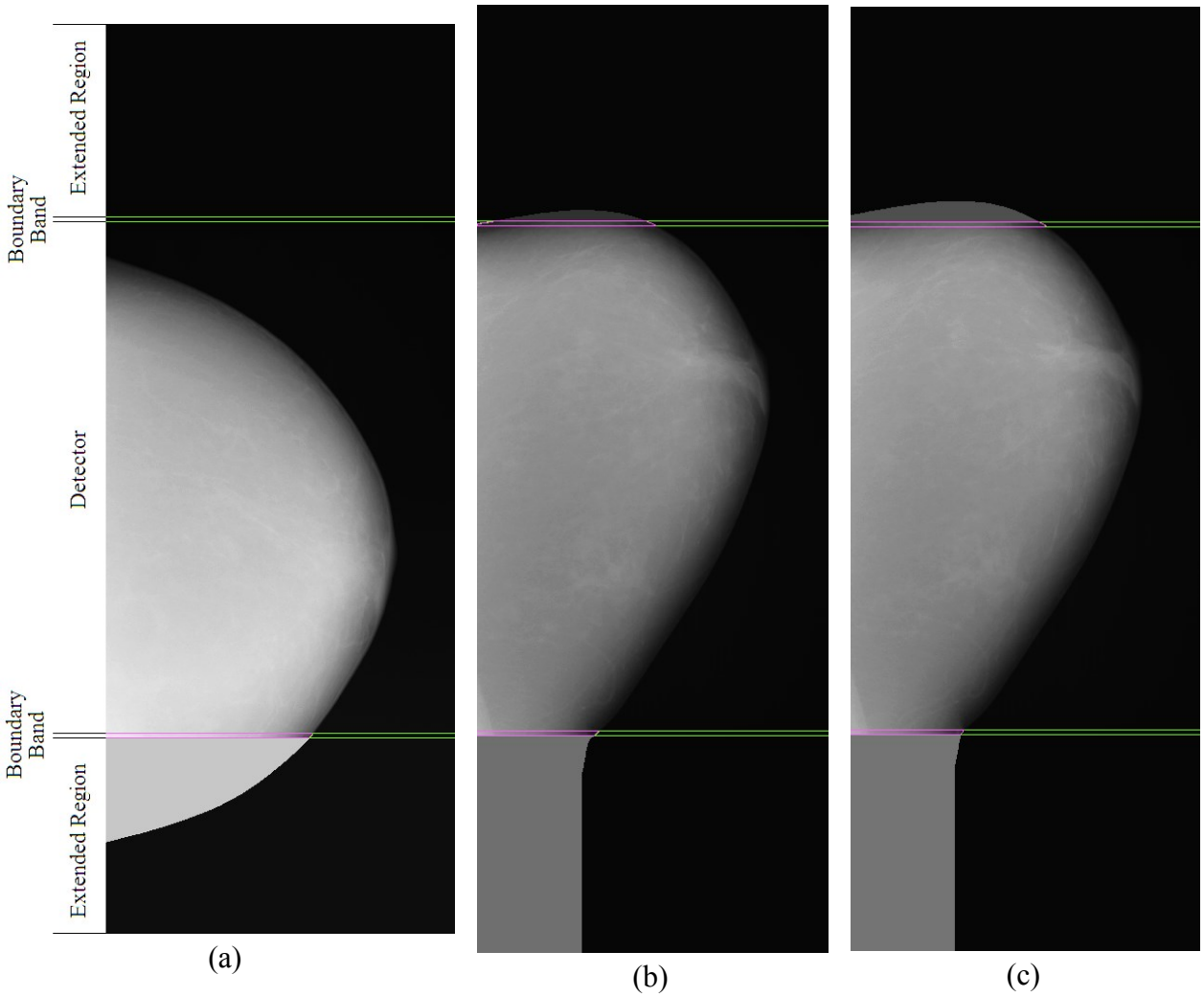

Figure 5.9. Initial condition of the diffusion for (a) RCC view, projection angle = -30°. This is the PV corresponding to contour #1 in Figure 5.5(a); (b) RMLO view, projection angle = -30°, corresponding to contour #1 in Figure 5.5(b); (c) RMLO view, projection angle = 15°, corresponding to contour #16 in Figure 5.5(b). The images are shown with the same scaling so the boundary bands are at the same vertical locations. The sizes of extended area are different for the RCC view and the RMLO view.

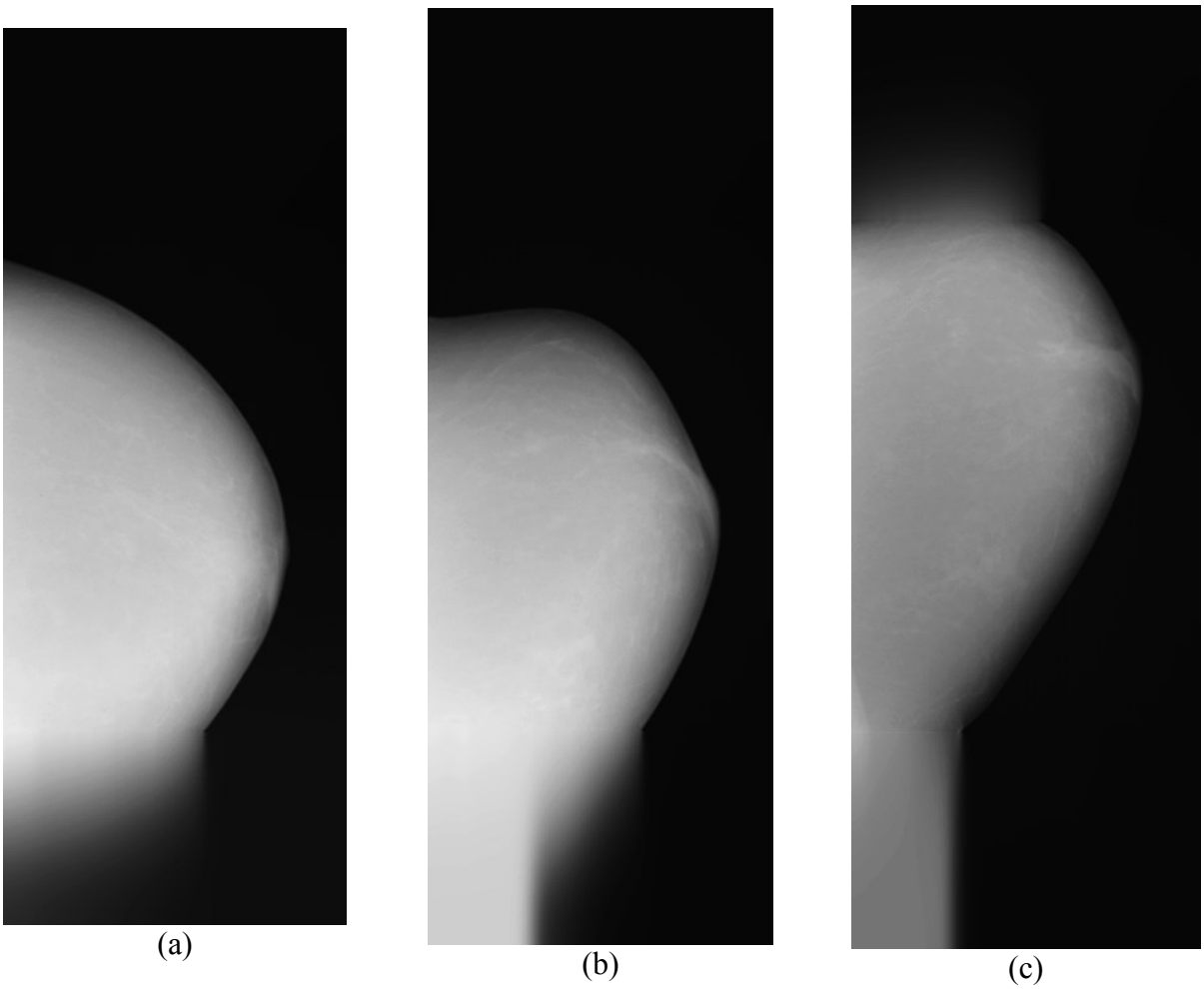

(a) (b) (c)

Figure 5.10. Diffusion results for (a) RCC view, projection angle = -30^{o}. This is the PV corresponding to contour #1 in Figure 5.5(a); (b) RMLO view, projection angle = -30^{o}, corresponding to contour #1 in Figure 5.5(b); (c) RMLO view, projection angle = 15^{o}, corresponding to contour #16 in Figure 5.5(b).

Figure 5.10 shows that the transition is smooth near the detector boundaries. As a final step, we set the values outside the extended breast masks to be the average pixel values in the region of the boundary bands between the green lines. Figure 5.11 shows the final PV extrapolation results.

As can be seen in Figure 5.11, the extrapolated PVs have smooth extended breast boundaries and smooth transition near the detector boundaries. They also have a trend that the pixel values are decreasing near the extended boundaries, which is desired as shown in Figure 5.3. The final extrapolated PVs can be used in DBT reconstruction as if they were originally measured with a larger detector. The reconstructed images will be shown and analyzed in Section V.4.

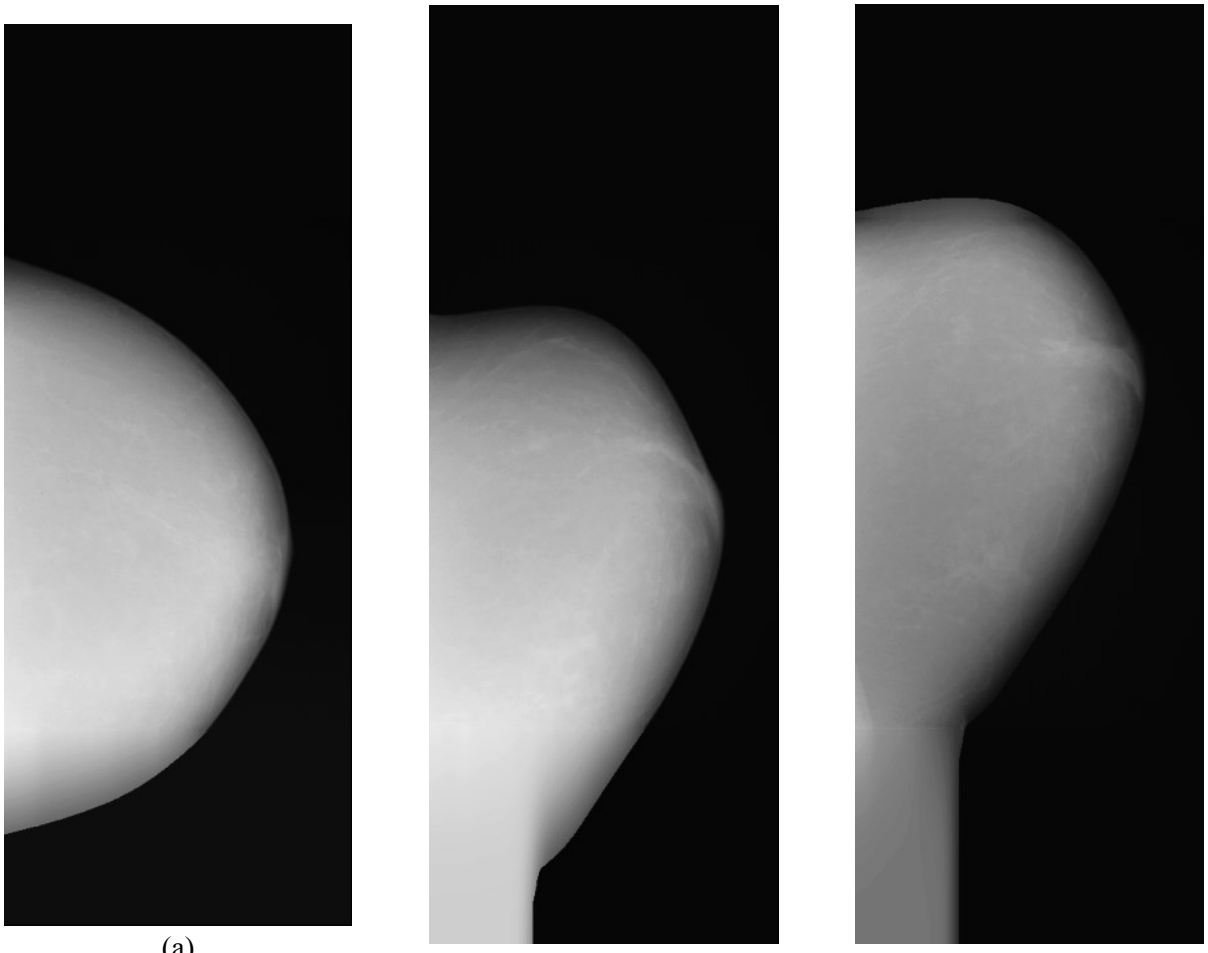

(a) (b) (c)

Figure 5.11. Final PV extrapolation results for (a) RCC view, projection angle = -30^{o}. This is the PV corresponding to contour #1 in Figure 5.5(a); (b) RMLO view, projection angle = -30^{o}, corresponding to contour #1 in Figure 5.5(b); (c) RMLO view, projection angle = 15^{o}, corresponding to contour #16 in Figure 5.5(b).

V.3.2 TPA removal with pre-reconstruction-based PV extrapolation

For this method, we use a pre-reconstructed volume to extrapolate the PVs. The implementation of this method is much less complicated than the contour-extension-diffusion method. The idea of this method is that we first obtain a reconstructed volume without TPA, then we re-project this volume to extrapolate the PVs. This volume is called the pre-reconstructed volume or the pre-reconstructed image and therefore this method is called the pre-reconstruction-based PV extrapolation method. The method is comparable to the method by Kinahan et al. [125], where the reconstructed image from the first FBP is re-projected onto the regions of missing projection data before a second FBP is done. We first introduce a simple and efficient pre-

reconstruction algorithm. Then we introduce the algorithm for generating the extrapolated PVs with the pre-reconstructed volume.

V.3.2.1 Pre-reconstruction with SART

Empirically, if only one or two SART iterations are used with TPA removal, TPA will be more obvious on one side than the other side, as shown in Figure 2.5. The same observation was reported by Lu et al. [67]. This can be explained by the sequential updates in SART. On the side of reconstructed volume where the PV is moving forward, the step artifacts are updated by the subsequent PVs, whereas on the side where the PV is leaving behind, the artifacts will keep their values until the next iteration. SART tends to enhance edges during each update. The TPA in the forward direction of the reconstruction is therefore stronger than those in the other direction. If we access all the PVs in the reverse order, then the TPA will be more obvious on the other side.

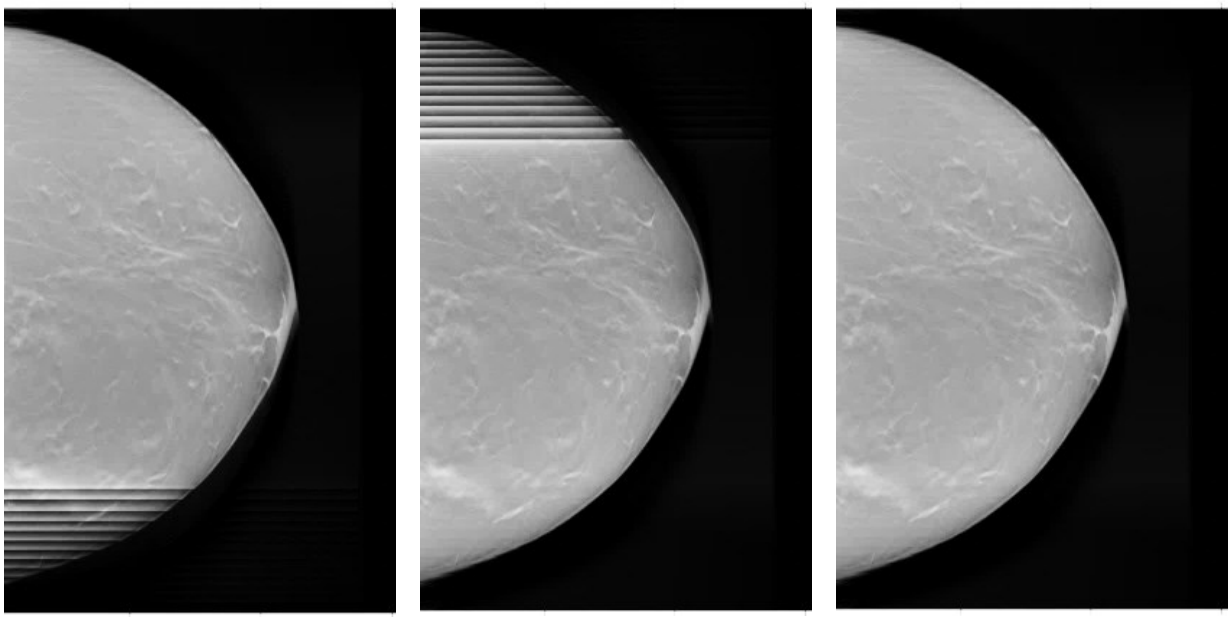

(a) (b) (c)

Figure 5.12. One slice ($z = -45.5\text{mm}$) of the forward-order, reverse-order and merged reconstruction slices for RCC view with one SART iteration (a) The forward-order reconstruction; (b) The reverse-order reconstruction; (c) The merged reconstruction by taking the upper part of the forward-order reconstruction and the lower part of the reverse-order reconstruction.

We take advantage of this property of SART to generate a pre-reconstructed volume for PV extrapolation. In SART, all PVs are accessed in successive order. We refer to the reconstructed

volume with the PV access order from the negative projection angles to positive projection angles as the forward-order reconstruction. The reconstructed volume with the reversed PV access order is referred to as the reverse-order reconstruction. Figure 5.12 (a) and (b) show a forward-order and a reverse-order reconstruction slice at the same depth after one SART iteration for the RCC view. This is the same RCC view as the RCC view used in Figure 5.5 to Figure 5.11. The TPA is hardly noticeable on the top part of the forward-order reconstruction and the bottom part of the reverse-order reconstruction. As a result, we can simply take the upper half of the forward-order reconstruction and the lower half of the reverse-order reconstruction slice by slice to create a merged volume, as shown in Figure 5.12(c). Some minor ripples can still be seen in Figure 5.12(c). But such a reconstructed image is good enough as a pre-reconstruction for PV extrapolation.

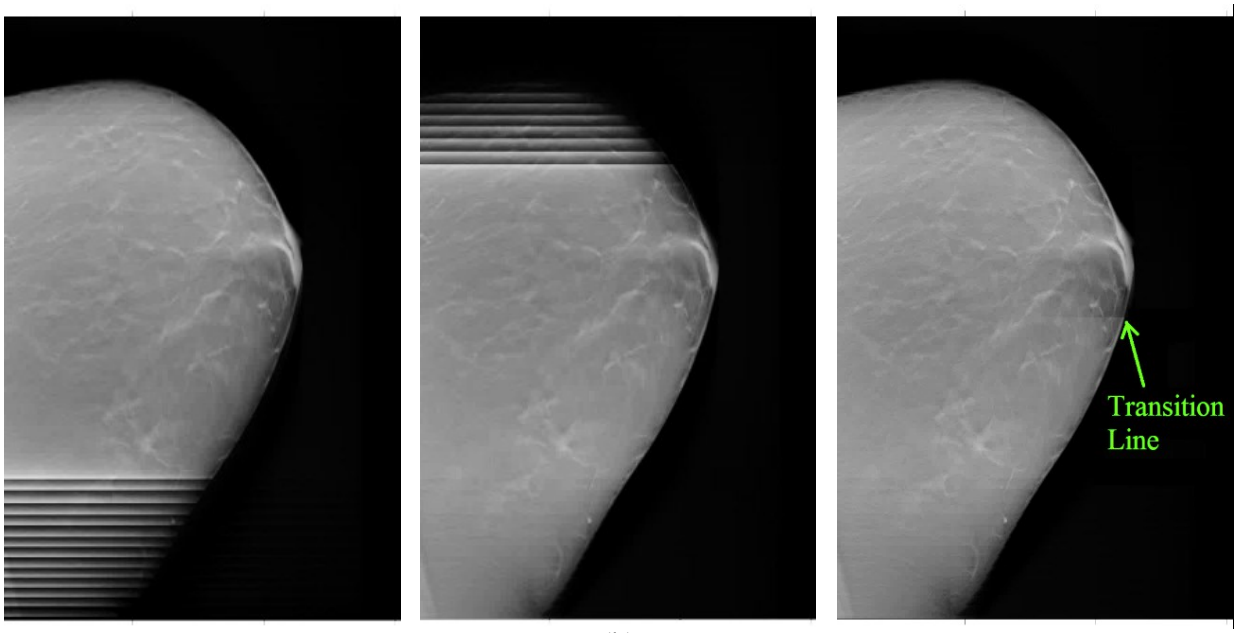

(a) (b) (c)

Figure 5.13. One slice (z = -54.5mm) of the forward-order, reverse-order and merged reconstruction slices for RMLO view with one SART iteration (a) The forward-order reconstruction; (b) The reverse-order reconstruction; (c) The merged reconstruction by taking the upper part of the forward-order reconstruction and the lower part of the reverse-order reconstruction.

Figure 5.13 shows the pre-reconstructed volume for the RMLO view (the same as the MLO view used in Figure 5.5 to Figure 5.11). Similar to the RCC view, after merging the forward and backward reconstructions, we can obtain a reconstructed volume with very minor artifacts.

Different from the RCC view, a transition line as marked in Figure 5.13(c) can be observed for at y = 0 (green arrow in Figure 5.13(c)). This transition line is commonly observed for the merged reconstruction of many cases but it will not be projected into the extrapolated regions of the PVs as shown in the next section. It therefore does not cause any problems when we use the pre-reconstruction to extrapolate the truncated PVs.

V.3.2.2 Extrapolating the PVs with the pre-reconstructed volume

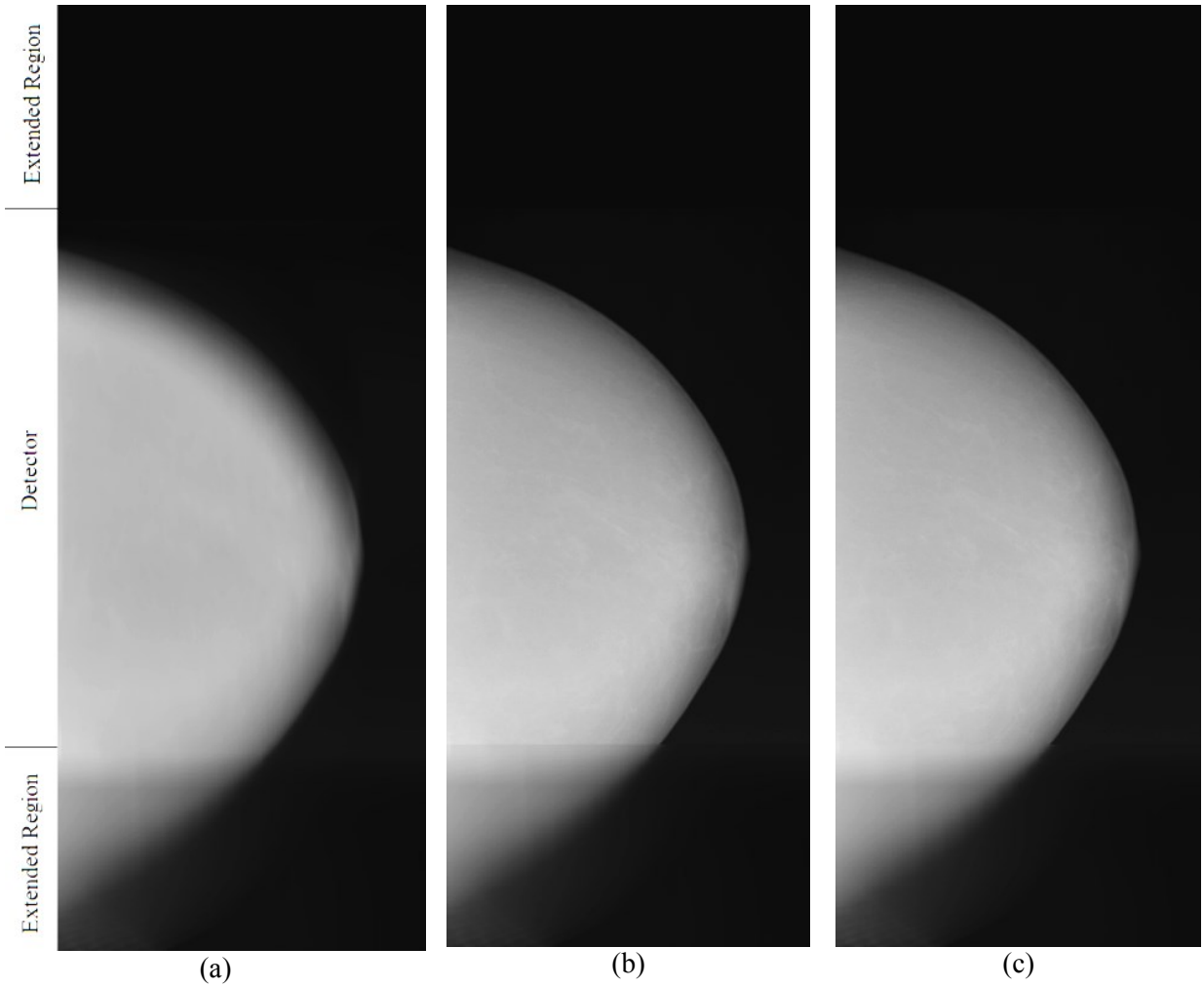

Figure 5.14. The procedure of generating extrapolated PVs from the pre-reconstructed volume. The detector region and extended region are marked on the image in (a). These marks also apply to the images in (b) and (c). (a) Projection of the pre-reconstructed volume; (b) The PV after replacing the detector region with the measured PV; (c) The final extrapolated PV after scaling the values in the extended regions.

After obtaining the pre-reconstructed DBT volume, we use it to extend the PVs. The procedure is shown in Figure 5.14. We first generate the forward projections of the pre-reconstructed volume for the entire extended detector, as shown in Figure 5.14(a). When generating the projections, the projection compensation multiplier in Section II.5 is used. As shown in Figure 5.14(a), the projection of the pre-reconstructed volume is very blurry, because of the low in-depth spatial resolution of DBT reconstruction in nature. This is in fact exactly what we need because we do not want the extrapolated PVs to contribute texture to the reconstructed volume. After computing the forward projection, we replace the detector region with the measured PV. The result is shown in Figure 5.14(b). The intensities of the two regions often do not match during this step, resulting in an obvious transition line. This transition line can cause step artifacts during the reconstruction and thus needs to be removed. We accomplish this by scaling the extrapolated region with a constant, as described below. The result is shown in Figure 5.14(c).

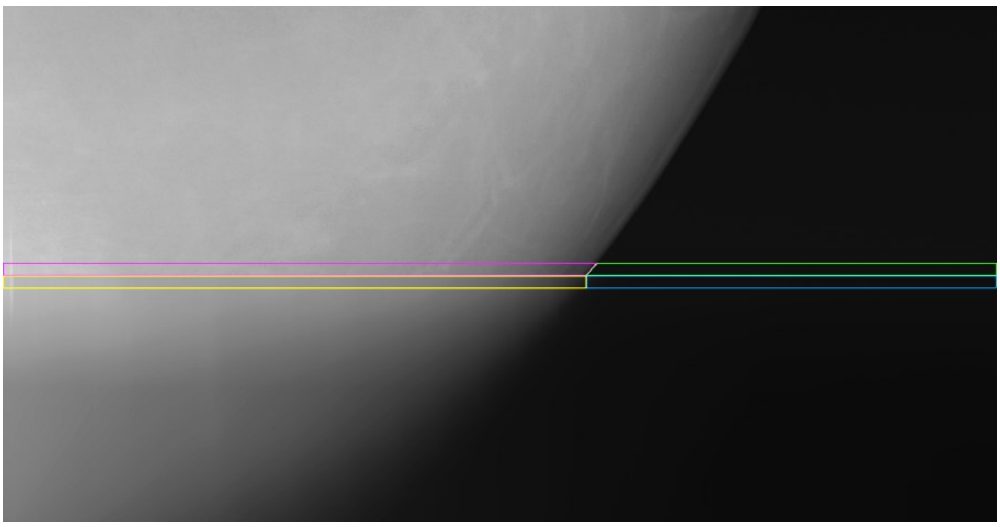

Figure 5.15. Scaling of the extrapolated PV with the information of breast boundary.

The scaling of the extrapolated region uses the same boundary bands as shown in Figure 5.9. Besides the boundary band, we need another band inside the extended region. Figure 5.15 shows the enlarged lower part of Figure 5.14(b). The yellow band in the extended region has the same width as the boundary band and the same length as the boundary band at the bottom of the breast mask. To reduce the discontinuity at the transition in Figure 5.14(b), we scale the extrapolated region such that the pink band and the yellow band have the same mean value. If the pink part of

the boundary band does not exist (i.e., the PV is not cut), we scale the extrapolated region such that the green and the blue bands have the same mean value. As shown in Figure 5.14(c). The transition line in Figure 5.14(b) is hardly visible after the scaling.

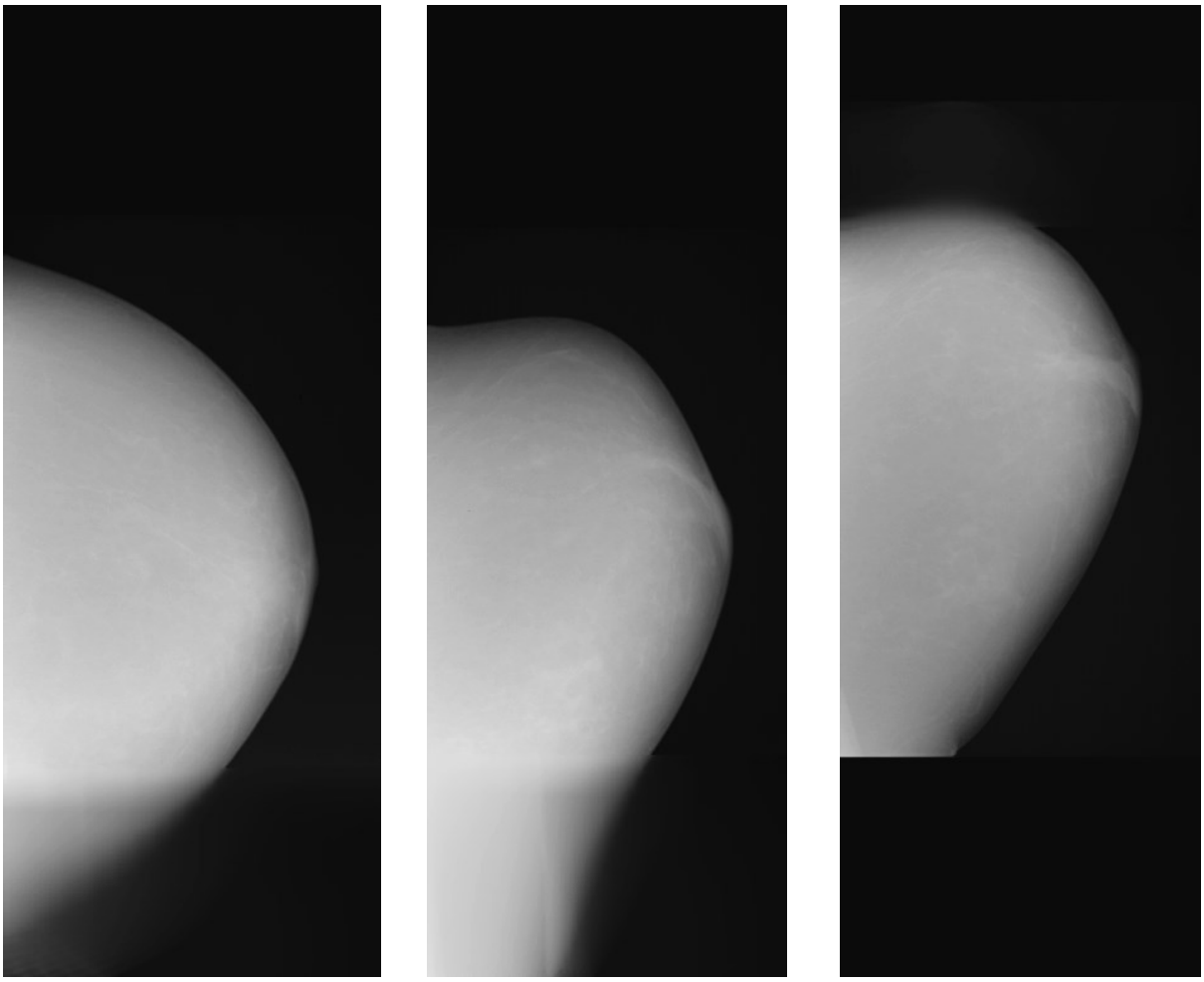

(a) (b) (c)

Figure 5.16. Final PV extrapolation results with pre-reconstruction for (a) RCC view, projection angle = -30^{o}. (b) RMLO view, projection angle = -30^{o}; (c) RMLO view, projection angle = 15^{o}. The order of the three images is the same as that in Figure 5.11.

To compare with the contour-extension-diffusion PV extrapolation method, Figure 5.16 shows the extrapolated PVs for the RMLO view. The three images in Figure 5.16 are compared with the three images in Figure 5.11. The most obvious difference is that Figure 5.16(c) is shorter on the bottom side, leaving a large blank region. As discussed in Section V.2.1, we can either extrapolate every PV up to the limits on both sides, or we can extrapolate every PV up to the required region of the corresponding projection angle. The contour-extension-diffusion PV

extrapolation method takes the first approach and the pre-reconstruction-based PV extrapolation method takes the second one. Comparing Figure 5.1 and Figure 2.2, the region we need to extrapolate the PVs is exactly the same as the region that we will get non-zero projection values in the forward projection. As a result, the region with positive projection values in Figure 5.16 (c) is exactly how much we need to extrapolate the PVs to force the TPA out of the VOI. The extra extrapolated region at the bottom of Figure 5.11(c) is not used in the reconstruction. For the same reason, most part of the extrapolated region with artificial-looking vertical boundary at the bottom of Figure 5.11(c) will not create artifact during the reconstruction.

Another major difference between Figure 5.11 and Figure 5.16 is that Figure 5.11 has much sharper boundaries in the extrapolated region. This is in fact an undesired feature since we do not want the extrapolated region of the PVs to have strong structure. We consider this to be a disadvantage of the diffusion-based method and will discuss this in Section V.4.2.

V.3.3 TPA removal by regularization

We also tried to use regularization to control TPA for DBT. Instead of extrapolating the PVs, this method aims to control TPA by compensating for the imaged volume in each update of the image, similar to the second category of TPA removal algorithms introduced in Section V.1.1. The idea of this method is similar to the work by Kunze et al. [113].

For DBT reconstruction, it is most important to have high reconstructed image quality. We cannot sacrifice image quality to control TPA. Any regularization method used to control TPA must be an appropriate method for DBT reconstruction. We have already introduced the SQS-DBCN algorithm in Chapter IV, a method that can enhance MCs and preserve texture in DBT reconstruction. In this study, we investigated the same algorithm for its effectiveness for controlling TPA.

When the SQS-DBCN algorithm is applied to DBT reconstruction, we usually perform 10 iterations with ordered subsets. However, it is possible that the required number of iterations for controlling TPA is more than that for practical DBT reconstruction. To alleviate this problem, one approach is to initialize the volume in a way that correctly reflects the general trend of the true volume. With a good initial condition, TPA will be weaker at the beginning, reducing the required number of iterations to control it. On the other hand, a good initial condition does not reduce the required number of iterations to achieve good image quality since the initial volume

may not contain enough details. The pre-reconstruction approach introduced in Section V.3.2.1 serves this purpose well. As a result, we will use the SQS-DBCN algorithm with its optimized parameters and the pre-reconstructed volume as the initial condition to study how TPA can be controlled.

V.4 Result and Discussion

V.4.1 Image reconstruction with three TPA removal methods

We first make a general comparison among the three TPA removal methods. Figure 5.17 and Figure 5.18 show the reconstructed images without TPA removal, with the three TPA removal methods we proposed and with Lu's TPA removal method as a reference point. The images reconstructed with SART (with or without TPA removal) used all 21 PVs with two iterations (Equation 2.11 in Section II.2). The SQS-DBCN reconstruction used $\delta = 0.002/mm$, $\beta = 70$ with 10 iterations, which have been demonstrated as the optimal parameters in Section IV.4.1. The SART reconstructions start with the same uniform initial condition. $\mathbf{f}^{(0)} = 0.05/mm$. The SQS-DBCN method used the pre-reconstructed volume as the initial condition. For the RCC view reconstruction (Figure 5.17), the thickness of the volume is 74mm. The slice shown is at z = -37.5mm, which is 36.5mm from the top plane of the imaged volume. For the RMLO view reconstruction (Figure 5.18), the imaged volume has a thickness of 83mm. The shown slice is at z = -41.5mm, 41.5mm from the top of the imaged volume. For diagnosis, the RCC and the RMLO views are usually flipped vertically after the reconstruction because of the clinical convention of reading mammograms from lateral to medial and from head to toe, respectively. For the current discussion, we do not flip them to be consistent with the previous images shown in this chapter (Figure 5.5 – Figure 5.16).

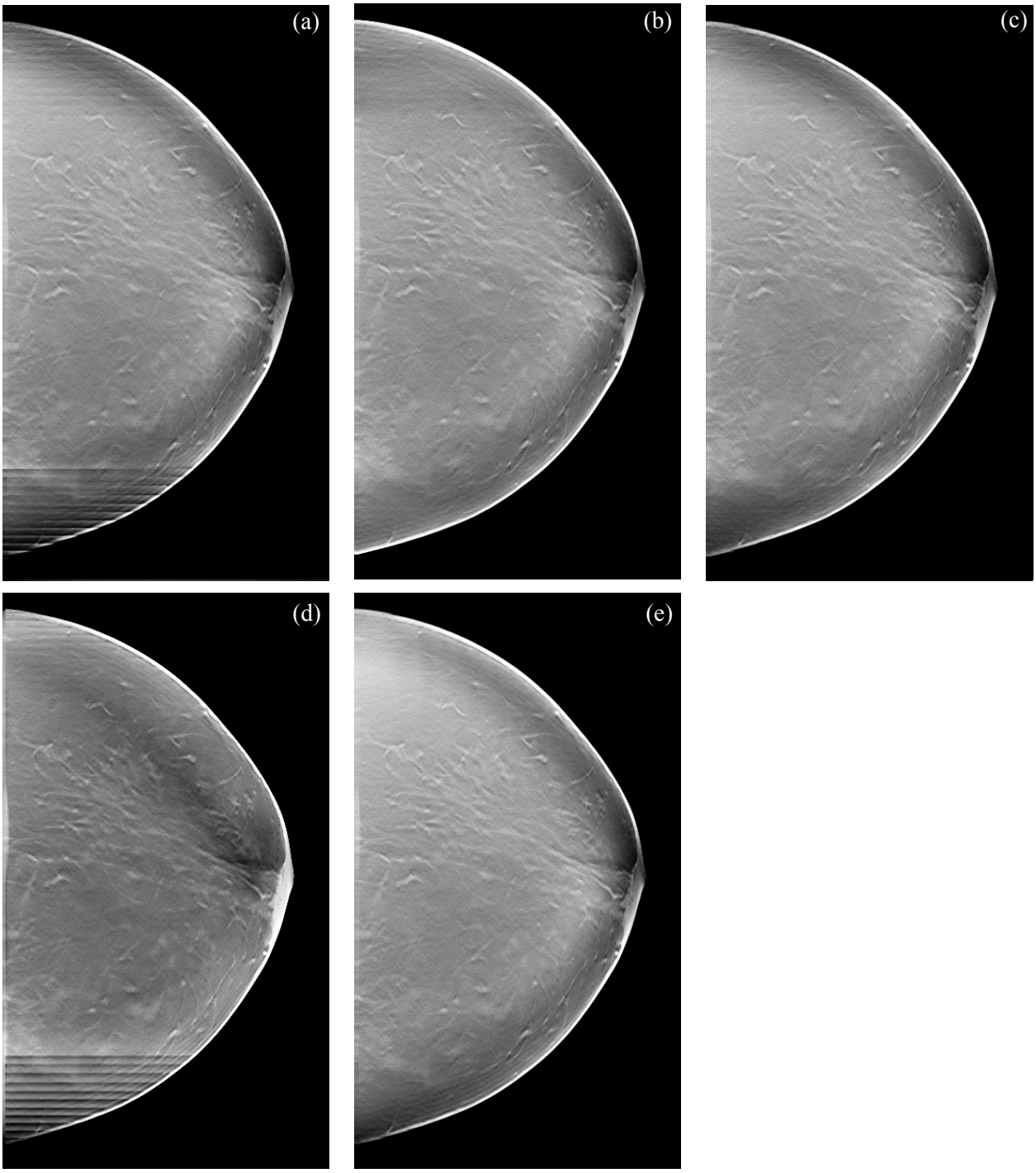

Figure 5.17. One slice at about the center of the imaged volume for the RCC view reconstructed with (a) SART at two iterations without TPA removal; (b) SART with TPA removal by contour-extension-diffusion PV extrapolation; (c) SART with TPA removal by pre-reconstruction-based PV extrapolation; (d) the SQS-DBCN method at 10 iterations. (e) SART with Lu's TPA removal method. All five images are displayed with the same gray scale and the same window level and width settings.

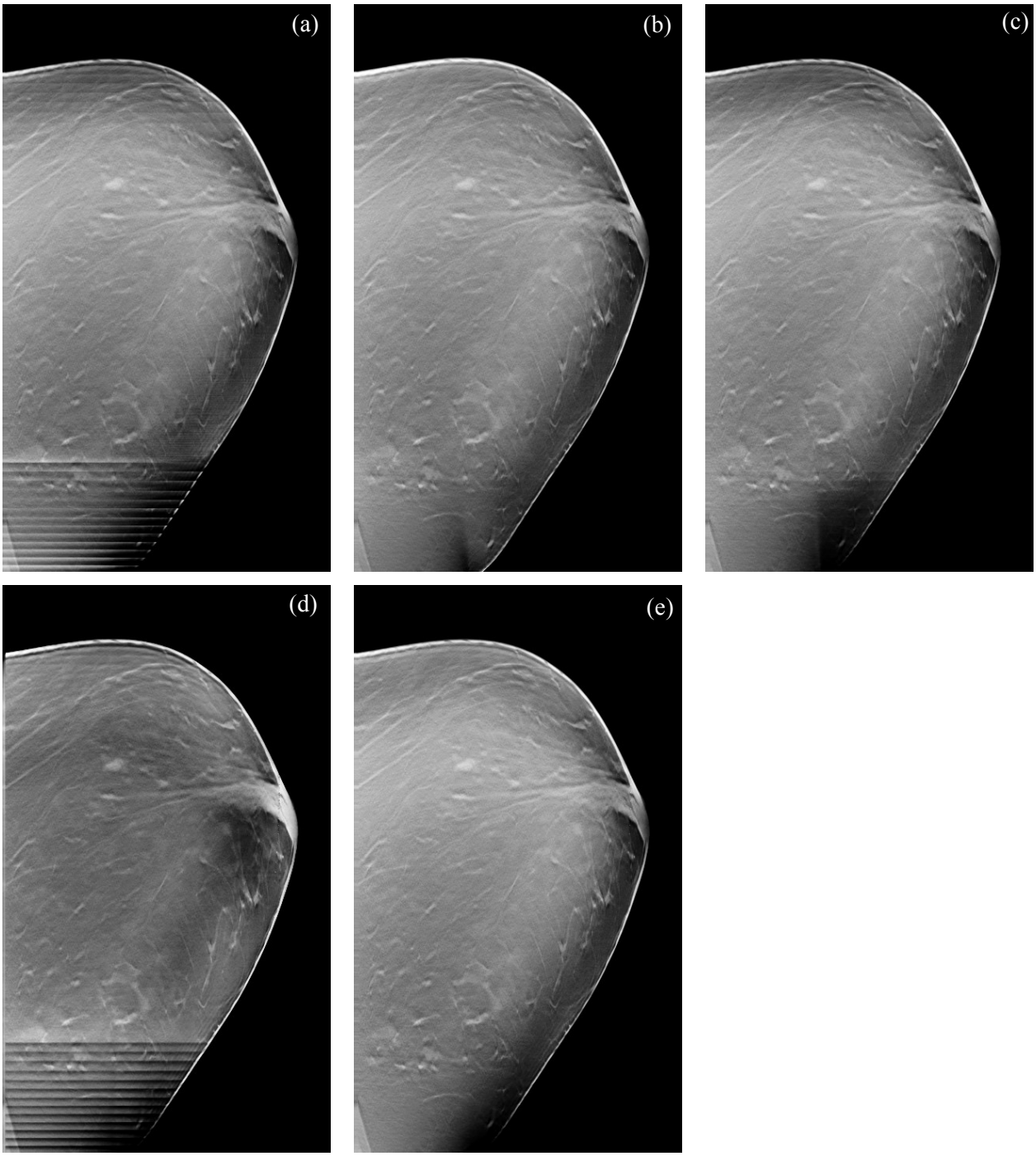

Figure 5.18. One slice at about the center of the imaged volume for the RMLO view reconstructed with (a) SART at two iterations without TPA removal; (b) SART with TPA removal by contour-extension-diffusion PV extrapolation; (c) SART with TPA removal by pre-reconstruction-based PV extrapolation; (d) the SQS-DBCN method at 10 iterations. (e) SART with Lu's TPA removal method. All five images are displayed with the same gray scale and the same window level and width settings.

For both the RCC and the RMLO view, without a TPA removal algorithm the reconstructed slices appear to have strong TPA, especially at the bottom. If more iterations are performed, the TPA at both the top and bottom will become more obvious. The level of TPA at the top will be more similar to that at the bottom with more iterations. The same observation has been reported by Lu et al. [67], where the same SART reconstruction was used. On the other hand, if either PV extrapolation-based TPA removal method is used, TPA will be mostly removed and is hardly visible in Figure 5.17(b)(c) and Figure 5.18(b)(c). Upon close inspection, Figure 5.17(b) and (c) have weak ripples at the top, but these ripples are much weaker than the sharp steps in Figure 5.17(a). Even if three more SART iterations are done, these ripples will not amplify to become as obvious as the TPA in Figure 5.17(a). Figure 5.17(e) and Figure 5.18(e) shows that as an established and reliable TPA removal algorithm for SART, Lu's method provides superior TPA removal results. For the RCC view, Lu's method does not generate ripples at the top of the slice as the PV extrapolation methods. For the RMLO view, Lu's method provides the most natural transition at the bottom of the slice near the breast boundary. Generally speaking, the TPA removal results by our new PV extrapolation methods are comparable with Lu's method but need further improvement to achieve the same image quality.

The SQS-DBCN method, on the other hand, does not control TPA effectively. We can observe very strong TPA in Figure 5.17(d) and Figure 5.18(d), although the transition lines have been blurred. The TPA is in fact stronger than that in Figure 5.17(a) and Figure 5.18(a), since many more iterations are done with the SQS-DBCN method.

It is difficult to develop a quantitative figure of merit for TPA. As a result, we applied the two PV extrapolation-based TPA removal methods to 67 human-subject DBT volumes (34 CC views and 33 MLO views). For image slices that are at least 1cm (ten slices) away from top of the volume, TPA was eliminated or mostly reduced such that only weak ripples are left, similar to Figure 5.17(b) and Figure 5.17(c). For the first ten reconstructed slices, difference can be observed between the contour-extension-diffusion method and the pre-reconstruction-based method. The difference will be discussed in the Section V.4.2. We did not apply the SQS-DBCN method to most of the human-subject DBT cases because it did not remove TPA effectively for a few cases that we tested, as represented by Figure 5.17(d) and Figure 5.18(d).

V.4.2 Comparison between the contour-extension-diffusion and the pre-reconstruction-based PV extrapolation methods

As discussed in the previous section, both the contour-extension-diffusion and the pre-reconstruction-based methods generate high-quality extrapolated PVs to remove TPA for DBT reconstruction. However, there are differences between the two methods and the reconstructed images will not be the same. Compared with the contour-extension-diffusion method, the reconstructed slice with the pre-reconstruction-based method is darker at the top and the bottom. This can be observed in Figure 5.17 and Figure 5.18, especially when the bottom parts of Figure 5.18(b) and Figure 5.18(c) are compared. This is not unexpected because the extended region of the PV images by the pre-reconstruction-based method (shown in Figure 5.16(a) and Figure 5.16(b)) is darker than that by the contour-extension-diffusion method (shown in Figure 5.11(a) and Figure 5.11(b)). This difference will not affect the diagnosis for breast cancer because the extrapolated part of the PVs is very blurry without any fine structures. For the top and bottom parts of the reconstructed slices, the trend of the extrapolated areas of the PVs, either being a little darker or brighter, may not add or remove any features that are clinically meaningful.

Similar to most studies on PV extrapolation for CT, our PV extrapolation methods try to recover lost information and are highly empirical. They can extrapolate PVs reasonably but not accurately. In fact, different PV extrapolation methods in CT also generate very different trends in the image volume affected by the extrapolated data. In addition, the voxel values of DBT are not accurate attenuation coefficients in principle, so that the general darker or brighter trend in an area is less likely to be interpreted as lower or higher attenuation of the tissue. As a result, based on the results shown in Figure 5.17 and Figure 5.18, we consider both methods to be comparable since they both serve our purpose to remove the sharp truncation artifacts.

On the other hand, for the first few slices near the top of the reconstructed volume, the contour-extension-diffusion method shows a major disadvantage. An example of a reconstructed slice at a depth of 4.5mm from the top of the imaged volume is shown in Figure 5.19. Comparing Figure 5.19(a) to Figure 5.19(c), the pre-reconstruction-based method removed TPA without changing the shape of the reconstructed volume. The contour-extension-diffusion method, however, shrinks the reconstructed breast while removing TPA. Close-up views of the region marked by the green box on the three images are shown in Figure 5.20. It can be seen that a section of the blood vessel is cut with the contour-extension-diffusion method. The same section

of blood vessel is well reserved with the pre-reconstruction-based method. Such a difference can potentially change the diagnosis results if the patient has abnormal tissue in this area.

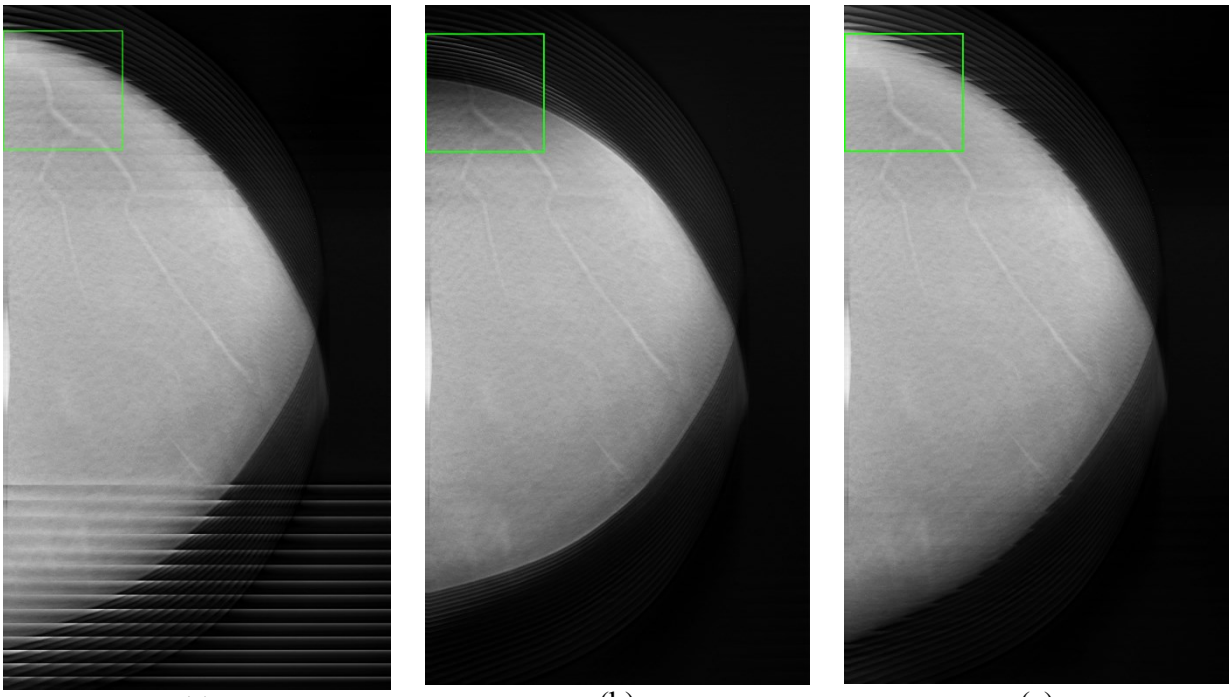

(a) (b) (c)

Figure 5.19. The slice at z = -69.5mm (4.5mm from the top of the imaged volume) for the RCC view reconstructed with (a) SART without TPA removal; (b) SART with TPA removal by the contour-extension-diffusion PV extrapolation method; (c) SART with TPA removal based on the pre-reconstruction-based PV extrapolation method. All three images are displayed with the same gray scale and the same window level and width settings.

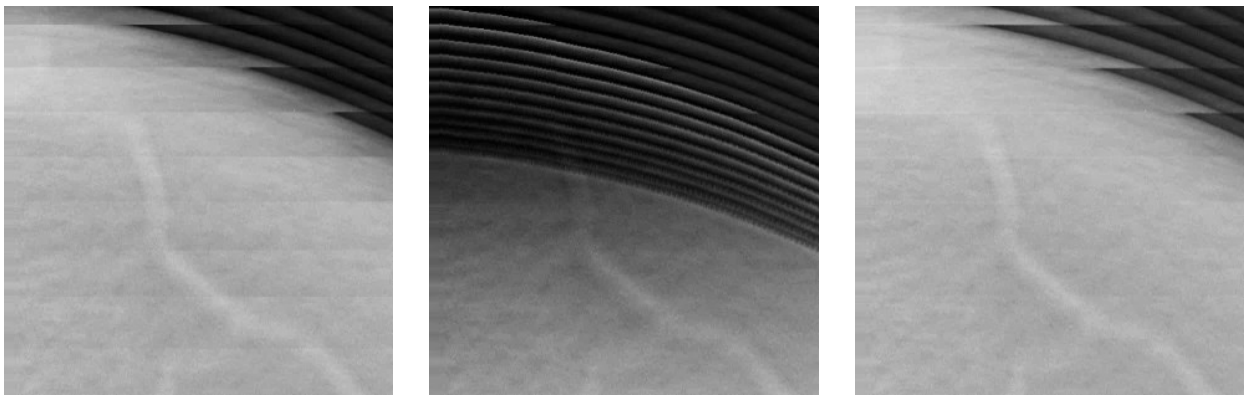

(a) (b) (c)

Figure 5.20. Close-up views of the region marked by the green box on the images in Figure 5.19 for (a) SART without TPA removal; (b) SART with TPA removal by the contour-extension-diffusion PV extrapolation method; (c) SART with TPA removal by the pre-reconstruction-based PV extrapolation method. All three images are displayed with the same gray scale and the same window level and width settings.

The problem with the contour-extension-diffusion method is caused by the underestimation of the shifted distance required to recover the truncated region between the consecutive PVs. As can be seen in Figure 5.20(a) and Figure 5.20(c), the consecutive PVs are not smoothly connected due to the large and discrete angular increments used in the DBT scan. Because of the somewhat round but unknown shape of the breast boundary in the depth direction, we cannot calculate accurately the shift distance required to extend the next projection. The criterion of smooth connection that we use to determine the shift distance inevitably leads to underestimation. The accumulation of the underestimated extension in the PVs causes a contraction of the reconstructed volume in the regions where TPA is being removed by using the under-extended PVs.

There are several possible approaches improve the contour-extension-diffusion method. First, we can develop better methods to estimate the required shift distance. This can potentially be done by using the estimated shape of the 3D breast surface [126]. Second, while keeping the current breast contour extension algorithm, we can apply an additional step to stretch the extended breast contours vertically. Third, we can keep the breast contour extension algorithm but use the extended breast masks in a less definite way. After the diffusion step, instead of eliminating the diffused values outside the extended breast contours, we can use the extended contours to create a slowly changing trend from the inside of the extended contours to the outside. We are investigating the effectiveness of these approaches. For most part of DBT reconstruction, the contour-extension-diffusion method still improves the reconstruction quality significantly by removing TPA.

V.4.3 Discussion regarding the convergence theory of the PV-extrapolation based TPA removal algorithms.

With the PV-extrapolation methods developed in this chapter, we can treat the extrapolated PVs as if they were originally measured by the detector and achieve monotonic decrease of a cost function with a data-fit term based on the extrapolated PVs. However, when we use the extrapolated PVs in image reconstruction, the importance of the convergence of the cost function is uncertain due to the lack of statistical model for the estimated data in the extrapolated regions, as shown in the derivation below.

Let $\mathbf{y}_{\text{real}}$ and $\mathbf{y}_{\text{ext}}$ denote the measured data and estimated data of the extrapolated PVs. Let $\mathbf{A}_{\text{real}}$ denote the system matrix for the FOV of the detector and $\mathbf{A}_{\text{ext}}$ denote the system matrix for the extrapolated regions. If we treat the entire extrapolated PVs as measured PVs and consider a penalized weighted least-squares optimization problem, the cost function $\Psi(\mathbf{f})$ can be written as

$$\Psi(\mathbf{f}) = \|\mathbf{A}_{\text{real}}\mathbf{f} - \mathbf{y}_{\text{real}}\|^2_{\mathbf{D}_{\text{real}}} + \|\mathbf{A}_{\text{ext}}\mathbf{f} - \mathbf{y}_{\text{ext}}\|^2_{\mathbf{D}_{\text{ext}}} + R(\mathbf{f}) \tag{5.13}$$

where $R(\mathbf{f})$ is the regularization term.

Minimizing $\|\mathbf{A}_{\text{real}}\mathbf{f} - \mathbf{y}_{\text{real}}\|^2_{\mathbf{D}_{\text{real}}}$ is equivalent to maximizing the probability of the realization of the random noise following a multivariate Gaussian distribution. The form of $\mathbf{D}_{\text{real}}$ can be decided by the statistical model of the noise. The elements of $\mathbf{D}_{\text{real}}$ can be estimated from the measured data. The statistical meaning of minimizing $\|\mathbf{A}_{\text{real}}\mathbf{f} - \mathbf{y}_{\text{real}}\|^2_{\mathbf{D}_{\text{real}}}$ is clear in statistical image reconstruction. However, the meaning of the second data-fit term $\|\mathbf{A}_{\text{ext}}\mathbf{f} - \mathbf{y}_{\text{ext}}\|^2_{\mathbf{D}_{\text{ext}}}$ in Equation 5.13 is doubtful. The noise model of $\mathbf{y}_{\text{ext}}$ depends on the PV extrapolation method and this model might not even exist. In fact, $\mathbf{y}_{\text{ext}}$ can appear to be nearly noiseless such as in our contour-extension-diffusion PV extrapolation algorithm, where the extrapolated regions of the PVs are slowly changing without local fluctuations. The form and the elements of $\mathbf{D}_{\text{ext}}$ are also unclear for the same reason. As a result, the importance of the convergence of $\Psi(\mathbf{f})$ in Equation 5.13 is doubtful. It remains an open question to decide a proper form of data-fit term for the extrapolated data when we use extrapolated PVs in statistical DBT reconstruction.

V.4.4 Discussion regarding the regularization-based TPA removal

The regularization-based TPA removal investigated here provided poor results, as shown in Section V.4.1. This section briefly discusses the reason and possible ways to improve the regularization-based TPA removal.

One observation in Figure 5.17 and Figure 5.18 is that the regularization method actually enhances rather than reduces the TPA. One of the reasons is that ten iterations are used in the SQS-DBCN method instead of two iterations as used in the SART method. Figure 5.21 compares SART without TPA removal and the SQS-DBCN method with two or ten iterations. It can be observed that with two SQS-DBCN iterations (Figure 5.21(b)), the TPA is comparable to that in Figure 5.21(a). The TPA becomes much more obvious using the SQS-DBCN method with ten iterations (Figure 5.21(c)).

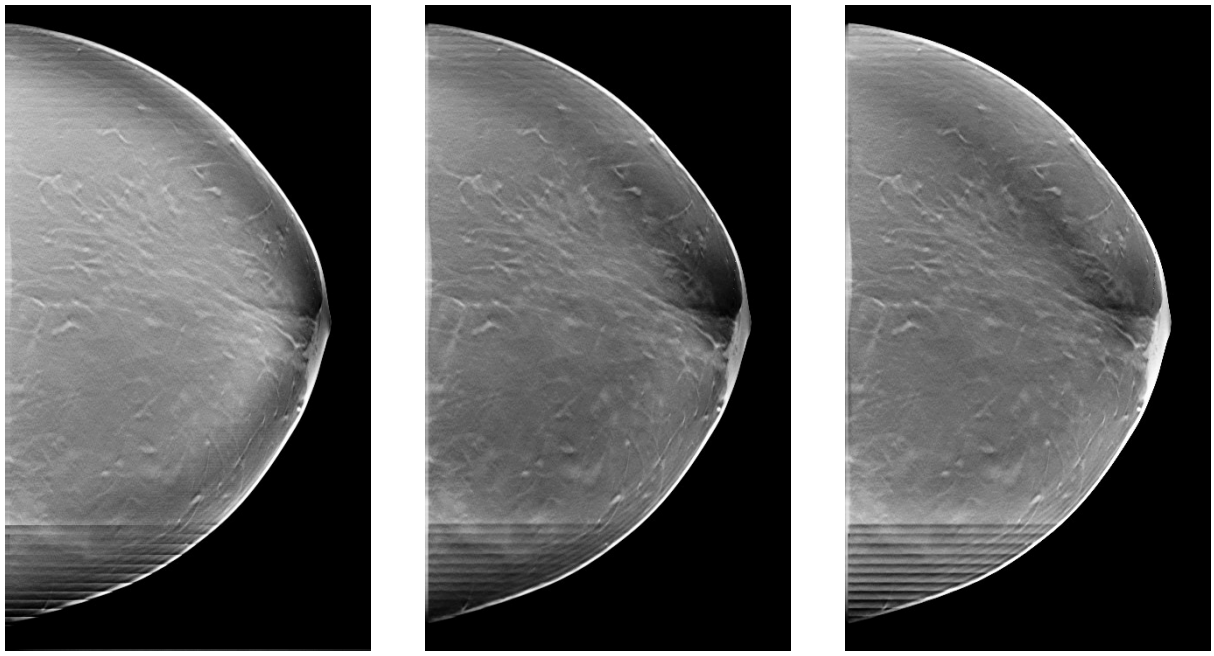

(a) (b) (c)

Figure 5.21. One slice at about the center of the imaged volume for the RMLO view reconstructed with (a) SART without TPA removal and with 2 iterations; (b) the SQS-DBCN method with 2 iterations; (c) the SQS-DBCN method with 10 iterations. All three images are displayed with the same gray scale and the same window level and width settings.

One possible reason for the SQS-DBCN method not to work well for removing TPA is the inaccuracy of the projection data. As described in Section V.3.3, we used the SART pre-reconstruction result to initialize the SQS-DBCN reconstruction. Ideally with a good initial condition, TPA will not be obvious if all PV images after log-transform are accurate. In this situation, the discontinuities created by the back-projection step of the reconstruction algorithm are minimal. In practice, we used a constant to perform log-transform on all PVs (Equation 4.4), which did not consider the non-uniformity of the x-ray radiation due to the heel effect of the anode or different incident angles of different rays. This neglected effect is especially strong near the detector boundary. As a result, the PVs after log transform used in reconstruction actually do not match each other on the general trend of the reconstructed volume. Although a good initial condition obtained from the pre-reconstruction is used, the back-projection step of the SQS-DBCN algorithm still creates discontinuities at the boundaries of the cone connecting the FOV of the detector to the current location of the source. The regularization of the SQS-DBCN method is not strong enough to smooth the discontinuities before they are strengthened again in the next iterations.

Another possible reason for the SQS-DBCN method not to work is the lack of convergence theory of our implementation. Our SQS-DBCN method uses ordered subsets, therefore the convergence of the cost function is not guaranteed. It is unclear whether a convergent regularized algorithm could eliminate or reduce TPA without PV extrapolation. Further investigations are required to confirm the reason of the poor performance of the SQS-DBCN method in TPA removal.

There are several approaches that could potentially improve the effectiveness of the SQS-DBCN method in controlling TPA. First, we can alleviate the inaccuracy of the log-transformed PVs by collecting the x-ray PVs at each projection angle without any imaged object between the plates. This way we can use these air scans in the log-transform to improve the accuracy of the PVs used in reconstruction. Since the air scans might not match the breast scans perfectly, mismatch among PVs might still exist but such weak artifacts can be controlled by the SQS-DBCN method. Second, we can use different regularization parameter β for different regions. By increasing the value of β in narrow bands where TPA will appear, TPA could be more effectively controlled. The problem this approach brings is the loss of contrast of breast tissue in the same area. Other solutions include developing better regularization methods that can control TPA while still generating high-quality reconstructed breast images in which subtle target signals such as MCs and masses are enhanced without distortion. The latter requirements make these "potential" solutions much more challenging in practice.

V.5 Conclusion

This chapter introduced our study on TPA removal for DBT reconstruction. A breast boundary detection algorithm is introduced. Then we introduced three TPA removal algorithms. Based on the analysis of the results, the contour-extension-diffusion algorithm, as it is currently implemented, removes the artifacts effectively while causing contraction in the reconstructed volume on the slices affected by TPA. The pre-reconstruction-based algorithm, however, effectively removes TPA without such problems. The investigated regularization-based algorithm was not effective due to several reasons. Further improvement in the contour-extension-diffusion and the regularization-based TPA removal algorithms is needed to make these methods practical.

CHAPTER VI.
Effect of Source Blur on DBT Reconstruction

VI.1 Introduction

In our SART or SQS-DBCN reconstructions in previous chapters, we assumed the x-ray source to be an ideal point source. In an actual mammography/DBT system, the focal spot of the x-ray tube has a finite size of around 0.3mm [44, 127, 128] that our previous reconstruction algorithms neglected. Until now, the U.S. Drug & Food Administration (FDA) has approved four breast imaging systems that can perform the tomosynthesis procedure. These systems are SenoClaire (or the new model Pristina) by GE Healthcare, Selenia Dimensions by Hologic, Mammomat Inspiration by Siemens and Aspire Cristalle by Fujifilm. The GE Pristina system operates in the step-and-shoot mode where the x-ray tube essentially stops at each angular location and exposes the projection image. The other three systems operate in a continuous-motion mode where the x-rays are generated within a short pulse at each angle while the gantry is continuously moving during the DBT procedure. While the continuous-motion mode can potentially reduce the total scan time and the motion of the breast, it introduces extra source blur along the direction of the motion of the source. This effect has been found to be an image-quality degrading factor in several studies [129-132]. The GE DBT system's step-and-shoot mode alleviates this problem. However, the time that the x-ray tube can be stationary is always limited. If the x-ray exposure time is longer than the time that the x-ray tube is stationary, it can still result in extra source blur although the amount of motion blur will be much less than the continuous-motion DBT systems [27, 131]. This chapter investigates the influence of the effect of source blur on DBT reconstruction.

Several studies can be found regarding the source blur (or more commonly called geometric unsharpness in x-ray imaging physics) in CT reconstruction. For fan-beam CT, Hofmann et al. studied the effect of modeling the source's ray profile [66, 133]. They used a simulated phantom

to estimate the critical size for the focal spot that affects the image reconstruction quality and concluded that for common fan-beam CT systems, the size of the focal spot can be neglected in image reconstruction. Tilley et al. studied the effect of modeling the source blur and detector blur for the flat-panel cone-beam CT (FP-CBCT) [94, 134]. Since the pixel size of the flat-panel detector is very small (~0.1mm), Tilley et al. demonstrated that modeling the source blur can significantly improve the reconstructed image quality. The reconstruction method proposed in their study considered the source blur to be shift-invariant, which greatly simplified the implementation of the effect in the system model. The DBT system also uses cone-beam x-ray and a flat-panel detector. But the geometry of DBT is very different from that of FP-CBCT. In DBT, since the imaged volume is close to the detector and the imaged object is much thinner than those in body CT, the magnification factor and its variation over the depth of the imaged volume are smaller than those in CBCT. We will analyze the source blur and its shift variance in Section VI.3.1 – VI.3.3. Since calculating the projection images with an accurate point spread function (PSF) of source blur is very complex in DBT, we use simulation with oversampled source to study the effect of the finite-sized focal spot on DBT reconstruction.

In this chapter, we first define parameters that describe the geometry of the finite-sized x-ray source. We choose our simulation parameters based on the range estimated from the three commercial DBT systems that use the continuous-motion data acquisition mode. Then we analytically calculate the source blur at different spatial locations over the detector FOV. Next, we introduce our work on using CatSim to simulate the effect of the finite-sized focal spot. Two phantoms with line pairs and BBs are configured and simulated with four sizes of the focal spot. We will discuss the details on the acceleration of the CatSim simulation, the configuration of the phantoms and the FOMs used to quantitatively compare the reconstructed images. In the Result section, we will show the contrast curves of different types of objects when different-sized sources are used to simulate the projections. These results will provide some useful information on constraints in designing DBT systems and under what conditions modeling the finite-sized x-ray source may improve the reconstructed image quality.

VI.2 Parameters of the finite-sized focal spot in DBT

VI.2.1 Definitions of the parameters

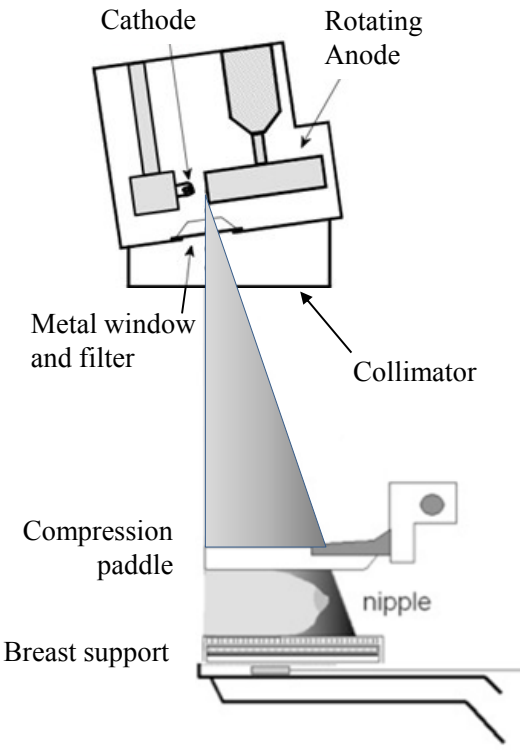

Figure 6.1. Schematic of the x-ray tube in a mammography/DBT system.

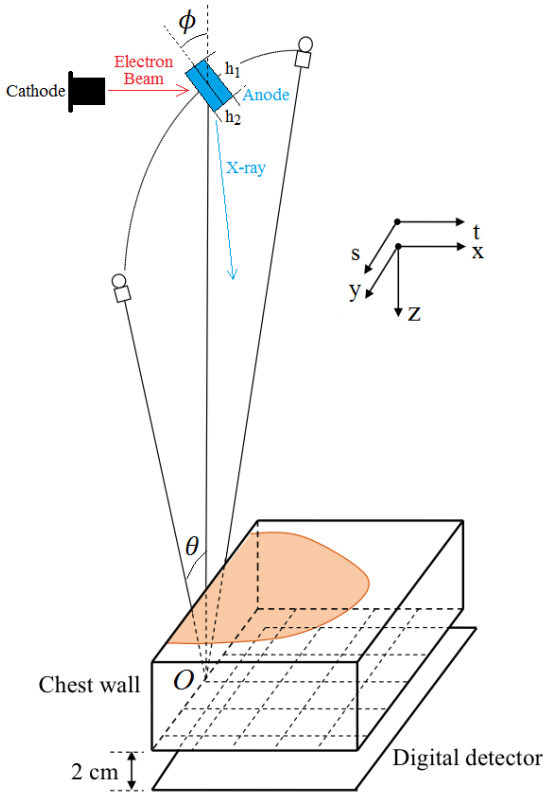

Figure 6.2. The simplified model for the finite-sized focal spot and the definition of parameters.

We review the principles of the x-ray tube. Figure 6.1 shows the structure of an x-ray tube used in DBT. The main components are the cathode and the anode. A high voltage is applied between the cathode and the anode such that the thermionic electrons generated by the cathode are accelerated to be high-energy electrons. When the high-energy electron beam hits the anode, x-ray photons are emitted from the surface of the anode. Therefore in the 3D space, the shape of the finite-sized focal spot is actually the same as the piece of surface of the anode that is hit by the electron beam. As shown in Figure 6.1, the anode is a disk rotating at high speed. At any instant of time, the electron beam hits a spot at the disk as if it is static. The rotation spreads the heat generated by the electronic bombardment over a circular track so that the anode can produce x-rays with a higher current and longer time without overheating. The effective focal spot is of the size of the projected beam, which is reduced by a factor that depends on the point of view

from the spatial location on the detector plane to the focal spot at the anode. This is known as the line focus principle in x-ray imaging.

As shown in Figure 6.1, in a typical mammography or DBT system, the anode-cathode axis is perpendicular to the chest wall edge of the detector with the cathode on the chest wall side. The electron beam is accelerated from the cathode to hit the anode. Then the x-ray beam is emitted towards the detector. Although the x-ray tube uses a rotating anode, the part of the anode hit by the electron beam is relatively small. The shape and the radiation strength distribution of the focal spot are unknown and can be very complicated.

To simplify the problem, we model the x-ray source as a rectangle with uniform x-ray emission, shown as the blue rectangle in Figure 6.2. The center of the finite-sized x-ray source is at the original location of the ideal point source. The rectangle of the focal spot is described with three parameters: its sizes along two directions h_1 and h_2 and the target angle ϕ. The target angle ϕ is defined as the angle between the rectangle plane and the direction from the rotation center (origin of the Cartesian coordinate system, marked as O in Figure 6.2) to the source. The target angle ϕ is usually smaller than $45°$. Figure 6.2 shows the situation that the projection angle θ is 0. Considering the geometry of the DBT system, if the projection angle θ is not 0, the blue rectangle will tilt by the same angle θ such that the h_2 edge of the rectangle is parallel to the direction that the x-ray source is moving.

The rest of this chapter uses this simplified model for the finite-sized x-ray source for both the analytical calculation of the PSF and the CatSim simulation. The definition of h_1, h_2 and ϕ will remain the same as defined in this section.

VI.2.2 Estimation of the h_2 for DBT systems with continuous-motion data acquisition

For DBT systems with continuous-motion x-ray source, the motion of the source during data acquisition results in additional blurring of the finite-sized focal spot. The additional blurring increases the effective h_2. In this section, we will estimate the effective h_2 using the source travel distance estimated from the typical exposure techniques of a thick breast for the three commercial DBT systems that use the continuous-motion mode. For DBT systems with a continuous-motion x-ray source and a detector moving in the opposite direction along a concentric arc with the same angle, the focal spot motion will be reduced relative to the detector. This geometry slightly reduces the additional blurring from the motion of the source but does not

eliminate it since the imaged volume is still moving relative to both the x-ray source and the detector. We will compare the source blur of DBT systems with moving detector and stationary detector in Section VI.5.4.

For each of these systems, the nominal size of the focal spot can be found in their technical documents (references will be shown in Table 6.1 – 6.3). The nominal focal spot size, denoted as h_{nominal}, refers to the effective size of the focal spot of the central ray (i.e., the ray perpendicular to the detector plane when the scan angle is 0). If the source is stationary during the data acquisition, h_2 should be equal to h_{nominal}. h_1 can be calculated given h_{nominal} and the target angle ϕ. If we consider the motion of the source, h_1 should remain the same. The source blur along the direction of the motion is given by the convolution of two rectangle functions, one with the width of h_{nominal} and the other with the width of the distance that the source moves, denoted as h_{motion}. The result of the convolution is trapezoidal and occasionally triangular (when $h_{\text{motion}} = h_{\text{nominal}}$). For the worst-case scenario, we consider the width of the non-zero part of the convolution result to be the effective h_2:

$$h_2 = h_{\text{motion}} + h_{\text{nominal}}. \tag{6.1}$$

Assuming the speed of the source is a constant for continuous-motion DBT systems, h_{motion} can be estimated given the distance from the source to the rotation center, the total acquisition angle and the total exposure time. We obtained the typical total current-time product (mAs) of the three commercial systems for different breast thicknesses from their technical documents (references can be found in Tables 6.1 – 6.3). The exposure time of one PV can be estimated from the total current-time product, the current and the total number of projections. The distance that the source travels during the exposure of one PV is then calculated by multiplying the speed of the source and the exposure time of one PV. Tables 6.1 – 6.3 show the results for the three commercial DBT systems together with other technical details and the references.

Tables 6.1 – 6.3 show that, for most breast thicknesses, the motion of the x-ray source contributes significantly to the effective h_2. Although the nominal size of the focal spot is 0.3mm, for thick breasts the effective h_2 can be as large as 1.6mm according to our estimation. For thicker breasts, a high total current-time product is required such that enough penetrated x-rays can be measured by the detector to avoid the projection images from being too noisy. Since the maximum current or output power of the x-ray tube is limited, a longer single-PV exposure time for each PV is required, resulting in a larger h_{motion}.

The effective h_2 listed in Tables 6.1 – 6.3 is estimated from the quality control documents or FDA's documents on the summary of safety and effectiveness data (SSED) that we can find online. The kilovoltage, total current-time product, current and other parameters might differ in clinical DBT procedures. Therefore the effective h_2 listed in Table 6.1 – 6.3 are only estimates. Despite this, Tables 6.1 – 6.3 still provides a range for h_2 as a reference. Later in this chapter we will use CatSim simulation to study the effect of source blur on DBT reconstruction. Based on Tables 6.1-6.3 and considering the uncertainties, we studied h_2 from 0.3 mm to 2 mm in our simulation to cover the range of possible effective source blur that is estimated from the exposure techniques used in DBT.

Table 6.1. Estimation of the Source Blur h_2 for Hologic Selenia Dimensions system. We used the maximum current of the x-ray tube in [127] as the current for each thickness of the breast, ignoring the possible dependence of the current on kV settings. The Hologic system bins 2 × 2 pixels during the image reconstruction. Therefore, the pixel size is 0.14mm for this system. The detector is rotated with the x-ray source during exposure so that the effective source blur may be less than the estimated value here assuming a stationary detector. Section VI.5.4 discusses the effect of the moving detector.

Pixel size					0.07mm (full resolution) 0.14mm (2 × 2 binning)		
Number of projections					15		
Distance from source to the rotation center (mm)					700		
Acquisition angle (degree)					15		
Total acquisition time (s)					3.7		
Total motion of the source (mm)					183		
Speed of the source (mm/s)					49.5		
Nominal focal spot size (mm)					0.3		
References					[26, 44, 127]		
Thickness of Breast (mm)	Kilovoltage (kV)	Total Current-Time Product (mAs)	Current (mA)	Total Exposure Time (s)	Exposure Time of One PV (s)	Motion of Source of One PV (mm)	Source Blur h_2 (mm)
20	26	32	200	0.160	0.011	0.5	0.8
40	29	43	200	0.215	0.014	0.7	1.0
60	33	60	200	0.300	0.020	1.0	1.3
80	38	81	200	0.405	0.027	1.3	1.6

Table 6.2. Estimation of Source Blur h_2 for Siemens Mammomat Inspiration system. The current cannot be found in the technical documents and is therefore estimated with the voltage and the fixed power output of the x-ray tube, which is 5 kW according to [128].

Pixel size					0.085mm		
Number of projections					25		
Distance from source to the rotation center (mm)					608		
Acquisition angle (degree)					50		
Total acquisition time (s)					25		
Total motion of the source (mm)					530.6		
Speed of the source (mm/s)					21.2		
Nominal focal spot size (mm)					0.3		
References					[44, 128]		
Thickness of Breast (mm)	Kilovoltage (kV)	Total Current-Time Product (mAs)	Current (mA)	Total Exposure Time (s)	Exposure Time of One PV (s)	Motion of Source of One PV (mm)	Source Blur h_2 (mm)
20	25	50	200	0.250	0.010	0.2	0.5
30	26	70	192	0.364	0.015	0.3	0.6
40	26	90	192	0.468	0.019	0.4	0.7
50	27	110	185	0.594	0.024	0.5	0.8
60	28	120	179	0.672	0.027	0.6	0.9
70	29	130	172	0.754	0.030	0.6	0.9
80	30	140	167	0.840	0.034	0.7	1.0
90	30	160	167	0.960	0.038	0.8	1.1
100	31	180	161	1.116	0.045	0.9	1.2

Table 6.3. Estimation of Source Blur h_2 for the Fujifilm Aspire Cristalle system. The current cannot be found in the technical documents and is therefore estimated with the kilovoltage and the fixed power output of the x-ray tube, which is 4.9 kW according to [135]. The breast thickness is converted from the PMMA phantom used in the Fujifilm quality control manual by interpolating curve of the equivalent breast thickness to the PMMA phantom thickness [136]. The digital detector uses an array of hexagonal pixels of a side width of 0.05mm. The area of a hexagonal pixel is the same as a square pixel of 0.08mm, therefore we estimate the equivalent pixel size to be 0.08mm.

Pixel size					0.05mm (Hexagonal), 0.08mm (Square)		
Number of projections					15		
Distance from source to the rotation center (mm)					650		
Acquisition angle (degree)					15		
Total acquisition time (s)					4.0		
Total motion of the source (mm)					170		
Speed of the source (mm/s)					42.5		
Nominal focal spot size (mm)					0.3		
References					[124, 135-137]		
Thickness of Breast (mm)	Kilovoltage (kV)	Total Current-Time Product (mAs)	Current (mA)	Total Exposure Time (s)	Exposure Time of One PV (s)	Motion of Source of One PV (mm)	Source Blur h_2 (mm)
21.0	26	36	188	0.191	0.013	0.5	0.8
33.0	28	32	175	0.183	0.012	0.5	0.8
45.0	30	40	163	0.245	0.016	0.7	1.0
52.5	32	40	153	0.261	0.017	0.7	1.0
60.0	33	42	148	0.283	0.019	0.8	1.1
75.0	36	50	136	0.367	0.024	1.0	1.3
90.0	37	63	132	0.476	0.032	1.3	1.6

VI.3 The point spread function of the source blur in DBT

In this section, we describe the analytical calculation to evaluate the spatial dependence of the source blur (i.e., geometric unsharpness) on the detector plane. We will first describe the concepts of the pinhole array, the magnification factor and the source blur scaling factor. Then we use theorems in solid geometry to calculate the projection of a rectangular source on the detector plane through a pinhole. The pinhole array and analytically calculated source blur will also be used in Section VI.4.1 to validate the CatSim simulation.

VI.3.1 The pinhole array and the source blur scaling factor

We use the pinhole array to calculate the effective shape and size of the focal spot as seen on the detector plane. A pinhole is an ideal point object. We refer to it as a pinhole since traditionally pinholes are used to experimentally measure the size of the x-ray focal spot [138, 139]. The pinholes we use in this simulation study serve the same purpose.

As shown in Figure 6.3, the pinhole array is an array of pinholes that is parallel to the detector plane. When a finite-sized source is used, its projection through the pinhole represents the blurring for a point object at the pinhole's location due to geometric unsharpness. Since the ideal projection of a point object (with and ideal point source) should be a point, the projection of the finite-sized source through the pinhole can be considered to be the source blur PSF for the location of the point object. Such a PSF depends on the depth and the spatial location on the x-y plane of the object. Therefore, the projection image with source blur cannot be obtained by convolution of a PSF with the ideal projection image of a whole volume. For simplicity, we will use the term 'source blur PSF' in the following discussion but it actually means 'source blur PSF for objects at a specific spatial location'. Alternatively, the pinhole array can be considered an array of pinhole cameras, the projections of the focal spot through the pinhole array generates the images of the focal spot (i.e., the size and shape of the focal spot) as seen at different locations on the detector plane at a magnification determined by the distances from the pinhole array to the focal spot and to the detector plane. In x-ray imaging, the ratio of the distance between the focal spot and the detector plane to the distance between the focal spot and the object plane is called the magnification factor (M). If the pinhole array is placed midway between the source and detector (i.e., magnification factor $M = 2$), the pinhole image of the focal spot will represent the physical size of the focal spot at the anode level seen at a given spatial location on the detector plane if the focal spot is parallel to the image plane (magnification of focal spot = $M - 1 = 1$). Conventionally the nominal focal spot size of an x-ray imaging system is measured at the central ray (the ray perpendicular to the detector plane) with a pinhole camera at midway. For mammography systems, the central ray is almost tangential to the chest wall edge of the detector, so the nominal focal spot size may be specified at a few centimeters from the chest wall, depending on the manufacturer. At an object magnification $M = 1$ (i.e., the object is in contact with the detector plane), the projected focal spot becomes a point so that there is no geometric unsharpness or source blur.

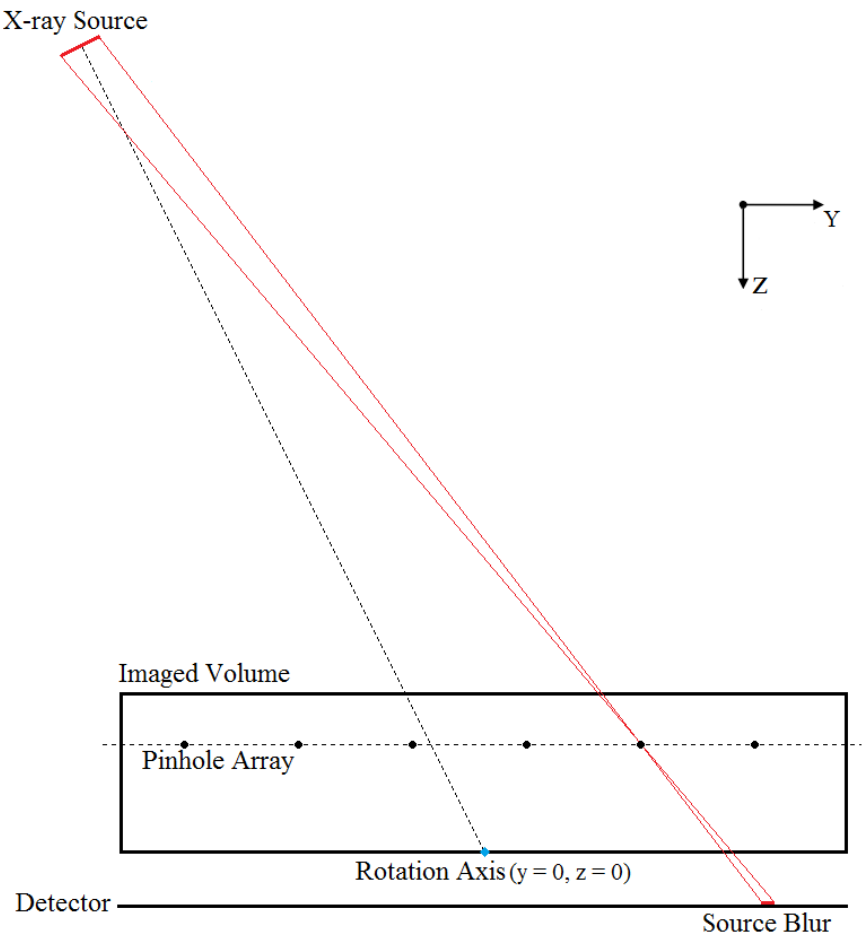

Figure 6.3. The pinhole array used to calculate the PSF of the source blur.

In Figure 6.3 all pinholes are drawn inside the imaged volume. However, they can be located at any location or any depth to obtain the distribution of PSFs in any region of the detector plane that we are interested in.

To facilitate discussion, we define the ratio of the distance from the array to the detector and the distance from the source to the array as the source blur scaling factor, which is equal to (M - 1). If the rectangular source shown in Figure 6.2 is parallel to the detector ($\phi = 90°$), the PSF of the source blur can be easily obtained by scaling the rectangle with the source blur scaling factor. If the source is not parallel to the detector plane, the source blur scaling factor is less meaningful but it still approximately reflects the size of the PSF of the source blur. When a pinhole is placed in the middle between the source and the detector plane to measure the size of the focal spot, the source blur scaling factor is 1 [138, 139]. Such a pinhole array will be used in Section VI.3.3 to illustrate the shift-variance of the source blur PSF.

VI.3.2 Algorithm to calculate the source blur PSF of the DBT system

With the simplified source blur model described in Section VI.2.1, the projection of the rectangular source through a pinhole can be analytically calculated on the detector plane. We first introduce the following lemma:

Lemma 1: The projection of a straight line segment l_1 on a plane P through a point O is contained in a straight line.

Proof: Let A denote an arbitrary point on l_1. The projection of A on the plane P through O is contained in the plane determined by l_1 and O. Let Q denote this plane. Obviously the projection of A on P is contained in P. Because the intersection of P and Q is a straight line and A is an arbitrary point on l_1, the projections of all the points on l_1 are contained in the same straight line.

Because of Lemma 1, the projection of a rectangular source on a plane through a pinhole can be obtained by calculating the projections of only the four corners. We simply need to connect the projections of the four corners to get the shape of the PSF of the source blur.

We derive the locations of the four corners of the rectangular focal spot and their projections. The finite-sized focal spot shown in Figure 6.2 is enlarged in Figure 6.4 to illustrate the locations of its corners. Let d_{SO} denote the distance from the center of the source (denoted as S) to the rotation center (denoted as O) and d_{OP} denote the distance from the rotation center to the origin of the detector (denoted as P). The center of the source (S) is located at:

$$\vec{r}_S = (0, d_{SO}\sin\theta, -d_{SO}\cos\theta). \tag{6.2}$$

The locations of the four corners (A, B, C and D in Figure 6.4) of the rectangular source are:

$$\begin{aligned} \vec{r}_A &= \vec{r}_S - \vec{d}_1 - \vec{d}_2, \\ \vec{r}_B &= \vec{r}_S + \vec{d}_1 - \vec{d}_2, \\ \vec{r}_C &= \vec{r}_S + \vec{d}_1 + \vec{d}_2, \\ \vec{r}_D &= \vec{r}_S - \vec{d}_1 + \vec{d}_2, \end{aligned} \tag{6.3}$$

where $\vec{d}_1$ and $\vec{d}_2$ are vectors of lengths $\frac{h_1}{2}$ and $\frac{h_2}{2}$ along the h_1 and h_2 directions in Figure 6.2, shown as red arrows in Figure 6.4:

$$\begin{aligned} \vec{d}_1 &= \left(\frac{h_1}{2}\sin\phi, -\frac{h_1}{2}\cos\phi\sin\theta, \frac{h_1}{2}\cos\phi\cos\theta\right), \\ \vec{d}_2 &= \left(0, \frac{h_2}{2}\cos\theta, \frac{h_2}{2}\sin\theta\right). \end{aligned} \tag{6.4}$$

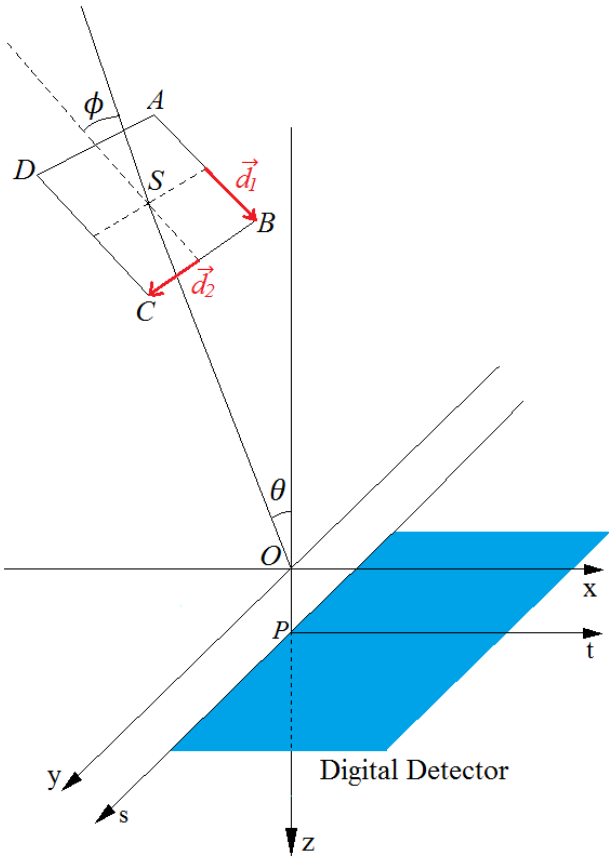

Figure 6.4. Derivation of the vectors along the edges of the rectangular source ($\vec{d}_1$ and $\vec{d}_2$). The blue rectangle shows the location of the digital detector.

The expressions of $\vec{d}_1$ and $\vec{d}_2$ are derived based on solid geometry. Obviously we have: $\overrightarrow{AB} \parallel \overrightarrow{DC}$ and $\overrightarrow{AD} \parallel \overrightarrow{BC}$. $\vec{d}_1$ are $\vec{d}_2$ are along the directions of $\overrightarrow{AB}$ and $\overrightarrow{BC}$. They are perpendicular to each other and their lengths are $\frac{h_1}{2}$ and $\frac{h_2}{2}$. If we can derive the direction vectors of $\overrightarrow{AB}$ and $\overrightarrow{BC}$, denoted as $\vec{n}_{\overrightarrow{AB}}$ and $\vec{n}_{\overrightarrow{BC}}$, $\vec{d}_1$ and $\vec{d}_2$ can be obtained by multiplying these direction vectors with $\frac{h_1}{2}$ and $\frac{h_2}{2}$.

We first derive $\vec{n}_{\overrightarrow{BC}}$. $\overrightarrow{BC}$ is parallel to the y-z plane and perpendicular to $\overrightarrow{OS}$. The direction vectors of the y-z plane and $\overrightarrow{OS}$ are:

$$\vec{n}_x = (1,0,0), \tag{6.5}$$

$$\vec{n}_{\overrightarrow{OS}} = (0, \sin\theta, -\cos\theta). \tag{6.6}$$

Therefore $\vec{n}_{\overrightarrow{BC}}$ can be obtained by calculating their cross product:

$$\vec{n}_{\overrightarrow{BC}} = \vec{n}_x \times \vec{n}_{\overrightarrow{OS}} = (0, \cos\theta, \sin\theta). \tag{6.7}$$

Next we derive $\vec{n}_{\overrightarrow{AB}}$. $\vec{n}_{\overrightarrow{AB}}$ is perpendicular to $\vec{n}_{\overrightarrow{BC}}$. We also know that the angle between $\vec{n}_{\overrightarrow{AB}}$ and $\vec{n}_{\overrightarrow{SO}}$ is ϕ. Therefore we have the follow equations:

$$\vec{n}_{\overrightarrow{AB}} \cdot \vec{n}_{\overrightarrow{BC}} = 0, \tag{6.8}$$

$$\vec{n}_{\overrightarrow{AB}} \cdot \vec{n}_{\overrightarrow{SO}} = \cos\phi, \tag{6.9}$$

$$\vec{n}_{\overrightarrow{AB}} \cdot \vec{n}_{\overrightarrow{AB}} = 1, \tag{6.10}$$

where Equation 6.10 is the constraint for the length of the direction vector. $\vec{n}_{\overrightarrow{SO}}$ is the opposite direction of $\vec{n}_{\overrightarrow{OS}}$: $\vec{n}_{\overrightarrow{SO}} = -\vec{n}_{\overrightarrow{OS}}$, where $\vec{n}_{\overrightarrow{OS}}$ is known as shown in Equation 6.6. $\vec{n}_{\overrightarrow{BC}}$ is shown in Equation 6.7. Therefore by solving Equations 6.8 – 6.10, we have:

$$\vec{n}_{\overrightarrow{AB}} = (\sin\phi\,, -\cos\phi\sin\theta\,, \cos\phi\cos\theta). \tag{6.11}$$

Multiplying $\vec{n}_{\overrightarrow{AB}}$ and $\vec{n}_{\overrightarrow{BC}}$ with $\frac{h_1}{2}$ and $\frac{h_2}{2}$ leads to the expressions of $\vec{d}_1$ and $\vec{d}_2$ in Equation 6.4.

Using solid geometry, the projection $\vec{p}$ of an arbitrary location $\vec{r}$ on the detector plane is:

$$\vec{p} = \vec{r} + \frac{(\vec{r}_{\text{detector}} - \vec{r}) \cdot \vec{n}_{\text{detector}}}{(\vec{r}_{\text{pinhole}} - \vec{r}) \cdot \vec{n}_{\text{detector}}} (\vec{r}_{\text{pinhole}} - \vec{r}), \tag{6.12}$$

where the operator $\cdot$ denotes inner product, $\vec{r}_{\text{pinhole}}$ is the known location of the pinhole and the two vectors that describe the detector plane are:

$$\vec{n}_{\text{detector}} = (0,0,1), \tag{6.13}$$

$$\vec{r}_{\text{detector}} = (0,0,d_{\text{od}}). \tag{6.14}$$

With Equation 6.2-6.4 and 6.12-6.14, we can analytically calculate the PSF of the source blur given the location of the pinhole $\vec{r}_{\text{pinhole}}$.

VI.3.3 The source blur PSF for the GE GEN2 prototype DBT system

In this section, we calculate the source blur PSF for our GE GEN2 Prototype DBT System because all DBT scans used as examples in the dissertation were acquired with this system. The analyses in this section are applicable to other similar DBT systems with stationary detectors, except for the differences in the geometric parameters. For DBT systems in which the detector is rotated about the fulcrum in opposite direction to the x-ray source such as the Hologic DBT system [44], the geometry relative to the compressed breast is slightly different at projection angles other than 0 degrees and the degree of blurring may be reduced but the principle is still applicable with appropriate modifications.

Instead of using the detector size 192.0×230.4 mm^2 of the prototype system, the size of the detector is assumed to be 240.0×300.0 mm^2, which is closer to the detector size of commercial DBT systems. The detector plane is parallel to the breast support plate and the compression paddle. The parameters d_{so} and d_{od} of the system are the same as the GE GEN2 prototype: $d_{\mathrm{so,GEN2}} = 640mm$, $d_{\mathrm{od,GEN2}} = 20mm$. The target angle is $\phi_{\mathrm{GEN2}} = 22.5°$. For the GE SenoClaire system, these values are: $d_{\mathrm{so,SenoClaire}} = 620mm$, $d_{\mathrm{od,SenoClaire}} = 40mm$ and $\phi_{\mathrm{SenoClaire}} = 22.5°$ according to [44, 140], which is the close to the GE GEN2 prototype system. The nominal size of the x-ray source is 0.3mm, which is assumed to be measured at the central ray that is perpendicular to the chest wall edge of the detector plane at the projection angle $\theta = 0°$. Therefore we can derive the values for h_1 and h_2:

$$h_{1,\mathrm{GEN2}} = \frac{0.3}{\sin \phi_{\mathrm{GEN2}}} = 0.78 \text{ mm},$$
$$h_{2,\mathrm{GEN2}} = 0.3 \text{ mm}. \tag{6.15}$$

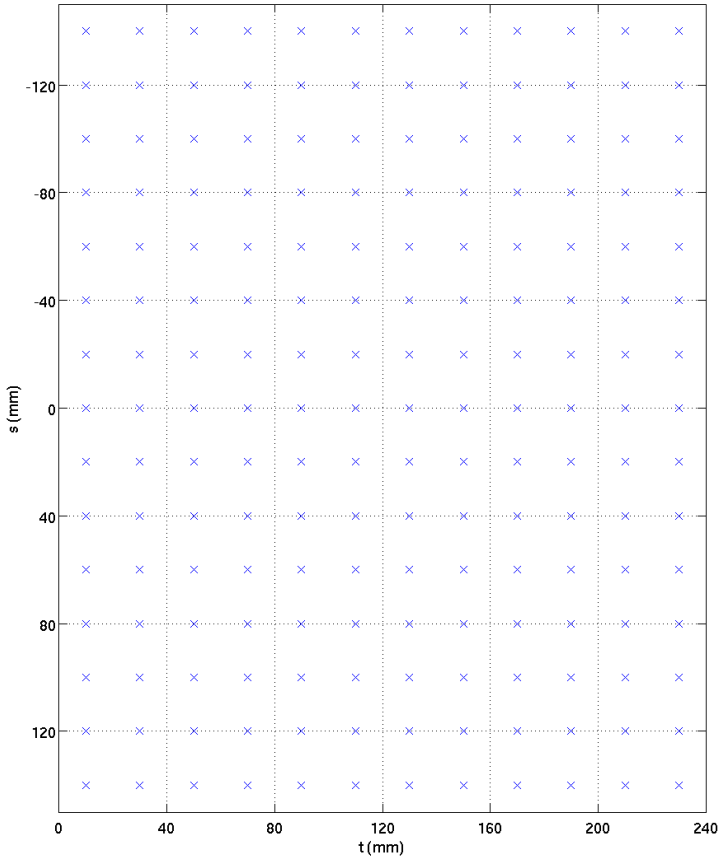

Figure 6.5. The array of locations to calculate PSF of source blur on the detector.

We are interested in the PSF of source blur over the detector plane as shown in Figure 6.5. Starting from the point t = 10 mm, s = 0 mm, we set up an array of locations every 20 mm along both the t- and s-direction. Given the array in Figure 6.5, the depth of the pinhole array and the projection angle, the in-plane locations of the pinholes can be easily derived.

To illustrate the spatial variations in the source blur PSF, we first calculate the PSFs for a large source with the nominal size of 6 mm. Such a large source will make the shape of the PSFs visible even when the entire detector is displayed. Given the projection angle θ, we set the depth of the pinhole array to be $z_{\text{pinhole}} = -(d_{\text{so,GEN2}} \cos\theta - d_{\text{od,GEN2}})/2$ such that the source blur scaling factor is 1. The contours of the calculated PSFs are shown in blue in Figure 6.6.

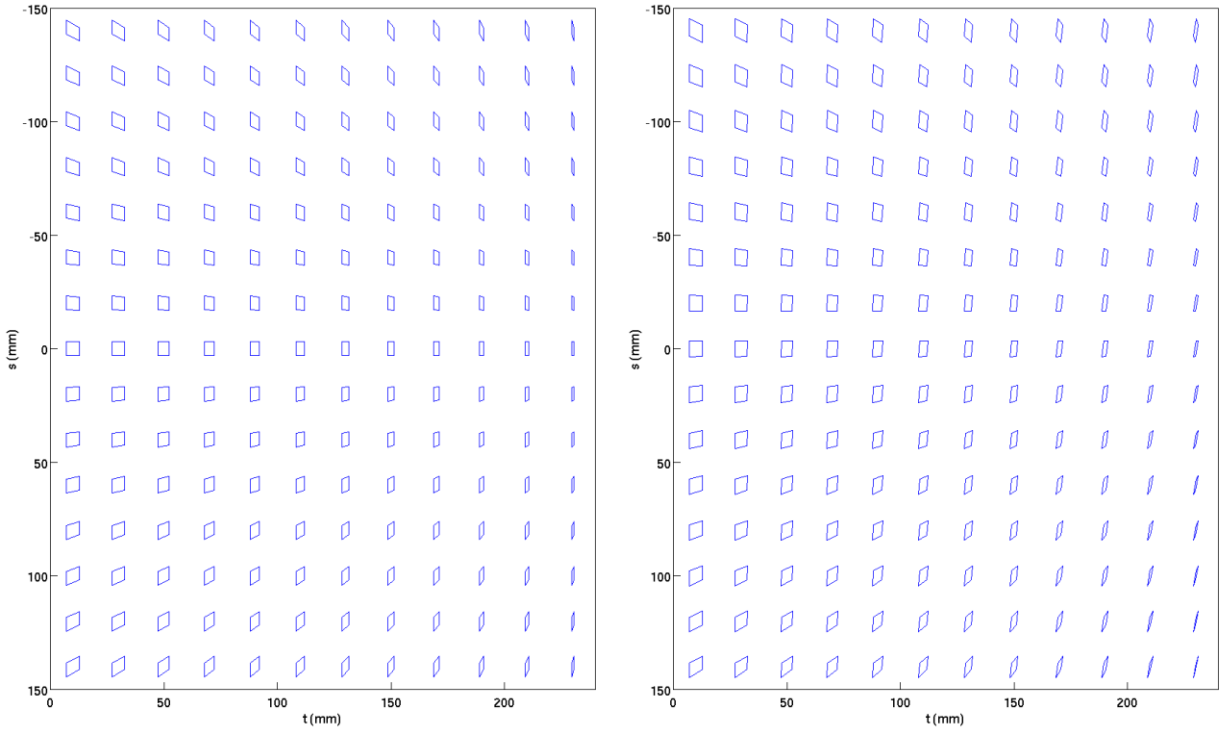

(a) (b)

Figure 6.6. The source blur PSFs for a source of nominal size of 6mm for pinholes at depth $z_{\text{pinhole}} = -(d_{\text{so,GEN2}} \cos\theta - d_{\text{od,GEN2}})/2$ with different projection angles: (a) $\theta = 0°$; (b) $\theta = 30°$.

Figure 6.6(a) shows the source blur PSF at the projection angle $\theta = 0°$. As expected, the distribution of the PSF is symmetrical along the s = 0 axis. The PSF closest to the central ray at t = 10mm, s = 0mm is approximately the shape of a square. This is reasonable considering that the nominal focal spot size is measured with the central beam at t = 0mm, s = 0mm. For most PSFs

that are not close to the rotation axis, their shape is more similar to a parallelogram. The area of the PSF gets smaller and smaller when t increases. If the detector is larger along the t-direction and this trend continues, the size of the PSF will eventually reach zero when the viewing direction is tangential to the anode surface. This observation can be intuitively understood considering the structure of the DBT system shown in Figure 6.2. If a point on the detector plane is too far away from the chest wall, it will not receive any radiation due to the self-absorption of the emitted x-rays photons by the anode material, and because the scattered radiation, off-focus radiation and small penetration through the anode are all neglected. Figure 6.6(b) shows the source blur PSF at a projection angle $\theta = 30°$. Most PSFs are of the shape similar to a parallelogram. For this projection angle, the shape of the PSF is difficult to intuitively estimate. But it can be observed that the PSF of the source blur changes gradually throughout the detector plane and is highly shift-variant.

Next we calculate PSF with the nominal focal spot size of 0.3 mm, which is a typical focal spot size in all four FDA-approved DBT systems. Instead of setting a source blur scaling factor of 1, now we set the pinhole array at a depth within the imaged volume for DBT reconstruction, e.g., $z_{\text{pinhole}} = -50\text{mm}$ (i.e., 50 mm above the breast support plane). The PSF of source blur is too small if we display the entire detector as Figure 6.6. Therefore we only show the enlarged PSF at four locations: (a) t = 10 mm, s = 0 mm, (b) t = 230 mm, s = 0 mm, (c) t = 10 mm, s = 140 mm and (d) t = 230 mm, s = 140 mm. The PSFs for the projection angles $\theta = 0°$ and $\theta = 30°$ are shown in Figure 6.7 and Figure 6.8.

As can be observed in Figure 6.7 and Figure 6.8, the shape of each of the PSFs is similar to that at the same location in Figure 6.6. Similar to Figure 6.6, the PSFs shown in Figure 6.7 and Figure 6.8 are highly shift-variant. The PSFs in Figure 6.8 are generally larger than that of Figure 6.7, since the distance from the source to the detector is smaller for Figure 6.8, resulting in a larger source blur scaling factor.

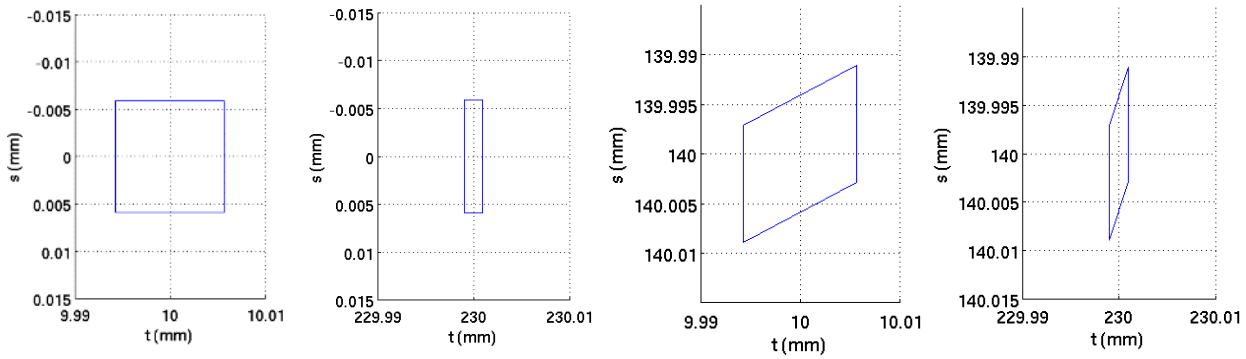

(a) (b) (c) (d)

Figure 6.7. The source blur PSFs for a source of nominal size of 0.3 mm for pinholes at depth $z_{\text{pinhole}} = -50mm$ at the projection angle $\theta = 0°$ at four different locations: (a) t = 10 mm, s = 0 mm; (b) t = 230 mm, s = 0 mm; (c) t = 10 mm, s = 140 mm; (d) t = 230 mm, s = 140 mm.

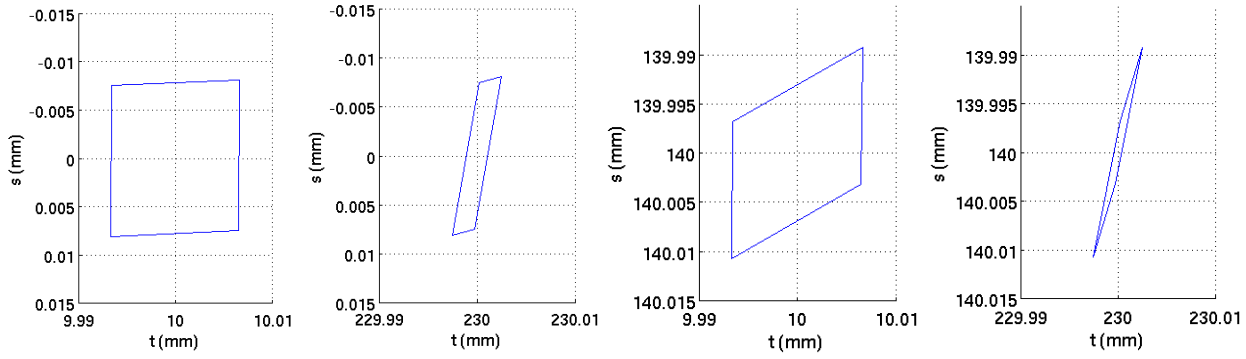

(a) (b) (c) (d)

Figure 6.8. The source blur PSFs for a source of nominal size of 0.3 mm for pinholes at depth $z_{\text{pinhole}} = -50mm$ at the projection angle $\theta = 30°$ at four different locations: (a) t = 10 mm, s = 0 mm; (b) t = 230 mm, s = 0 mm; (c) t = 10 mm, s = 140 mm; (d) t = 230 mm, s = 140 mm.

In both Figure 6.7 and Figure 6.8, we can observe that the size of the PSFs is at most about 0.02mm along one direction. Considering that the pixel size of our detector is 0.1mm, it is possible that the source blur PSF does not strongly affect the projection images for DBT systems if the effective h_2 stays as 0.3 mm such as an ideal step-and-shoot system. On the other hand, for DBT systems designed with continuous scanning motion and pulsed x-ray exposure during the acquisition of the projections, the effective h_2 can be as large as 1.6mm, as shown in Table 6.1 and Table 6.3. The x-ray pulse width depends on the tube current-time product required for the projection, which in turn depends on a number of factors, such as the beam quality (target/filter and kilovoltage), the output current of the x-ray system at the given target and kilovoltage, the detective quantum efficiency (DQE) of the detector, the breast thickness and density, and the

preferred glandular dose. Given the large number of variables, we will not be able to simulate specific systems and imaging techniques. We will use our prototype DBT system geometry as an example. A range of effective focal spot sizes (0.3 mm to 2 mm) that is estimated from possible exposure techniques used in DBT (Section VI.2.2) will be used to simulate projections of objects at different spatial locations for a wide range of projection angles. The reconstruction results from these projection images will demonstrate our approach and provide useful information for estimating the tolerance limits of the effective focal spot size (or source motion) for the design of DBT systems and the potential need of correcting source blur in DBT reconstruction under certain imaging conditions. In the next section, we will use CatSim simulation [65, 66] to study the influence of the source blur PSF on DBT reconstruction.

VI.4 Simulating the effect of source blur with CatSim: materials and methods

VI.4.1 Configuration and validation of CatSim simulation

The CatSim simulation is configured similarly as our study on the SG projector. The x-ray source is an Rh target/Rh filter x-ray tube and the kilovoltage is set to 29 kV. We simulated a complete set of 21 projections every 3° from $-30°$ to 30°. The detector pixel pitch is 0.1×0.1 mm^2, and has a size of 2400×3000 pixels, which is close to the FOV size of clinical DBT systems. We used an oversampling rate of 10 for the detector. The oversampling rate for the source is set to 6 due to the limited available memory. According to the study by Carvalho [141], an oversampling rate of 5 for the source is enough to generate accurate projection values for the focal spot without additional contribution of the x-ray source motion. As a result, an oversampling rate of 6 is enough for Source 1. For Source 2 and Source 3, a higher oversampling rate along the h_2 direction might improve the accuracy of the simulation. To use a higher oversampling rate for Source 2 and Source 3, CatSim needs to be configured in a more memory-efficient way; for example, instead of simulating the entire detector, only the area for the projected objects is simulated at the different projection angles.

Because the detector is stationary in the simulated DBT, we shifted the x-ray source to implement the rotation of the source instead of using the default rotation option in CatSim. Therefore one configuration file is needed for each projection angle. CatSim supports the usage of a rectangular finite-sized x-ray source. However, since CatSim is designed for CT simulation,

there is no option to tilt the source such that the h_2 edge of the rectangle is parallel to the direction that the x-ray source is moving, as mentioned in Section VI.2.1. To solve this problem, we wrote a new source callback function in CatSim that allows us to rotate the source with regard to the x-direction. By setting this rotation angle the same as the projection angle θ, we were able to implement the tilting of the rectangular source such that its h_2 edge is perpendicular to the line from the center of the source to the center of rotation (origin of the coordinate system in Figure 6.2).

Before simulating the phantoms with objects, we first use the pinhole array phantoms to validate the results of CatSim for a finite-sized rectangular source. We configured two pinhole phantoms for the two cases shown in Figure 6.6, where the nominal size of the source is 6mm and the pinholes are located at $z_{\text{pinhole}} = -(d_{\text{so,GEN2}} \cos\theta - d_{\text{od,GEN2}})/2$. We use the nominal size of 6 mm rather than 0.3 mm since the pixelated PSF for the 0.3mm source is only as large as about 3 × 3 pixels at the same depth $z_{\text{pinhole}} = -(d_{\text{so,GEN2}} \cos\theta - d_{\text{od,GEN2}})/2$, which is too small to show a meaningful pattern. For this simulation, we set the background material of the phantoms to be air. Each pinhole is configured as a lead sphere with the diameter of 0.01mm.

The simulation results are shown in Figure 6.9 and Figure 6.10. The simulated PSFs are displayed as the pixelated images. We also displayed the white contours of the analytically calculated PSFs at the same locations. As observed in Figure 6.9 and Figure 6.10, the simulated PSFs are 6×6 dot arrays. This is because we used a source oversampling rate of 6 in the configuration. According to the CatSim manual [66], if the oversampling rate for the source is γ_s, the rectangular x-ray source is simulated by equally dividing the rectangle into $\gamma_s \times \gamma_s$ pieces and putting a sub point source at the center of each piece, where the strength of each sub point source is $1/\gamma_s^2$ of the total strength of the x-ray source. Obviously, if we equally divide each analytical PSFs in Figure 6.9 and Figure 6.10 into 6×6 small pieces, the dots of the 6×6 dot arrays of the simulated PSFs will be located at exactly the center of each small piece. The only exception might be Figure 6.10(d) that the analytical PSF is very narrow and the simulated PSF is pixelated. But we can still observe in Figure 6.10(d) that the dot pattern aligns with the contour of the analytical PSF very well. Therefore this comparison validates that CatSim can correctly simulate the PV images when a finite-sized rectangular x-ray source is configured.

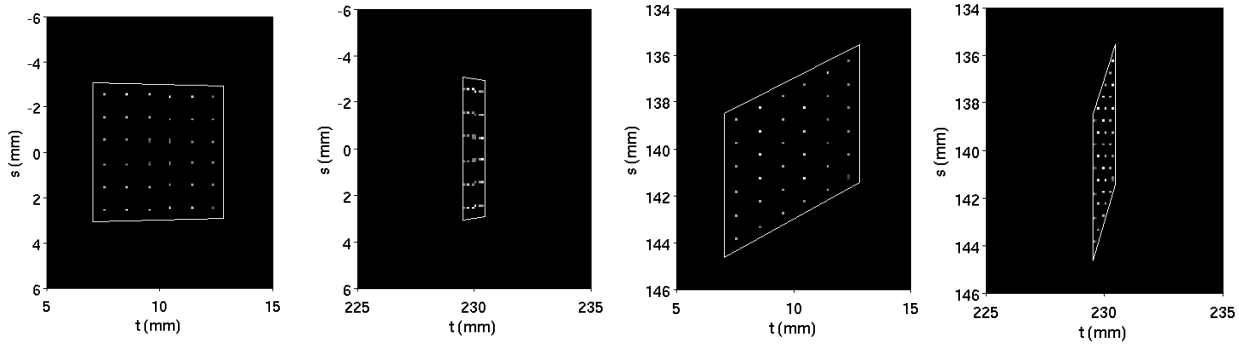

Figure 6.9. The simulated and the analytical source blur PSFs for a rectangular source of nominal size 6 mm at depth $z_{\text{pinhole}} = -(d_{\text{so,GEN2}} \cos\theta - d_{\text{od,GEN2}})/2$ for the projection angle $\theta = 0°$ at four different locations: (a) t = 10 mm, s = 0 mm; (b) t = 230 mm, s = 0 mm; (c) t = 10 mm, s = 140 mm; (d) t = 230 mm, s = 140 mm. The analytical source blur PSFs (white contours) are the same as the PSFs at the same locations in Figure 6.6 (a).

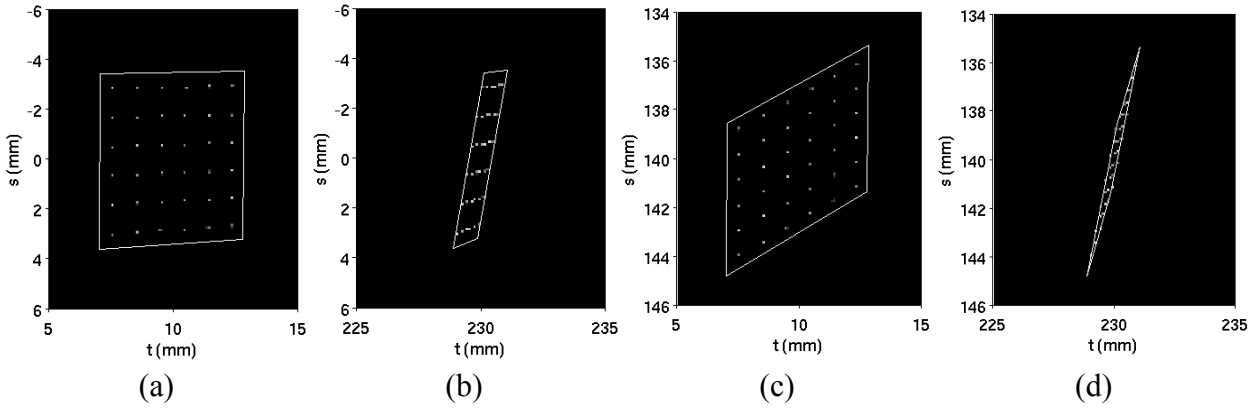

Figure 6.10. The simulated and the analytical source blur PSFs for a rectangular source of nominal size 6 mm at depth $z_{\text{pinhole}} = -(d_{\text{so,GEN2}} \cos\theta - d_{\text{od,GEN2}})/2$ at projection angle $\theta = 30°$ at four different locations: (a) t = 10 mm, s = 0 mm; (b) t = 230 mm, s = 0 mm; (c) t = 10 mm, s = 140 mm; (d) t = 230 mm, s = 140 mm. The analytical source blur PSFs (white contours) are the same as the PSFs at the same locations in Figure 6.6 (b).

One might wonder that the sampling of the source is too sparse as shown in Figure 6.9 and Figure 6.10. This is not a problem in our simulation for digital phantoms since our simulation does not use a source of the size 6 mm as in Figure 6.6. In addition, the depth of the objects in our simulation will not be located at $z = -(d_{\text{so,GEN2}} \cos\theta - d_{\text{od,GEN2}})/2$. Instead the distance between the objects and the detector plane is much smaller. The PSFs in our simulation of digital phantoms will be more similar to the cases shown in Figure 6.7 and Figure 6.8, where generally a source oversampling rate of 6 is enough to generate accurate projection images. For largest

source that we simulated in the next section (Source 3 in Table 6.4), the maximum length of its PSF is about 0.2mm, which is equivalent to 2 pixels. Sampling 6 points within 2 pixels is likely to be accurate enough, but further investigations are needed to confirm this assumption.

VI.4.2 Configuration of different sources

We used four sets of parameters for the source in the simulation to study the effect of source blur on DBT reconstruction. The parameters of the four sources are specified in Table 6.4. As a reference point, Source 0 is the ideal point source. Since CatSim simulates the source blur with an array of sub point sources, setting the oversampling rate to 1 is equivalent to using an ideal point source. The other parameters are trivial for Source 0. Source 1 uses the standard nominal size and the target angle of a GE GEN2 prototype DBT System [141], as introduced in Section VI.3.3 and expressed in Equation 6.15. The comparison between Source 0 and Source 1 will indicate the importance of modeling the source blur in DBT reconstruction for DBT systems with step-and-shoot data acquisition. For Source 2 and Source 3, we increased the value of h_2 to 1.0 mm and 2.0 mm. The purpose of these two sources is to simulate the influence of the motion of the source during the image acquisition, since the effective h_2 can be as large as 1.6 mm according to Table 6.1 and Table 6.3. The values in these tables are not accurate since we could not obtain all technique details. Therefore we used $h_2 = 2.0\text{mm}$ instead of 1.6 mm as a conservative choice. The comparison of Source 1, Source 2 and Source 3 will demonstrate the effect of the source motion on the reconstructed image quality.

Table 6.4. Sources simulated in this study. Note that Source 0 is simulated with an oversampling rate of 1, for which any finite-sized focal spot is equivalent to a point source in CatSim.

Name	Source 0	Source 1	Source 2	Source 3
Oversampling rate	1	6	6	6
Target angle (ϕ)	22.5°	22.5°	22.5°	22.5°
h_1 (mm)	0.784	0.784	0.784	0.784
h_2 (mm)	0.3	0.3	1.0	2.0

VI.4.3 Configuration of the LPBB phantom and the MC phantom

We configured two digital phantoms to study the influence of source blur on DBT reconstruction. The first phantom is similar to the phantom we used for studying the SG

projector [77] and introduced in Section III.3 (Figure 3.3), which contains lead line pairs (LP) and lead beads (BBs). We refer to this phantom as the LPBB phantom. The second phantom only contains BBs of calcium carbonate (the same material we used to simulate MCs in the experimental phantom [142] as shown in Section IV.3.2 (Figure 4.2)). The purpose of this phantom is to simulate the MCs in DBT. This phantom is referred to as the MC phantom. Both phantoms are analytically specified in configuration files using the FORBILD syntax [66]. The quantum noise, detector noise, and the scattered radiation are turned off so that we can focus on the investigation of the effects of the source blur on DBT reconstruction.

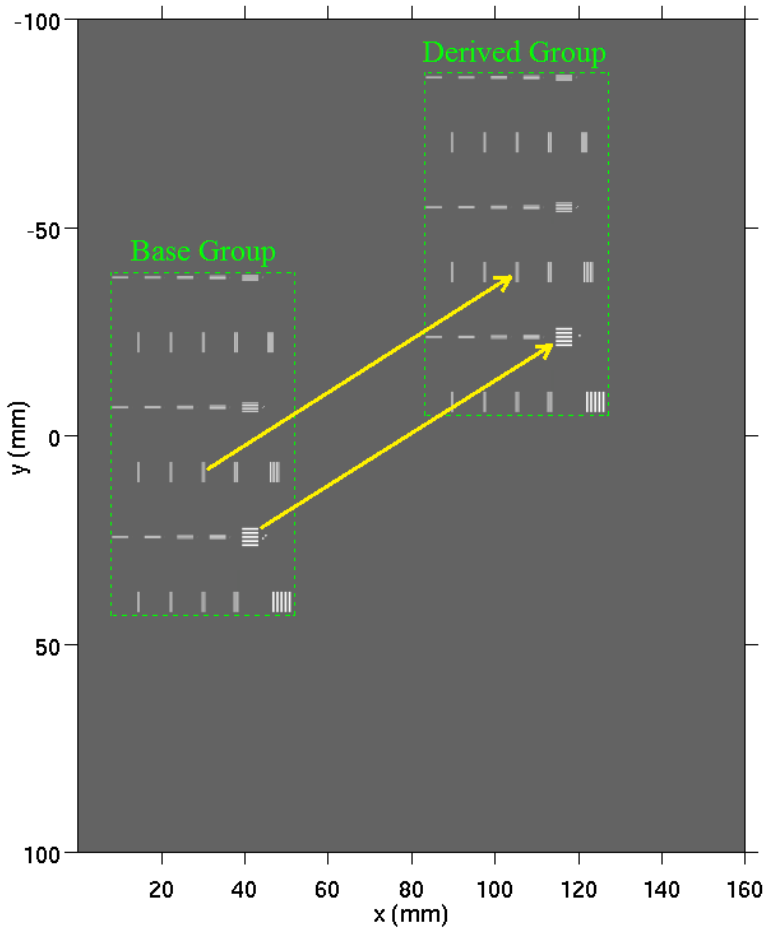

Figure 6.11. The base group is shifted to create the derived group in the phantom. Every object in the base group is shifted by the same distance along the x- and the y-direction. The relative locations of the objects are the same within each group.

Different from how we configured the phantom for the study on the SG projector, we need to configure multiple groups of objects in the current study. As shown in Figures 6.6 - 6.8, the PSF of the source blur is highly shift-variant and location-dependent. We therefore analyze the spatial

resolution for high-contrast objects by placing line pairs and BBs at different locations. To configure such a phantom, we first configure a group of objects called the base group. Then we shift all the objects of the base group to create a derived group of objects, as shown in Figure 6.11. The shifting is only along the in-plane directions so the depth of objects in the derived group is the same as the ones in the base group.

We first introduce the configuration of the LPBB phantom. For this phantom, the in-plane locations of the objects in the base group are the same as the objects in the phantom we used for the study on the SG projector (Figure 3.3 and Table 3.1). The background material is configured as breast tissue with 50% glandular/50% fat based on the data from ICRU report 46 [143]. The thickness of the background material is set to be 6 cm. The distance from the objects to the bottom of the volume is set to be 50.6mm. Four derived groups are created by shifting the base group, as shown in Figure 6.12.

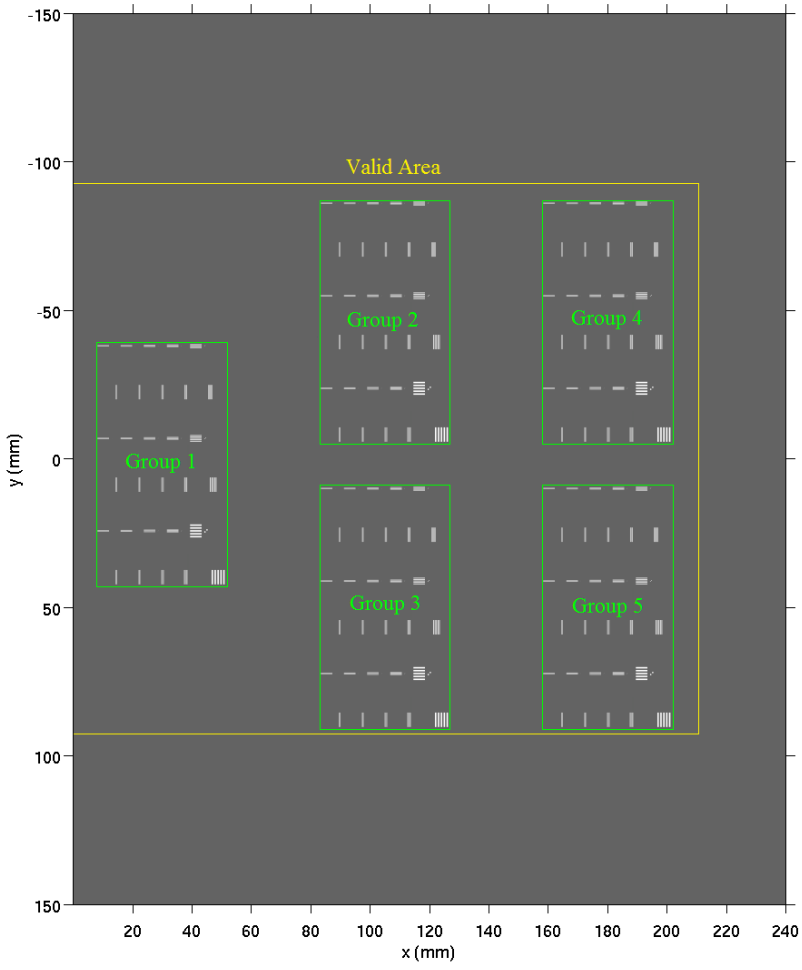

Figure 6.12. The in-plane locations of the objects for the LPBB phantom. Group 1 is the base group and Group 2-5 are the derived groups.

In Figure 6.12, Group 1 is the base group. Group 2 is created by shifting Group 1 by 75 mm along the x-direction and by -48 mm along the y-direction. Group 3 is created by shifting Group 1 by 75 mm along the x-direction and by 48 mm along the y-direction. Both Group 4 and Group 5 are shifted from Group 1 by 150 mm along the x-direction. Their vertical locations are the same as Group 2 and Group 3. We chose these shift distances such that all derived groups are right within the 'valid area' of the slice. If an object is too far from the rotation center (outside the valid area), it will not be imaged within the detector FOV at some or all of the projection angles. Their reconstructed images will be in the region of truncation artifacts that will change its contrast. The 'valid area' refers to the area where an object will image within the detector FOV at all projection angles. The valid area depends on the size of the detector, the maximum projection angles and the depth of the objects. The yellow line in Figure 6.12 shows the valid area based on the depth of the objects and the geometrical parameters of the system.

Next we introduce the configuration of the MC phantom. This phantom only contains BBs of calcium carbonate to simulate MCs in DBT. The in-plane locations of the objects in the base group of the MC phantom are shown in Figure 6.13. Similar to the LPBB phantom, we configured 15 pairs of BBs for this phantom. The diameters of the BBs are identical to the configuration of the LPBB phantom, as shown in Table 6.5.

For the MC phantom, the background material is also set to be breast tissue with 50% glandular/50% fat, based on the data from ICRU report 46 [143]. The thickness of the background material is set to be 6 cm. The distance from the objects to the bottom of the volume is set to be 50.6mm. These configurations are the same as the LPBB phantom. The base group of objects and the four derived groups are shown in Figure 6.14. The valid area is the same as that shown in Figure 6.12. For the MC phantom, Group 2 is created by shifting Group 1 by 75 mm along the x-direction and by -56 mm along the y-direction. Group 3 is created by shifting Group 1 by 75 mm along the x-direction and by 56 mm along the y-direction. Both Group 4 and Group 5 are shifted from Group 1 by 150 mm along the x-direction. Their vertical locations are the same as Group 2 and Group 3. The shift distances along the y-direction for Group 2-5 are different from that of the LPBB phantom. The area that each group occupies is smaller in the MC phantom than that of the LPBB phantom. Therefore for the MC phantom we can shift the base group farther along the y-direction to take better use of the valid area.

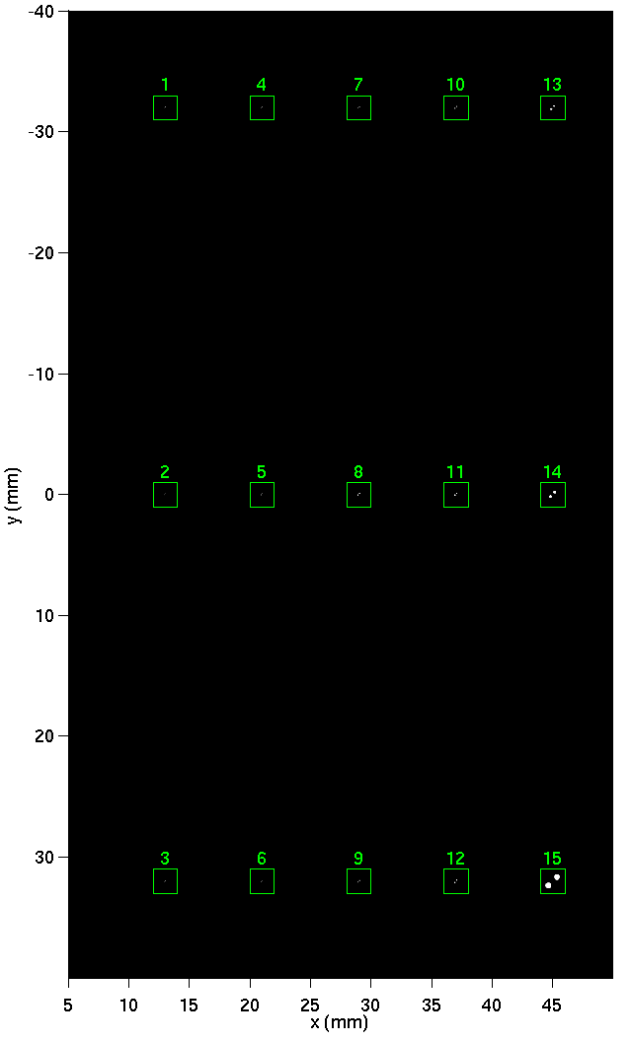

Figure 6.13. The base group of the MC phantom. The background is displayed as black to make the BBs more visible. The background material of this phantom is the same as that of the LPBB phantom, i.e., breast tissue with 50% glandular/50% fat, in Figure 6.12.

Table 6.5. Objects sizes (mm) in the MC phantom. The object set number corresponds to the number next to each box in Figure 6.13. The center-to-center distance between the two BBs in a pair is equal to the BB diameter.

Object Set Number	1	4	7	10	13
BB Diameter	0.053	0.063	0.077	0.100	0.167
Object Set Number	2	5	8	11	14
BB Diameter	0.056	0.067	0.083	0.111	0.250
Object Set Number	3	6	9	12	15
BB Diameter	0.059	0.071	0.091	0.125	0.500

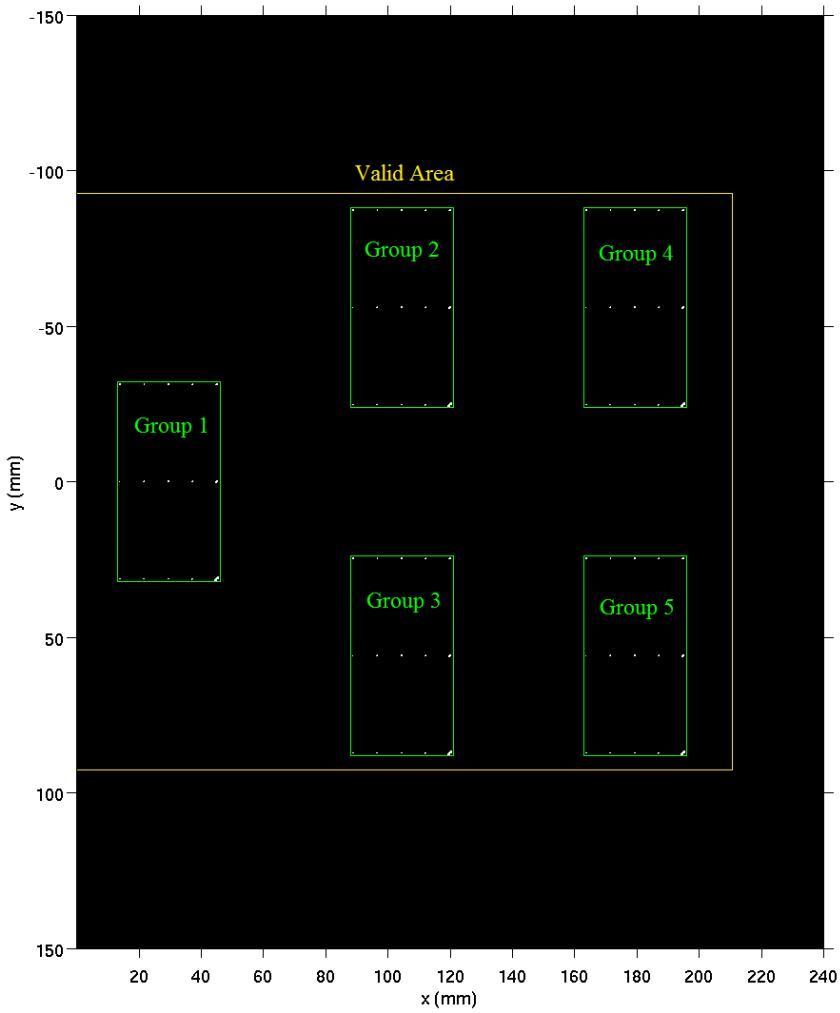

Figure 6.14. The in-plane locations of the objects for the MC phantom. Similar to Figure 6.13, we use the black background to make the BBs more visible.

VI.4.4 Accelerating CatSim with the hybrid simulation

After configuring the phantoms, we need to run CatSim to generate the PV images. Similar to our discussion for the SG projector (Section III.3), the alignment of the objects to the pixel grid will affect the resolution and contrast of the reconstructed objects. To analyze the average effect of source blur on an object randomly aligned with the pixel grid, we simulated projections with the test patterns placed at 25 locations with respect to the pixel grid and the results were averaged over the different alignments. These 25 locations are identical to the study on the SG projector (Section III.3) and the same definition of the "shift tag" L$d_x d_y$ is used.

Before using CatSim for the simulation, we estimate the computation time for the current study. Compared with the simulation for the SG projector, we decrease the oversampling rate of

the detector from 20 to 10. But the oversampling rate of the source has been increased from 1 to 6. These two changes combined result in 9 times of computation time since both the projection images and the rectangular finite-sized source are two dimensional. The size of the detector has increased from 1920 × 2304 to 2400 × 3000, resulting in a 62% increase in the computation time. In addition, in this study we need to simulate two phantoms with four sources as shown in Table 6.4. Although Source 0 uses an oversampling rate of 1, the other three sources all have an oversampling rate of 6. Considering all these factors together and that the previous simulation for the SG projector took a week to finish, the CatSim simulation in this study will take 87.9 weeks, which is obviously impractical.

To solve this problem, we proposed a hybrid simulation method to accelerate CatSim. The basic idea of the method is to use different oversampling rates for different areas with different resolution requirements. For area of the PV images with only uniform breast tissue and no objects, smaller oversampling rates are acceptable to simulate accurate projection values. High oversampling rates are only used for area with the projection of test objects. The hybrid simulation method is derived as below.

We consider the x-ray source to be mono-energetic with energy E. Let γ_s denote the oversampling rate of the source and γ_d denote the oversampling rate of the detector (γ_s and γ_d must be integers in CatSim). Then the rectangular source will be simulated as an array of $\gamma_\mathrm{s} \times \gamma_s$ points. Similarly, one pixel on the detector will be simulated as the average of a $\gamma_\mathrm{d} \times \gamma_\mathrm{d}$ point array. As a result, there exist $\gamma_\mathrm{s}^2\gamma_\mathrm{d}^2$ sub-rays that the projection values need to be calculated. We use i_sd as an index for the sub-rays ($i_\mathrm{sd} = 1,2,\dots,\gamma_\mathrm{s}^2\gamma_\mathrm{d}^2$). For each sub-ray, the projection value $I_\mathrm{p}(i_\mathrm{sd}, E)$ is calculated based on the Lambert-Beer law. The projection value of the entire pixel with the entire source, denoted as $I_\mathrm{p}(E)$, is the average of the projection values of all sub-rays:

$$I_\mathrm{p}(E) = \frac{1}{\gamma_\mathrm{s}^2\gamma_\mathrm{d}^2}\sum_{i_\mathrm{sd}=1}^{\gamma_\mathrm{s}^2\gamma_\mathrm{d}^2} I_\mathrm{p}(i_\mathrm{sd}, E). \tag{6.16}$$

The phantoms we simulate are slabs of the breast tissue embedded with fine objects. We use $d_\mathrm{t}(i_\mathrm{sd})$ to denote the path-length of the i_sdth sub-ray in the slab of the breast tissue if there are no fine objects. We use $d_\mathrm{o}(i_\mathrm{sd})$ to denote path-length of the i_sdth sub-ray within the fine objects. Let $\mu_\mathrm{t}(E)$ and $\mu_\mathrm{o}(E)$ denote the linear attenuation coefficients of the breast tissue and fine objects, we have:

$$I_{\mathrm{p}}(i_{\mathrm{sd}},E)=I_{\mathrm{a}}(i_{\mathrm{sd}},E)\exp\Big(-\big(d_{\mathrm{t}}(i_{\mathrm{sd}})-d_{\mathrm{o}}(i_{\mathrm{sd}})\big)\mu_{\mathrm{t}}(E)-d_{o}(i_{\mathrm{sd}})\mu_{\mathrm{o}}(E)\Big),\tag{6.17}$$

where $I_{\mathrm{a}}(i_{\mathrm{sd}},E)$ denotes the projection value for the i_{sd}th sub-ray when no phantom is present. The subscript 'a' represents 'air', 't' represents 'tissue' and 'o' represents 'object'.

We then have the following expression for $I_{\mathrm{p}}(i_{\mathrm{sd}},E)$:

$$\begin{aligned}
&I_{\mathrm{p}}(i_{\mathrm{sd}},E)=I_{\mathrm{a}}(i_{\mathrm{sd}},E)\exp\Big(-\big(d_{\mathrm{t}}(i_{\mathrm{sd}})-d_{\mathrm{o}}(i_{\mathrm{sd}})\big)\mu_{\mathrm{t}}(E)-d_{o}(i_{\mathrm{sd}})\mu_{\mathrm{o}}(E)\Big)\\
&=I_{\mathrm{a}}(i_{\mathrm{sd}},E)\exp\Big(-d_{\mathrm{t}}(i_{\mathrm{sd}})\mu_{\mathrm{t}}(E)-d_{\mathrm{o}}(i_{\mathrm{sd}})\big(\mu_{\mathrm{o}}(E)-\mu_{\mathrm{t}}(E)\big)\Big)\\
&=\frac{I_{\mathrm{a}}(i_{\mathrm{sd}},E)\exp\big(-d_{\mathrm{t}}(i_{\mathrm{sd}})\mu_{\mathrm{t}}(E)\big)\,I_{\mathrm{a}}(i_{\mathrm{sd}},E)\exp\Big(-d_{\mathrm{o}}(i_{\mathrm{sd}})\big(\mu_{\mathrm{o}}(E)-\mu_{\mathrm{t}}(E)\big)\Big)}{I_{\mathrm{a}}(i_{\mathrm{sd}},E)}\\
&=\frac{I_{\mathrm{t}}(i_{\mathrm{sd}},E)I_{\mathrm{o/t}}(i_{\mathrm{sd}},E)}{I_{\mathrm{a}}(i_{\mathrm{sd}},E)},
\end{aligned}\tag{6.18}$$

where

$$I_{\mathrm{t}}(i_{\mathrm{sd}},E)=I_{\mathrm{a}}(i_{\mathrm{sd}},E)\exp\big(-d_{\mathrm{t}}(i_{\mathrm{sd}})\mu_{\mathrm{t}}(E)\big),\tag{6.19}$$

$$I_{\mathrm{o/t}}(i_{\mathrm{sd}},E)=I_{\mathrm{a}}(i_{\mathrm{sd}},E)\exp\Big(-d_{\mathrm{o}}(i_{\mathrm{sd}})\big(\mu_{\mathrm{o}}(E)-\mu_{\mathrm{t}}(E)\big)\Big).\tag{6.20}$$

The physical meanings of $I_{t}(i_{\mathrm{sd}},E)$ and $I_{\mathrm{o/t}}(i_{\mathrm{sd}},E)$ are clear. $I_{t}(i_{\mathrm{sd}},E)$ is the projection value for the i_{sd}th sub-ray if the phantom only has the slab of breast tissue. $I_{\mathrm{o/t}}(i_{\mathrm{sd}},E)$ is the projection value for the i_{sd}th sub-ray if the phantom only has the fine objects, but made of a different material that has the attenuation coefficient of $\mu_{\mathrm{o}}(E)-\mu_{\mathrm{t}}(E)$.

The value $d_{\mathrm{t}}(i_{\mathrm{sd}})$, which denotes the path-length of the i_{sd}th sub-ray within the slab of breast tissue, is slowly changing and is approximately constant given the small size of the source and the pixel. Similarly, the air scan value $I_{\mathrm{a}}(i_{\mathrm{sd}},E)$ is also slowly changing and approximately constant. So we have:

$$I_{\mathrm{t}}(i_{\mathrm{sd}},E)=I_{\mathrm{t}}(E),\tag{6.21}$$

$$I_{\mathrm{a}}(i_{\mathrm{sd}},E)=I_{\mathrm{a}}(E),\tag{6.22}$$

where $I_{\mathrm{t}}(E)$ and $I_{\mathrm{a}}(E)$ denote the averaged projection value for the entire pixel with only the slab of breast tissue or with only air.

Combining Equations 6.16, 6.18, 6.21 and 6.22, we have:

$$
\begin{aligned}
I_{\mathrm{p}}(E) &= \frac{1}{\gamma_{\mathrm{s}}^2\gamma_{\mathrm{d}}^2}\sum_{i_{\mathrm{sd}}=1}^{\gamma_{\mathrm{s}}^2\gamma_{\mathrm{d}}^2} I_{\mathrm{p}}(i_{\mathrm{sd}},E) \\
&= \frac{1}{\gamma_{\mathrm{s}}^2\gamma_{\mathrm{d}}^2}\sum_{i_{\mathrm{sd}}=1}^{\gamma_{\mathrm{s}}^2\gamma_{\mathrm{d}}^2} \frac{I_t(i_{\mathrm{sd}},E)I_{\mathrm{o/t}}(i_{\mathrm{sd}},E)}{I_{\mathrm{a}}(i_{\mathrm{sd}},E)} \\
&= \frac{1}{\gamma_{\mathrm{s}}^2\gamma_{\mathrm{d}}^2}\sum_{i_{\mathrm{sd}}=1}^{\gamma_{\mathrm{s}}^2\gamma_{\mathrm{d}}^2} \frac{I_{\mathrm{t}}(E)I_{\mathrm{o/t}}(i_{\mathrm{sd}},E)}{I_{\mathrm{a}}(E)} \\
&= \frac{I_{\mathrm{t}}(E)}{I_{\mathrm{a}}(E)}\frac{1}{\gamma_{\mathrm{s}}^2\gamma_{\mathrm{d}}^2}\sum_{i_{\mathrm{sd}}=1}^{\gamma_{\mathrm{s}}^2\gamma_{\mathrm{d}}^2} I_{\mathrm{o/t}}(i_{\mathrm{sd}},E) \\
&= \frac{I_{\mathrm{t}}(E)I_{\mathrm{o/t}}(E)}{I_{\mathrm{a}}(E)}
\end{aligned}
\tag{6.23}
$$

where $I_{\mathrm{o/t}}(E)$ denote the averaged projection value of the entire pixel if the phantom only has fine objects of a material with the attenuation coefficient of $\mu_{\mathrm{o}}(E) - \mu_{\mathrm{t}}(E)$.

In summary, to get the simulation value $I_{\mathrm{p}}(E)$, we need to use simulation to calculate three values: $I_{\mathrm{a}}(E)$, $I_{\mathrm{t}}(E)$ and $I_{\mathrm{o/t}}(E)$. $I_{\mathrm{a}}(E)$ can be calculated without the phantom and with low oversampling rates. $I_{\mathrm{t}}(E)$ can be calculated with low oversampling rates with a phantom configuration that only has the slab of breast tissue. On the other hand, $I_{\mathrm{o/t}}(E)$ needs to be calculated with high oversampling rates. CatSim has been optimized such that if a pixel on the detector is not affected by any objects, it will not be oversampled. Since $I_{\mathrm{o/t}}(E)$ is calculated with a phantom of only fine objects, most pixels on the detector plane will not be oversampled so that the calculation of $I_{\mathrm{o/t}}(E)$ is much faster than directly simulating $I_{\mathrm{p}}(E)$ with high oversampling rates. Therefore, by calculating $I_{\mathrm{a}}(E)$, $I_{\mathrm{t}}(E)$ and $I_{\mathrm{o/t}}(E)$ separately, we implemented the simulation with low oversampling rates for the breast tissue and high oversample rates for the fine objects. We call this the hybrid simulation method for CatSim.

There are some details to clarify for the actual implementation of the hybrid simulation:

First, in CatSim a material is defined with its density and mass ratio of each chemical element. The attenuation coefficient of the material is then derived with these parameters, given the x-ray photon energy *E*. It is difficult to define a material that satisfies $\mu_{\mathrm{o/t}}(E) = \mu_{\mathrm{o}}(E) - \mu_{\mathrm{t}}(E)$ for arbitrary *E*. To solve this problem, we modified the main script of CatSim that allows us to specify an "offset" material. During the simulation, the attenuation coefficient of the offset material is subtracted from the attenuation coefficient of the material of the objects. By using breast tissue as the offset material, we can simulate $\mu_{\mathrm{o/t}}(E)$ easily.

Second, the hybrid simulation method can only be applied for mono-energetic x-ray. To get the simulation results for the full polyenergetic x-ray spectrum, we need to apply the hybrid simulation to each energy bin of the x-ray spectrum and combine all of the results to get the final simulated PV image. CatSim allows outputting the simulation results of each energy bin. So we do not need to create a CatSim configuration file for each energy bin.

Third, as we mentioned at the beginning of this section, we need to shift the fine objects at 25 locations with respect to the pixel to simulate the PVs. Since $I_{\mathrm{a}}(E)$ and $I_{\mathrm{t}}(E)$ are not affected by the shifts of the objects, they are only calculated once for the 25 locations, saving a lot of computation time.

Fourth, as observed in the study on the SG projector, shifting the horizontal line pairs horizontally does not affect their contrast. The contrasts of horizontal line pairs with shift tags 'L0d_y', 'L1d_y', …, 'L4d_y' are identical, where d_y denotes an arbitrary integer from 0 to 4. Similarly, for the vertical line pairs, the contrasts for shift tags 'Ld_x0', 'Ld_x1', …, 'Ld_x4' are also identical, where d_x denotes another arbitrary integer from 0 to 4. In our simulation, each shift of the digital phantom is specified by a phantom configuration file. To save simulation time without changing the shift-averaged contrasts, we only simulate both the line pairs and BBs for 9 shift tags: 'L00', 'L10', 'L20', 'L30', 'L40', 'L01', 'L02', 'L03' and 'L04'. The phantom configuration files of the other 16 shift locations do not include the line pairs to save computation time. But they still include the BBs, since all 25 location shifts are required to obtain reliable location-averaged contrasts for BBs.

With the hybrid simulation method for CatSim and the implementation details we introduced above, the simulation for all sources and location shifts took about two weeks to complete.

VI.4.5 Figures of merit for line pairs and BBs

To quantitatively analyze the image quality with different source blurs, we need to define FOMs for the line pairs and BBs. For the BBs, we use the same definition for the contrast as our study on the SG projector (Equation 3.13 in Section III.5.4). For the line pairs, we use the same method as our study on the SG projector to obtain their profiles as described in Section III.5.4. But after obtaining the profiles, a different method is used to calculate their contrasts.

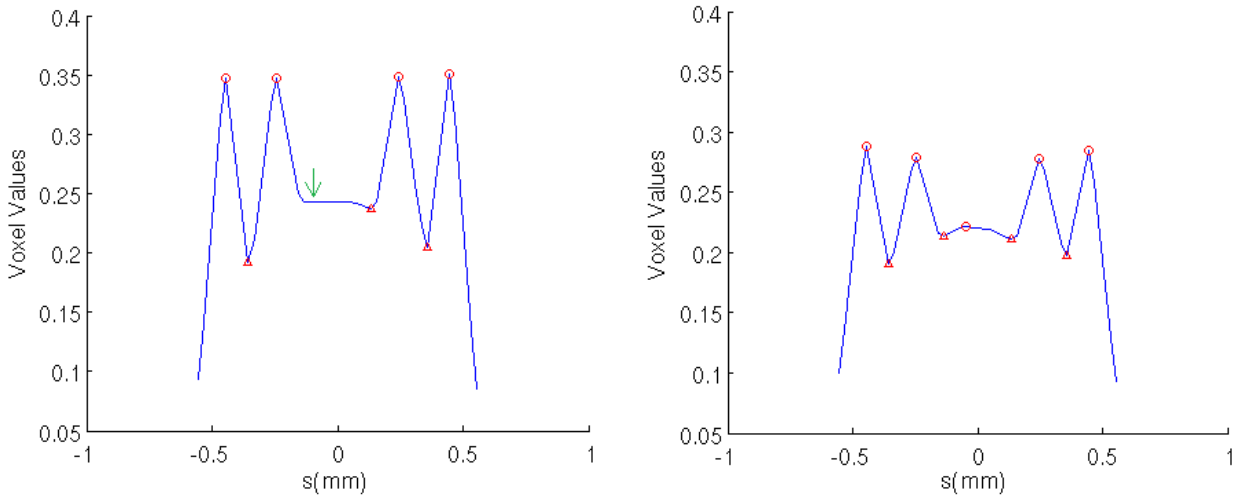

(a) (b)

Figure 6.15. The profiles of the reconstructed horizontal line pairs of spatial frequency f = 4.5/mm in Group 1 for the shift L00 for (a) Source 1; (b) Source 2. The circles mark the detected peaks and the triangles mark the detected valleys.

The reason we changed the calculation of contrast for line pairs can be explained with Figure 6.15. Figure 6.15(a) shows the profile of a set of reconstructed horizontal line pairs when Source 1 was used to simulate the projections. For this set of line pairs, only four peaks are detected. Therefore its contrast is considered to be zero with our previous calculation and criterion. Figure 6.15(b) shows the results with Source 2. The same set of line pairs has an additional detectable peak in the center. Although this peak has a small voxel value, the values of the other four detectable peaks are high enough such that a high contrast will be obtained for this set of line pairs. The same four peaks are much stronger in Figure 6.15(a), but their contribution to the contrast is neglected because of the undetectable peak in the center, leading to the conclusion that Source 2 makes the line pairs more resolvable than Source 1. In fact, the center of the profile in Figure 6.15(a) is almost a detectable peak. If the value at the green arrow in Figure 6.15(a) decrease by 0.01/mm, it is possible that we will get a non-zero contrast and will find that Source 1 generates more resolvable line pairs than Source 2. In summary, our previous calculation of the contrast for line pairs is too sensitive to barely detectable peaks of the profiles and could result in misleading conclusions when comparing different conditions.

The new method for calculating the contrast of line pairs is explained in Figure 6.16. In our phantoms, the line pairs are analytically configured. Their exact locations are known so we can calculate the ideal profile based on the true locations of the line pairs. The magenta curves in

Figure 6.16 show the ideal profile with the voxel value of 1. As expected, the peaks of the reconstructed profile match the peaks of the ideal profile. So we can use the ideal profile to help calculate the contrast of the reconstructed line pairs. The part of the ideal profile with the voxel value of 1 is called the 'peak region', which consists of 5 sections. Between the first and the last sections of the peak region, 4 sections of the ideal profile have the voxel value of 0. These 4 sections are called the 'valley region'. We calculate the mean values of the reconstructed profile in the peak region and in the valley region. The contrast is then calculated as the difference between these two mean values, normalized to the contrast value of the line pairs in the voxelized image of the analytical phantom, which had the same constant value for all line pair frequencies. With this new calculation, the contrast of line pairs is insensitive to weak peaks as shown in Figure 6.15.

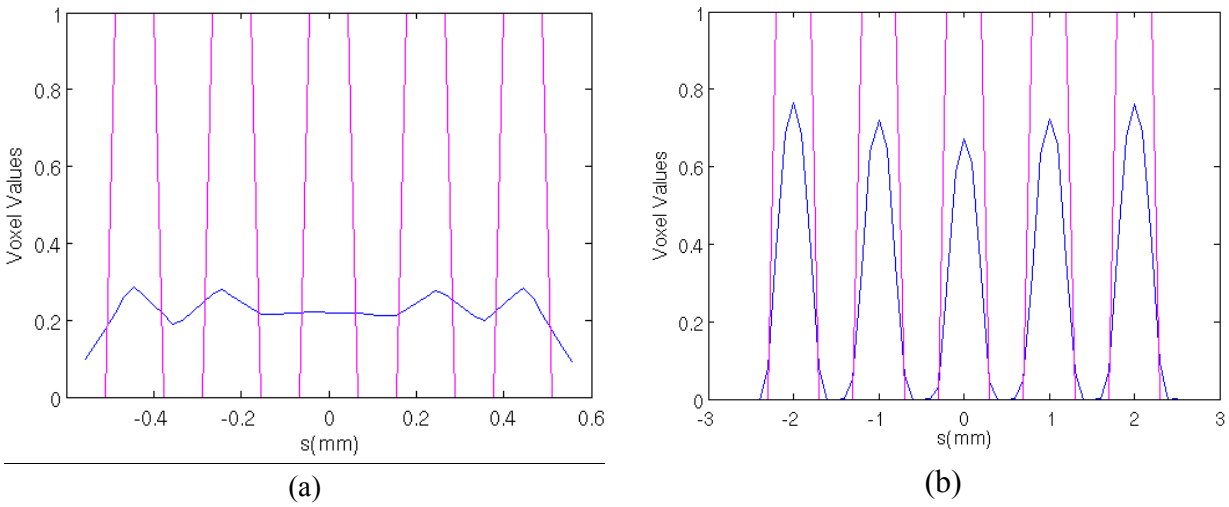

Figure 6.16. The blue curve shows the profile of the reconstructed horizontal line pairs for the shift L00 for Source 2. The magenta curve shows the ideal profile of the line pairs with the peak voxel value of 1. The spatial frequencies are (a) $f = 4.5$/mm, (b) $f = 1$/mm.

In the next section, we will use our new method to calculate the contrast for the line pairs. Similar to our study on the SG projector, the contrast of line pairs will be plotted as a function of the spatial frequency of the line pairs for each condition we included in the study. These contrast-verse-frequency curves are similar to the commonly used MTF in x-ray imaging, but they are calculated with rectangular waves instead of sinusoidal functions. Despite the difference, these curves still reflect the spatial resolution of the reconstruction with the influence of source blur and other factors.

VI.5 Simulating the effect of source blur with CatSim: results and discussions

In this section, we will quantitatively analyze the objects reconstructed from projection images simulated with different sources. Five SART iterations were performed for all reconstructions. The three types of objects (horizontal line pairs, vertical line pairs and BBs) will be analyzed one by one. The FOM we described in Section VI.4.5 are calculated for all objects and all shifts relative to the pixel grid. All curves we show in this section are the average result of all the shifted locations for the objects. The mean contrast curves are compared for the different test objects and different source blur conditions.

VI.5.1 The horizontal line pairs in the LPBB phantom

Figure 6.17 shows the curves of mean contrast as a function of the spatial frequency for the horizontal line pairs in the LPBB phantom. The horizontal line pairs are perpendicular to the source motion direction. As shown in Figure 6.17(a), for Source 0, the reconstructed line pairs in different groups of object present similar contrast at different spatial frequencies, indicating that the contrast does not depend on the locations. For Source 3, the observation is similar as shown in Figure 6.17(b). We did not show the curves for Source 1 and Source 2, but the same observation has been confirmed. When a set of horizontal line pairs is shifted horizontally, the contrast of a set of line pairs does not change. As a result, it is reasonable that the horizontal line pairs will have the same contrast in Group 3 and Group 5, or in Group 2 and Group 4. The interesting finding is that although Group 2 and Group 3, or Group 4 and Group 5 are vertically shifted from Group 1 by 48 mm in the opposite directions, they all have very similar curves of contrast for all the sources we simulated. This observation could be explained by the relatively large scan angle we used in the simulation. As described in Section VI.4.1, the distance from the rotation axis to the source is 640 mm and that our maximum projection angle is $\pm 30°$. The motion of the source is ± 320 mm along the *y*-direction between the maximum projection angles on both sides. A distance of 48 mm is small compared with the total motion of the source, which is 640 mm. As a result, for the same spatial frequency, the contrast of a set of horizontal line pairs does not change much among different groups of objects. Because of the limited "valid" region that we can prevent TPA from influencing the reconstructed images of the test objects, we are not able to compare the horizontal resolution in the regions near the two ends of the imaged volume so that it is unclear whether this observation still holds in those regions.

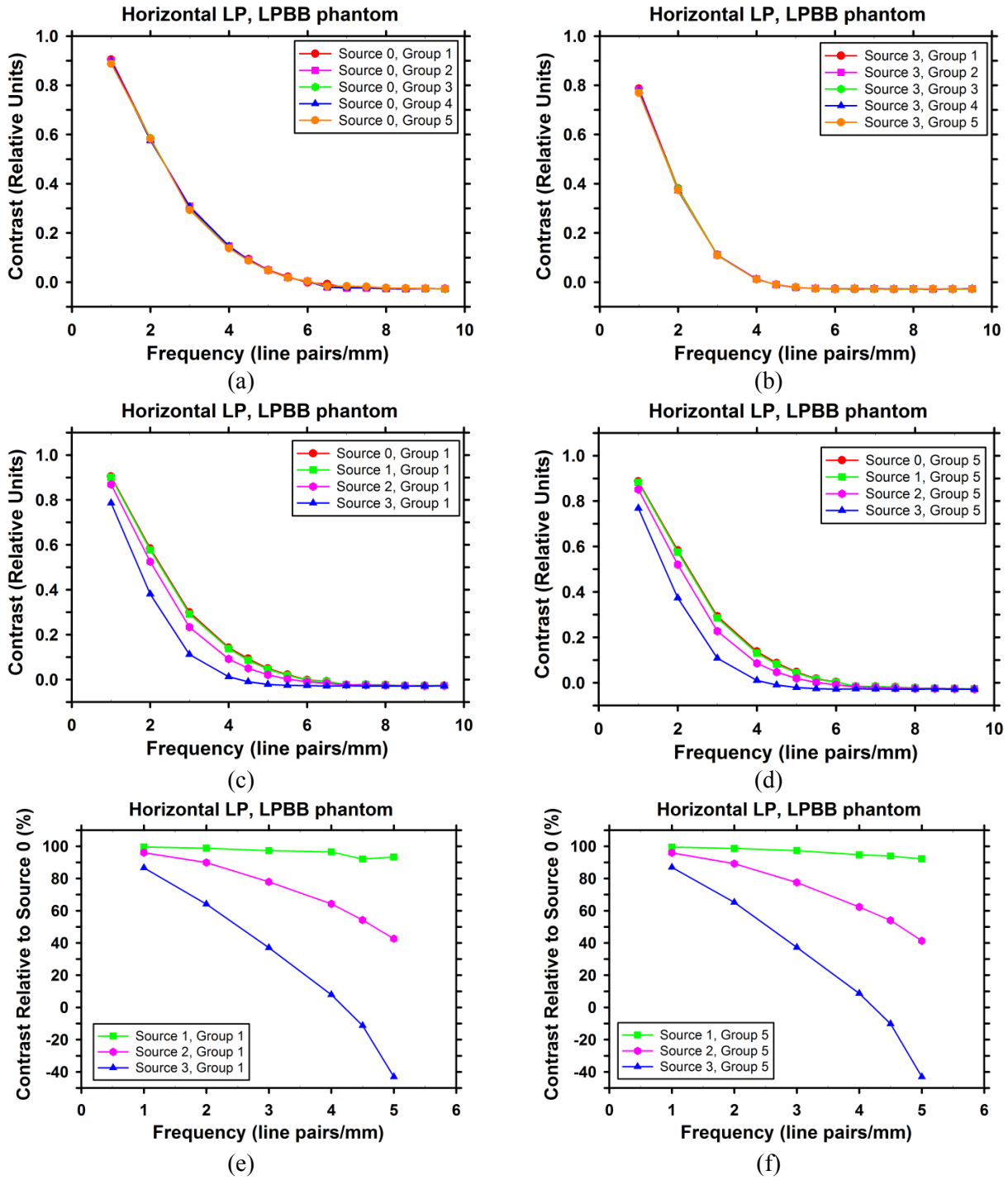

Figure 6.17. Dependence of the mean contrast of the horizontal line pairs on the group of the objects and the source in the LPBB phantom: (a) The dependence on the group of the objects for Source 0; (b) The dependence on the group of objects for Source 3; (c) The dependence on the source for Group 1; (d) The dependence on the source for Group 5; (e) Contrast of Source 1, 2 and 3 relative to Source 0 for Group 1; (f) Contrast of Source 1, 2 and 3 relative to Source 0 for Group 5.

Figure 6.17(c) and (d) show the dependence of the contrast on the source for the horizontal line pairs in Group 1 and Group 5. Figure 6.17(e) and (f) show the contrast curves of Source 1, 2 and 3 relative to Source 0 at different spatial frequencies, representing how much spatial resolution along the vertical direction is preserved with the finite-sized sources compared with the ideal point source. The curves in Figure 6.17(e) and (f) are plotted up to the Nyquist frequency (5 line pairs/mm) since the line pairs with Source 0 are almost non-resolvable at higher spatial frequencies. For the spatial frequencies above the Nyquist frequency, the resolution of the line pairs is mainly constrained by the pixel size, rather than the influence of the source blur. Comparing different sources in this frequency range does not provide much meaningful information.

Figure 6.17(c) shows that the contrast of horizontal line pairs is almost identical for Source 0 and Source 1 at different spatial frequencies. Since Source 0 is the ideal point source and Source 1 has a finite size, the green curve is slightly lower than the red curve, indicating a small decrease in the contrast. Figure 6.17(d) shows very similar results, which is expected considering that the contrast curves of different groups almost overlap in Figure 6.17(a) and (b). Figure 6.17(e) and (f) show that Source 1 preserves most of the contrast of the ideal point source, ranging from 92.1% to 99.5%. Since Source 1 has a typical focal spot size of a DBT system (~0.3 mm) if the source is stationary at exposure, Figure 6.17(c)-(f) indicate that treating the 0.3 mm source as a point source does not affect the reconstructed quality for the horizontal line pairs if the pixel size of the detector or at reconstruction is 0.1 mm.

Figure 6.17(c) and (d) also show that the contrast of horizontal line pairs decreases significantly if Source 2 or Source 3 is used. As shown in Figure 6.17(e) and (f), the relative decrease of the contrast for Source 2 and Source 3 is substantial at higher spatial frequencies, indicating that the source blur has stronger influence on small objects. For the spatial frequencies higher than about 5 line pairs/mm, the horizontal line pairs are not resolvable with Source 3. The negative relative contrasts for Source 3 near the Nyquist frequency indicate a phase shift of 180° compared with the ideal profile. If Source 2 is used, the horizontal line pairs are resolvable near the Nyquist frequency although the contrast has decreased compared with Source 0. We can also see that the difference between Source 0 and Source 2 is smaller than the difference between Source 2 and Source 3. Figure 6.17(e) and (f) show that the contrast loss with Source 2 compared with the point source is between 4.0% and 60% in the frequency range of 1 to 5 line pairs/mm.

Since the motion of the x-ray source is along the vertical direction, the horizontal line pairs are more sensitive to the extra source blur from the motion than the vertical line pairs and the BBs. In summary, if the focal spot is not stationary such that the effective size of the x-ray source is 1mm (Source 2) or 2mm (Source 3) along the direction of the motion of the x-ray tube, the reconstructed contrast of horizontal line pairs, i.e., the spatial resolution in the direction of source motion, will decrease. Compared with Source 3 where the horizontal line pairs are non-resolvable at 5 line pairs/mm, Source 2 preserves about 40% of the contrast of Source 0 but such a decrease in resolution can have a substantial impact on small objects such as MCs.

VI.5.2 The vertical line pairs in the LPBB phantom

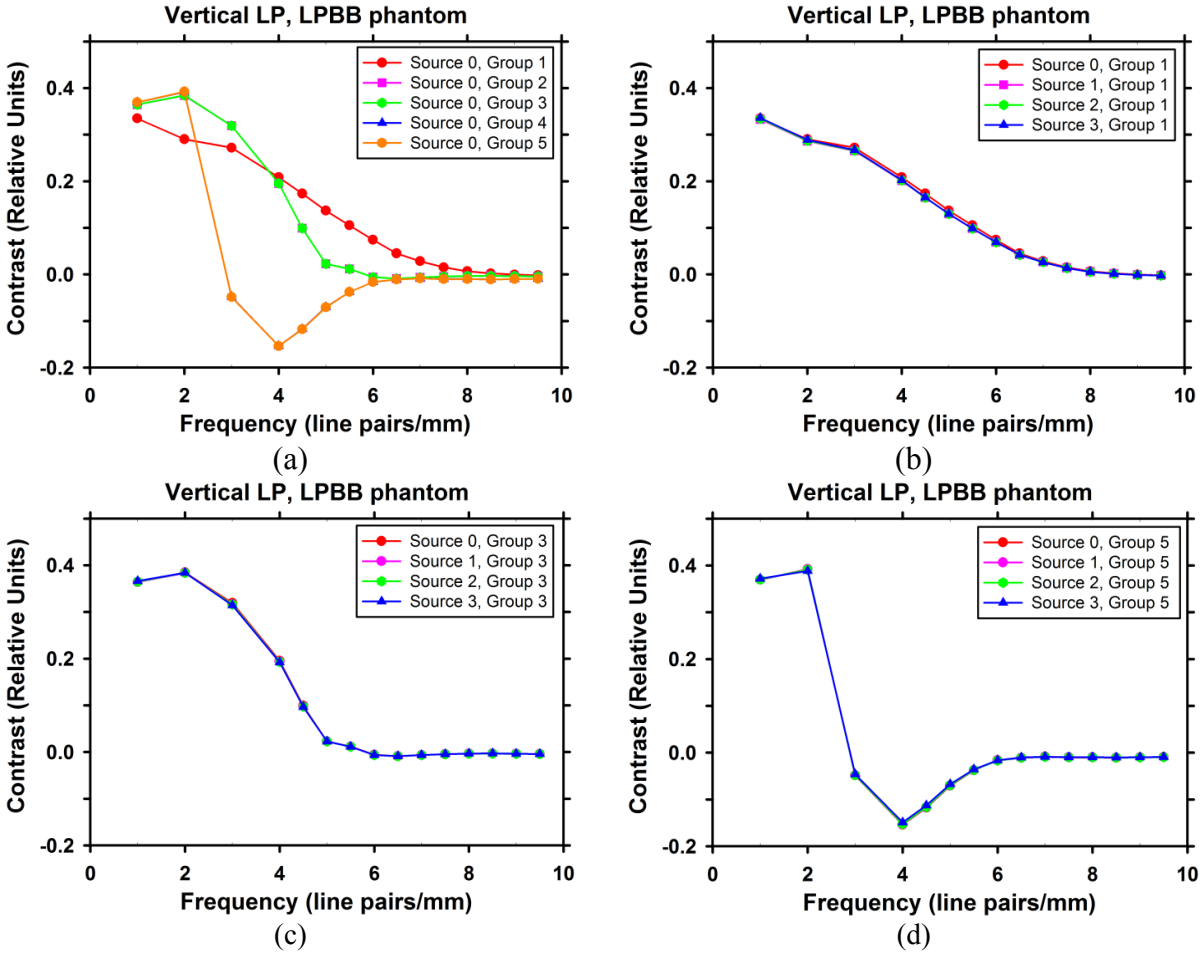

Figure 6.18. Dependence of the mean contrast of the vertical line pairs on the group of the objects and the source in the LPBB phantom: (a) The dependence on the group of the objects for Source 0; (b) The dependence on the source for Group 1; (c) The dependence on the source for Group 3; (d) The dependence on the source for Group 5.

Figure 6.18 shows the contrast curves as a function of the frequency for the vertical line pairs in the LPBB phantom. Figure 6.18(a) shows the dependence of the contrast of the vertical line pairs on the group of the object with Source 0 used in the simulation of the projection images. We can observe that the curves of Group 2 and Group 3 are identical. This is expected since Group 2 can be moved vertically to overlap with Group 3 or vice versa as shown in Figure 6.14. For the same reason, the curves of Group 4 and Group 5 are also almost identical in Figure 6.18(a). We can also observe that the contrast curve of Group 1 is very different from the contrast curves of Group 2 and Group 3. The contrast curves of Group 4 and Group 5 are more different with negative contrasts for spatial frequencies higher than 2 line pairs/mm. The meaning of the negative contrast is that the reconstructed line pairs has a phase shift of about 180° compared with the ideal profile of the line pairs, such that the bright lines become dark and the dark lines become bright. Generally, Figure 6.18(a) shows that the vertical line pairs of high spatial frequencies are less resolvable if they are farther away from the chest wall even though the focal spot dimension perpendicular to the line pairs decreases as the distances from the chest wall (x-direction) increases. The comparison in Figure 6.18(a) for the other three sources is not shown since the contrast of vertical line pairs is almost independent of the source, as shown in Figure 6.18(b) – (d).

Figure 6.18(b) – (d) show the dependence of contrast on the source size for the vertical line pairs in Group 1, Group 3 and Group 5. Different from the horizontal line pairs, the contrast of the vertical line pairs is not obviously affected by the source sizes used in the simulation, as indicated by the overlapping curves. The curves for Group 2 and Group 4 are very similar to the curves for Group 3 (Figure 6.18(c)) and Group 5 (Figure 6.18(d)), respectively as shown in Figure 6.18(a) and explained above. This observation is reasonable since compared with Source 1, the extra blur caused by the motion of the source for Source 2 and Source 3 is mainly along the vertical direction. Blurring a set of vertical line pairs along the vertical direction will not affect its contrast.

The only noticeable difference among the sources can be observed in Figure 6.18 (b), where the contrast curve with Source 0 is slightly higher than the overlapping contrast curves with Source 1, Source 2 and Source 3. This is because Source 1, Source 2 and Source 3 have the same target angle ϕ and the same value of h_1 as shown in Table 6.4. The finite h_1 value results in a source blur along the horizontal direction and will therefore affect the vertical line pairs.

Therefore, for Source 1, Source 2 and Source 3, a small decrease in the contrast compared with the ideal point source (Source 0) is observed. Such an effect is weaker for Group 3 (Figure 6.18(c)) and Group 5 (Figure 6.18(d)) since the effective source blur along the horizontal direction is smaller for locations farther away from the chest wall.

To summarize our observations, if the source is of a typical focal spot size (~0.3 mm) and is stationary during exposure, treating the finite-sized source as a point source does not affect the reconstructed quality for the vertical line pairs if the pixel size of the detector or at reconstruction is 0.1 mm. Even if the source is not stationary such that the effective size of the source blur is as large as 1mm (Source 2) or 2mm (Source 3) along the direction of the motion of the x-ray tube, there is essentially no change in the reconstructed contrast of vertical line pairs.

VI.5.3 The BBs in the LPBB phantom and the MC phantom

Figure 6.19 shows the dependence of the contrast of BBs on the group of the object for Source 0 and Source 3 in the LPBB phantom and the MC phantom. For both sources in both phantoms, the contrast of the BBs has strong dependence on the group of objects or the locations of objects. Generally speaking, the contrast of the BBs is higher in Group 1 than in Group 2/Group 3 and it further decreases in Group 4/Group 5. In summary, the contrast of the BBs decreases as their distance from the rotation center increases. The dependence of the contrast of the BBs on the group of objects is not as obvious as that of the vertical line pairs shown in Figure 6.18(a). In Figure 6.19(a) - (d), the difference between the curves of Group 1 and Group 5 is smaller than the difference between Group 1 and Group 5 in Figure 6.18(a). But the difference between Group 1 and Group 5 in Figure 6.19 is much more obvious than that in Figure 6.17(a), where the contrast of horizontal line pairs is almost independent of the group of objects. Therefore the level of dependence of the contrast of the BBs on the location of objects falls between the level of the horizontal line pairs and the level of the vertical line pairs as expected because the contrast of BBs is affected by the resolution of the imaging system in both the horizontal and the vertical directions.

Another interesting observation in Figure 6.19 is the difference in contrast curves between Group 2 and Group 3 and the difference between Group 4 and Group 5. In Figure 6.19, we can see that with either source or with either phantom, the contrast of the BBs in Group 3 is higher than that in Group 2. The contrast of BBs in Group 5 is also consistently higher than that in

Group 4. Group 2 and Group 4 are in the upper half of the reconstructed slice. Group 3 and Group 5 are in the lower half as shown in Figure 6.14. In Figure 6.17 (a)(b) and Figure 6.18(a), we did not observe the difference between Group 2 and Group 3 or between Group 4 and Group 5 for the horizontal or the vertical line pairs.

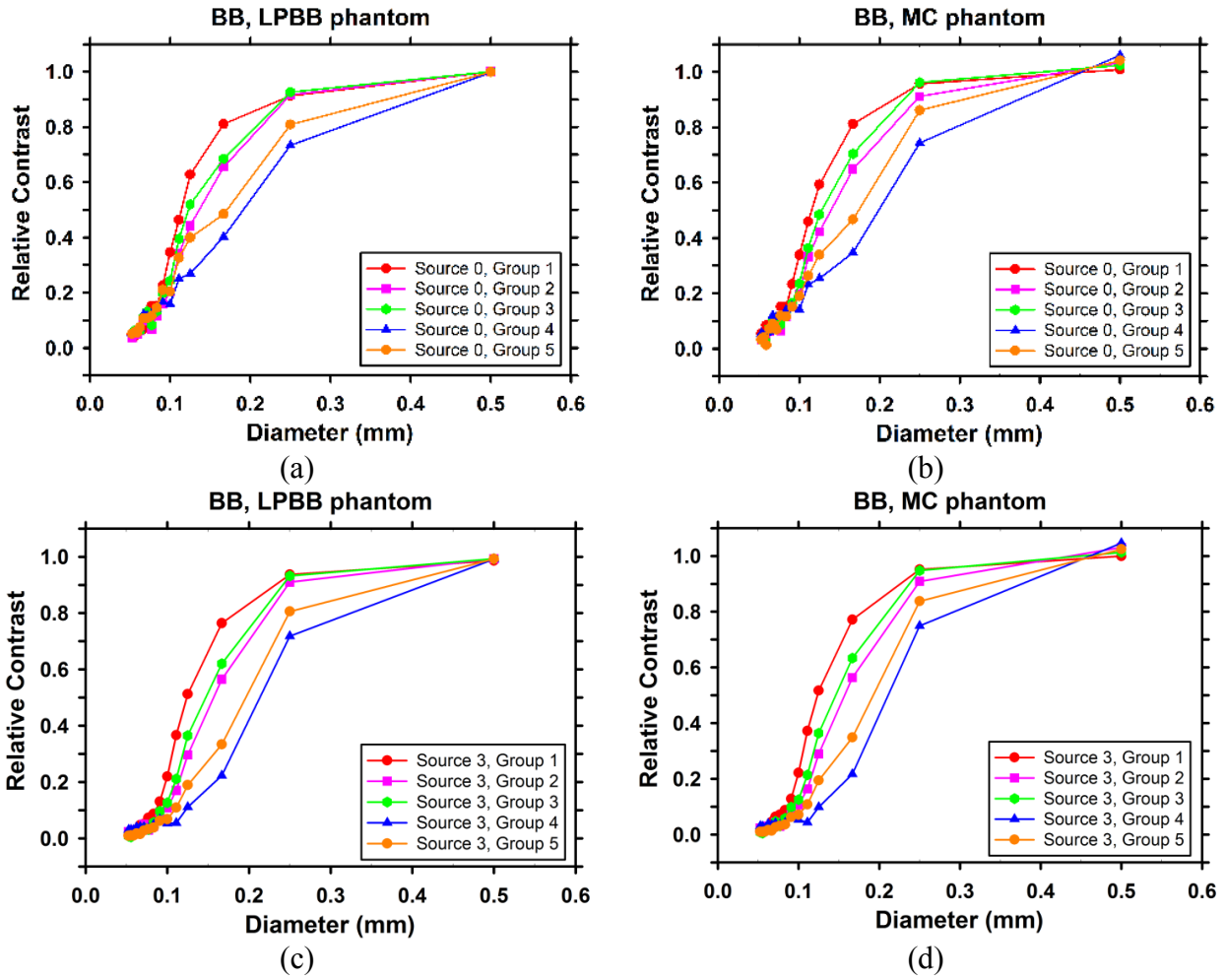

Figure 6.19. Dependence of the mean contrast of the BBs on the group of objects for: (a) Source 0, the LPBB phantom; (b) Source 0, the MC phantom; (c) Source 3, the LPBB phantom; (d) Source 3, the MC phantom.

The difference between Group 2 and Group 3 or between Group 4 and Group 5 may be explained with Figure 6.20. We use Group 4 and Group 5 as an example but the explanation for Group 2 and Group 3 is similar. The configuration of the phantom has been described in Section VI.4.3 that Group 4 and Group 5 are generated by shifting Group 1. No vertical flip is done after the shifting. As a result, the alignments of BBs in Group 4 and Group 5 are not symmetrical

about the x-axis. This asymmetry may have resulted in the difference in the contrast of the reconstructed BBs. For example, during reconstruction, more PVs will cast a shadow of the BBs to the gap between the BBs for the pair in Group 4 than that for the pair in Group 5, thereby reducing the contrast between the BB and the gap and therefore the resolution. If Group 5 were arranged as shown by Group 6, it would be symmetrical about the x-axis with Group 4 and might have similar contrast curves. Since we have not studied an arrangement like Group 6, this is yet to be proven.

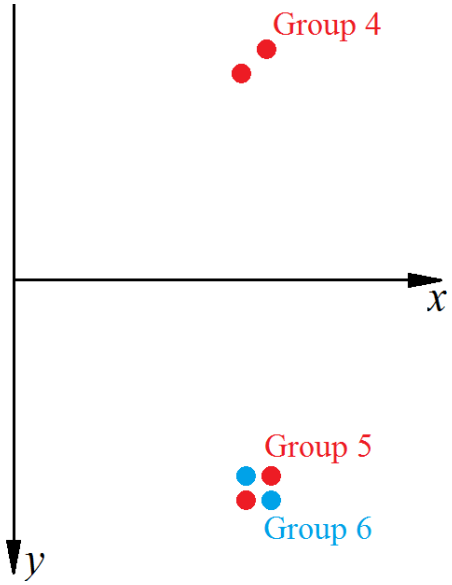

Figure 6.20. Alignment of BBs in Group 4 and Group 5. The Alignment of BBs in Group 2 and Group 3 are similar.

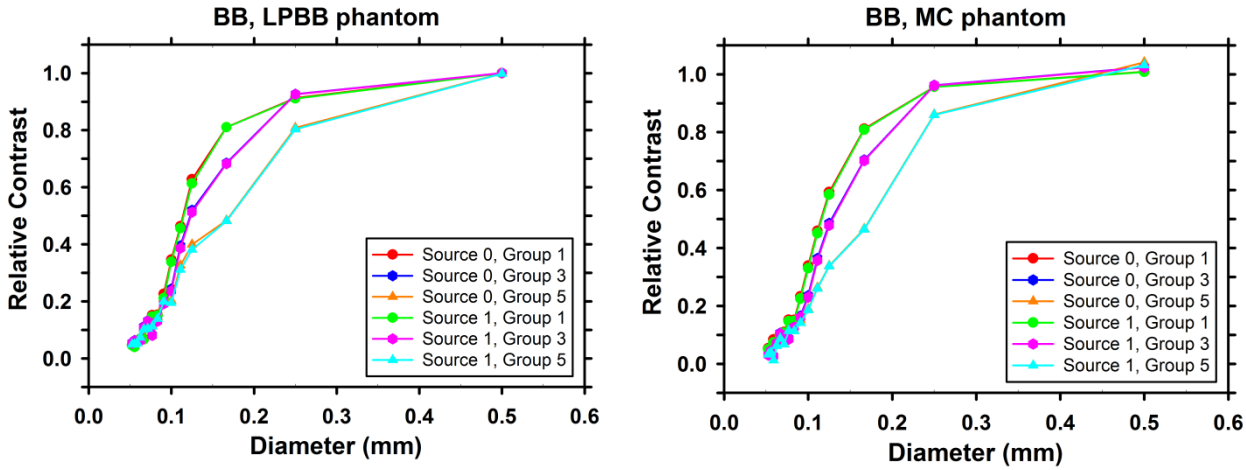

(a) (b)

Figure 6.21. Comparison between Source 0 and Source 1 for BBs in three groups of objects for: (a) the LPBB phantom; (b) the MC phantom.

Figure 6.21 shows the comparison between Source 0 and Source 1. As can be seen, for any one of the three groups of objects (Group 1, Group 3 and Group 5), the contrast curves of Source 1 are just slightly lower than the contrast curves of Source 0. Group 2 and Group 4 are not shown since the observation is similar. We already observed in Figure 6.17(c)(d) and Figure 6.18(b)-(d) that the difference between Source 0 and Source 1 is minimal. So Figure 6.21 once again supports the observation that treating a finite-sized source of 0.3mm as a point source may not degrade the reconstructed quality substantially if the x-ray tube is stationary during the exposure of the projections.

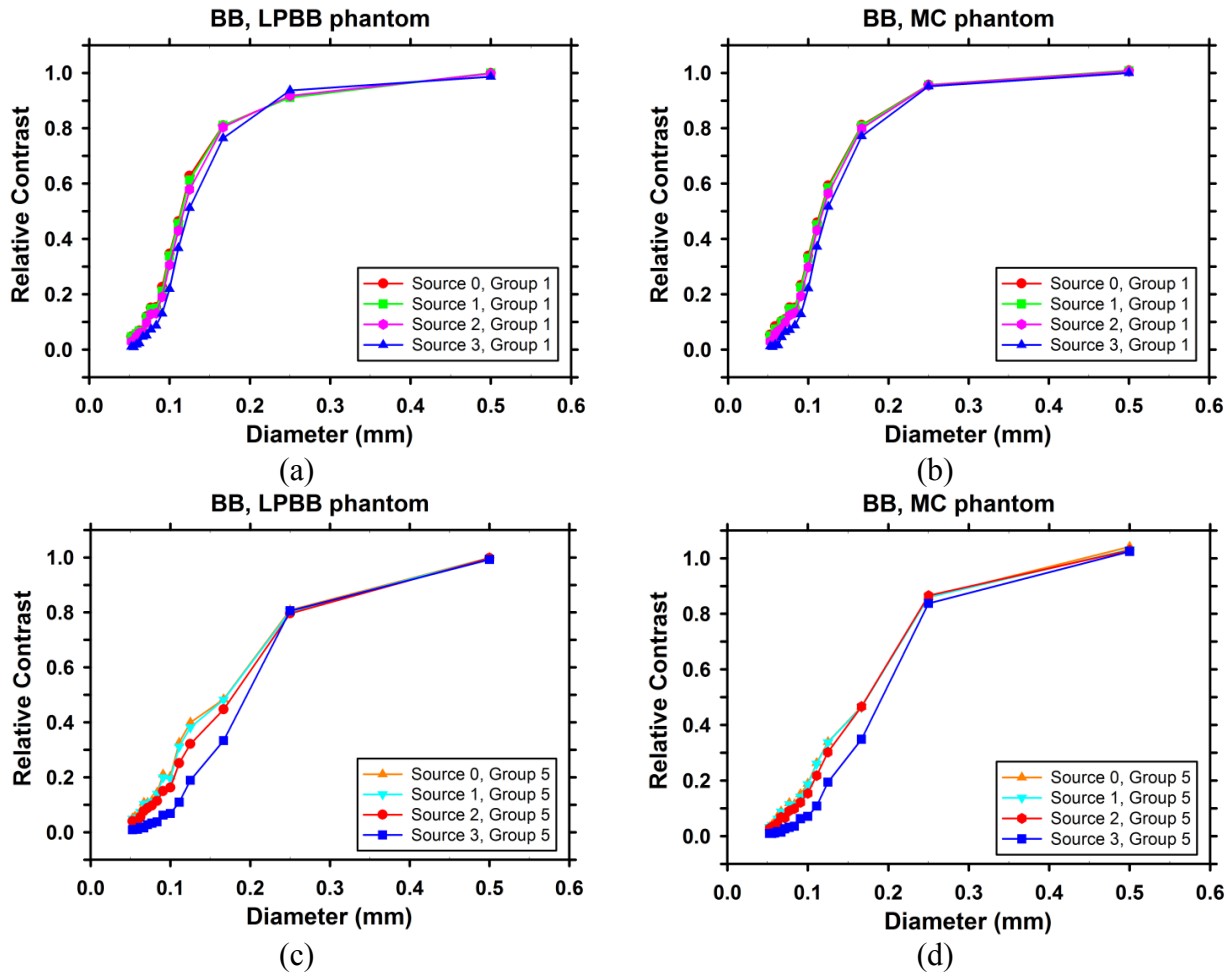

Figure 6.22. Dependence of the mean contrast of the BBs on the source for: (a) Group 1 of the LPBB phantom; (b) Group 1 of the MC phantom; (c) Group 5 of the LPBB phantom; (d) Group 5 of the MC phantom.

Figure 6.22 shows the dependence of the contrast of the BBs on the source for Group 1 and Group 5. In each graph, we fix the group number and compare the four sources. We observe that

for BBs with a diameter larger than 0.15 mm, the two BBs in the pair are highly resolvable with a contrast close to or higher than 0.8. The difference of the four sources is small and not significant for these BBs. For BBs with a diameter smaller than 0.15 mm but larger than 0.10 mm, the decrease in contrast with Source 2 and Source 3 becomes noticeable. For BBs with a diameter of 0.10 mm or smaller, the contrast of BBs decreases more significantly, especially with Source 3. For example, in the LPBB phantom, the contrast of the BBs of the diameter 0.1mm is 0.347 when Source 0 is used. The contrast decreases by 12% to 0.306 when Source 2 is used and by 37% to 0.219 when Source 3 is used in the simulation. Similar to the horizontal line pairs (Figure 6.17(c) and (d)), we can observe in Figure 6.22(a) and (b) that the difference between Source 0 and Source 2 is smaller than the difference between Source 2 and Source 3.

Figure 6.22 (c) and (d) show the comparison of four sources for Group 5. The contrast of the BBs of diameter 0.167mm is much lower than that in Group 1. For BBs of diameter equal to or smaller than 0.167mm, the decrease in contrast is large when Source 3 is used. The difference between Source 0 and Source 2 is still smaller than the difference between Source 2 and Source 3. Comparing the contrast curves for Source 0 and Source 2, the contrast of the BBs in Group 5 is reduced by 16% to 33% for BB diameters from 0.053mm to 0.125mm in the LPBB phantom and by 5% to 33% for the same diameter range in the MC phantom. Overall, the dependence of the resolution of the BBs on the spatial location on the image plane is stronger than the dependence on the source blur over the range of source sizes studied.

VI.5.4 Comparison between the moving detector and the stationary detector

This section discusses the influence on source blur of a moving detector compared with a stationary detector. We will use the geometry of the Hologic Selenia Dimensions system, which uses a moving detector, as example for our analysis. For this system, the distance between the rotation center and the detector is 0, which means that the rotation axis is within the detector plane [44]. Assuming that the detector is moved synchronously with the source, the detector will rotate about the rotation axis by the same angle of the source and the central ray of the x-ray beam remains normal to the detector plane during image acquisition.

We investigate the influence of the moving detector on source blur by applying a small motion to a point source along the direction of the motion of the source. For a given projection angle, we slightly move the point source from its original location by $\pm 0.65\text{mm}$, corresponding

to the maximum motion of 1.3 mm in Table 6.1. In other words, the finite-sized source we use in this section to compare the two detectors is a 1.3-mm-wide one-dimensional line source parallel to the motion of the source. At the central projection angle, the line source is parallel to the y-direction. Given that the distance from the source to the rotation center is 700 mm, a motion of $\pm 0.65\text{mm}$ corresponds to a rotation angle of $\pm 0.053°$ and the detector should also rotate by $\pm 0.053°$ in the process. The location of the projection of a point in the imaged volume on the detector plane will change with the small motion of the source. This location can be geometrically calculated before and after the motion, and the distance between these two points can be obtained. This distance represents the level of source blur for one point in the imaged volume due to the motion of the source. For convenience, we call it the blurring distance in the following discussion. The blurring distance can be calculated as a distribution in the imaged volume for the moving detector. If a stationary detector is used that is parallel to the x-y plane (refer to Figure 6.2 for the coordinate system), we can also calculate the distribution of the blurring distance in the imaged volume.

The distributions of the blurring distance for two projection angles (0 and 7.5°) and two y-z planes (x = 0 and x = 200 mm) are calculated and shown in Figure 6.23 and Figure 6.24. Similar to Figure 6.2, we still use the rotation center as the origin of the coordinate system. The z-coordinate of the imaged volume then starts from -25 mm, since the distance from the rotation center to the imaged volume is 25 mm according to [44]. The sizes of the imaged volume along the y- and z-directions are 290 mm and 100 mm, respectively, assuming that the thickness of the imaged volume is 100 mm and that the imaged volume has the same size as the detector in image reconstruction [44].

The first rows of Figures 6.23 and 6.24 show the distribution of the blurring distance with a stationary detector. The second rows show the distribution with a moving detector. The first and second rows all use the same color bar settings. The third rows show their relative difference calculated by subtracting the first rows from the second rows (moving detector – stationary detector) and dividing the results by the maximum blurring distance with the stationary detector. A negative value in the third rows therefore means that the moving detector reduces the blurring distance. The third rows also use the same color bar settings in Figure 6.23 and 6.24.

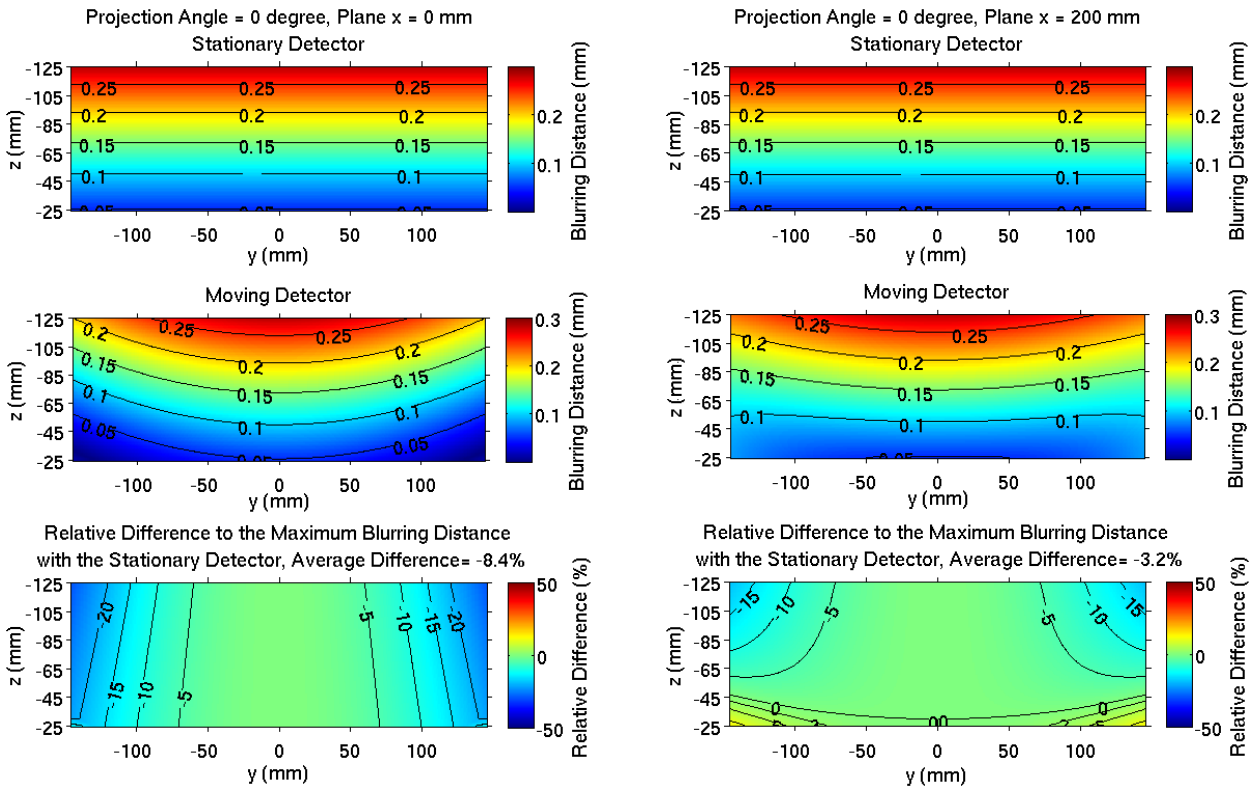

Figure 6.23. Spatial dependence of the blurring distance on a y-z plane for the central projection angle ($\theta = 0°$) plotted with contours for (a) x = 0; (b) x = 200 mm. The third row shows the relative difference of the blurring distance between the moving detector and the stationary detector. A negative relative difference means that the moving detector reduces the blurring distance.

Figure 6.23 shows the distribution of the blurring distance for the central projection angle. As expected, the distribution is symmetric about y = 0 for both detectors on both y-z planes. For the stationary detector, the distribution of the blurring distance does not depend on the x- or y-coordinate. This is because for the central projection angle, the 1-D line source blur is parallel to the detector plane for the stationary detector. The blurring distance increases when the location is farther away from the detector plane, reaching a maximum value of 0.28 mm at z = -125 mm. This is expected considering that the source blur scaling factor reaches its maximum value at z = -125 mm. If the moving detector is used, for the x = 0 plane, the blurring distance reduces by 0% to 29.3% compared with the stationary detector. The average relative reduction of the blurring distance is 8.4%. As shown in the second row of Figure 6.23(a), the blurring distance is still substantial and cannot be neglected even with the moving detector, especially for the top slices.

With the moving detector, the maximum blurring distance is 0.28 mm at y = 0, z = -125 mm, which is the same as the stationary detector.

Comparing the second row in Figure 6.23(a) and (b) indicates that the distribution of the blurring distance depends on the x-location of the plane if the moving detector is used. The blurring distance is larger for planes farther away from the chest wall. For x = 200 mm, the blurring distance of the moving detector is actually larger than that of the stationary detector in the bottom slices, as indicated by a positive relative difference. On average, the moving detector reduces the blurring distance by 3.2%. In summary, for the central projection angle, the moving detector slightly reduces the source blur caused by its motion.

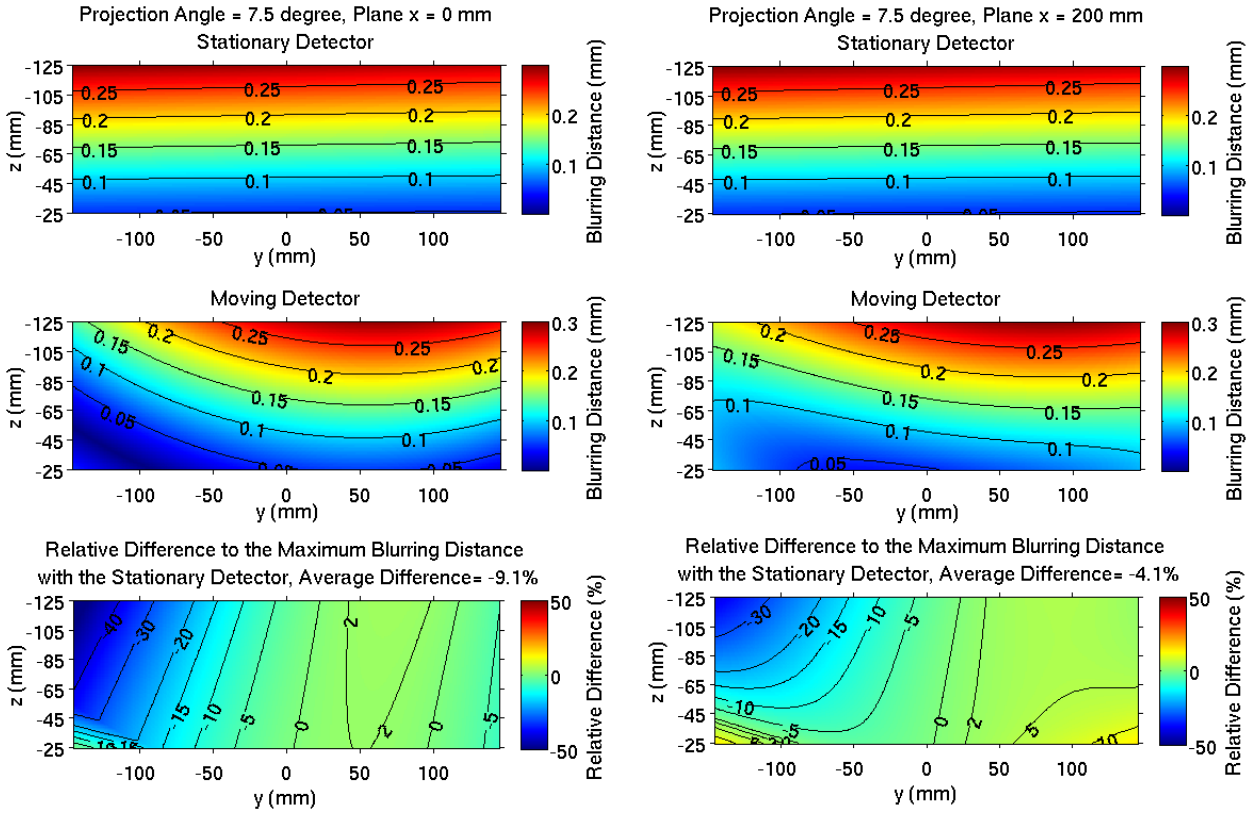

Figure 6.24. Spatial dependence of the blurring distance on a y-z plane for the maximum projection angle ($\theta = 7.5°$) plotted with contours for (a) x = 0; (b) x = 200 mm. The third row shows the relative difference of the blurring distance between the moving detector and the stationary detector. A negative relative difference means that the moving detector reduces the blurring distance.

Figure 6.24 shows the comparison for projection angle $\theta = 7.5°$ (the maximum projection angle of the Hologic DBT system). For the x = 0 plane, the moving detector can reduce the blurring distance by as much as 52.0%, as observed in the upper-left corner in the third row of Figure 6.24(a). The average relative reduction of the blurring distance is 9.1%. The maximum blurring distance with the moving detector is 0.29 mm, which is larger than that at the central projection angle. For the x = 200 mm plane, the blurring distance of the moving detector is larger than that of the stationary detector in the right half of the plane, as shown in the third row of Figure 6.24(b). The average reduction of the blurring distance is 4.1%, mainly contributed by the left half of plane shown in the second row of Figure 6.24(b). As a result, at this projection angle, the moving detector reduces the source blur more than the central projection angle, but the remaining source blur is still significant.

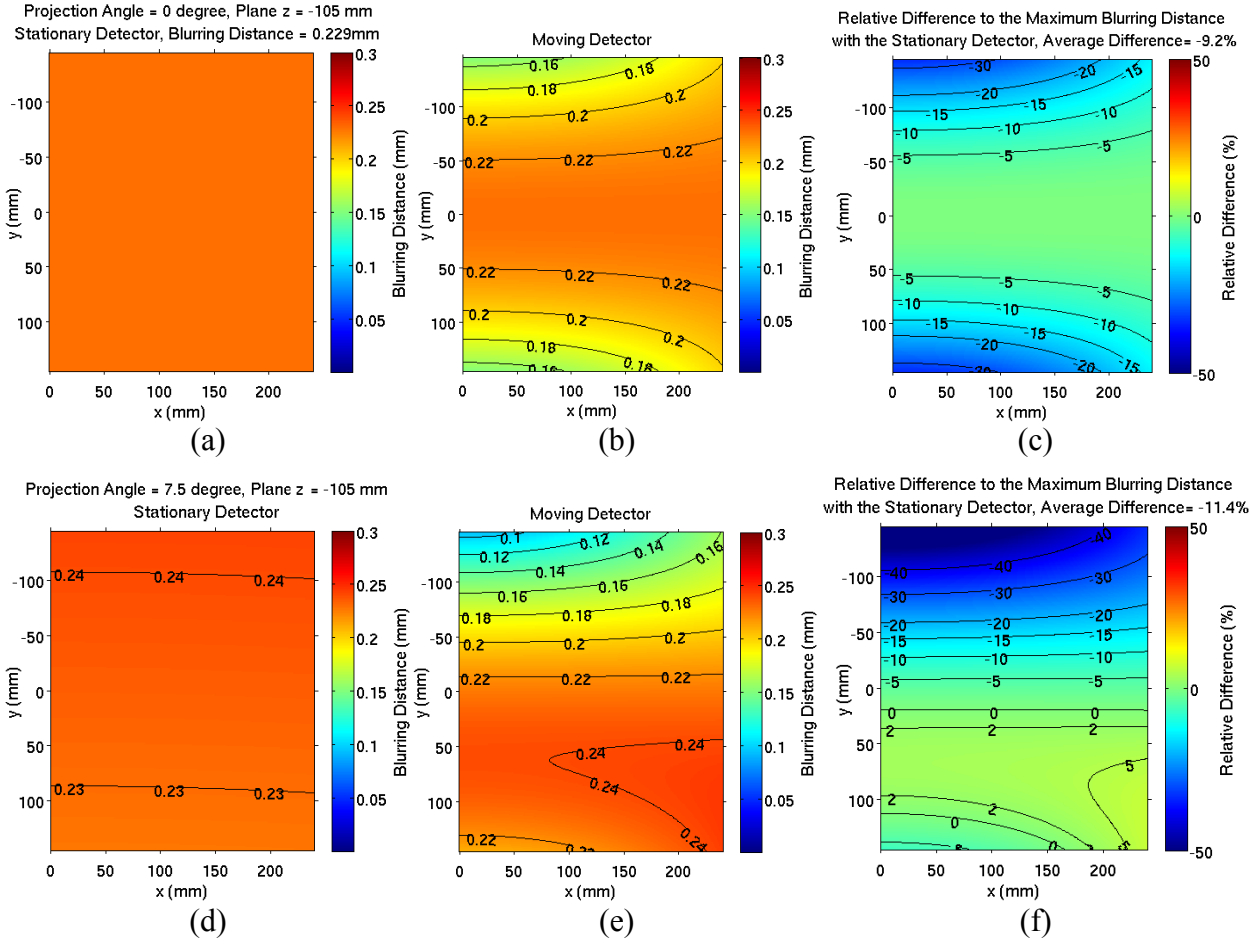

Figure 6.25. Spatial dependence of the blurring distance in an x-y plane (z = -105 mm) plotted with contours for: first row: projection angle $\theta = 0°$; second row: projection angle $\theta = 7.5°$. (a) does not show the contours since it is uniform with blurring distance = 0.229 mm.

Figure 6.25 shows the comparison between the moving detector and the stationary detector in an x-y plane at z = -105 mm, which is 80 mm from the bottom of the imaged volume. The distribution of the blurring distance for the stationary detector is uniform at the central projection angle, as shown in Figure 6.25(a). This observation is similar to the first row of Figure 6.23, for the same reason that the equivalent finite-sized source is 1-D and is parallel to the detector. While the distribution of the blurring distance is generally uniform with the stationary detector, it is non-uniform with the moving detector that the blurring distance is reduced at the top and bottom of the slice. For the central projection angle, the average reduction of blurring distance is 9.2%. At a projection angle of 7.5 degrees, the average reduction is 11.4%, but the blurring distance actually increases locally by more than 5% in the lower-right corner in Figure 6.25(f).

In summary, our calculation indicates that the additional source blur caused by the motion of the x-ray tube during data acquisition cannot be neglected even if one uses a moving detector in synchrony with the source. It is likely that the general trends of our analysis of spatial resolution with the CatSim simulation (Section VI.5.1-VI.5.3) that uses the stationary detector also apply to the situation where a moving detector is used. To confirm this, simulations with a moving detector need to be performed and analyzed.

VI.5.5 Summary of the influence of source blur

In this section we summarize our observations of the impact of x-ray focal spot blur on the spatial resolution of high-contrast objects. Our simulation results indicate that for a stationary source of a typical focal spot size (~0.3 mm), treating the finite-sized source as a point source has negligible effect on the reconstructed image resolution in both the directions parallel and perpendicular to the source motion direction as shown by the horizontal and vertical line pairs and BBs (with 5 SART iterations). If the source is not stationary such that the effective size of the source blur (h_2) increases to about 1mm (Source 2), the spatial resolution in the direction parallel to the source motion (the contrast of horizontal line pairs) and BBs will have a noticeable decrease. If the effective size of the source blur is 2mm (Source 3), the contrast of horizontal line pairs and BBs will decrease substantially, especially for BBs that are far away from the rotation center. How much source blur is tolerable will depend on the specific imaging task and other factors in the imaging and reconstruction processes.

Although we made a rough estimation of the potential source blur of the commercial DBT systems (Tables 6.1-6.3) based on the published system parameters, typical exposure techniques, and simple constant motion of the x-ray source, we cannot investigate the different combinations of parameters for the various systems. For example, the number of PVs, acquisition angle, detector pixel size, reconstruction voxel size and reconstruction algorithm etc. differ from one vender's system to another. The Hologic system uses a moving detector (non-stationary) and the Fujifilm system uses a detector with hexagonal elements, which are very different from our CatSim simulation. For any DBT systems, the selection of the system design parameters involves many other factors in addition to minimizing the source blur and much of the information is proprietary. In addition, we do not include other image quality degrading factors such as noise or scattered radiation, making it more difficult to predict the relative influence of source blur on the reconstructed image quality and the overall benefit of modeling the source blur in image reconstruction in practice for a specific system. Nevertheless, we will make some general discussion based on our simulation results as a reference that might be helpful for other researchers and DBT manufacturers.

For DBT systems that use a step-and-shoot scanning mode such as the GE SenoClaire/Pristina DBT system, our simulation shows that treating a finite-sized source as a point source causes minimal loss in resolution if the focal spot size is about 0.3mm and the detector has a pixel size of 0.1mm. Neglecting the source blur may not affect the reconstructed image quality. The benefit of modeling the source blur in reconstruction for this type of systems is therefore limited.

For narrow-angle DBT systems that use a continuous-motion scanning x-ray source with a moving detector such as the Hologic Selenia Dimensions system, our simulation shows that the source motion blur is substantial and the moving detector does not significantly reduce the source blur, especially if small pixel size such as 0.07mm is used. If the detector pixel size is binned to 0.14 mm as in the Hologic system [44], the relative impact of the source motion blur is reduced. According to our estimates in Table 6.1, the effective h_2 is about 1.3mm for 6-cm-thick breasts and 1.6mm for 8-cm-thick breasts. If we consider the size of the source blur relative to the pixel size, a source blur of 1.3 mm is comparable to a source blur of about 0.8 mm and 1.6mm is about 1 mm (Source 2) in our simulation that uses a pixel size of 0.1mm. The source blur is therefore not negligible in DBT for slightly above average to thick breasts and modeling

the source blur in reconstruction may be beneficial. The experimental study in [144] supports our conclusion, where replacing the rotating x-ray tube in the Hologic Selenia Dimensions DBT system with a stationary carbon nanotube x-ray source array demonstrates increased system spatial resolution.

For wide-angle DBT systems with a continuous-motion scanning x-ray source and a stationary detector, the impact of motion source blur is strong unless the source is moved at a relatively slow speed such as the Siemens Mammomat Inspiration system. According to our estimates in Table 6.2, the effective h_2 is 1.2 mm for thick breasts (thickness ~ 10cm). The pixel size is 0.085mm for this system [44]. For a 10-cm-thick breast, an effective h_2 of 1.2 mm is between Source 2 and Source 3 in our simulation. For a 5-cm-thick breast, the effective h_2 is 0.8 mm, which is comparable to Source 2. Our simulation shows that Source 2 causes noticeable decrease in the spatial resolution. Roughly speaking, the source motion might result in image quality degradation for average to thick breasts. For this system, modeling the source blur may be beneficial for improving the image quality. Modeling the source blur may also allow the system to scan with faster motion of the x-ray source, which will decrease the potential motion blur of the breast and improve the comfort of DBT imaging.

For narrow-angle DBT systems with continuous x-ray source motion and a stationary detector the source motion blur can be substantial, especially when the detector is stationary and the pixel size is small such as the Fujifilm Aspire Cristalle system. This system has a detector with hexagonal pixels with a side length of 0.05mm [124, 137], which is equivalent by pixel area to a square pixel of 0.08mm. If we simply assume a square pixel of 0.08mm for the system, then the effective $h_2 = 1.6\text{mm}$ for thick breasts (thickness ~ 9cm) is comparable to Source 3 in our simulation and could result in significant degradation in spatial resolution. Modeling the source blur in reconstruction may therefore improve the image quality. In general, increasing the total scan time or reducing the x-ray pulse width will alleviate the problem of source motion blur but it depends on other system design considerations. Furthermore, increasing the total scan time also increases the possibility of motion blur of the breast.

In summary, our simulation results indicate that the step-and-shoot approach may suffice to preserve the resolution of objects despite the finite size of the focal spot in typical DBT systems. The continuous motion approach will be the main contributor to the source blur and may result in different levels of image quality degradation depending on the thickness of the breast and other

parameters of the DBT system. The latter type of DBT systems may benefit from modeling source blur in reconstruction but the specific gain in image quality should be studied by taking into account other system design and imaging parameters.

VI.6 Limitation of the study

Although our simulation results provide some meaningful conclusions on the effect of source blur in DBT reconstruction, the study introduced in this chapter has several limitations. First, the simulation introduced in this chapter needs more sampling points for the size of the source. As shown in Tables 6.1-6.3, the effective h_2 of the source varies in a range as the thickness of the breast changes. More sampling points for the size of the source need to be simulated for a systematic analysis to find the tolerance of the motion of the x-ray tube for the continuous-motion systems. Second, we only used SART with 21PVs in reconstruction. Simulating DBT systems with different geometries and reconstructions by other algorithms need to be studied to give a better prediction of the influence of source blur on the image resolution. Third, simulations with different pixel sizes for a fixed source need to be performed to understand how the detector pixel size will affect the effect of source blur. Finally, our simulation neglects quantum noise, readout noise, scattered radiation and other factors. A comparison between the ideal point source and a finite-sized source taking into account these factors will better indicate the significance of modeling source blur in DBT reconstruction.

VI.7 Conclusion

In this study, we used analytical calculation and CatSim simulation to study the effect of the source blur on the spatial resolution of reconstructed DBT. Our analytical calculation demonstrates that the PSF of source blur is highly shift-variant. The shape of the PSF of the source blur also strongly depends on the spatial location over the image plane, making it challenging to be implemented precisely in the system model. We used CatSim to simulate phantoms that contain line pairs and BBs at different locations with sources of four different sizes. To make the simulation practical in terms of computation time, we proposed the hybrid simulation method for CatSim. The reconstructed results of the simulated phantoms demonstrate that a typical finite-sized focal spot (~ 0.3 mm) will not affect the image quality if the x-ray tube

is stationary during data acquisition. If the x-ray tube is moving, the extra source blur due to the motion of the source may degrade image resolution, depending on the effective size of the source along the direction of the motion. By analyzing the available technical parameters of the clinically available DBT systems and our simulation results, we roughly estimated the influence of source blur on the reconstructed image quality and the potential benefit of modeling the source blur in image reconstruction.

CHAPTER VII.
Summary and Proposed Future Work

VII.1 Summary

This dissertation introduced my studies to improve the reconstructed image quality for DBT. The idea of MBIR inspires many studies we have conducted. This section is a brief summary of this dissertation.

Chapter III introduced the SG projector and its application for the subpixel reconstruction. By theory and simulation, we demonstrated the superior accuracy of the SG projector compared with the traditional RT projector. The SG projector outperforms the RT projector in terms of reconstruction quality without increasing the computation time. With the simulated projections of a digital phantom, we demonstrated that the SG projector improves the image quality for regular and the subpixel DBT reconstructions. We also showed that the subpixel reconstruction can significantly improve image resolution, especially when it is used with the SG projector.

Chapter IV proposed the SQS-DBCN reconstruction algorithm that incorporates detector blur and a correlated noise model for DBT. We have shown quantitatively and qualitatively that the SQS-DBCN method can better enhance MCs than SART while preserving the image quality of mass spiculations and tissue texture. We have also demonstrated the effectiveness of the SQS-DBCN method as a result of incorporating the detector blur, the noise correlation and the regularization at the same time, indicating that a more complete model-based reconstruction may further improve the DBT image quality.

Chapter V introduced our study on TPA removal for DBT reconstruction. Three TPA removal algorithms were introduced. The results show that our contour-extension-diffusion PV extrapolation algorithm removes TPA effectively while causing contraction in the reconstructed volume on the top few slices. The pre-reconstruction-based PV extrapolation algorithm effectively removes TPA without such problems. The investigated regularization-based

algorithm was not effective due to the inaccuracy of the log-transform of the PVs and other factors. Further improvement in the contour-extension-diffusion PV extrapolation and the regularization-based TPA removal algorithms is needed to make these methods more practical.

Chapter VI used analytical calculations and CatSim simulations to study the effect of the source blur on DBT reconstruction. We first used analytical calculations to demonstrate that the PSF of source blur is highly shift-variant. Then we used CatSim to configure phantoms that contain line pairs and BBs and to simulate projections with sources of four different sizes. The analysis of the reconstructed digital phantoms demonstrates that a typical finite-sized focal spot (~0.3 mm) will not affect the image quality if the x-ray tube is stationary during data acquisition. For DBT systems with the continuous-motion scanning mode, the continuous motion of the x-ray tube might cause significant loss in the resolution. Modeling the source blur for these DBT systems could potentially improve the reconstructed image quality.

VII.2 Proposed future studies

Based on the studies introduced in this dissertation, I propose the following future studies:

(1) Modeling of the scattered radiation in DBT reconstruction –

In Chapter III and Chapter IV, our study on the SG projector and the SQS-DBCN algorithm both support the idea that modeling the physics of the DBT system can improve the reconstructed image quality. For DBT systems that use a flat-panel detector without an anti-scatter grid, removing the scattered x-ray intensity or modeling this effect in the reconstruction might improve DBT image quality.

(2) A comparative study of TPA removal algorithms –

In Chapter V, we tested three TPA removal algorithms. The contour-extension-diffusion PV extrapolation method and the regularization-based TPA removal algorithm both have their own problems. The contour-extension-diffusion method tends to underestimate the shift distance of the contour. For the regularization-based TPA removal method, more tests need to be done to determine the reason of the ineffectiveness of this method. We have proposed possible improvements of these two algorithms. The pre-reconstruction-based PV extrapolation method provides the best performance. We used two SART iterations to obtain the pre-reconstruction DBT volume. For the case that we perform two SART iterations to obtain the final reconstructed image, using the pre-reconstruction method will double the

computation time. In addition, using the extrapolated PVs also make the execution time of forward and backward projections longer. The time cost of the pre-reconstruction-based PV extrapolation method will need to be evaluated and compared with other TPA removal methods. As discussed in Section V.4.3, the PV extrapolation methods will complicate the form of the cost function and therefore might not be appropriate for statistical image reconstruction. A TPA removal algorithm satisfying a convergence theory for statistical image reconstruction is yet to be established. TPA removal is crucial for improving the appearance of the reconstructed images in DBT. A thorough study on this topic could provide researchers more options to control this type of reconstruction artifact.

(3) A systematic analysis of the effect of source blur on image reconstruction –

Although our study in Chapter VI provides some valuable conclusions, due to the limit of time we were not able to finish more simulations to provide a systematic analysis of the effect of source blur. In this dissertation, we have described the hybrid simulation acceleration for CatSim that can efficiently simulate the projections of fine objects with high oversampling rates of the detector and the source blur. In the future, a thorough analysis of the source blur effect in combination with other system design parameters and image quality factors could make a valuable reference for researchers and the manufacturers to optimize their DBT systems.

(4) A DBT reconstruction algorithm that models the motion of the x-ray source –

In Chapter VI, we demonstrated the shift-variance of the source blur in DBT. The shift-variance makes source blur very challenging to be incorporated in the reconstruction. Our simulation results also demonstrate that for a step-and-shoot DBT system with a typical focal spot size, the effect of source blur is insignificant. As a result, for the continuous-motion DBT systems, it is possible that we can ignore the physical shape of the finite-sized focal spot and only model the source blur contributed by the motion of the source, which is a 1-D effect that is much easier to implement than the complicated 2-D source blur PSF. If this effect were incorporated in the DBT reconstruction, it might significantly improve the image quality. It would allow the manufacturers of DBT systems to reduce the total scan time to reduce the potential motion blur of the breast during the scan and to improve the comfort of DBT imaging.

(5) A quantitative FOM for the soft tissue –

In our study on the SQS-DBCN algorithm, we visually assessed the reconstructed quality of the soft tissue. An FOM needs to be established to quantitatively measure the image quality of the reconstructed soft tissue. Such an FOM has to take into account the effect of artificial and patchy images generated by over-regularized image reconstructions. The currently available FOMs such as the various formulations of detectability indices and model observers are not sensitive to the subtle texture changes and distortions although some already include the power spectrum of the structured background.

(6) Fast and convergent iterative reconstruction for DBT –

In this dissertation, all our DBT images were reconstructed with limited number of iterations. We used SART with a limited number of iterations to avoid the amplification of noise since no regularization is applied. For the SQS-DBCN algorithm, we also performed a limited number of iterations. Due to the usage of the ordered-subset acceleration and Lu's TPA removal algorithm, the cost function of the SQS-DBCN algorithm does not converge even after many iterations. The regularization of the SQS-DBCN algorithm is applied to each 2-D slice separately. A well-designed 3-D regularization method might further improve the quality of the converged DBT image. Such an algorithm also needs to be optimized to be computationally efficient so the computation time to obtain the converged image is practical in clinical settings.

BIBLIOGRAPHY

[1] H.-P. Chan, "Computer-Aided Diagnosis of Breast Cancer with Tomosynthesis Imaging," *Medical Image Analysis and Informatics: Computer-aided Diagnosis and Therapy,* vol. Boca Raton, FL: Taylor & Francis Group, LLC. CRC Press, 2017 (in press).

[2] H. P. Chan, M. M. Goodsitt, M. A. Helvie, S. Zelakiewicz, A. Schmitz, M. Noroozian*, et al.*, "Digital Breast Tomosynthesis: Observer Performance of Clustered Microcalcification Detection on Breast Phantom Images Acquired with an Experimental System Using Variable Scan Angles, Angular Increments, and Number of Projection Views," *Radiology,* vol. 273, pp. 675-685, Dec 2014.

[3] J. Ferlay, I. Soerjomataram, R. Dikshit, S. Eser, C. Mathers, M. Rebelo*, et al.*, "Cancer incidence and mortality worldwide: sources, methods and major patterns in GLOBOCAN 2012," *Int J Cancer,* vol. 136, pp. E359-86, Mar 01 2015.

[4] C. DeSantis, J. M. Ma, L. Bryan, and A. Jemal, "Breast Cancer Statistics, 2013," *Ca-a Cancer Journal for Clinicians,* vol. 64, pp. 52-62, Jan 2014.

[5] C. Schairer, P. J. Mink, L. Carroll, and S. S. Devesa, "Probabilities of Death From Breast Cancer and Other Causes Among Female Breast Cancer Patients," *JNCI Journal of the National Cancer Institute,* vol. 96, pp. 1311-1321, 2004.

[6] M. J. Yaffe, "Digital mammography," in *Technical aspects of breast imaging*, A. G. Haus and M. J. Yaffe, Eds., ed Oak Brook: Radiological Society of North America, 1992, pp. 245-255.

[7] M. J. Yaffe, "Digital Mammography," in *Handbook of Medical Imaging: Physics and Psychophysics*. vol. 1, J. Beutel, H. L. Kundel, and R. L. VanMetter, Eds., ed Bellingham, WA: SPIE, 2000, pp. 329-372.

[8] E. D. Pisano and M. J. Yaffe, "Digital mammography," *Radiology,* vol. 234, pp. 353-362, 2005.

[9] R. Hodgson, S. H. Heywang-Kobrunner, S. C. Harvey, M. Edwards, J. Shaikh, M. Arber*, et al.*, "Systematic review of 3D mammography for breast cancer screening," *Breast,* vol. 27, pp. 52-61, Jun 2016.

[10] K. Kerlikowske, D. Grady, J. Barclay, E. A. Sickles, and V. Ernster, "Effect of age, breast density, and family history on the sensitivity of first screening mammography," *Jama-Journal of the American Medical Association,* vol. 276, pp. 33-38, Jul 1996.

[11] R. E. Hendrick and M. A. Helvie, "United States Preventive Services Task Force Screening Mammography Recommendations: Science Ignored," *American Journal of Roentgenology,* vol. 196, pp. W112-W116, Feb 2011.

[12] P. A. Carney, D. L. Miglioretti, B. C. Yankaskas, K. Kerlikowske, R. Rosenberg, C. M. Rutter*, et al.*, "Individual and combined effects of age, breast density, and hormone replacement therapy use on the accuracy of screening mammography," *Ann Intern Med,* vol. 138, pp. 168-75, Feb 04 2003.

[13] U. S. P. S. T. Force, "Screening for breast cancer: U.S. Preventive Services Task Force recommendation statement.," *Annals of Internal Medicine,* vol. 151, pp. 716-726, 2009.

[14] B. G. Z. d. Plantes, "Eine neue methode zur differenzierung in der roentgenographie (planigraphie)," *Acta Radiol.,* vol. 13, pp. 182-192, 1932.

[15] L. T. Niklason, B. T. Christian, L. E. Niklason, D. B. Kopans, D. E. Castleberry, B. H. Opsahl-Ong*, et al.*, "Digital tomosynthesis in breast imaging," *Radiology,* vol. 205, pp. 399-406, 1997.

[16] M. A. Helvie, M. A. Roubidoux, L. M. Hadjiiski, Y. Zhang, P. L. Carson, and H.-P. Chan, "Research Digital Tomosynthesis Mammography: Detection of T1 Invasive Breast Carcinomas not Diagnosed by Conventional Breast Imaging or Physical Exam," *RSNA Program Book,* vol. 2008, p. 468, 2008.

[17] S. P. Poplack, T. D. Tosteson, C. A. Kogel, and H. M. Nagy, "Digital breast tomosynthesis: Initial experience in 98 women with abnormal digital screening mammography," *American Journal of Roentgenology,* vol. 189, pp. 616-623, Sep 2007.

[18] A. P. Smith, E. A. Rafferty, and L. Niklason, "Clinical performance of breast tomosynthesis as a function of radiologist experience level," *IWDM 2008 - Lecture Notes in Computer Science,* vol. 5116, pp. 61-66, Jul 20-23 2008.

[19] G. Gennaro, E. Baldan, E. Bezzon, M. La Grassa, L. Pescarini, and C. di Maggio, "Clinical performance of digital breast tomosynthesis versus full-field digital mammography: Preliminary results," *IWDM 2008 - Lecture Notes in Computer Science,* vol. 5116, pp. 477-482, Jul 20-23 2008.

[20] M. A. Helvie, H. P. Chan, L. M. Hadjiiski, B. Sahiner, P. L. Carson, and A. Schmitz, "Digital Breast Tomosynthesis Mammography: Successsful Assessment of Benign and Malignant Microcalcifications," *RSNA Program Book,* vol. 2009, p. 389, 2009.

[21] D. Gur, G. S. Abrams, D. M. Chough, M. A. Ganott, C. M. Hakim, R. L. Perrin*, et al.*, "Digital Breast Tomosynthesis: Observer Performance Study," *American Journal of Roentgenology,* vol. 193, pp. 586-591, Aug 2009.

[22] E. A. Rafferty, J. M. Park, L. E. Philpotts, S. P. Poplack, J. H. Sumkin, E. F. Halpern*, et al.*, "Assessing Radiologist Performance Using Combined Digital Mammography and

Breast Tomosynthesis Compared with Digital Mammography Alone: Results of a Multicenter, Multireader Trial," *Radiology,* vol. 266, pp. 104-113, Jan 2013.

[23] P. Skaane, A. I. Bandos, R. Gullien, E. B. Eben, U. Ekseth, U. Haakenaasen*, et al.*, "Comparison of Digital Mammography Alone and Digital Mammography Plus Tomosynthesis in a Population-based Screening Program," *Radiology,* vol. 267, pp. 47-56, Apr 2013.

[24] S. L. Rose, A. L. Tidwell, L. J. Bujnoch, A. C. Kushwaha, A. S. Nordmann, and R. Sexton, "Implementation of Breast Tomosynthesis in a Routine Screening Practice: An Observational Study," *American Journal of Roentgenology,* vol. 200, pp. 1401-1408, Jun 2013.

[25] J. T. Dobbins and D. J. Godfrey, "Digital x-ray tomosynthesis: Current state of the art and clinical potential," *Physics in Medicine and Biology,* vol. 48, pp. R65-R106, 2003.

[26] J. A. Baker and J. Y. Lo, "Breast Tomosynthesis: State-of-the-Art and Review of the Literature," *Academic Radiology,* vol. 18, pp. 1298-1310, Oct 2011.

[27] E. Shaheen, N. Marshall, and H. Bosmans, "Investigation of the effect of tube motion in breast tomosynthesis: continuous or step and shoot?," *Medical Imaging 2011: Physics of Medical Imaging,* vol. 7961, 2011.

[28] A. K. Hara, R. G. Paden, A. C. Silva, J. L. Kujak, H. J. Lawder, and W. Pavlicek, "Iterative Reconstruction Technique for Reducing Body Radiation Dose at CT: Feasibility Study," *American Journal of Roentgenology,* vol. 193, pp. 764-771, 2009.

[29] P. J. Pickhardt, M. G. Lubner, D. H. Kim, J. Tang, J. A. Ruma, A. M. del Rio*, et al.*, "Abdominal CT With Model-Based Iterative Reconstruction (MBIR): Initial Results of a Prospective Trial Comparing Ultralow-Dose With Standard-Dose Imaging," *American Journal of Roentgenology,* vol. 199, pp. 1266-1274, 2012.

[30] T. Wu, A. Stewart, M. Stanton, T. McCauley, W. Phillips, D. B. Kopans*, et al.*, "Tomographic mammography using a limited number of low-dose cone-beam projection images," *Medical Physics,* vol. 30, pp. 365-380, 2003.

[31] Y. Zhang, H.-P. Chan, B. Sahiner, J. Wei, M. M. Goodsitt, L. M. Hadjiiski*, et al.*, "A comparative study of limited-angle cone-beam reconstruction methods for breast tomosynthesis," *Medical Physics,* vol. 33, pp. 3781-3795, 2006.

[32] E. Y. Sidky, X. Pan, I. Reiser, R. M. Nishikawa, R. H. Moore, and D. B. Kopans, "Enhanced imaging of microcalcifications in digital breast tomosynthesis through improved image-reconstruction algorithms," *Medical Physics,* vol. 36, pp. 4920-4932, 2009.

[33] M. Das, H. C. Gifford, J. M. O'Connor, and S. J. Glick, "Penalized maximum likelihood reconstruction for improved microcalcification detection in breast tomosynthesis," *IEEE Trans Medical Imaging,* vol. 30, pp. 904-914, 2011.

[34] J. G. Bian, K. Yang, J. M. Boone, X. Han, E. Y. Sidky, and X. C. Pan, "Investigation of iterative image reconstruction in low-dose breast CT," *Physics in Medicine and Biology,* vol. 59, pp. 2659-2685, Jun 2014.

[35] E. Haneda, J. E. Tkaczyk, G. Palma, R. Iordache, S. Zelakiewicz, S. Muller*, et al.*, "Toward a dose reduction strategy using model-based reconstruction with limited-angle tomosynthesis," *Proc. SPIE,* vol. 9033, p. 90330V, 2014.

[36] E. Samei, J. Thompson, S. Richard, and J. Bowsher, "A Case for Wide-Angle Breast Tomosynthesis," *Academic Radiology,* vol. 22, pp. 860-869, Jul 2015.

[37] P. Aguiar, M. Rafecas, J. E. Ortuno, G. Kontaxakis, A. Santos, J. Pavia*, et al.*, "Geometrical and Monte Carlo projectors in 3D PET reconstruction," *Medical Physics,* vol. 37, pp. 5691-702, Nov 2010.

[38] F. J. Beekman, H. W. de Jong, and S. van Geloven, "Efficient fully 3-D iterative SPECT reconstruction with Monte Carlo-based scatter compensation," *IEEE Trans Med Imaging,* vol. 21, pp. 867-77, Aug 2002.

[39] Y. Long, J. A. Fessler, and J. M. Balter, "3D Forward and Back-Projection for X-Ray CT Using Separable Footprints," *IEEE Trans Medical Imaging,* vol. 29, pp. 1839-1850, Nov 2010.

[40] K. Michielsen, K. Van Slambrouck, A. Jerebko, and J. Nuyts, "Patchwork reconstruction with resolution modeling for digital breast tomosynthesis," *Medical Physics,* vol. 40, p. 031105, Mar 2013.

[41] K. Kim, T. Lee, Y. Seong, J. Lee, K. E. Jang, J. Choi*, et al.*, "Fully iterative scatter corrected digital breast tomosynthesis using GPU-based fast Monte Carlo simulation and composition ratio update," *Medical Physics,* vol. 42, pp. 5342-5355, Sep 2015.

[42] S. Xu, J. Lu, O. Zhou, and Y. Chen, "Statistical iterative reconstruction to improve image quality for digital breast tomosynthesis," *Medical Physics,* vol. 42, pp. 5377-5390, Sep 2015.

[43] K. Michielsen and J. Nuyts, "Multigrid reconstruction with block-iterative updates for breast tomosynthesis," *Medical Physics,* vol. 42, pp. 6537-48, Nov 2015.

[44] I. Sechopoulos, "A review of breast tomosynthesis. Part I. The image acquisition process," *Medical Physics,* vol. 40, Jan 2013.

[45] I. Sechopoulos, "A review of breast tomosynthesis. Part II. Image reconstruction, processing and analysis, and advanced applications," *Medical Physics,* vol. 40, p. 014302, Jan 2013.

[46] I. A. Elbakri and J. A. Fessler, "Statistical image reconstruction for polyeneregetic x-ray computed tomography," *IEEE Trans Medical Imaging,* vol. 21, pp. 89-99, 2002.

[47] J. Radon, "On the Determination of Functions from Their Integral Values along Certain Manifolds," *IEEE Trans Med Imaging,* vol. 5, pp. 170-6, 1986.

[48] G. Lauritsch and W. Haerer, "A theoretical framework for filtered back-projection in tomosynthesis," *Proc. SPIE,* vol. 3338, pp. 1127-1137, 1998.

[49] B. E. H. Claus, J. W. Eberhard, A. Schmitz, P. Carson, M. Goodsitt, and H.-P. Chan, "Generalized filtered back-projection reconstruction in breast tomosynthesis," Manchester, ENGLAND, 2006, pp. 167-174.

[50] T. Mertelmeier, J. Orman, W. Haerer, and M. K. Dudam, "Optimizing filtered backprojection reconstruction for a breast tomosynthesis prototype device," *Proc. SPIE,* vol. 6142, p. 61420F, 2006.

[51] Y. H. Hu, B. Zhao, and W. Zhao, "Image artifacts in digital breast tomosynthesis: Investigation of the effects of system geometry and reconstruction parameters using a linear system approach," *Medical Physics,* vol. 35, pp. 5242-5252, Dec 2008.

[52] G. J. Gang, D. J. Tward, J. Lee, and J. H. Siewerdsen, "Anatomical background and generalized detectability in tomosynthesis and cone-beam CT," *Medical Physics,* vol. 37, pp. 1948-1965, 2010.

[53] R. Gordon, R. Bender, and G. T. Herman, "Algebraic reconstruction techniques (ART) for three dimensional electron microscopy and X-ray photography," *J. Theor. Biol.,* vol. 29, pp. 471-481, 1970.

[54] G. T. Herman, *Image Reconstruction from Projections: The Fundamentals of Computerized Tomography*. New York: Academic Press, 1980.

[55] A. Kak and M. Slaney, *Principle of Computerized Tomographic Imaging*. New York: IEEE Press, 1988.

[56] A. H. Andersen and A. C. Kak, "Simultaneous algebraic reconstruction technique (SART): a new implementation of the ART algorithm," *Ultrason. Imaging,* vol. 6, pp. 81-94, 1984.

[57] A. H. Andersen, "Algebraic reconstruction in CT from limited views," *IEEE Trans. Med. Imag.,* vol. 8, pp. 50-55, 1989.

[58] D. Van de Sompel, S. M. Brady, and J. Boone, "Task-based performance analysis of FBP, SART and ML for digital breast tomosynthesis using signal CNR and Channelised Hotelling Observers," *Medical Image Analysis,* vol. 15, pp. 53-70, Feb 2011.

[59] K. Lange and J. A. Fessler, "Globally convergent algorithms for maximum a posteriori transmission tomography," *IEEE Trans Image Processing,* vol. 4, pp. 1430-1438, 1995.

[60] J. B. Thibault, K. D. Sauer, C. A. Bouman, and J. Hsieh, "A three-dimensional statistical approach to improved image quality for multislice helical CT," *Medical Physics,* vol. 34, pp. 4526-4544, Nov 2007.

[61] B. De Man and J. A. Fessler, "Statistical Iterative Reconstruction for X-Ray Computed Tomography," in *Biomedical Mathematics: Promising Directions in Imaging, Therapy Planning, and Inverse Problems*. vol. 2010, Y. Censor, M. Jiang, and G. Wang, Eds., ed WI: Medical Physics Publishing, 2010, pp. 113-140.

[62] J. Nuyts, B. De Man, J. A. Fessler, W. Zbijewski, and F. J. Beekman, "Modelling the physics in the iterative reconstruction for transmission computed tomography," *Physics in Medicine and Biology,* vol. 58, pp. R63-R96, Jun 2013.

[63] M. Persson, D. Bone, and H. Elmqvist, "Total variation norm for three-dimensional iterative reconstruction in limited view angle tomography," *Physics in Medicine and Biology,* vol. 46, pp. 853-866, 2001.

[64] J. Zheng, J. A. Fessler, and H.-P. Chan, "Digital Breast Tomosynthesis Reconstruction using Spatially Weighted Non-convex Regularization," *Proc. SPIE,* vol. 9783, p. 978369, 2016.

[65] B. De Man, S. Basu, N. Chandra, B. Dunham, P. Edic, M. Iatrou*, et al.*, "Catsim : a new computer assisted tomography simulation environment," *Proc. SPIE,* vol. 6510, pp. U1191-U1198, 2007.

[66] B. De Man, J. Pack, P. FitzGerald, and M. Wu, *CatSim Manual Version 6.0*: GE Global Research, 2015.

[67] Y. Lu, H. P. Chan, J. Wei, and L. M. Hadjiiski, "A diffusion-based truncated projection artifact reduction method for iterative digital breast tomosynthesis reconstruction," *Physics in Medicine and Biology,* vol. 58, pp. 569-587, Feb 2013.

[68] Y. Lu, H.-P. Chan, J. Wei, and L. M. Hadjiiski, "Improving Image Quality of Digital Breast Tomosynthesis by Artifact Reduction," *Lecture Notes in Computer Science,* vol. 7361, pp. 745-752, 2012.

[69] Y. Zhang, H.-P. Chan, B. Sahiner, J. Wei, C. Zhou, and L. M. Hadjiiski, "Artifact reduction methods for truncated projections in iterative breast tomosynthesis reconstruction," *Journal of Computer Assisted Tomography,* vol. 33, pp. 426-435, 2009.

[70] Y. Lu, H.-P. Chan, J. Wei, L. Hadjiiski, and C. Zhou, "Improving Image Quality of Iterative Reconstruction for Digital Breast Tomosynthesis: Diffusion-Based Truncated Projection Artifact Reduction," *RSNA Program Book,* p. SSE23, 2011.

[71] W. A. Murphy and K. DeSchryver-Kecskemeti, "Isolated clustered microcalcification in the breast: radiologic-pathologic correlation," *Radiology,* vol. 127, pp. 335-341, 1978.

[72] M. Lanyi, "Morphologic analysis of microcalcifications," in *Early Breast Cancer. Histopathology, Diagnosis and Treatment*, J. Zander and J. Baltzer, Eds., ed Berlin: Springer-Verlag, 1985.

[73] H. P. Chan, K. Doi, S. Galhotra, C. J. Vyborny, H. MacMahon, and P. M. Jokich, "Image feature analysis and computer-aided diagnosis in digital radiography. 1. Automated detection of microcalcifications in mammography," *Medical Physics,* vol. 14, pp. 538-548, 1987.

[74] L. Tabar and P. B. Dean, *Teaching Atlas of Mammography*. New York: Thieme, 1985.

[75] F. E. Boas and D. Fleischmann, "CT artifacts: causes and reduction techniques," *Imaging in Medicine,* vol. 4, pp. 229-240, 2012/04/01 2012.

[76] S. Kligerman, K. Lahiji, E. Weihe, C. T. Lin, S. Terpenning, J. Jeudy*, et al.*, "Detection of pulmonary embolism on computed tomography: improvement using a model-based iterative reconstruction algorithm compared with filtered back projection and iterative reconstruction algorithms," *J Thorac Imaging,* vol. 30, pp. 60-8, Jan 2015.

[77] J. Zheng, J. A. Fessler, and H. P. Chan, "Segmented separable footprint projector for digital breast tomosynthesis and its application for subpixel reconstruction," *Medical Physics,* vol. 44, pp. 986-1001, Mar 2017.

[78] R. L. Siddon, "Fast calculation of the exact radiological path for a three-dimensional CT array," *Medical Physics,* vol. 12, pp. 252-255, 1985.

[79] F. Jacobs, E. Sundermann, B. D. Sutter, M. Christiaens, and I. Lemahieu, "A fast algorithm to calculate the exact radiological path through a pixel or voxel space," *Journal of computing and information technology,* vol. 6, pp. 89-94, 1998.

[80] H. X. Zhao and A. J. Reader, "Fast ray-tracing technique to calculate line integral paths in voxel arrays," *2003 IEEE Nuclear Science Symp. Conf. Record,* vol. 4, pp. 2808-2812, 2004.

[81] B. De Man and S. Basu, "Distance-driven projection and backprojection in three dimensions," *Physics in Medicine and Biology,* vol. 49, pp. 2463-2475, Jun 2004.

[82] B. Li, G. B. Avinash, R. Uppaluri, J. W. Eberhard, and B. E. H. Claus, "The impact of acquisition angular range on the z-resolution of radiographic tomosynthesis," *Computer Assisted Radiology and Surgery,* vol. CARS 2004 June 23 - 26, 2004 2004.

[83] Y. Lu, H. P. Chan, J. Wei, L. Hadjiiski, and R. Samala, "Study of Image Quality in Digital Breast Tomosynthesis by Subpixel Reconstruction," *Proc SPIE,* vol. 8668, p. 86680I, 2013.

[84] R. J. Acciavatti and A. D. A. Maidment, "Observation of super-resolution in digital breast tomosynthesis," *Medical Physics,* vol. 39, pp. 7518-7539, Dec 2012.

[85] ICRU, "Photon, Electron, Proton and Neutron Interaction Data for Body Tissues," *ICRU Report,* vol. 46, 1992.

[86] M. Jiang and G. Wang, "Convergence of the simultaneous algebraic reconstruction technique (SART)," *IEEE transactions on image processing,* vol. 12, pp. 957-961, 2003.

[87] J. Ge, H.-P. Chan, B. Sahiner, Y. Zhang, J. Wei, L. M. Hadjiiski*, et al.*, "Digital tomosynthesis mammography: Intra- and interplane artifact reduction for high-contrast objects on reconstructed slices using a priori 3D geometrical information," *Proc. SPIE,* vol. 6512, pp. 4Q1-4Q8, 2007.

[88] Y. Lu, H.-P. Chan, J. Wei, L. M. Hadjiiski, and R. K. Samala, " Improving Image Quality for Digital Breast Tomosynthesis: Automatic Detection and Inpainting Method for Metal Artifact Reduction.," *RSNA Program* vol. 2016, pp. SSM21-06, 2013.

[89] E. Y. Sidky, I. Reiser, R. M. Nishikawa, X. C. Pan, R. Chartrand, D. B. Kopans*, et al.*, "Practical iterative image reconstruction in digital breast tomosynthesis by non-convex TpV optimization - art. no. 691328," *Proc of SPIE,* vol. 6913, pp. 91328-91328, Feb 17-19 2008.

[90] T. Wu, R. H. Moore, E. A. Rafferty, and D. B. Kopans, "A comparison of reconstruction algorithms for breast tomosynthesis," *Medical Physics,* vol. 31, pp. 2636-2647, 2004.

[91] J. Zheng, J. A. Fessler, and H.-P. Chan, "Digital Breast Tomosynthesis Reconstruction with Detector Blur and Correlated Noise," *Proc. 4th International Conference on Image Formation in X-Ray Computed Tomography,* vol. CT-Meeting 2016, pp. 21-24, 2016.

[92] J. Zheng, J. A. Fessler, and H. P. Chan, "Detector Blur and Correlated Noise Modeling for Digital Breast Tomosynthesis Reconstruction," *IEEE Trans Med Imaging,* Jul 27 2017.

[93] S. Tilley, J. H. Siewerdsen, and J. W. Stayman, "Iterative CT Reconstruction using Models of Source and Detector Blur and Correlated Noise," *Proc Int Conf Image Form Xray Comput Tomogr.,* vol. 2014, pp. 363–367, 2014.

[94] S. Tilley, J. H. Siewerdsen, and J. W. Stayman, "Model-based iterative reconstruction for flat-panel cone-beam CT with focal spot blur, detector blur, and correlated noise," *Physics in Medicine and Biology,* vol. 61, pp. 296-319, Jan 07 2016.

[95] S. Tilley, J. H. Siewerdsen, W. Zbijewski, and J. W. Stayman, "Nonlinear statistical reconstruction for flat-panel cone-beam CT with blur and correlated noise models," *Proc. SPIE,* vol. 9783, p. 97830R, 2016.

[96] H. Erdogan and J. A. Fessler, "Ordered subsets algorithms for transmission tomography," *Physics in Medicine and Biology,* vol. 44, pp. 2835-2851, 1999.

[97] D. Kim, D. Pal, J. B. Thibault, and J. A. Fessler, "Accelerating Ordered Subsets Image Reconstruction for X-ray CT Using Spatially Nonuniform Optimization Transfer," *IEEE Trans Medical Imaging,* vol. 32, pp. 1965-1978, Nov 2013.

[98] K. Sauer and C. Bouman, "A Local Update Strategy for Iterative Reconstruction from Projections," *IEEE Trans Signal Processing,* vol. 41, pp. 534-548, Feb 1993.

[99] R. Garcia-Molla, R. Linares, and R. Ayala, "Study of DQE dependence with beam quality on GE essential mammography flat panel," *J Appl Clin Med Phys,* vol. 12, p. 3176, Nov 25 2010.

[100] E. Samei, M. Flynn, and D. Reimann, "A method for measuring the presampled MTF of digital radiographic systems using an edge test device," *Medical Physics,* vol. 25, pp. 102–113, 1998.

[101] Y. T. Wu, C. Zhou, H.-P. Chan, C. Paramagul, L. M. Hadjiiski, C. P. Daly*, et al.*, "Dynamic multiple thresholding breast boundary detection algorithm for mammograms," *Medical Physics,* vol. 37, pp. 391-401, Jan 2010.

[102] H. R. Shi and J. A. Fessler, "Quadratic regularization design for 2D CT," *IEEE Trans Medical Imaging,* vol. 28, pp. 645-656, 2009.

[103] H. M. Hudson and R. S. Larkin, "Accelerated Image Reconstruction Using Ordered Subsets of Projection Data," *IEEE Trans Medical Imaging,* vol. 13, pp. 601-609, 1994.

[104] M. S. Andersen and P. C. Hansen, "Generalized row-action methods for tomographic imaging," *Numerical Algorithms,* vol. 67, pp. 121-144, Sep 2014.

[105] M. K. Ng and J. Pan, "Approximate Inverse Circulant-plus-Diagonal Preconditioners for Toeplitz-plus-Diagonal Matrices," *SIAM Journal on Scientific Computing,* vol. 32, pp. 1442-1464, 2010.

[106] R. M. Lewitt, "Processing of incomplete measurement data in computed tomography," *Medical Physics,* vol. 6, pp. 412-417, 1979.

[107] K. Ogawa, M. Nakajima, and S. i. Yuta, "A Reconstruction Algorithms from Truncated Projections," *IEEE Trans Med Imaging,* vol. 3, pp. 34-40, 1984.

[108] D. J. Kadrmas, R. J. Jaszczak, J. W. McCormick, r. E. Coleman, and C. B. Lim, "Truncation artifact reduction in transmission CT for improved SPECT attenuation compensation," *Physics in Medicine and Biology,* vol. 40, pp. 1085-1104, 1995.

[109] W. Chang, S. Loncaric, G. Huang, and P. Sanpitak, "Asymmetric fan transmission CT on SPECT systems," *Physics in Medicine and Biology,* vol. 40, pp. 913-928, 1995.

[110] S. Loncaric, W. Chang, and G. Huang, "A processing technique for the truncated projections of asymmetric-fan-beam transmission imaging," *IEEE Transactions on Nuclear Science,* vol. 42, pp. 2292-2297, 1995.

[111] J. Hsieh, E. Chao, J. Thibault, B. Grekowicz, A. Horst, S. McOlash*, et al.*, "A novel reconstruction algorithm to extend the CT scan field-of-view," *Medical Physics,* vol. 31, pp. 2385-2391, 2004.

[112] B. Ohnesorge, T. Flohr, K. Schwarz, J. P. Heiken, and K. T. Bae, "Efficient correction for CT image artifacts caused by objects extending outside the scan field of view," *Medical Physics,* vol. 27, pp. 39-46, 2000.

[113] H. Kunze, W. Härer, and K. Stierstorfer, "Iterative extended field of view reconstruction," *Proc. SPIE,* vol. 6510, p. 65105X, 2007.

[114] B. Li, G. Avinasha, B. Claus, and S. Metz, "3-D view weighted cone-beam filtered backprojection reconstruction for digital tomosynthesis," *Proc. SPIE,* vol. 6510, p. 65104X, 2007.

[115] N. Otsu, "Threshold Selection Method from Gray-Level Histograms," *Ieee Transactions on Systems Man and Cybernetics,* vol. 9, pp. 62-66, 1979.

[116] T. W. Ridler and S. Calvard, "Picture Thresholding Using an Iterative Selection Method," *Ieee Transactions on Systems Man and Cybernetics,* vol. 8, pp. 630-632, 1978.

[117] D. Marr and E. Hildreth, "Theory of Edge Detection," *Proceeding of the Royal Society of London, Series B, Biological Science,* vol. 207, pp. 187-217, 1980.

[118] L. Alvarez, P. Lions, and J. Morel, "Image selective smoothing and edge-detection by nonlinear diffusion," *SIAM Journal on Numerical Analysis* vol. 29, pp. 845-866, 1992.

[119] M. Kass, A. Witkin, and D. Terzopoulos, "Snakes - Active Contour Models," *International Journal of Computer Vision,* vol. 1, pp. 321-331, 1987.

[120] T. F. Chan and L. A. Vese, "Active contours without edges," *IEEE Transactions on Image Processing,* vol. 10, pp. 266-277, 2001

[121] D. J. Williams and M. Shah, "A fast algorithm for active contours and curvature estimation," *CVGIP: Image Understanding,* vol. 55, pp. 14-26, 1992.

[122] H. Derin and H. Elliot, "Modeling and segmentation of noisy and textured images using Gibbs random fields," *IEEE Transactions on Pat. Anal. Mach. Int.,* vol. 9, pp. 39-55, 1987.

[123] K. I. Laws, "Textured image segmentation," School of Engineering, The Unviersity of Southern California, Los Angeles, 1980.

[124] U.S. Food and Drug Administration, "Summary of Safety and Effectiveness for Aspire Crstalle DBT Option," 2017.

[125] P. E. Kinahan and J. G. Rogers, "Analytic 3D image reconstruction using all detected events," *IEEE Transactions on Nuclear Science,* vol. 36, pp. 964-968, 1989.

[126] Y. Zhang, H.-P. Chan, B. Sahiner, Y.-T. Wu, C. Zhou, J. Ge*, et al.*, "Application of boundary detection information in breast tomosynthesis reconstruction," *Medical Physics,* vol. 34, pp. 3603-3613, 2007.

[127] University of Michigan Hospitals and Health Centers, "Validation of Hologic Selenia Dimensions Mammography System," 2016.

[128] Siemens AG, "MAMMOMAT Inspiration Tomosynthesis Option," 2015.

[129] Y.-H. Hu, B. Zhao, and W. Zhao, "Image artifacts in digital breast tomosynthesis: Investigation of the effects of system geometry and reconstruction parameters using a linear system approach," *Medical Physics,* vol. 35, pp. 5242-5252, 2008.

[130] R. Peng, R. Zeng, E. O'Bryan, C. Marini-Bettolo, B. Sahiner, K. J. Myers*, et al.*, "An Experimental Comparison of Continuous Motion and Step-and-Shoot Modes in Digital Breast Tomosynthesis," *Breast Imaging. IWDM 2012. Lecture Notes in Computer Science,* vol. 7361, pp. 650-657, 2012.

[131] D. Kontos, T. G. Flohr, J. Y. Lo, M. U. Ghani, D. Wu, M. D. Wong*, et al.*, "Quantitative comparison of spatial resolution in step-and-shoot and continuous motion digital breast tomosynthesis," *Proc SPIE,* vol. 9783, p. 97836D, 2016.

[132] N. J. Pelc, E. Shaheen, E. Samei, N. Marshall, H. Bosmans, and R. M. Nishikawa, "Investigation of the effect of tube motion in breast tomosynthesis: continuous or step and shoot?," *Proc SPIE,* vol. 7961, p. 79611E, 2011.

[133] C. Hofmann, M. Knaup, and M. Kachelriess, "Effects of ray profile modeling on resolution recovery in clinical CT," *Medical Physics,* vol. 41, Feb 2014.

[134] S. Tilley, M. Jacobson, Q. Cao, M. Brehler, A. Sisniega, W. Zbijewski*, et al.*, "Penalized-Likelihood Reconstruction with High-Fidelity Measurement Models for High-Resolution Cone-Beam Imaging," *IEEE Transactions on Medical Imaging,* pp. 1-1, 2017.

[135] Varian Medical Systems, "Product Details of Varian M-113 Rotating Anode X-ray Tube," 2010.

[136] Fujifilm Corporation, "ASPIRE Cristalle Quality Control Program Manual (2nd Edition)," 2014.

[137] Fujifilm Corporation, "FUJIFILM Medial Systems Produce Profiles," 2014.

[138] A. Robinson and G. M. Grimshaw, "Measurement of the focal spot size of diagnostic x-ray tubes--a comparison of pinhole and resolution methods," *Br J Radiol,* vol. 48, pp. 572-80, Jul 1975.

[139] B. Nielsen, "Measurement of the focal spot size of diagnostic X-ray tubes by the pinhole camera technique. The influence of the pinhole on the measured focal spot size," *Health Phys,* vol. 38, pp. 683-6, Apr 1980.

[140] "Presentation from the GE Healthcare representative at the 2011 AAPM tomosynthesis subcommittee meeting in Vancouver, Canada, on July 31, 2011."

[141] P. M. d. Carvalho, "Low-Dose 3D Quantitative Vascular X-ray Imaging of the Breast," PhD, University of Paris-Sud, 2014.

[142] H.-P. Chan, M. M. Goodsitt, M. A. Helvie, C. P. Paramagul, C. H. Neal, P. L. Carson*, et al.*, "Digital Breast Tomosynthesis (DBT): Observer Performance Study of Microcalcification Cluster Detection in Breast Phantom DBT Acquired with Variable Tomographic Angles, Angular Increments, and Number of Projections," *RSNA Program Book,* vol. 2012, pp. VSBR41-08, 2012.

[143] ICRU, *International Commission on Radiation Units and Measurements (ICRU).Medical Imaging - The Assessment of Image Quality, Report 54* Bethesda, MD, 1996.

[144] X. Qian, A. Tucker, E. Gidcumb, J. Shan, G. Yang, X. Calderon-Colon*, et al.*, "High resolution stationary digital breast tomosynthesis using distributed carbon nanotube x-ray source array," *Medical Physics,* vol. 39, pp. 2090-2099, Apr 2012.